THÈSE DE DOCTORAT

Mécanismes de locomotion ondulatoire sous-marine

Jesús SÁNCHEZ RODRÍGUEZ
Institut de Physique de Nice

Présentée en vue de l'obtention du grade de docteur en Physique **de** l'Université Côte d'Azur

Dirigée par : Médéric Argentina
Co-dirigée par : Christophe Raufaste

Soutenue le : 7 décembre 2021

Devant le jury, composé de:

Médéric Argentina, PR,
Université Côte d'Azur
Christophe Eloy, PR,
École Centrale Marseille
Ramón Fernández-Feria, PR,
Université de Malaga
François Gallaire, PR,
École Polytechnique Fédérale de Lausanne
Christophe Raufaste, MdC,
Université Côte d'Azur
Agnese Seminara, PR,
Université de Gênes
Benjamin Thiria, MdC,
École Supérieure de Physique et de Chimie Industrielles de Paris

DOCTORAL THESIS

Mechanisms of undulatory underwater locomotion

A Thesis submitted in partial fulfillment

of the requirements for the degree of

Doctor of Philosophy in Physics by

Jesús Sánchez Rodríguez

Université Côte d'Azur

Institut de Physique de Nice

Supervisors: **Médéric Argentina**, Professor, Université Côte d'Azur
Christophe Raufaste, Associate Professor, Université Côte d'Azur

Examining Board: **Ramón Fernández-Feria**, Professor, Universidad de Málaga
Benjamin Thiria, Associate Professor, École Supérieure de Physique et de Chimie Industrielles de Paris
Christophe Eloy, Professor, École Centrale de Marseille
François Gallaire, Professor, École Polytechnique Fédérale de Lausanne
Agnese Seminara, Professor, Università di Genova

December 2021

Mécanismes de locomotion ondulatoire sous-marine

Jury:

Président
François Gallaire, Professeur, École Polytechnique Fédérale de Lausanne

Rapporteurs
Ramón Fernández-Feria, Professeur, Universidad de Málaga
Benjamin Thiria, Maître de Conférences, École Supérieure de Physique et de Chimie
Industrielles de Paris

Examinateurs
Christophe Eloy, Professeur, École Centrale de Marseille
Agnese Seminara, Professeure, Università di Genova

Directeur de Thèse
Médéric Argentina, Professeur, Université Côte d'Azur

Co-directeur de Thèse
Christophe Raufaste, Maître de Conférences, Université Côte d'Azur

Résumé

Dans cette thèse, nous nous intéressons à la nage ondulatoire des animaux aquatiques à des nombres de Reynolds élevés, et donc à des régimes pour lesquels les forces inertielles prédominent. La locomotion aquatique implique une interaction complexe entre le corps du nageur et l'écoulement induit dans l'environnement. Pour étudier cette question, nous devons considérer à la fois l'interaction fluide-structure d'un nageur se déplaçant dans un fluide et la perception sensorielle qui en résulte et dicte l'activité motrice. L'interaction fluide-structure est d'abord étudiée dans le premier chapitre à l'aide d'un nageur rigide en forme de profil d'aile qui effectue des mouvements de rotation qui entraînent un déplacement translationnel du nageur. Ensuite, les forces du fluide générées par le mouvement du nageur sont calculées à l'aide de la théorie des fluides parfaits, et la vitesse de locomotion est obtenue en résolvant les lois de Newton. Une résolution numérique des équations est complétée par des calculs perturbatifs dans la limite des petites amplitudes d'oscillation. Ces deux approches permettent d'obtenir une expression de la vitesse de nage en fonction des autres paramètres du problème. Dans le deuxième chapitre, l'activité motrice du poisson n'est plus prescrite mais dépend de l'interaction avec l'environnement. Nous formulons l'hypothèse qu'une boucle de rétroaction basée sur le sens de la proprioception entraîne une instabilité qui engendre la locomotion. Cette hypothèse est testée sur une plateforme expérimentale en utilisant un robot biomimétique attaché à un capteur de force. Nous prouvons que la proprioception est capable de générer des oscillations spontanées de la nageoire du robot, ce qui nous permet de valider l'idée que les nageurs sous-marins pourraient sélectionner leur amplitude et leur fréquence de battement à l'aide de capteurs mécaniques. Nous comparons les résultats expérimentaux à un modèle simple mais générique avec un excellent accord. Enfin, dans le troisième chapitre, nous analysons les allures ondulatoires en fonction de l'adaptation du nageur à son environnement en optimisant deux quantités fondamentales: la vitesse de nage et la dépense énergétique. En imposant différentes cinématiques de déformation, nous étudions dans quelles conditions la vitesse de nage est maximisée. En recherchant des solutions qui minimisent la dépense d'énergie pour des contraintes données, différentes allures de nage sont trouvées. L'allure à mouvement sinusoïdal correspond à celle qui minimise le "cost of transport" pour une amplitude de nage typique donnée. Les résultats analytiques sont comparés à des simulations numériques de type Reinforcement Learning.

Mots clés: Nage, Interaction Fluide-Structure, Proprioception, Instabilités, Optimisation

Abstract

In this thesis, we are interested in the undulatory swimming of aquatic animals at high Reynolds numbers, where the inertial forces predominate. Aquatic locomotion involves an intricate interaction between a swimmer and its environment. Therefore, understanding this process requires to consider the fluid-structure interaction of the swimmer moving within a fluid and the sensory perception that feeds back its motile activity. The fluid-structure interaction is studied in the first chapter utilizing a rigid airfoil-shaped swimmer that performs an oscillatory motion converted into a translational motion. Then, the fluid forces generated by the imposed kinematics are calculated using inviscid fluid theory, and the locomotion velocity is obtained by solving Newton's laws. The numerical solution of the equations is further complemented with perturbative calculations in the limit of small oscillation amplitudes. Both approaches are consistent and give predictions of the swimming velocity as a function of the parameters of the system. In the second chapter, the interaction with the environment is extended and the motile activity of the fish is not prescribed anymore but is driven by the fluid-structure interaction. We hypothesize that a feedback loop based on the proprioception sense results in an instability, driving the locomotion. This hypothesis is tested on an experimental platform using a biomimetic robot attached to a sensor force. We prove that proprioception is able to generate spontaneous undulations of the robot, which validates the idea that underwater swimmers might select their amplitude and beating frequency using mechanical sensors. We compare the experimental results to a simple yet generic model with excellent agreement. Finally, in the third chapter, we investigate the undulatory gaits as functions of the swimmer's adaptation to the environment by optimizing two fundamental quantities: the swimming speed and the energy expenditure. By imposing different deformation kinematics, we study what are the conditions to maximize the swimming speed. By requiring that satisfactory swimming gaits are solutions that minimize the energy expenditure for some given constraints, several sets of gaits are found. The harmonic gait is recovered as the one that minimizes the cost of transport for a given typical tail beat amplitude. The analytical results are compared with numerical simulations performed with a Reinforcement Learning algorithm.

Keywords: Swimming, Fluid-Structure Interaction, Proprioception, Instabilities, Optimization

A mi madre

Y cuando llegue el día del último viaje,
y esté al partir la nave que nunca ha de tornar,
me encontraréis a bordo ligero de equipaje,
casi desnudo, como los hijos de la mar.

Antonio Machado
Retrato

Agradecimientos

Tras tres años de duro trabajo para construir un proyecto tan importante tanto en lo académico como, por supuesto, en lo personal, hay muchas personas que, de alguna forma u otra, han contribuido a finalizar esta etapa. Aunque me encantaría dedicar unas palabras a todos los que han pasado por mi vida y que para bien o mal han forjado la persona que soy, algo así queda fuera totalmente de la intención de este humilde reconocimiento, y aunque mi agradecimiento para todos ellos sea tácito, me gustaría enumerar en estas páginas a aquellos que mi memoria, a veces traicionera, considera que deben quedar plasmados por escrito.

Quiero agradecer en primer lugar a todos y cada uno de los miembros del jurado por haber aceptado evaluar y asistir al acto de defensa en estos momentos en los que los actos presenciales se han convertido en inusuales. Gracias a los examinadores, Christophe Eloy y Agnese Seminara, por sus cuestiones y comentarios sobre mi trabajo. Mi más sincero reconocimiento a Ramón Fernández Feria y a Benjamin Thiria, por aceptar erigirse como rapporteurs, por su lectura concienzuda y sus comentarios enriquecedores sobre el manuscrito. Igualmente también mi especial reconocimiento a François Gallaire, que además de honrarme aceptando presidir el jurado, me recibió con emoción y anhelo en la EPFL durante dos estancias, y además vuelve a darme su confianza de nuevo, acogiendome como investigador postdoctoral en su laboratorio.

No tengo ni probablemente tendré suficientes palabras tampoco para agradecer a mis directores de tesis, Médéric Argentina y Christophe Raufaste. La primera vez que contacté con Médéric no podía llegar a imaginar cómo de esa presentación tan peregrina el proyecto de tesis que ocupan estas líneas se materializaría poco después. Desde el principio apostaste por mí de una forma ciega, diste todo lo que estaba en tu mano para que las probabilidades se pusieran de mi lado, y de hecho así ocurrió. Me has formado como un investigador en todas las facetas posibles, no sólo en enseñarme todas las herramientas que sabías y que ahora yo utilizo también con soltura, sino en animarme a viajar, a exponer mis resultados, a discutir con otros colegas, a tejer una red sólida de contactos. Has estado siempre ahí y por eso no podría haber elegido a un mejor mentor que tú. De Christophe tengo únicamente buenas palabras; aunque en un principio pensaba que nuestros contextos eran diferentes, pronto me di cuenta de lo equivocado que estaba, pues de él he aprendido tanto como de Médéric, en áreas diferentes que en ningún momento pensé que iba siquiera a tratar, pero que han supuesto conocimientos imprescindibles para mi formación. Sin embargo, de él recalco su valía como persona y su ética de investigador, que también en todo momento se ha encargado de inculcarme, de una forma directa pero sin presiones, de forma que fuese yo el que decidiera absorberla y entenderla como mía. Ambos me habeis tratado siempre con respeto, me habeis valorado y escuchado, dándome la autonomía que pedía sin rechistar, pero a la vez guiándome cuando era más necesario que nunca. Por todo esto y más, gracias.

Quiero, por supuesto, agradecer a todos los compañeros del laboratorio. A Nathalie Hamel, François-Regis Huc e Isabelle Larochette, por su eficacia y simpatía en todo momento. A todos los miembros del equipo Fluidos Complejos, donde estaba integrado, por todo el tiempo pasado entre reuniones y discusiones, especialmente a Nathalie Fraysse, Franck Celestini y Harunori Yoshikawa. A Patrizia Vignolo por su cariño y trato en la docencia que compartimos juntos y que tantas cosas buenas me ha dado. A Giovanna Tissoni, por su deportividad y su buen trato, por aceptar formar parte de mi comité de tesis y por sus buenos consejos. Sin duda a todos los doctorandos y post-docs con los cuales he compartido tantos momentos. Un especial recuerdo y cariño a Vittorio, Marius, Antonin y Ana. A Li Fu, mi querido compañero en el proyecto, con el cual he trabajado tanto a lo largo de este último año y con quien me he compenetrado tanto en el avance de nuestras investigaciones, con visiones diferentes pero complementarias, que han contribuido a aumentar aún más la calidad del trabajo que realizamos. Pero sin duda, a quienes más agradecido estoy es a Pierre Azam, Adrián Bartolo y Alexis Verschelde, los compañeros

Contents

Chapter 1

Introduction

Nature constitutes the living system par excellence. Over millions of years, it has proven to have sufficient mechanisms for managing and using its resources efficiently and continuously. These mechanisms, moreover, have made the life and organisms of the planet an excellent model to imitate in a multitude of aspects of our lives. Animals, plants, and living beings in general, through evolution, have developed biological mechanisms to cope with the challenges of the environment with the sole purpose of survival [1]. The variety of habitats and ecosystems is gigantic, yet the organisms living there have always found ways to optimize and devise new strategies to ensure the perpetuation of the species. That is why nature constitutes the reference and the primary source of inspiration that has enabled the progress of humanity throughout history [2]. The sustainable design demonstrates that the human being, to evolve, has to explore and learn from the place they come from. Among all the possible interactions between man and his environment, the seas have fascinated humans ever since they first became aware of the world in which they live in [3]. The vast and unreachable expanses of water that stretch before the eyes of man have always provoked his curiosity. Civilizations have always tried to develop their potential by the seas, taking advantage of the enormous resources they can provide and giving men an immense desire to dominate the oceans to explore the unknown. Nevertheless, and in spite of this close relationship, even today, there is not a complete knowledge of what happens in these places that constitute about three-quarters of the Earth. Over 80 percent of the oceans are still unexplored [4]. One of the reasons is the lack of efficient locomotion strategies to move in this huge three-dimensional space. The total lack of maneuverability in the marine environment has led humans to conceptualize and develop strategies to make sailing or extracting food and different goods from the sea possible. The technological and industrial progress emerged over the years has substantially improved the means used to carry out these two tasks while adding new interactions between the environment and man through leisure in the form of recreational travel or water sports. All this brings a growing industrial interest in offshore applications, constituting a backbone in the economies of many countries and sectors. For example, only in 2017, the cruise industry contributed 47.86 billion to the European economy [5]. Similarly, USA Navy's shipbuilding plan is estimated to cost about $ 21 billion, also in 2017 [6], and the impact of commercial and recreational saltwater fishing in the United States in the same year supported 1.7 million jobs in communities across the country [7].

To master what happens in the oceans, we have to look at how their principal inhabitants behave. Fish exhibit an optimized locomotion strategy, both in terms of energy consumption and maneuverability, with efficiencies clearly exceeding those achieved by human designers. Such is the case that even studies carried out on actual swimmers could not explain this gigantic efficiency, since according to some of the swimmers' muscle power was not enough to overcome the drag power experienced. This fact is known as Gray's paradox [8], who formulated this statement when studying dolphins swimming, but that today is considered solved thanks to revisions of his work and genuine results issued by advanced experimental methods [9, 10].

This is partly due because the physics of fish locomotion is still an open field of research and essential challenges need to be overcome. Understanding the physics at play is a prerequisite to imagine smart innovations in the field of transport and exploration (marine vehicles) as well as for the survey of the oceans (autonomous underwater robots). For the latter, robotic fish constitute the natural solution inspired by nature and an unimaginable source of future opportunities and applications [11]. In the context of the scientific exploration of the seabed, this will help to better analyze and understand marine animals' ecology and ethology and the biodiversity of habitats at great depths (especially micro-habitats). Such robots can also be used by oceanographers to study the oceans' currents, salinity, and oxygen and carbon dioxide content. Finally, exploring shipwrecks or archaeological submarines sites could be facilitated by the use of highly maneuverable robots. Another possible field of application that might be interesting is bio-hydraulic studies. For example, the construction of structures on rivers, like locks or dams, impacts the environment. These robots might be beneficial to explore as fish the consequence of constructions led by humans. Actually, fishlike robotic systems have proven to be very efficient underwater vehicles from early attempts [12, 13] to very advanced prototypes [14–16]. Their ability to probe the environment [17–19] or their own deformation [20] opens the route toward fully autonomous artificial swimmers in the near future.

Imitating as much as possible natural swimmers is a proposed goal to extrapolate this information to artificial systems. First, however, it is fundamental to really understand how fluid mechanics works in this system to decipher the way forward in optimizing these devices. Nevertheless, modeling swimming is not straightforward, as we will adequately justify in this manuscript. The first significant breakthroughs in the understanding of swimming mechanisms were made in the 1950s by Richard Bainbridge [21]. Bainbridge's work was one of the first experimental setup to study the relation between the kinematic characteristics of swimmers (mainly tip-to-tip tail beat amplitude A and frequency f) and the swimming speed, U.
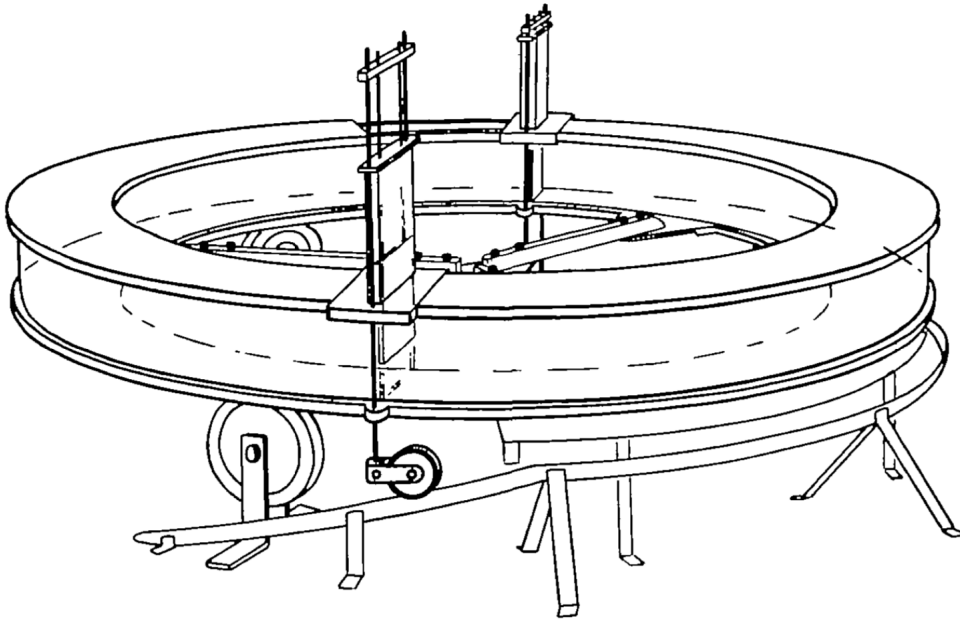
Figure 1.1: Annular rotating vessel used by Bainbridge to perform the experiments on actual swimmers. From Bainbridge [21].

For this purpose, Bainbridge devised an ingenious experimental device, depicted in figure 1.1. It consists of an annular rotating vessel whose control parameter is the rotational speed. A fish is introduced into this vessel; as soon as it starts swimming, the wheel is rotated at the same speed but in the opposite direction to his movement, keeping him stationary relative

to the observer [21]. Then, in the steady-state regime, a camera placed just above the place where the fish swims gets the images from which amplitude and frequency can be measured. He obtained a simple relation linking length, frequency and velocity:

$$\frac{U}{L} = \frac{3}{4}f - 1.$$

In addition, Bainbridge showed that the tail amplitude of the swimmers remained approximately constant for any oscillation frequency or velocity, and that this constant value was around 0.2:

$$\frac{A}{L} \approx 0.2.$$

These two empirical results motivate finding a direct relationship of the swimming speed with two fundamental quantities that the swimmer can vary, the amplitude and the frequency. This relationship is realized through a dimensionless number known as Strouhal number and defined by the following expression:

$$St = \frac{fA}{U}.$$

This quantity receives much attention because it turns out to be approximately constant for animals of many different species and scales. Actually, it is shown that these animals cruise in a relatively narrow range of Strouhal numbers, around 0.3 [22–25], as depicted in figure 1.2. According to Bainbridge's measurements, the Strouhal number resulting from his empirical relationship is 0.27, which is in good agreement with the data for biological swimmers.
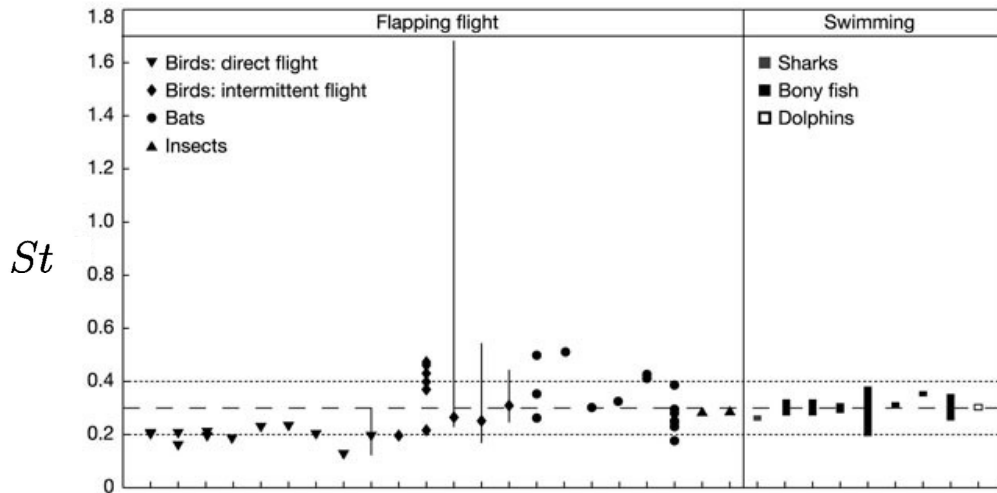
Figure 1.2: Strouhal number for 42 species of flying and swimming animals. Most of these animals cruise at a Strouhal number between 0.2 and 0.4. From Taylor et al. [23].

Theoretical models attempting to explain these facts were subsequently developed and we give them an extensive treatment in chapter 2. However, along with the flourishing of analytical and numerical models to describe the swimming mechanisms, new experimental methods aimed at establishing new relationships and uncovering new mechanisms. The methods involving living animals are, although much more realistic, undoubtedly complicated since total control over the animals does not exist, and their physical condition can affect their performance. Nevertheless, over the last few years, real technological challenges have been achieved in acquiring data from actual swimmers, such as the placement of accelerometers on cetaceans to understand how these animals move [26, 27].

This is why numerous artificial systems have been studied, such as rigid foils undergoing heaving and pitching motions [12, 28, 29], flexible panels [25, 30], or robots [15, 16]. Although conceptually different, most experiments consist in varying the kinematic parameters A and f and finding the free-swimming velocity U, as well as characterizing the force exerted by the fluid on the swimmer. These experiments have yielded promising results in the understanding of the swimming phenomenon: experiments performed with NACA airfoils [31] to mimic the motion of the caudal fin have proposed as an energy efficiency explanation the setting of the value of St (figure 1.3a). The maximum efficiency of the appendage for a fixed A/L value is found around the value $St \sim 0.3$, implying that natural selection has tuned animals to use this range of Strouhal numbers because it confers high-efficiency [31]. Similarly, experiments with flexible panels [25] have shown that fixing the value of St is not the only requirement for higher energy efficiency, but also the value of A/L is critical. These experimental results issued by Saadat et al. (figure 1.3b) suggest that a swimmer can minimize its input power by selecting a value of A/L close to 0.2, which would agree with Bainbridge's experimental results.
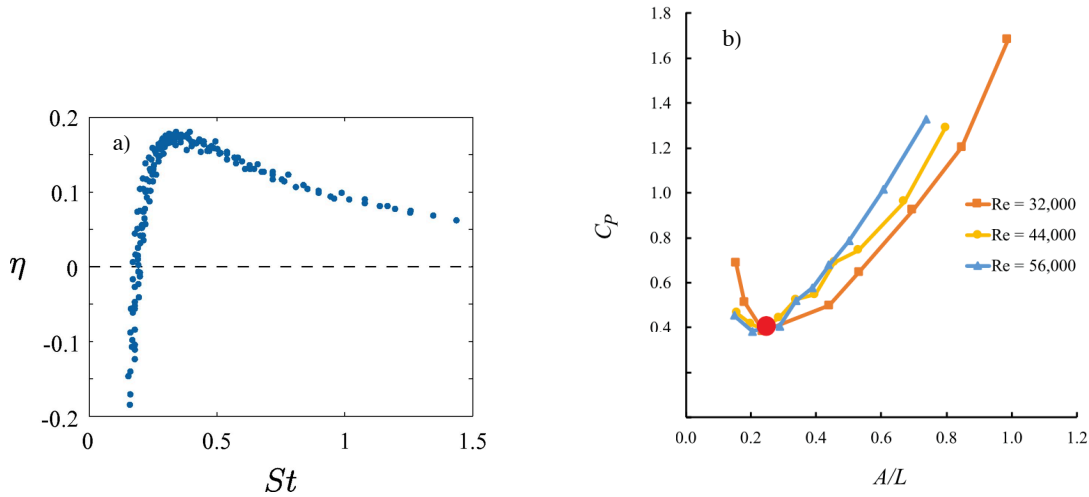
Figure 1.3: a) Efficiency curve as a function of St. The maximum value of efficiency is achieved for $St \sim 0.3$. From Floryan et al. [31]. b) Power coefficient for different Reynolds number as a function of A/L. There is a value of A/L around 0.2 which minimizes the power coefficient. From Saadat et al. [25].

All these experimental results are further supported by theoretical considerations using scaling laws. The complete understanding of swimmers' locomotion involves an enormous number of different and complicated shapes and geometries. Thus, instead of finding exact expressions taking into account all the characteristics of the swimmers' shapes, it is advantageous to know the functional relationships between swimmers and fluid as a function of the most important parameters. Formulating a scaling law requires a large and statistically acceptable set of data collected in nature, which is usually challenging to obtain. Performing the experiments to collect such data is an investigation in itself. In addition, the data are not always published, and accessing them usually means an extensive literature search. For example, let us consider the relationship between the oscillation frequency of a swimmer f and its length L. As a general rule, it seems clear that smaller animals move their appendages faster than larger ones. This observation could be perfectly described by a scaling law connecting the two variables by the following expression:

$$f \sim L^{-a}, \tag{1.0.1}$$

with a a strictly positive coefficient realizing that for increasing lengths the frequency must be

a decreasing function.

A relationship such as the above is called an allometric relationship [32] since it relates some characteristics of an animal to its body size or body mass. Many papers have tried to establish a reasonable explanation for this relationship; however, not all of them agree on the exponents they give, and the comparison with measurements taken from biological swimmers may appear biased at some point. Wu [33] presents the exponent a of equation 1.0.1 as a function depending on the metabolic rate, Bale et al. [34] and Sato et al. [35] find an exponent $a = 1$ while Bejan and Marden [36] and Gough et al. [37] recover a value near 0.5. Our swimmers data are represented in figure 1.4. These data consist in length, amplitude, frequency and velocity of the swimmer, and are collected from a multitude of animals ranging from some centimeters to 20 meters and from different species and shapes. The articles we have used to extract these data are cited next [21, 38–51].
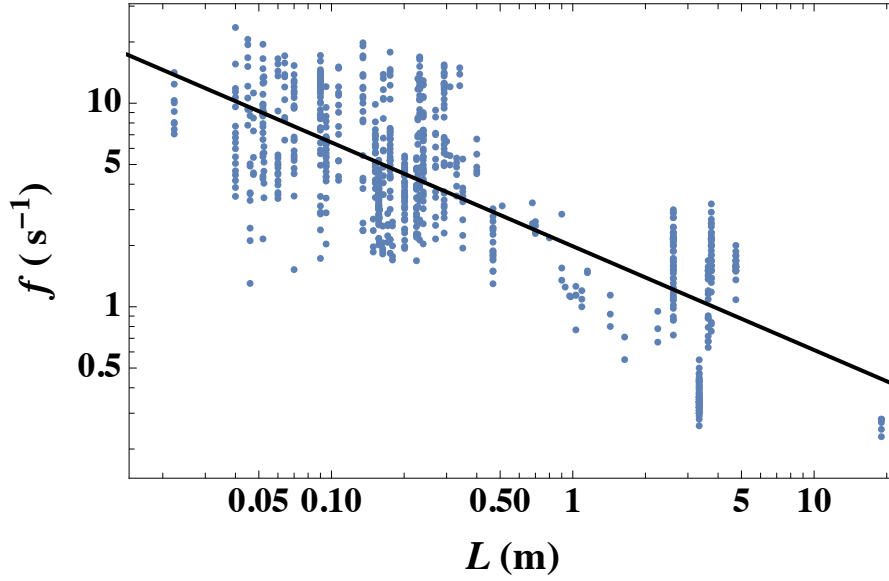
Figure 1.4: Oscillation frequency as a function of animal's length. The blue points represent the experimental data gathered in actual swimmers while the black line correspond to the fit $f = 1.98L^{-0.51}$.

According to the graph, we see a large dispersion of the data. We do not know under which conditions these experiments have been performed nor what levels of activity each of these swimmers were developing, factors that might cause this dispersion. Scaling laws have already been obtained with experiments performed at the same performance level, such as the one from Hirt et al. [52] where an allometric law of the maximum locomotion velocity is deduced. However, we realize that a fit of the type $f \sim L^{-0.51}$ recovers the decreasing trend of the frequency quite well, a trend that we also find in the literature [36, 37] (figure 1.5a). Our hypothesis to explain this behavior is that the lateral power generated by the muscles must be of a sufficient order of magnitude to overcome the power dissipated by the drag force. The power of the muscles is equal to the force generated by the muscles, EL^2, multiplied by the lateral displacement velocity, i.e., the tail velocity:

$$P_{\text{lat}} \sim EL^2Af,$$

with E the Young's modulus.

On the other hand, the drag force reads:

$$F_{\text{drag}} \sim \rho L^2U^2,$$

which, multiplied by the swimming speed yields the expression for the power dissipated:

$$P_{\mathrm{drag}} \sim \rho L^2 U^3,$$

with ρ the density of water. If we balance both quantities and use the fact that $U \sim Af$ and $A/L \sim$ cte we finally obtain that the oscillation frequency of the tail should be written as:

$$f \sim \sqrt{\frac{E}{\rho}} L^{-1}.$$
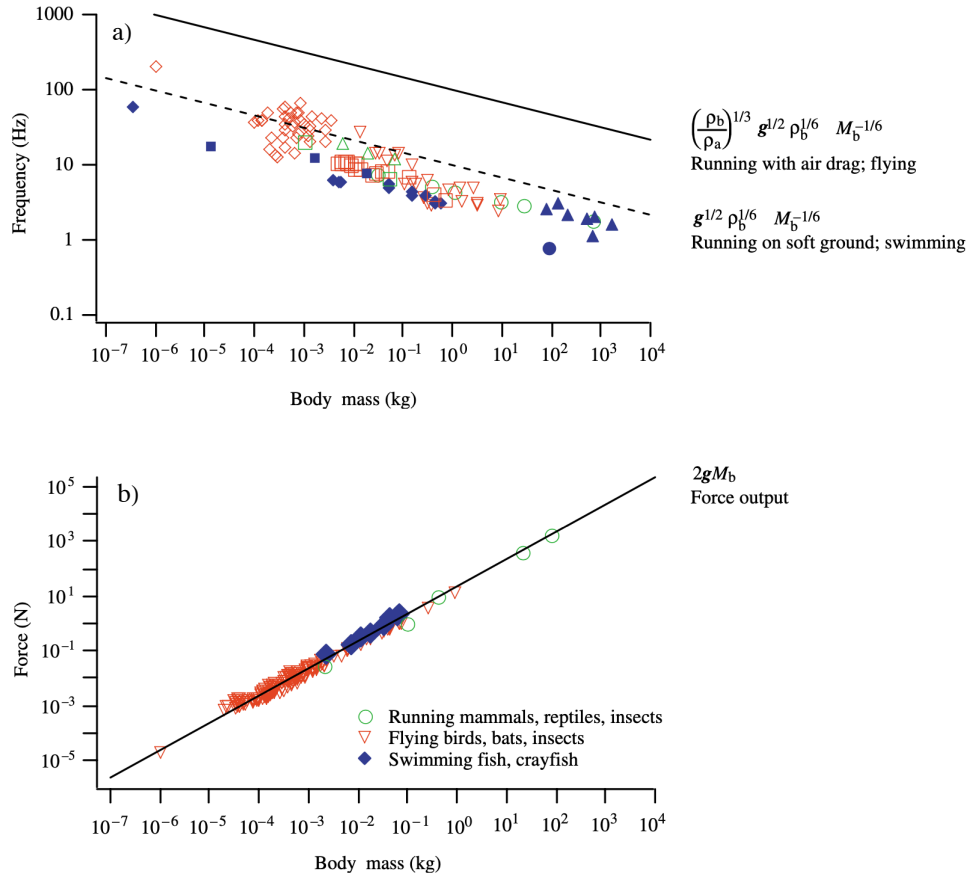
Figure 1.5: Comparison of theoretical predictions with the motion frequencies a) and force outputs b) for a wide variety of running, swimming and flying animals. From Bejan and Marden [36].

As we can see, the coefficient we obtain is not at all the one we observe in the figure 1.4. For both to coincide, the velocity of wave propagation in the swimmer, which is precisely the term $\sqrt{E/\rho}$, should be proportional to the length of the swimmer in order to obtain the desired exponent. The stiffness of swimming animals is a feature susceptible to be varied to achieve a better swimming performance [53–55], which could mean a possible dependence of the propagation velocity with the swimmer's length. We aim at exploring a different supposition, so, in what follows, we consider that the density of the medium is a constant quantity and so is the Young's modulus of the animal muscles [56]. The point where our argument seems to fail is in the scaling of the muscle force that produces the lateral undulations. This force is proportional to a cross-sectional area, which implies that this area must be proportional to L^2 for geometrically

similar animals. Structures of different sizes are geometrically similar if each of their linear dimensions can be related by a common proportion [57]. This characteristic is true for aquatic animals: cetaceans ranging from small dolphins to blue whales have lengths proportional to $M^{0.34}$, with M the mass of the animal, very close to geometric similarity [58], and fish of different sizes also tend to be close to geometric similarity [32]. Even when complying with the precepts of geometric similarity, like a large majority of terrestrial mammalian species [59], the force-generating capacity of some limb muscles is bigger than expected in this theory due to the positive allometric scaling (exponent of L larger than 2) of muscle fiber cross-sectional area [60]. In addition, the maximum force capable of delivering the muscles of swimming animals appears to scale as a single isometric function of the animal mass [61], as shown in figure 1.5b.

In this case, we need to take into consideration that forces may not depend on a cross-sectional area but on the animal's mass. Muscle cells are composed of contractile elements called sarcomeres, which are the basic units of contraction generation [62]. The hypothesis is that the length of a sarcomere does not vary much depending on the animal's length and can be considered almost a constant quantity. However, the size of the muscles does depend on the size of the animals, being bigger the larger they are. To relate both observations, we can suppose that, although the size of the sarcomeres does not vary from animal to animal, the number of sarcomeres N_{sarc} does vary from individual to individual and can be written as:

$$N_{\text{sarc}} \sim \frac{L^3}{l_0^3},$$

where l_0 is the typical length of a sarcomere.

Thus, the lateral force generated by a muscle will be equal to the force generated by a single sarcomere, F_0, multiplied by the number of sarcomeres present:

$$F_{\text{lat}} \sim N_{\text{sarc}} F_0 = \frac{L^3}{l_0^3} F_0.$$

Multiplying by the lateral velocity, Af, to obtain the power and balancing with the drag power, $\rho L^2 U^3$, we get the scaling law for the oscillation frequency, which in this case reads:

$$f \sim \sqrt{\frac{F_0}{\rho l_0^3}} L^{-\frac{1}{2}}.$$

The value of the coefficient $\sqrt{F_0/\rho l_0^3}$ is approximately 6 $\text{m}^{1/2}.\text{s}^{-1}$ for typical values of $l_0 \approx 3$ μm [63] and $F_0 \approx 1$ pN [64], which is in entire agreement with the data in the figure 1.4. This scaling result also shows how the acceleration provided by the muscles $F_0/\rho l_0^3 \sim 36$ would be of the same order of magnitude as the gravity acceleration, g, which would imply the ability of animals to counteract gravitational effects.

The introduction that we have developed here shows problems that require an elaborated understanding to comprehend swimming. The scaling laws we have just derived do not yet show a satisfactory explanation of the relationship between length and frequency of oscillation of aquatic animals. It is a challenge to know how the kinematic parameters of these animals, such as the frequency and amplitude of oscillations, are configured in the way we observe them in nature. Or understand how the Strouhal number, which relates the kinematic parameters to the cruising speed, is a quantity that remains almost constant for the vast majority of aquatic organisms, despite their morphological or physiological differences. It is an open question whether these facts respond to energetic criteria or synergies between the interaction of the swimmer with its surroundings. The optimization of locomotion according to undulatory gaits or the selection of the swimmer's dynamics from a closed-loop feedback with the environment are some of the hypotheses that we tackle in this manuscript to attempt to answer these questions satisfactorily.

Organization of the thesis

Apart from the introduction and conclusions, this thesis is divided into three chapters:

In the second chapter, we introduce the traditional mathematical models in the study of swimming. We then enunciate a model that contain the minimal ingredients to trigger swimming. We make a dynamic analysis to understand how the swimming speed and Strouhal number depend on the kinematic characteristics of the swimmer and the physical parameters of the fluid.

In the third chapter, we point out the problem that exists in many models and experiments where the kinematics of the swimmer must be imposed. Employing a simple model of interaction with the environment, we propose a mechanism that induces the swimmer to select its amplitude and swimming frequency according to the interaction with its surroundings. The predictions of the model are compared with experimental results obtained with a biomimetic robotic swimmer.

In the fourth chapter, we explore different optimization strategies. We study different tail dynamics and maximize the speed or thrust force as a function of different parameters. Moreover, without considering any prefixed motion, we obtain the tail movement that minimizes the energy spent by the swimmer to move. Finally, the theoretical results are compared with numerical simulations performed with Machine Learning.

Moreover, three appendices at the end of the manuscript provide complementary information to better understand our approaches. The first one describes exhaustively the experimental setup and the techniques to perform the measurements. The second one introduces the multiple scale method for solving problems using a perturbative development, which we exploit in the chapters 2 and 3. Finally, the third appendix introduces the notions of dynamical system and bifurcation, paying particular attention to the change of stability of a system by means of a Hopf bifurcation, a concept that constitutes a fundamental part of the chapter 3.

Chapter 2

A minimal model of self propelled locomotion

2.1 Introduction and context

The motion of an organism in a fluid results from the coupling of the dynamics of the swimmer and the surrounding fluid. In this fluid-structure interaction (FSI) problem, the exact resolution becomes very complicated for two fundamental reasons. First, the deformation of the animal itself viewed solely from a mechanical point of view (i.e., without consideration of how the information is transmitted from the motor neurons to the movement mechanisms) introduces severe problems in identifying and calculating the stresses and loads applied to the animal. Even with all the loads completely calculated, the equations governing the dynamics of the deformations are not simple and depend strongly on the magnitude of the deformations and/or rotations produced and the materials of the structure itself. The theory of linear elasticity deals with the dynamics of small deformations. However, it ceases to be valid as soon as the difference between the shape of the deformed and undeformed structure is very different, which usually occurs in the case of biological soft tissue, which composes the animals material. This will then lead to the application of more general frameworks where nonlinear terms taking account of large deformations are included (large deformation theory) [65]. However, many exciting results have indeed been obtained in the case of small deformations, simplifying the complex shapes of animals to that of beams and consequently using the classical beam theory, mainly Euler-Bernoulli [66–68].

In addition to its deformations, animals move in a fluid medium generating a distribution of velocities and pressures in its environment. The knowledge of the forces distribution that the fluid exerts on the organism is essential to understand the loads and the fluid-structure coupling, and this knowledge is only possible if the velocity and pressure fields in the animal's environment are known. The unknowns, in this case, are the three components of the fluid velocity, $\boldsymbol{u}$, (since the animals move in a three-dimensional space) and the pressure, p, which is a scalar quantity. The first equation is the mass balance equation, which links the temporal evolution of the density to the mass flux [69]; it writes as:

$$\frac{\partial \rho}{\partial t} + \nabla \cdot (\rho \boldsymbol{u}) = 0,$$

where we introduce the density of the fluid, ρ.

However, most of aquatic animals live in water, whether fresh or salt, whose density does not crucially depend on either space or time (for a given pressure and temperature set). Fluid is defined as incompressible, and the continuity equation takes the following form:

$$\nabla \cdot \boldsymbol{u} = 0. \tag{2.1.1}$$

The fluid can be considered incompressible as long as the typical velocity of the fluid is considerably less than the propagation velocity of pressure waves. Bearing in mind that under standard conditions of pressure and temperature, the speed of sound for fresh and saltwater is approximately 1500 m.s^{-1} [70] we can ensure at all times that the displacement of the animal is in the subsonic regime and therefore the velocity field will remain divergence-free.

The conservation of momentum equations are the three additional equations which, coupled to the continuity equation, constitutes the system to be solved. The vector equation reads:

$$\rho \left(\frac{\partial}{\partial t} + \boldsymbol{u} \cdot \nabla \right) \boldsymbol{u} = -\nabla p + \mu \nabla^2 \boldsymbol{u}, \tag{2.1.2}$$

with μ the dynamic viscosity of the fluid.

The set of equations 2.1.1 and 2.1.2 is known as the Navier-Stokes equations and governs the dynamics of Newtonian and incompressible fluids. In addition to these equations, the boundary conditions must be given, forcing the compliance that the fluid velocity in the region bounded by the swimmer must be identical to the velocity of the material point on the body's surface, S.

Analytical solutions are not abundant and are reduced to a scarce number of cases [71]. In addition, another fundamental problem is added, and that is that the surface, S, can have a time-dependent shape, which will also depend on the response of the fluid. To simplify the problem somewhat, it is always possible to take a rigid surface and observe the fluid forces exerted on the body to deduce the thrust and the lift forces. In case there is no hypothesis about the surface, its motion must also be found as part of the solution [72].

Therefore, once the problem has been solved, the forces on the organism are calculated as follows:

$$\boldsymbol{F} = \iint_S \sigma \cdot \boldsymbol{n} dS,$$

where $\boldsymbol{n}$ denotes the normal vector to the surface and σ is the classical stress tensor in fluid mechanics, defined as:

$$\sigma = -p \, \mathrm{I_d} + \mu \left[\nabla \boldsymbol{u} + (\nabla \boldsymbol{u})^{\mathrm{T}} \right],$$

where $\mathrm{I_d}$ denotes the identity matrix and the superscript T the transpose of a matrix.

The stress tensor is composed of two terms, one dependent only on the pressure field and another that captures the effects of viscosity. Whether one force dominates over the other depends mainly on the characteristics of the flow produced by the motion of the organism. A dimensionless quantity known as the Reynolds Number, Re, is defined to distinguish which regime dominates or when the overlap between them occurs. This dimensionless number measures the ratio of the orders of magnitude of the inertial terms to the viscous forces. For example, by introducing a characteristic length of the system, the size of the animal, L, and a characteristic velocity, the swimming speed, U, the Reynolds number reads:

$$Re \sim \frac{\rho \left(\boldsymbol{u} \cdot \nabla \right) \boldsymbol{u}}{\mu \nabla^2 \boldsymbol{u}} \sim \frac{\rho U^2 / L}{\mu U / L^2} = \frac{\rho U L}{\mu}.$$

Very small Reynolds numbers $Re \ll 1$ exhibit a predominance of viscous forces and are the typical scenarios where microorganisms and animals of sizes typically smaller than a millimeter coexist. In this case, the inertial terms of the equation 2.1.2 disappear and the equation becomes linear, and traditional mathematical methods based on the superposition principle can be exploited. The Navier-Stokes equations reduce to the Stokes equations with significant consequences for locomotion [73–75]:

$$\nabla p = \mu \nabla^2 \boldsymbol{u}.$$
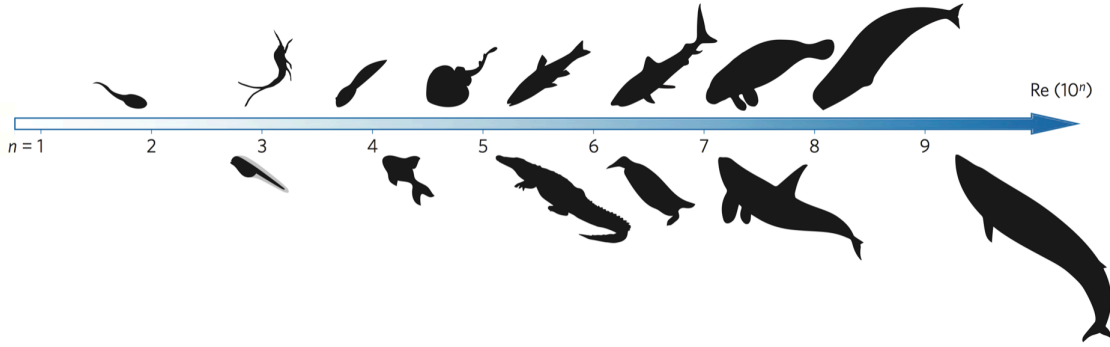
Figure 2.1: Inertial swimmers considered in this manuscript and their associated Reynolds number, gathering larvae, fish, amphibians, reptiles, marine birds and large mammals. From Gazzola et al. [24].

The objective of my PhD project is the study of locomotion in animals of macroscopic size, as those depicted in figure 2.1. These animals vary in length from a few centimeters to the approximately 30 meters that can reach blue whales, the largest animal inhabiting the oceans, and that therefore will not be affected by viscous forces in the same way as by the inertial terms of the Navier-Stokes equations, where the latter will dominate the dynamics. The main difference with the Stokesian case is the loss of linearity due to the nonlinear convection terms and thus the reduction of analytical methods to treat the system.

However, in this vast range of animals coexist species from different kingdoms with various physiological characteristics, but among which we find an enormous variety in morphology, size and shape. This diversity influences the behavior of macroscopic animals and has led to evolutionary groups of animals sharing very similar swimming patterns. We can consider, for example, animals that propel themselves using their appendages as oars, either employing their wings or legs, as in the case of aquatic birds or certain amphibians. Others manage to propel themselves by ejecting a jet of water out of their specially prepared contracting body cavities, as is the case of jellyfish, squids or cephalopods and even bivalves (figure 2.2). We refer to Alexander's fantastic book [76] which delves into the mathematical description of these modes of locomotion.

The large group that we focus on are those animals that move their spines and propagate deformation waves throughout the body to propel themselves [77] (figure 2.2). This mode of locomotion has long aroused the curiosity of scientists and engineers because it allows good maneuverability, high energy efficiency and an elevated swimming speed. Within this group, there is also a great variety, and classification has been established according to the distribution of amplitudes during undulation along the body by Lauder and Tytell [77]. These authors consider four possible locomotion modes: Anguilliform, Subcarangiform, Carangiform and Thunniform (figure 2.3). Each of these modes is named after a characteristic fish species that performs that mode of locomotion: the first is typical of eels and very slender fish and is characterized by the almost total oscillation of the entire body with wavelengths that do not usually exceed the length of the animal at any time [78]. Subcarangiform and Carangiform modes are characterized by oscillations concentrated closer to the tail where the whole body is not involved and with larger amplitudes, locomotion typically used by animals such as trouts, jacks, or mackerels. Finally, the Thunniform mode, whose name is reminiscent of larger animals such as tuna and also includes sharks, exhibits hardly any body movement; oscillation occurs in the tail while the rest of the body remains fixed and without any apparent bending. These modes of locomotion also share certain similarities with the first group of animals that moved thanks to their appendages. Especially in the Thunniform case, we can consider most of the body as a non-flexible surface with a tail that acts as a hydrofoil and is responsible for the inertial thrust. In addition, the

various dorsal, pectoral and ventral fins influence the swimming gait by shedding vortices and accelerating the flow [77].
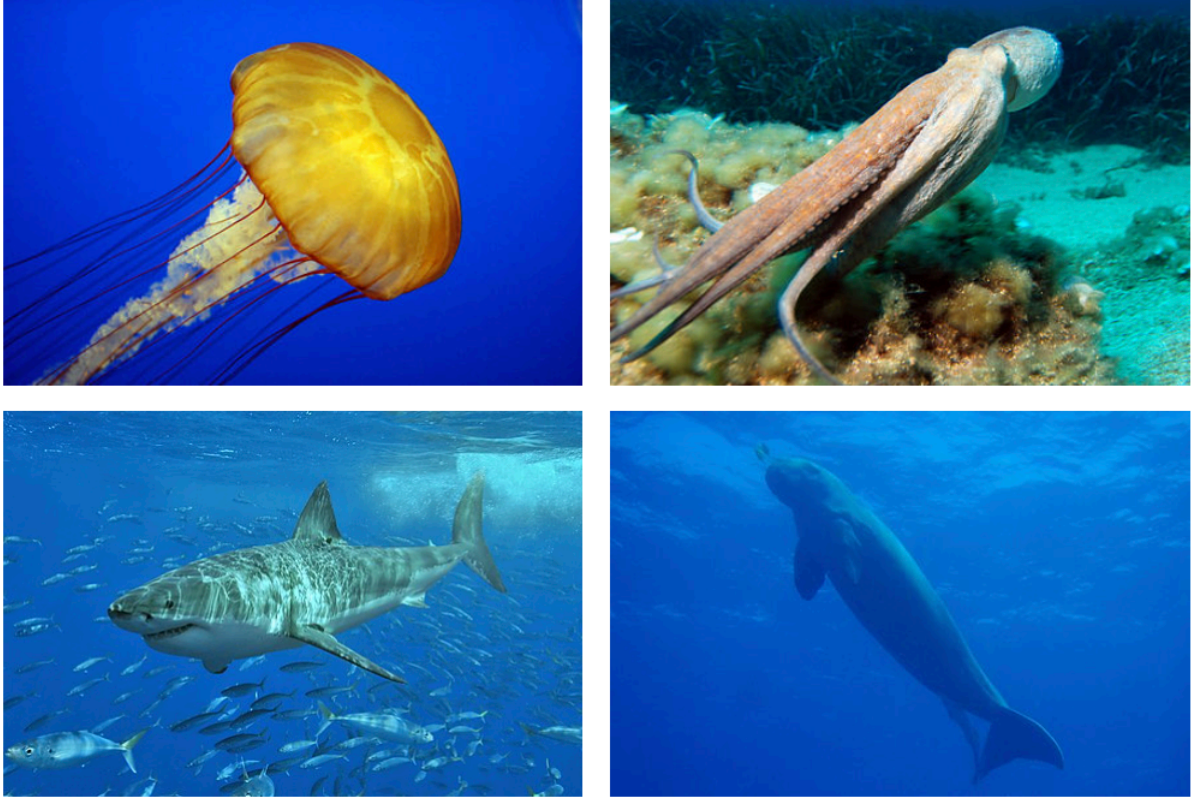
Figure 2.2: Different swimming patterns in aquatic environments. In the upper part of the figure, we consider propulsion by jet ejection, a method of locomotion used by jellyfish and octopuses, and in the lower part locomotion by body undulations, which is the swimming that sharks and manatees perform. From [79–82].

A theory that regroups all these modes and attempts to describe them in a single framework will have to consider the kinematic characteristics of the swimmers, which are primarily the frequency with which the oscillations occur, ω, and the amplitude of these oscillations. One way to account for body undulations is to admit as a representative parameter the amplitude of the tail oscillations, A. This choice is quite natural in the Thunniform and Carangiform modes since most of the oscillations occur around the tail. For the other modes, although ripples are propagating beyond the tail, the most important in magnitude occur at the tip of the tail [83,84]. These two kinematic parameters, ω and A, together with the physical parameters of the fluid, such as its density ρ and dynamic viscosity μ or kinematic ν, determine the locomotion of these swimmers.
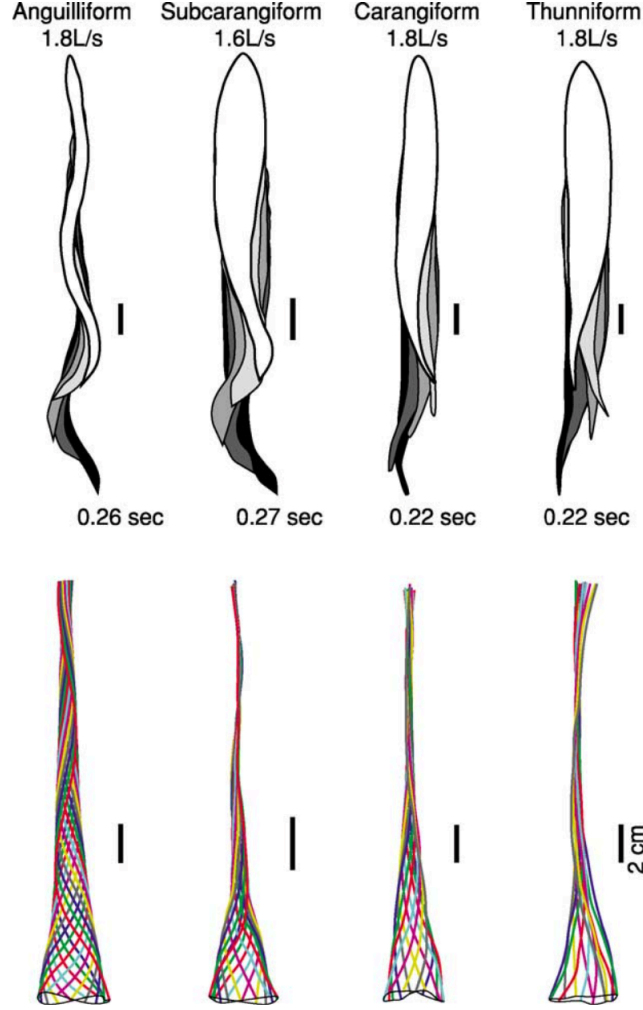
Figure 2.3: Classification of swimming undulation gaits according to total or partial oscillation of the whole body. From Lauder and Tytell [77].

Calculating the exact dependence of the aquatic gait on these parameters is, as we have already stated above, a task that, in principle, exceeds our capabilities. The work of Gazzola et al. [24], however, essentially solves this problem by shedding light on what is the mathematical relationship between swimming velocity U, beating frequency ω, tail amplitude A and kinematic viscosity of the fluid ν. To do so, the authors rely on simple scaling arguments about the forces acting on the system by imposing only the equality of the two forces that dominate locomotion, the thrust force, T, and the drag force, D. When both forces are equal, the animal's swimming speed is nearly constant, being perturbed only by small terms that, on average, do not affect the value of the velocity. The thrust force is calculated as a function of the fluid displaced by the tail movement, assuming that the amplitude of oscillation of the motion is small compared to the length of the organism, L and that it is slender, implying that the acceleration of the fluid can be channeled into longitudinal thrust. The approach is two-dimensional because the undulatory motions are considered to be in the plane, so forces are all calculated per unit depth. Thrust force per unit depth scales as:

$$T \sim \rho \omega^2 A^2 L.$$

Concerning the drag force, there are two different regimes to study depending on the value of the Reynolds number. Since the Reynolds numbers we consider are significantly larger than unity,

viscous forces can be neglected throughout the fluid around the body except in a small region where velocity gradients will be high. This region is confined in the boundary layer, where most of the body's drag is generated. This boundary layer is affected by the Reynolds number and undergoes a transition around a critical value $Re_c \approx 3000$ [24]. For Reynolds numbers lower than this critical value, which we call the laminar regime, the skin drag force is dominated by the viscous shear. For higher values, the boundary layer becomes turbulent, and the pressure drag dominates the skin friction. The drag forces per unit depth corresponding to each of these situations are:

$$D \sim \rho(\nu L)^{1/2}U^{3/2} \quad , \quad Re < 3000.$$
$$D \sim \rho LU^2 \quad\quad\quad , \quad Re > 3000.$$
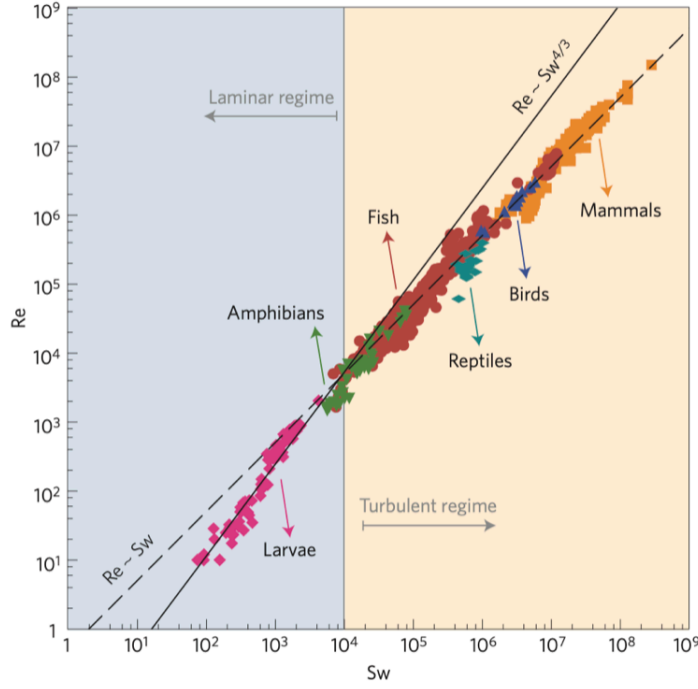
Figure 2.4: Reynolds number as a function of the swimming number Sw for different species of animals showing the existence of two regimes for inertial swimmers, a laminar and a turbulent regime. From Gazzola et al. [24].

Balancing thrust and drag predicts the animal's swimming speed in each of the different regimes.

$$U \sim A^{4/3}\omega^{4/3}L^{1/3}\nu^{-1/3} \quad , \quad Re < 3000.$$
$$U \sim A\omega \quad\quad\quad\quad , \quad Re > 3000. \tag{2.1.3}$$

These two scaling laws deduced from simple arguments turn out to be efficient and perfectly predict swimming speed as a function of A and ω. A dimensionless quantity called Swimming Number, Sw, has been introduced, defined by

$$Sw = \frac{\omega A L}{\nu},$$

which is a kind of transverse Reynolds number since it takes as its characteristic velocity the tail velocity. The tendency 2.1.3 can be rewritten in terms of Sw and $Re = UL/\nu$ as:

$$Re \sim Sw^{4/3} \quad , \quad Re < 3000.$$
$$Re \sim Sw \quad\quad , \quad Re > 3000.$$

And whose behavior has been validated both in numerical simulations [24] and in the natural behavior of biological swimmers, as shown in figure 2.4, remarkably matching theory and data beyond seven orders of magnitude in Re.

Although there is a large amount of works developed since the middle of the last century, we will focus primarily on the seminal work of Lighthill and Wu and the use of airfoils to describe these movements' swimmers. In addition, we present the simple model we have derived, which, although straightforward, captures the fundamental characteristics of locomotion and the relationship of the kinematic parameters of the swimmer to its velocity.

2.2 Classical models of undulatory locomotion

Before exploiting the mathematical techniques to adress the problem of aquatic locomotion, it is necessary to establish the hypotheses that will be taken for granted from now on. As discussed at the beginning of the chapter, swimming is based on the interaction between an organism and the surrounding fluid. A complete theory must describe the forces generated by the muscles and their effect on the fluid, as well as the feedback that exists between the force generated by the fluid and detected by the organism. The animal will adapt its form and the intensity of its muscular activity according to this force. In what follows, such coupling will not be granted, and we will consider a prescribed shape and kinematics of the swimmer to calculate the forces exerted by the fluid. Another approach that is often used when dealing with theoretical models is to reduce the dimensionality of the problem. Aquatic animals live in three-dimensional space. Models of locomotion try to describe the shape of these animals as much as possible, which generally share a common geometrical characteristic with few exceptions; their bodies have a finite length and width. Still, they are thin in the third dimension, which leads to disregarding one dimension and establishing the movement only in the other two. Aquatic organisms have also evolved mechanisms to be neutrally buoyant so that dispensing with a third spatial dimension is an approach that we should find moderately justified. Last but not least, viscosity effects will be neglected at all times, except in the boundary layer. The fluid is considered inviscid unless otherwise stated.

In the models we deal with, the thrust calculation becomes the fundamental magnitude to be solved. The drag forces can be calculated quite accurately taking into account the behavior of the boundary layer and paying special attention to the conduct of the drag coefficient as a function of the Reynolds number and the surface area exposed to the fluid, which also has to be correctly considered. These models are mainly divided into two main types, resistive and reactive, depending on the thrust search strategy. These models are named after how this force is calculated: resistive models are based on estimating the thrust from the drag forces that a system receives and must overcome for locomotion to occur. Such models are found in the work of Taylor [85], in which the swimmer's body is divided into many segments, and in each segment the drag forces per unit length, $\boldsymbol{D}$, are estimated as a function of the fluid velocity and the angle between the flow and the position of the element:

$$\boldsymbol{D} = \frac{1}{2}\rho U^2 d \boldsymbol{C_D},$$

where U is the velocity of the incoming flow, d is a characteristic length of the segment and $\boldsymbol{C_D}$ the vectorial drag coefficient, which depends on the angle between the flow and the position of the segment.

Following the notation of Taylor [85] in each of the segments into which the body is divided, the drag coefficient is calculated using:

$$\boldsymbol{C_D} = [C_D]_p + [C_D]_f,$$

where the subscripts p and f represent the normal and tangential components to the surface, respectively. The main drawback of this procedure is the geometrical calculation of the coefficients for all the divisions into which the body has been divided, which results in a lengthy and tedious method.

Reactive models have been more fruitfully developed and are the cornerstones of the analytical theory of swimming. These models calculate thrust by analyzing the reaction in the fluid caused by the accelerations of the organism itself, a much less passive method than that used in the resistive models. They consider the effect of added mass, which arises when a body is accelerated in a fluid. If we think a body of mass m accelerated by an acceleration a, we are not only accelerating the body but also the surrounding fluid, which gains velocity [86]. Therefore, the force that is intended to move the body has to do work on increasing the kinetic energy not only of the body but also of the fluid, which leads to this force having an additional term:

$$F = (m + m_{add})a,$$

where m_{add} is the fluid added mass.

2.2.1 Lighthill Model

Lighthill [87,88] developed his first work on swimming based on the small perturbation theory of slender swimmers. Lighthill defines a swimmer as slender when its dimensions and movements perpendicular to its direction of locomotion can be judged small compared to the length of the animal, L, as shown in the figure 2.5. Furthermore, we can consider the swimmer permanently in the same position x while performing lateral movements in order to counteract the force arising from a flow coming from the left in the positive direction of the axis with velocity U, which is no more than the swimming speed.
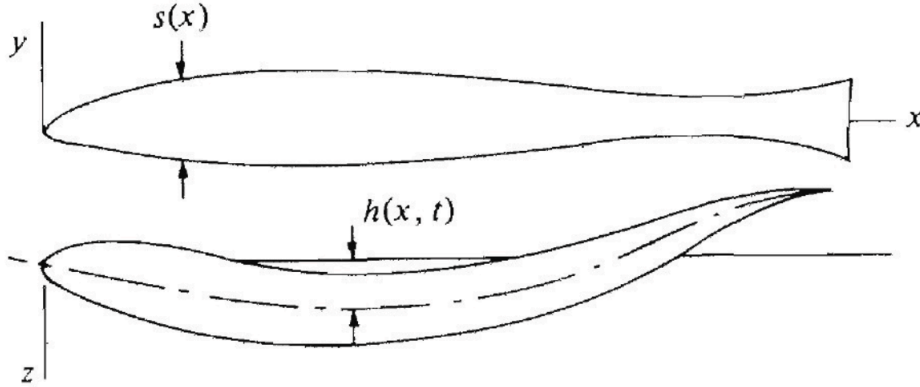
Figure 2.5:   Sketch of a slender swimmer, see text for description of variables. From Childress [72].

The variable $s(x)$ represents the cross-sectional area at position x. Besides, we also require that the tangent plane to the surface forms at all times and positions a small angle with respect to the direction of locomotion, as well as that the variation of $s(x)$ is smooth. Mathematically, this condition is fulfilled if:

$$\left| \frac{ds}{dx} \right| \ll 1.$$

The variable $h(x,t)$ represents the lateral deformation of the organism, and based on the theory of small amplitudes, we require:

$$\left| \frac{\partial h}{\partial x} \right| \ll 1, \qquad \left| \frac{\partial h}{\partial t} \right| \ll U.$$

The objective is then to calculate the thrust forces produced by the animal to overcome the drag. For this, we consider that the flow can be decomposed into two contributions, one corresponding to the steady flow when the animal does not make any movement and $h(x, t)$ is null for any position x; and the other in which we take into account the flow produced by the oscillations of the lateral movements $h(x, t)$. Finally, the velocity of this flow is given by the material derivative of the lateral displacements:

$$V(x, t) = \frac{D}{Dt} h = \left(\frac{\partial}{\partial t} + U \frac{\partial}{\partial x} \right) h.$$

This flow has a momentum per unit length associated with it which can be written as

$$\rho A(x) V(x, t),$$

where $\rho A(x)$ has dimensions of mass per unit length and is what we call added mass term. $A(x)$ is the area of an infinite cylinder in the z direction inscribed in $s(x)$. We need the force per unit length in the direction z produced by the fluid on the body (called lift, F_L) to be equal and of opposite sign to the material derivative of the fluid momentum passing over $s(x)$. Then we have

$$F_L(x, t) = -\rho \left(\frac{\partial}{\partial t} + U \frac{\partial}{\partial x} \right) (A(x) V(x, t)).$$

The work done by the fish in maintaining the transverse oscillations is

$$W = \rho \int_0^L \frac{\partial h}{\partial t} \left(\frac{\partial}{\partial t} + U \frac{\partial}{\partial x} \right) (A(x) V(x, t)) \, dx$$
$$= \frac{\partial}{\partial t} \left[\rho \int_0^L \frac{\partial h}{\partial t} V A(x) dx - \frac{1}{2} \rho \int_0^L V^2 A(x) dx \right] + \rho U \left[\frac{\partial h}{\partial t} V A(x) \right]_0^L.$$

If we average over a very long time, we see that the only term contributing to the average is the last one, evaluated between the length of the animal L and 0. The first term is 0 on average because it is the average of the derivative of a fluctuating quantity. $A(0) = 0$ is usually taken as a value at $x = 0$, as we can see in the figure 2.5. Assuming then a finite value of the surface at the trailing edge, we have that the time average value of the work is:

$$\overline{W} = \rho U A(L) \overline{\left[\frac{\partial h}{\partial t} \left(\frac{\partial h}{\partial t} + U \frac{\partial h}{\partial x} \right) \right]}_{x=L}.$$

On the other hand, there is also a "spent energy" term, which represents the rate at which the kinetic energy of the fluid is shed to the wake at the trailing edge. This term is written as:

$$\frac{1}{2} \rho V(L, t)^2 A(L).$$

However, these two quantities do not precisely compensate each other, at least not generally. Therefore, subtracting the last two quantities, we obtain the power available for a thrust force to be produced on average, that is:

$$\overline{T} U = \overline{W} - \frac{1}{2} \rho \overline{V^2} A U,$$

with $\overline{T}$ the mean thrust force. Isolating and simplifying this quantity we obtain:

$$\overline{T} = \frac{1}{2} \rho A(L) \overline{\left[\left(\frac{\partial h}{\partial t} \right)^2 - U^2 \left(\frac{\partial h}{\partial x} \right)^2 \right]}_{x=L}.$$

Thus, the thrust force is perfectly calculated as a function of the animal's kinematics, particularly the lateral displacements' variations in time and space. This theory is only valid for small amplitudes of movement. Subsequently, Lighhill in [89–91] developed a theory on long amplitudes, moving from his slender body theory model to elongated body theory (EBT). Candelier [92] extended EBT to account for motions in three-dimensional space, as well as non-uniform flow. Yu and Eloy [93] have corrected certain aspects of that theory to allow aspect ratios of order unity as well as to consider the effect of the Kutta condition.

2.2.2   Wu Model

In the same way that Lighthill developed his model of a slender and flexible swimmer, Wu performs the same study to find the propulsive forces of a waving plate in the case where its depth is large enough we can neglect the effects on this dimension [94, 95]. Wu's theory is intimately related to the linear theory of airfoils, which we will see in the next section. Consider then a flexible flat body of negligible thickness spanning from $x = -1$ to $x = 1$ performing lateral motions of small amplitude immersed in a flow of constant velocity U in the positive direction of x. The lateral motion of the plate is given by the expression.

$$y = h(x, t), \qquad -1 < x < 1.$$

Again, being in a linear frame, the maximum amplitude h and its derivative with respect to the position must be required to be small compared to unity. The flow is decomposed into the constant velocity U and the velocities created by the oscillations of the plate, which we write, following Wu's notation as:

$$\boldsymbol{q} = (U + u, v).$$

Of course we have an incompressible fluid, so the velocity fields originated by the vertical translation of the organism must obey the continuity equation:

$$\nabla \cdot \boldsymbol{q} = \frac{\partial u}{\partial x} + \frac{\partial v}{\partial y} = 0.$$

Considering at all times that the velocities u and v are small compared to U, in the same way as we demanded above, the equations governing the fluid dynamics are:

$$\left(\frac{\partial}{\partial t} + U \frac{\partial}{\partial x} \right) \boldsymbol{q} = -\frac{1}{\rho} \nabla p = \nabla \phi,$$

where we have introduced the Prandtl's acceleration potential defined as

$$\phi = \frac{p_\infty - p}{\rho},$$

with p_∞ the fluid pressure at infinity. By taking the divergence of the Euler equations we derive the Laplace equation for the potential:

$$\frac{\partial^2 \phi}{\partial x^2} + \frac{\partial^2 \phi}{\partial y^2} = 0.$$

Laplace equation is a more familiar type of partial derivative equation with more standard methods for giving a final solution than the original Euler equation. Once the solution is obtained, the difference of pressures between the top and bottom face of the plate is calculated as:

$$\Delta p = p(x, 0^-, t) - p(x, 0^+, t) = \rho \left[\phi(x, 0^+, t) - \phi(x, 0^-, t) \right].$$

The lift force is calculated by simply integrating this pressure variation over the entire surface:

$$F_L = \int_{-1}^{1} \Delta p \, dx.$$

And the organism thrust with:

$$T = \int_{-1}^{1} \Delta p \frac{\partial h}{\partial x} dx + T_s,$$

where T_s is a force known as leading-edge suction, whose physical meaning will be rationalized in the next section. To maintain the motion of $h(x,t)$ an external force equal but of opposite sign to the fluid force on the organism must be applied. The power, P, required for this purpose is equal to the time rate of work done by the plate against the reaction of the fluid in the direction of transverse motion:

$$P = -\int_{-1}^{1} \Delta p \frac{\partial h}{\partial t} dx.$$

From the principle of conservation of energy, the energy supplied by the animal per unit time must be equal to the rate of change of the work done by the thrust force, TU, plus the kinetic energy supplied to the fluid per unit time, E. Therefore, mathematically the relationship between these three variables is:

$$P = TU + E.$$

This equation determines whether the swimmer can develop a full thrust force sufficient to propel itself or, on the contrary, will suffer a drag that will prevent it from moving forward. First, assume that E, which is nothing more than the energy losses of the organism, is a quantity greater than or equal to 0 for a given velocity U and motion $h(x,t)$. According to the energy balance we have that:

$$P \geq TU.$$

Locomotion can only exist if $T > 0$ and large enough to counteract the drag force, which automatically implies that $P > 0$ too. Consequently, there must be a power that can maintain the oscillations. The conditions for finding a positive thrust depend on how the lateral motions and the resulting pressure distribution are organized. The development for certain cases of interest, such as harmonic lateral displacements, is described in Wu [94]. An extension towards a nonlinear theory can be found in the literature [96–98].

2.3 Theory of unsteady airfoils

Another possibility that we have in terms of modeling the behavior of aquatic swimmers lies in the theory of unsteady airfoils. Strongly developed throughout the 20th century [99–108], its main objective is to determine the characteristics of the flow around a streamlined structure moving at a velocity $U(t)$ while performing unsteady motions in the direction perpendicular to the direction of travel. Although mainly focused on the characterization of flows around aircraft, this theory has been easily extended to the description of the locomotion of flying animals [109–112], as well as of aquatic animals [12, 13, 28, 29]. In the latter case, which is the one we focus on, the use of the theory is due to the enormous similarity between the shape of an airfoil and the tail of an animal that propels itself by means of tail undulations [76].

We now describe two different formulations of the theory of unsteady airfoils. First of all, we explain Theodorsen's model and Garrick's application in detail since it has been the starting point for developing our self-propelled locomotion model. Then, we study the model by Von Karman and Sears as a more general framework to deal with this kind of problems and achieve a more precise physical interpretation by identifying the force terms that depend on the added mass and the wake contribution. Both formalisms share approximations that allow us to solve the models: we are dealing with linear theories. So it is required that the amplitudes of the motion and velocity perturbations created by the airfoil are small. As in Wu [94, 95], the model is carried out in the plane considering that the wings have infinite span, which leads to a two-dimensional treatment of the problem. Unlike this one, the bodies' flexibility is forgotten and we will deal only with rigid structures. The remaining approximations concern the character of the

wake: the various forces on the airfoil are affected not only by the instantaneous position of the airfoil but also by the strength and position of the wake vortices, which implies that the entire history of the airfoil motion will affect the value of these forces. To simplify this effect as much as possible, a flat wake is considered by exploiting the fact that airfoil lateral displacements are small. Moreover, the advection velocity of the wake is the same velocity as the one of the free stream U, which again, considering that the lateral motion of the airfoil induces only tiny perturbations in the flow, allows approximating the velocity of the airfoil correctly.
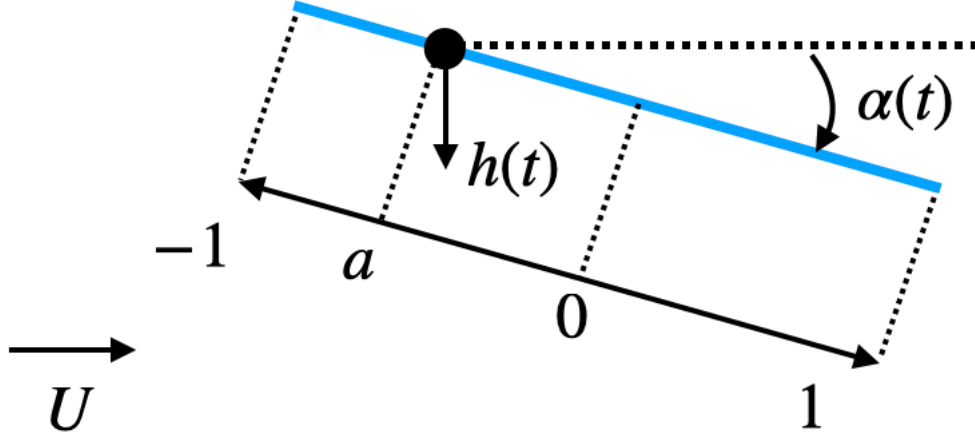
Figure 2.6: Representation of a thin airfoil in the Theodorsen formalism, with the definition of all relevant parameters.

2.3.1 Theodorsen and Garrick

In his seminal work, Theodorsen calculates all the hydrodynamic forces exerted on a plate of zero thickness with a flap [100]. The effect of the flap is perfectly taken into account in the original article; however, since in our future model we do not make use of it, in this introduction we consider that the airfoil is composed of a single piece without a flap. This corresponds, following the notation of the original article, to take $c = 1$ and $\beta = \beta' = \beta'' = 0$. All the lengths in the system are made dimensionless by using the half chord, $L/2$. With this normalization, the plate has a length equal to 2, where a represents the point of rotation of the entire foil. h is the vertical coordinate of the axis of rotation with respect to a fixed reference frame and is positive downward. α is the angle of attack referred to the direction of incident flow, represented by U, and is positive clockwise. The parameters are defined in figure 2.6.

Theodorsen's approach consists of solving the entire flow from the calculation of the velocity potential. Recall that for an inviscid, incompressible, and irrotational fluid, there is a scalar function called velocity potential which is related to the velocity according to this relation:

$$\boldsymbol{u} = \nabla \phi.$$

The fluid is not assumed irrotational as a whole. In the boundary layer, the influence of viscosity cannot be neglected, and then we will have to assume that the fluid remains irrotational elsewhere [113]. Using the equation 2.1.1, we obtain that the velocity potential obeys:

$$\nabla^2 \phi = 0.$$
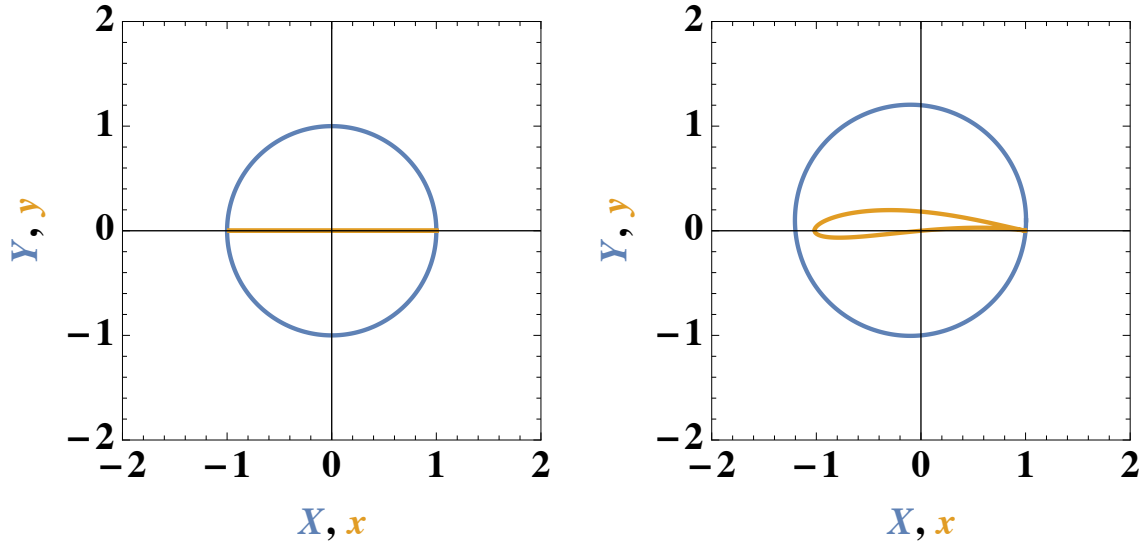
Figure 2.7: Conformal transformation of a circle using the equation 2.3.1. The blue circle becomes the orange outline. The position of the center of the circle as well as the value of its radius generates different types of airfoil like shaped.

The Laplace equation has a fundamental characteristic that makes it suitable to solve the problem. It is a linear PDE: given any n solutions, the linear combination of those will also be. This is, the flow is solved by calculating the velocity potential of each of the parts of the system independently and then applying the superposition principle to all of them. Theodorsen separates the two potential contributions into non-circulatory terms, representing the disturbance caused by the airfoil, and circulatory terms taking into account the vorticity of the wake. As the infinitely thin plate is a delicate geometry to solve all the potentials associated with the different movements, Theodorsen's cunning uses a very well-known geometry where it is easy to implement the different flows: a cylinder. The passage from one geometry to another is done through a conformal transformation, that is, an application in the complex plane whose most important characteristic is that it preserves the angles [114]. In particular, the transformation that allows going from the flow around a cylinder to the flow around an airfoil is depicted in figure 2.7 and is known as Joukowsky transformation:

$$z = \frac{1}{2}\left(Z + \frac{R^2}{Z}\right), \tag{2.3.1}$$

with $z = x + iy$ and $Z = X + iY$ the complex coordinates in the transformed and unmapped variables, respectively, and R is the radius of the cylinder.

Non-circulatory terms

The non-circulatory terms correspond to the disturbance produced by the airfoil in the fluid. For this, Theodorsen imposes a set of sources in the upper half of the cylinder and the same number of sources in the lower half to model the obstacle, in the same way as a Rankine solid [69]. The potential of the source or sink is given in the cylinder coordinates by

$$\Phi = \pm\frac{\epsilon}{4\pi}\log\left[(X - X_1)^2 + (Y - Y_1)^2\right],$$

where (X_1, Y_1) and ϵ refer to the coordinates and the strength of the source or sink, respectively. The variables in capital represent the magnitudes in the unmapped space before aplying the conformal transformation.

Being a source or a sink corresponds to taking the positive or negative sign of the potential. So, by placing a source of strength 2ϵ at a point (X_1, Y_1) and a sink of strength -2ε at $(X_1, -Y_1)$ the total potential is the sum of the individual potentials:

$$\Phi = \frac{\epsilon}{2\pi} \log \left[\frac{(X - X_1)^2 + (Y - Y_1)^2}{(X - X_1)^2 + (Y + Y_1)^2} \right].$$

The transformation to the plate is carried out by means of the equation 2.3.1, where the relationship established between the variables before (lowercase) and after (uppercase) the transformation are:

$$x = X, \quad y = 0.$$

So the potential on the plate reads:

$$\phi = \frac{\epsilon}{2\pi} \log \left[\frac{(x - x_1)^2 + \left(\sqrt{1 - x^2} - \sqrt{1 - x_1^2} \right)^2}{(x - x_1)^2 + \left(\sqrt{1 - x^2} + \sqrt{1 - x_1^2} \right)^2} \right].$$

However, this only represents having placed a source and a sink at two opposite points on the cylinder. To extend the procedure to the whole circle, let us consider that the strength is a function possibly dependent on distance and time and integrate over the whole x_1 to obtain the response of the whole structure.

$$\phi = \frac{L/2}{2\pi} \int_{-1}^{1} \epsilon(x, t) \log \left[\frac{(x - x_1)^2 + \left(\sqrt{1 - x^2} - \sqrt{1 - x_1^2} \right)^2}{(x - x_1)^2 + \left(\sqrt{1 - x^2} + \sqrt{1 - x_1^2} \right)^2} \right] dx_1.$$

The impermeability condition requires that the flow normal to the surface be zero. Applying this condition gives a relationship between the strength of the potential and the shape of the airfoil which leads to [115]:

$$\epsilon(x, t) = U \frac{\partial y}{\partial x} + \frac{L}{2} \frac{\partial y}{\partial t}$$

Furthermore, by performing the integrals, we obtain the classical Theodorsen terms: the effect of the angle of attack α, the effect of the airfoil moving with a velocity h', and the rotation around a point a at an angular velocity α':

$$\phi_\alpha = U\alpha \frac{L}{2} \sqrt{1 - x^2},$$

$$\phi_{h'} = h' \frac{L}{2} \sqrt{1 - x^2},$$

$$\phi_{\alpha'} = \alpha' \left(\frac{L}{2} \right)^2 \left(\frac{1}{2} x - a \right) \sqrt{1 - x^2},$$

$$\phi_{NC} = \phi_\alpha + \phi_{h'} + \phi_{\alpha'}.$$

Once the potentials are known, we calculate the pressures and by integration the forces on the plate. For unsteady potential flow, the pressure is determined with the unsteady Bernoulli equation and the local pressure is defined as:

$$p_{\text{local}} = -\rho \left(\frac{u_{\text{local}}^2}{2} + \frac{\partial \phi}{\partial t} \right),$$

where u_{local} is defined as:

$$u_{\text{local}} = U + \frac{\partial \phi}{\partial x}.$$

Considering that U is much larger than the velocity perturbations given by the derivative of the potential, we calculate the pressure difference between the top and bottom of the plate as:

$$\Delta p = -2\rho \left(U \frac{\partial \phi}{\partial x} + \frac{\partial \phi}{\partial t} \right). \tag{2.3.2}$$

The integration of this pressure difference yields the non-circulatory lift per unit length:

$$F_{L,NC} = -\rho \pi \left(\frac{L}{2} \right)^2 \left(U\alpha' + h'' - \frac{L}{2}a\alpha'' \right).$$

Circulatory terms

The problem with the potential calculated from the non-circulatory terms is that it generates a diverging velocity at the leading edge of the plate ($x = 1$), which is not physically acceptable. To compute the final solution of the flow, circulatory terms must be added to solve this problem. Theodorsen then considers the effect of a vortex element in the wake and its mirror image in the cylinder so that, by virtue of Kelvin's theorem, the circulation remains constant. The potential due to a vortex of strength $\Delta\Gamma$ is:

$$\Phi = \frac{\Delta\Gamma}{2\pi} \tan^{-1} \left(\frac{Y - Y_1}{X - X_1} \right),$$

where X_1 and Y_1 refer in this case to the coordinates of the vortex. Considering that the vortex in the wake is at a position X_0 from the center of the cylinder and outside the cylinder and its mirror image with opposite strength at $1/X_0$ but inside the cylinder, the potential of both flows is:

$$\Phi = \frac{\Delta\Gamma}{2\pi} \left[\tan^{-1} \left(\frac{Y - Y_0}{X - X_0} \right) - \tan^{-1} \left(\frac{Y - Y_0}{X - \frac{1}{X_0}} \right) \right] = \frac{\Delta\Gamma}{2\pi} \tan^{-1} \left[\frac{Y \left(X_0 - \frac{1}{X_0} \right)}{X^2 + Y^2 - X \left(X_0 - \frac{1}{X_0} \right) + 1} \right].$$

The transformation implies $X_0 = x_0 + \sqrt{x_0^2 - 1}$ on the x axis and $X = x$, $Y = \sqrt{1 - X^2}$ on the circle. Therefore the potential in the geometry of the plate is:

$$\phi_C = -\frac{\Delta\Gamma}{2\pi} \tan^{-1} \left(\frac{\sqrt{1 - x^2}\sqrt{x_0^2 - 1}}{1 - xx_0} \right).$$

We apply Bernoulli's relation 2.3.2 again but we note that the vortex element propagates at the free stream velocity U and then:

$$\frac{\partial \phi}{\partial t} = U \frac{\partial \phi}{\partial x_0}.$$

Therefore, the pressure difference in this case reads:

$$\Delta p = -2\rho U \left(\frac{\partial \phi}{\partial x} + \frac{\partial \phi}{\partial x_0} \right).$$

Deriving the potentials with respect to x and x_0 the final expression becomes:

$$\Delta p = -\rho U \frac{\Delta\Gamma}{\pi} \frac{x_0 + x}{\sqrt{1 - x}\sqrt{x_0^2 - 1}}.$$

We express the strength of the circulation as:

$$\Delta\Gamma = \gamma dx_0, \tag{2.3.3}$$

where $\gamma = f(Ut - x_0)$ is a function representing the wake surface strength and t is the time since the motion started.

We then integrate to obtain the expression for the lift force per unit length corresponding to the circulatory terms:

$$F_{L,C} = -\rho \frac{L}{2} \int_1^\infty \frac{x_0}{\sqrt{x_0^2 - 1}} \gamma dx_0,$$

Kutta's condition determines the magnitude of the vorticity γ [116]. The condition states that the velocity of the flow at the trailing edge must be finite. It is then required that:

$$\frac{\partial}{\partial x} \left(\phi_{NC} + \phi_C \right) \big|_{x=1} = \text{finite}.$$

This leads directly to:

$$\frac{1}{2\pi} \int_1^\infty \frac{\sqrt{x_0 + 1}}{\sqrt{x_0 - 1}} \gamma dx_0 = U\alpha + \frac{L}{2} \left(\frac{1}{2} - a \right) \alpha' + h' = Q.$$

The circulatory lift becomes after introducing the constraint imposed by the Kutta condition:

$$F_{L,C} = -\pi L \rho U Q C,$$

with the parameter C expressed as:

$$C = \frac{\int_1^\infty \frac{x_0}{\sqrt{x_0^2 - 1}} \gamma dx_0}{\int_1^\infty \sqrt{\frac{x_0 + 1}{x_0 - 1}} \gamma dx_0}. \tag{2.3.4}$$

To solve these integrals, it is necessary to prescribe the behavior of γ, defined in equation 2.3.3, as a function of x_0. However, given the wake approximations we made to develop the model, it is more beneficial to prescribe the airfoil behavior and then determine the resulting value of γ. Theodorsen imposes a sinusoidal airfoil motion of frequency ω with small amplitude for α and h. In this case, the form of γ is sinusoidal near the airfoil and we write

$$\gamma = \gamma_0 e^{i\omega t} e^{-i\omega \frac{L}{2} x_0/U}.$$

An additional parameter called reduced frequency, $k = \omega L/2U$, is defined to express the equation 2.3.4 as a function of a single parameter:

$$C(k) = \frac{\int_1^\infty \frac{x_0}{\sqrt{x_0^2 - 1}} e^{ikx_0} dx_0}{\int_1^\infty \sqrt{\frac{x_0 + 1}{x_0 - 1}} e^{ikx_0} dx_0} = \frac{H_1^{(2)}(k)}{H_1^{(2)}(k) + iH_0^{(2)}(k)} = F(k) + iG(k).$$

The function $C(k)$ is known as Theodorsen function [100], $H_1^{(2)}, H_0^{(2)}$ are Hankel functions of the first and second kind defined as of Bessel functions of first and second kind [117] and F, G represent the real and imaginary part of Theodorsen function, respectively.

The total lift can then be written as:

$$F_L = F_{L,NC} + F_{L,C} = -\rho\pi \left(\frac{L}{2} \right)^2 \left(U\alpha' + h'' - \frac{L}{2} a\alpha'' \right) - \pi L \rho U Q C(k). \tag{2.3.5}$$

Thrust derivation

In his paper, Garrick takes up Theodorsen's work on the periodic oscillations of an infinitely thin plate and calculates the propulsive forces that such a structure experiences in a constant air stream [101]. The energy balance formula that Garrick proposes is:

$$\overline{W} = \overline{E} + \overline{T}U,$$

with $\overline{W}$ the average work done per unit time to maintain the oscillations against the fluid forces and moments. $\overline{E}$ represents the average increase in kinetic energy per unit time in the vortex wake, and $\overline{T}U$ denotes the average work done per unit time by the propulsive force.

The instantaneous rate of work W' is easily defined from the plate motion:

$$W' = -(F_L h' + M\alpha'),$$

where M is the moment of force that the fluid exerts on the plate.

We are interested in calculating the thrust force T. According to Garrick, the propulsive force has two contributions:

$$T = \alpha F_L + \pi\rho S^2.$$

The first term is the projection taking into account the small-angle regime of the lift force in the direction of motion, and the second corresponds to what is known as the leading-edge suction force, which represents a suction force due to the flow passing around the leading edge [113]. Indeed, if we look close at the non-circulatory potential, we remark that there are two divergences in it. One at $x = 1$ (trailing-edge), which has already been solved with the application of the Kutta condition, and the other at $x = -1$ (leading-edge), which causes an infinite velocity at this point and which we cannot physically admit. The application of the Kutta condition imposed a relation between the circulatory and non-circulatory potentials to avoid the divergence of the velocity at the trailing edge and assume that it is equal to 0 so that the flow leaves the trailing edge smoothly. In the case of the leading edge, there is no possibility of establishing another relation between the potentials, so Garrick's idea, based on the work of Von Karman and Burgers [118], is to calculate S knowing that the leading edge suction tends to infinity in a functional form given by $1/\sqrt{1+x}$. The leading-edge vorticity may be written as

$$2\frac{\partial}{\partial x}\left(\phi_{NC} + \phi_C\right)\big|_{x=-1} = \frac{2S}{\sqrt{1+x}}.$$

By introducing the expression of the potentials, together with the Theodorsen function and the value of Q the expression of S is:

$$S = \frac{\sqrt{2}}{2}\left[2C(k)Q - \frac{L}{2}\alpha'\right].$$

Thus, the total propulsive force can be written as a function of the variables α, h and their derivatives as follows

$$T = \alpha\left(-\rho\pi\left(\frac{L}{2}\right)^2\left(U\alpha' + h'' - \frac{L}{2}a\alpha''\right) - \pi L\rho U Q C(k)\right) + \pi\rho\frac{1}{2}\left(2C(k)Q - \frac{L}{2}\alpha'\right)^2.$$

The propulsion efficiency is, according to Garrick's definition:

$$\eta = \frac{\overline{TU}}{\overline{W}}.$$

For example, for the case of an airfoil that has no pitch motion, i.e., $\alpha(t) = 0\ \forall t$, but does heave, $h(t) \neq 0$, the efficiency takes the following form as a function of the real and imaginary parts of the Theodorsen function:

$$\eta = \frac{F^2 + G^2}{F}.$$

Investigating the behavior of F and G as a function of the frequency of motion, this equation shows that the efficiency tends to 0.5 when the frequency of oscillation tends to infinity, a result that is not physically possible. In the spirit of correcting this behavior in Garrick's framework,

Fernandez-Feria [119, 120] applies Sears and Von Karman theory to improve this result with efficiency tending to 0 for infinite oscillation frequencies.

Theodorsen and Garrick's work lays the cornerstone upon which many modifications and improvements have been made to extend the applicability of Theodorsen's formalism. Greenberg [106] performed the calculation of forces considering a time-dependent flow velocity in a sinusoidal shape, Edwards [121] supposed plate oscillations not purely sinusoidal, or Patil and Walker, among others, examined the possibility of having deformable airfoils by applying Chebychev polynomials [115, 122, 123]

2.3.2 Von Karman and Sears

The theory developed by Theodorsen for oscillatory motions of an airfoil mainly lacks a clear physical interpretation of the various calculated force terms. While only circulatory and non-circulatory terms enter into his classification, the theory now discussed by Sears and Von Karman [103], in the words of the authors, eliminates unnecessary mathematical complications and attempts to use only the basic concepts of vortex theory. They separate the lift contributions into steady, added mass, and wake contributions. In the description of this theory, we use Johnston's approach [124], which in turn is based on McCune [108], to derive Von Karman and Sears' formulation of unsteady airfoil theory.

The unsteady Bernoulli equation is written acording to [113] as:

$$\Delta p = \rho U(t)\gamma(x,t) + \rho \frac{\partial}{\partial t}\int_0^x \gamma(x_0,t)dx_0,$$

where γ is the vorticity in an airfoil extending from $x = 0$ to $x = L$, where L is the length of the airfoil. Integrating this pressure difference we obtain the lift force:

$$F_L = \rho U(t)\int_0^L \gamma(x,t)dx + \rho \int_0^L \frac{\partial}{\partial t}\int_0^x \gamma(x_0,t)dx_0.$$

Integrating the second term by parts we have:

$$F_L = \rho U(t)\int_0^L \gamma(x,t)dx + \frac{\partial}{\partial t}\rho \left[x\int_0^x \gamma(x_0,t)dx_0 \Big|_0^L - \int_0^L x\gamma(x,t)dx \right],$$

which is equivalent to:

$$F_L = \rho U(t)\int_0^L \gamma(x,t)dx + \frac{\partial}{\partial t}\rho \left[\int_0^L (L-x)\gamma(x,t)dx \right]. \qquad (2.3.6)$$

The first term is defined as the Jowkoski lift because it corresponds to the force that appears due to the application of the Kutta-Jowkoski theorem, and the second is the term corresponding to the added mass. For the development of the expression, it is necessary to understand what is the nature of the vorticity γ. The circulation, Γ, around the airfoil is related to the vorticity employing:

$$\Gamma = \int_0^L \gamma(x,t)dx.$$

Kelvin's theorem states that the circulation in an incompressible, inviscid, irrotational fluid must remain constant, implying that the change in vorticity around the airfoil must be equal to the vorticity shed into the wake. This leads to:

$$\frac{d}{dt}\int_0^L \gamma(x,t)dx = \frac{d}{dt}\int_L^\infty \gamma_w(\xi,t)d\xi,$$

where γ_w is the vorticity distribution strength due to the wake. Vorticity may then be decomposed into two contributions:

$$\gamma = \gamma_0 + \gamma_1,$$

where γ_0 is the quasi-steady component of the vorticity due to the instantaneous state of the airfoil and is computed using steady thin airfoil theory. γ_1 is the wake induced component of the vorticity, which may be written by integrating into the entire wake as:

$$\gamma_1 = \frac{1}{2\pi} \int_L^\infty \frac{\gamma_w(\xi)}{\xi - x} \sqrt{\frac{L-x}{x}} \sqrt{\frac{\xi}{\xi - L}} d\xi.$$

If the new γ expression is entered in equation 2.3.6, the lift reads

$$F_L = \rho U(t) \int_0^L (\gamma_0 + \gamma_1) dx + \frac{\partial}{\partial t} \rho \left[\int_0^L (L-x)(\gamma_0 + \gamma_1) dx \right],$$

which can be separated into two terms in which each accounts for the contribution of γ_0 and γ_1:

$$\Delta F_{L,\gamma_0} = \rho U(t)\Gamma_0 - \frac{\partial}{\partial t} \rho \left[\int_0^L \left(x - \frac{L}{2} \right) \gamma_0 dx \right] + \rho \frac{L}{2} \frac{\partial \Gamma_0}{\partial t},$$

$$\Delta F_{L,\gamma_1} = \rho U(t)\Gamma_1 - \frac{\partial}{\partial t} \rho \left[\int_0^L \left(x - \frac{L}{2} \right) \gamma_1 dx \right] + \rho \frac{L}{2} \frac{\partial \Gamma_1}{\partial t},$$

with

$$\Gamma_0 = \int_0^L \gamma_0 dx,$$

$$\Gamma_1 = \int_0^L \gamma_1 dx = \int_L^\infty \gamma_w(\xi) \left(\sqrt{\frac{\xi}{\xi - L}} - 1 \right) d\xi,$$

representing the circulations due to γ_0 and γ_1, respectively. The contribution to the lift $\Delta F_{L,\gamma_1}$ can be further simplified if we perform the integral inside using the above relation between γ_1 and γ_w:

$$\int_0^L \left(x - \frac{L}{2} \right) \gamma_1 dx = \int_L^\infty \gamma_w(\xi) \left(\sqrt{\xi^2 - \xi L} - \xi + \frac{L}{2} \right) d\xi.$$

If we derive the latter expression with respect to time:

$$\frac{d}{dt} \rho \int_L^\infty \gamma_w(\xi) \left(\sqrt{\xi^2 - \xi L} - \xi + \frac{L}{2} \right) d\xi = -\rho \frac{L}{2} \frac{d\Gamma_w}{dt} + \rho U(t) \left[\Gamma_1 - \int_L^\infty \gamma_w(\xi) \frac{\frac{L}{2}}{\sqrt{\xi^2 - \xi L}} d\xi \right].$$

Recalling that Kelvin's theorem imposes the conservation of the total circulation:

$$\frac{\partial \Gamma_0}{\partial t} + \frac{\partial \Gamma_1}{\partial t} + \frac{\partial \Gamma_w}{\partial t} = 0,$$

the total lift can be rewritten in a much more abbreviated form taking into account the latter equality and the cancellation of the $\rho U(t)\Gamma_1$ terms:

$$F_L = \rho U(t)\Gamma_0 - \frac{\partial}{\partial t} \rho \int_0^L \left(x - \frac{L}{2} \right) \gamma_0 dx + \rho U(t) \int_L^\infty \gamma_w(\xi) \frac{\frac{L}{2}}{\sqrt{\xi^2 - \xi L}} d\xi.$$

This is the result of Von Karman and Sears. The first term, $F_{L,0}$, represents the quasi-steady Joukowski lift. The second $F_{L,1}$, represents the added mass of a foil with zero or constant circulation. Finally, the third term, $F_{L,2}$, models the influence of the wake on the foil's lift:

$$F_{L,0} = \rho U(t)\Gamma_0,$$
$$F_{L,1} = -\frac{\partial}{\partial t}\rho \int_0^L \left(x - \frac{L}{2}\right)\gamma_0 dx,$$
$$F_{L,2} = \rho U(t) \int_L^\infty \gamma_w(\xi) \frac{\frac{L}{2}}{\sqrt{\xi^2 - \xi L}} d\xi.$$

It is interesting to note how with this approach, the case of oscillating Theodorsen airfoils can be recovered, as indicated by Sears, [104] and Johnston [124]. If we consider a sinusoidal variation of $F_{L,0}$ that has occurred for a very long time, so that the wake extends to infinity:

$$F_{L,0} = (A + iB)e^{i\omega t},$$

with A and B constants and ω the frequency of oscillation. Then, $F_{L,2}$ can be rewritten as:

$$F_{L,2} = (C(k) - 1)F_{L,0}.$$

To calculate the thrust, we rely on the article by Fernandez-Feria [119] which uses the Sears and Von Karman formulation to determine the thrust of the three lift forces calculated above:

$$T = T_0 + T_1 + T_2.$$

where the first term coincides precisely with the Garrick vertical force projection term, T_1 is the added mass contribution and T_2 is the wake contribution.

The framework of Sears and Von Karman can be extended to include nonlinear terms in their formulation. In fact, this is the idea that Wu later develops for his nonlinear swimming theories [96–98].

2.4   A minimal model of self-propelled locomotion

In order to understand how swimming is influenced by the kinematic parameters of the animal and the physical characteristics of the fluid, we have developed a minimal model of aquatic locomotion to explain the mechanics associated with the fluid-structure interaction problem. Therefore, a large part of our study will consist of calculating the Strouhal number, St, associated with this swimmer which, as already stated in the Introduction is an approximately constant quantity for most biological swimmers. The experiments carried out in order to obtain this magnitude consist in varying the kinematic parameters, the tail beat amplitude A and the frequency f, to find the free swimming velocity U. Experiments performed with flexible panels [25, 30] and robots [15] undergoing heaving or pitching motions show that St is relatively constant, independently of f, as long as the dimensionless amplitude A/L remains small. As an example it varies less than 50% up to $A/L = 0.35$ for the robotic fish studied by Gibouin et al. [15]. On the other hand, experiments performed with rigid foils undergoing heaving and pitching motions propose a slightly different approach: the Strouhal number is found to depend on the tail beat frequency for a given value of A/L. For instance it varies in the range 0.1–1.5 for $A/L \sim 0.2$ in experiments by Quinn et al. [125]. Our motivation and the underlying question is whether or not the Strouhal number depends on the tail beat frequency since results are different depending on the experimental systems and this discussion should help to understand the mechanisms at play.
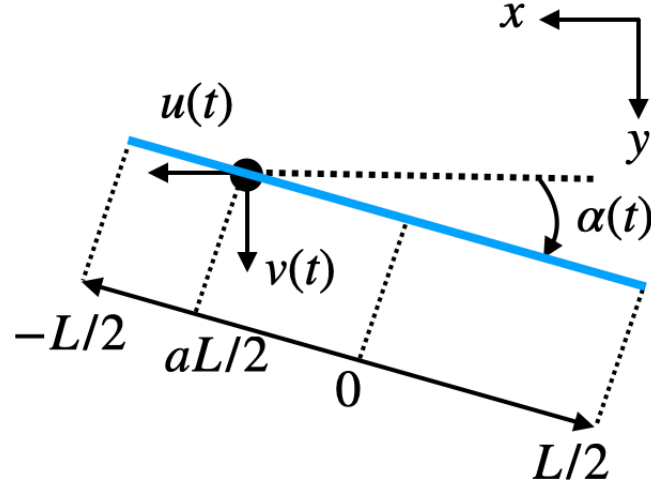
Figure 2.8: Sketch of the swimmer and relevant quantities. We note m the mass of the swimmer per unit length in the third dimension and ρ the density of the fluid. Angles are counted positively clockwise.

Here we consider a simple model of aquatic locomotion to give further insights. Our model is not aimed at describing a specific fish in particular, we focus on the minimal ingredient to trigger motion. We consider an airfoil-shaped, rigid and two-dimensional body performing a kinematic motion of amplitude A and frequency f. This body is free to move contrary to the experiments and is not prescribed to a given position. Only the orientation of the body with respect to a fixed frame of reference is forced and the rest is predicted by the second law of Newton. Expressions of the thrust and drag forces are based upon Theodorsen's approach [100, 101] in the realm of perfect fluid, but we take into account an additional pressure drag, which cannot be predicted in this framework. First, we show that such a swimmer initially at rest, starts to propel itself as the body oscillates. It exhibits both heaving and pitching motions and will finally cruise at constant speed whatever the initial conditions. Second, in the limit of small tail beat amplitude, we predict the locomotion velocity, and the Strouhal number. The latter does not depend on the tail beat frequency but is strongly correlated with the drag coefficient. For classical values of this coefficient, we find that St is almost constant, around 0.1–0.3, in agreement with natural and artificial systems. In addition to this very good predictive capacity, we demonstrate how the physical parameters prescribe the phase angle between pitch and heave.

We assume our swimmer to be a two-dimensional thin body, composed by a point mass (2D mass m, unit kg m^{-1}) attached to a straight, rigid and massless foil of length L, which models the tail. In the reference frame of the laboratory, this tail is inclined by an angle α with respect to the x axis and is counted positive clockwise, as seen in figure 2.8. The center of mass is located at the algebraic distance $aL/2$ from the center of the tail, with a a dimensionless number in the range $[-1, 1]$. As example, for $a = 0$, the center of mass coincides with the center of the tail. The swimmer evolves inside an inviscid fluid of density ρ. Swimming is triggered by imposing the harmonic forcing of amplitude α_0 and angular frecuency $\omega = 2\pi f$:

$$\alpha(t) = \alpha_0 \sin(\omega t).$$

We expect the swimmer to evolve in average in the x direction, because the trailing edge sits in the right part of the foil. We note $u(t)$ and $v(t)$ respectively the instantaneous velocities of the center of mass in the x and y directions. In the following, we will define $U = \langle u(t) \rangle$ as the average swimming velocity in steady state, where $\langle . \rangle$ consists in averaging over one period of the harmonic forcing α:

$$\langle X(t) \rangle = \frac{\omega}{2\pi} \int_0^{2\pi/\omega} X(t) dt.$$

Assuming small angles ($\alpha_0 \ll 1$), we rely on the linear approach developed by Theodorsen and Garrick to calculate the forces at play. In Theodorsen's equations we can set the position of the center of mass at $aL/2$ by setting $x_\alpha = 0$ and $h' = v(t)$ with Theodorsen's notations. In addition, $\beta = 0$ since we do not consider any flap. The y direction force, F_y, writes, as we stated in equation 2.3.5:

$$
\begin{aligned}
F_y = &-\pi\rho \left(\frac{L}{2}\right)^2 \left[u(t)\alpha'(t) + u'(t)\alpha(t) + v'(t) - a\frac{L}{2}\alpha''(t) \right] \\
&- \pi\rho L u(t) C(k) \left[u(t)\alpha(t) + v(t) + \left(\frac{1}{2} - a\right)\frac{L}{2}\alpha'(t) \right],
\end{aligned}
\tag{2.4.1}
$$

where $C(k = \omega L/2u(t))$ is the Theodorsen function, defined in equation 2.3.4, introduced to account for the history of the shed vortices. Even if $C(k)$ is difficult to compute because it is a non-local quantity that accounts for the vorticity distribution in the entire wake of the airfoil we use the Theodorsen approach by assuming sinusoidal oscillations to write $C(k)$ as a composition of Hankel functions.

Note that the term $\alpha(t)u'(t)$ does not appear in Theodorsen's derivation, in equation 2.3.5, but arises immediately as soon as we consider temporal variations of u, as remarked in Greenberg [106]. Theodorsen's approach exploits the linearity of the equation of the velocity potential, and predicts $F_y(t)$ by adding the potentials induced by the motions of the airfoil like the vertical displacement and the variation of the attack angle. To take into account the effect of an unsteady streaming flow, it is necessary to add the supplementary potential induced by a longitudinal velocity $u(t)$, which turns out to be zero, because the airfoil is infinitely thin. Consequently the potential flow of an airfoil, submitted to an unsteady velocity $u(t)$ does not lead to an additional contribution to the non-circulatory velocity potential and takes the same form as prescribed in Theodorsen's model. Nevertheless, to compute the pressure exerted by the fluid, we use, as usual, the Bernoulli relation which generates the extra term $\alpha(t)u'(t)$, as in Greenberg [106].

An important point we make is the identification of the pitch axis with the center of mass, i.e., when a changes, it is not the position of the pivot that changes but the center of mass. Since our swimmer is free to move, the position of the axis of rotation defined in Theodorsen is not relevant here, and everything can be expressed in terms of the position of the center of mass only. This identification does not change the results for those obtained by Theodorsen but gives a different interpretation. To show that both equations are equivalent, let us take the equation of motion in the vertical coordinate according to Theodorsen [100], with $C_h = 0$ and $\beta = 0$, as well as all its derivatives with respect to time:

$$
mh'' + m\frac{L}{2}x_\alpha\alpha'' = F_y(a),
$$

where we have made explicit only the dependence of equation 2.4.1 with respect to the parameter a. We recall that Theodorsen's formulation is based on taking h as the vertical coordinate of the axis of rotation referred to point a [100], whereby, if we want to express the equation of motion in terms of the center of mass, whose position is given by:

$$
y_{cm}(t) = h(t) + \frac{L}{2}x_\alpha\alpha(t).
$$

If we reintroduce this variable in the equation of motion we obtain:

$$
my''_{cm} = F_y(a + x_\alpha),
$$

which results in the new position $a + x_\alpha$ being the only quantity of interest in the kinematics. Therefore choosing as center of mass the point a by imposing $x_\alpha = 0$ does not generate any additional problems in the equations.

Following Garrick [101], the force F_x induced by the inviscid fluid in the x direction accounts for two contributions:

$$F_x = \alpha F_y + F_{LE}.$$

The first contribution αF_y corresponds to the projection of the Theodorsen pressure in the x direction and F_{LE} stands for the leading-edge force which results from the presence of a singular flow: an infinitely thin body would lead to a divergence of the pressure at the leading-edge of the swimmer. To avoid for this non physical effect, we use the expresion of Garrick [101] by adding F_{LE}.

$$F_{LE} = \pi \rho \frac{L}{2} \frac{1}{2} \left[2C(k) \left(v(t) + u(t)\alpha(t) + \left(\frac{1}{2} - a \right) \frac{L}{2} \alpha'(t) \right) - \frac{L}{2} \alpha'(t) \right]^2.$$

We remark here that Garrick introduced a regularization to smooth the horizontal velocity, i.e., the horizontal component of the gradient of the velocity potential, and therefore does not introduce any temporal derivative of $u(t)$, $v(t)$ or $\alpha'(t)$. The resulting force, known as the leading edge suction, appears to be significant for biological swimmers, as shown by recent measurements [126].

In this approach, note that F_y is a second-order approximation in α, while F_x accounts for third-order terms as well. Finally, the velocities of the swimmer are calculated following the second law of Newton:

$$mu' = F_x - \rho c_d L u^2,$$
$$mv' = F_y.$$

We recall here that these momentum balances are written per unit length. To take into account the drag induced by the boundary layers, we have added a horizontal pressure drag force. This coefficient is measured using the "wetted area" as the reference area since fish are considered as slender bodies [91, 127–130], defining the wetted perimeter as $2L$, this force writes $\frac{1}{2}\rho u^2 c_d(2L)$, with the drag coefficient c_d. We keep the same definition for consistency.

In short, the locomotion problem resides in this case in solving both equations of motion and analyzing the behavior of the swimming velocity $u(t)$ as a function of the different parameters included in these equations. A thorough analysis of the system leads us to make dimensionless both equations to obtain a simplification of the equations and uncover the number of relevant parameters in the system. According to the Buckingham π theorem [131], if we define the number of fundamental quantities in our problem (in this case 3: length, mass and time) and the number of parameters in the equations (we have 7: length and mass of the swimmer, L and m, the density of the fluid ρ, drag coefficient c_d, position of the center of mass a, amplitude and angular frequency of the oscillations α_0 and ω), we can find that any dimensionless quantity will be a function of only 4 parameters [131] which we will define later.

To transform the equations into dimensionless we introduce a new time and velocity that scales as $1/\omega$ and $\omega L/2$, respectively, and define the new dimensionless variables:

$$\tilde{t} = \omega t, \qquad \tilde{u} = \frac{2u}{L\omega}, \qquad \tilde{v} = \frac{2v}{L\omega}.$$

Using these variables, we obtain the two dimensionless differential equations that we use for the resolution of our system:

$$M\tilde{u}'(\tilde{t}) = \tilde{F}_x - \frac{2}{\pi} c_d \tilde{u}(\tilde{t})^2,$$
$$M\tilde{v}'(\tilde{t}) = \tilde{F}_y,$$

where the following definitions stand for $\tilde{F}_x$ and $\tilde{F}_y$:

$$\tilde{F}_x = \alpha(\tilde{t})\tilde{F}_y + \frac{1}{2}\left[2C\left(\frac{1}{\tilde{u}(\tilde{t})}\right)\left(\tilde{v}(\tilde{t}) + \tilde{u}(\tilde{t})\alpha(\tilde{t}) + \left(\frac{1}{2} - a\right)\alpha'(\tilde{t})\right) - \alpha'(\tilde{t})\right]^2,$$

$$\tilde{F}_y = -\left[\tilde{u}(\tilde{t})\alpha'(\tilde{t}) + \tilde{u}'(\tilde{t})\alpha(\tilde{t}) + \tilde{v}'(\tilde{t}) - a\alpha''(\tilde{t})\right] - 2\tilde{u}(\tilde{t})C\left(\frac{1}{\tilde{u}(\tilde{t})}\right)\left[\tilde{u}(\tilde{t})\alpha(\tilde{t}) + \tilde{v}(\tilde{t}) + \left(\frac{1}{2} - a\right)\alpha'(\tilde{t})\right].$$

And where the only 4 dimensionless parameters that we will use for the complete characterization of the system appear:

1. The parameter M stands for the ratio of the swimmer mass to the added mass and it will be called henceforth dimensionless mass of the swimmer. It is defined by:

$$M = \frac{4m}{\pi\rho L^2}.$$

2. The drag coefficient, c_d.

3. The dimensionless position of the center of mass, a.

4. The driving amplitude of the oscillation, α_0, which appears in the expression of α.

The Strouhal number St, the fundamental quantity on which our study is based will be represented in dimensionless variables by:

$$St = \frac{Af}{U} = \frac{\tilde{A}\frac{L}{2}f}{\frac{L}{2}\omega\tilde{U}} = \frac{\tilde{A}}{2\pi\tilde{U}},$$

where A is the peak-to-peak tail beat amplitude.

The only thing that remains to be clarified is the value that the Theodorsen function takes in all the dynamics. As we will introduce later, both in the perturbative calculation and in the numerical resolution of the system, the argument of the Theodorsen function $1/\tilde{u}(\tilde{t})$ is going to be much larger than unity, which allows us to get rid of the imaginary character of the function and set its real part to $1/2$, as can be seen in figure 2.9. In fact, if we use the asymptotic development of Hankel functions for large arguments, $k \gg 1$, we get [132]:

$$H_p^{(2)}(k) \sim \sqrt{\frac{2}{\pi k}}\exp\left[-i\left(k - p\frac{\pi}{2} - \frac{\pi}{4}\right)\right].$$

If we calculate the Theodorsen function taking into account this development:

$$C(k \gg 1) = \frac{\exp\left[-i\left(k - \frac{3\pi}{4}\right)\right]}{\exp\left[-i\left(k - \frac{3\pi}{4}\right)\right] + i\exp\left[-i\left(k - \frac{\pi}{4}\right)\right]} = \frac{1}{2} + 0i,$$

which justifies taking this value when the arguments of the function are very large compared to unity.
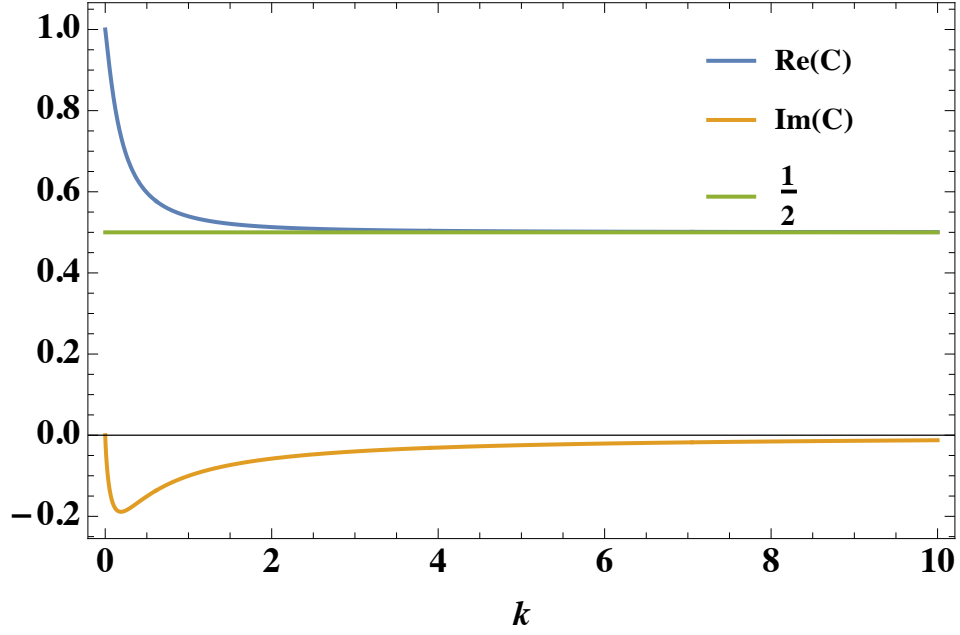
Figure 2.9: Behavior of the Theodorsen function C as a function of its argument k.

2.4.1 Perturbative approach

To go in depth in understanding this minimal model and how the different parameters influence swimming, we perform a perturbative development in order to determine an analytical expression for the velocities. Self propelled swimmers rarely exhibit high values for α. In fact, $\alpha_0 = 0.2$ is a typical value for fish [21, 25, 38, 133], so α and α_0 are assumed small compared to unity. We make a perturbative expansion with the assumption $\alpha_0 \ll 1$. For simplicity, we remove the tilde above the dimensionless quantities and we use the notation $\varepsilon = \alpha_0$ to emphasize this hypothesis. The angle $\alpha(t)$ writes:

$$\alpha(t) = \frac{\varepsilon}{2i} e^{it} + \text{c.c.},$$

where i is the imaginary unit, and c.c. means complex conjugate. In the spirit of perturbation theory and following the Appendix B, we proceed to solve the system using the multiscale method by introducing a slow time scale $\tau = \varepsilon t$ to capture transient regimes. We develop both horizontal and vertical velocities as:

$$u(t) = \varepsilon u_1(t, \tau) + \varepsilon^2 u_2(t) + \varepsilon^3 u_3(t) + \mathcal{O}(\varepsilon^4),$$
$$v(t) = \varepsilon v_1(t, \tau) + \varepsilon^2 v_2(t) + \mathcal{O}(\varepsilon^3).$$

The equations we find at first order are:

$$\frac{\partial}{\partial t} u_1(t, \tau) = 0,$$
$$\frac{\partial}{\partial t} v_1(t, \tau) = \frac{a}{2(1 + M)} \left(i e^{it} + \text{c.c.} \right).$$

Integrating the system we obtain:

$$u_1(t, \tau) = U_1(\tau),$$
$$v_1(t, \tau) = V_1(\tau) + \frac{a}{2(1 + M)} \left(e^{it} + \text{c.c.} \right),$$

where we observe how the swimming velocity does not depend on t at the first order but on the slow time τ. Subsequently, we will calculate this quantity that will mark the behavior of the transient period and the final value of the swimming velocity. On the other hand, the vertical velocity has an associated term also dependent on τ and that, a priori, prevents the average of v to be zero, as we should expect in the movement of the animal only in the x direction. To understand this, it is necessary to write the equations to second order, which, once introduced the previous solutions and putting at all times the value of the Theodorsen's function equal to $1/2$ remain:

$$
\begin{aligned}
\frac{\partial}{\partial t} u_2(t,\tau) &= -\frac{\partial}{\partial \tau} U_1(\tau) + \frac{1}{16M}\left(8V_1(\tau)^2 - \frac{32 c_d U_1(\tau)^2}{\pi} + \frac{(1+M-2aM)^2}{(1+M)^2}\right) \\
&\quad - V_1(\tau)\frac{1+M+2aM}{4M(1+M)}e^{it} + \frac{1+M(2+M+4a(3+(3+a)M))}{32M(1+M)^2}e^{2it} + \text{c.c.}, \\
\frac{\partial}{\partial t} v_2(t,\tau) &= -\frac{\partial}{\partial \tau} V_1(\tau) - \frac{U_1(\tau)V_1(\tau)}{1+M} + U_1(\tau)\frac{M(2a-3)-3}{4(1+M)^2}e^{it} + \text{c.c.} .
\end{aligned}
$$

In both equations at second-order, we detect a constant term followed by specific periodic terms. In both ODEs, we observe that if the constant terms are not equal to zero, then the amplitudes of u_2 and v_2 will increase linearly in time, so that we will have $u_2 \gg u_1$ and $v_2 \gg v_1$ for large times, which breaks our expansion. To maintain the validity of the ansatz, we need to set these terms to 0 as a solvability condition. In other words, we invoke the Fredholm Alternative as we define it in [Appendix B]. In this case, both equations are decoupled and no formal treatment is extremely necessary. Applying the theorem to each equation separately, we obtain the following two conditions:

$$
\frac{\partial}{\partial \tau} U_1(\tau) = \frac{1}{16M}\left(8V_1(\tau)^2 - \frac{32 c_d U_1(\tau)^2}{\pi} + \frac{(1+M-2aM)^2}{(1+M)^2}\right), \tag{2.4.2}
$$

$$
\frac{\partial}{\partial \tau} V_1(\tau) = -\frac{U_1(\tau)V_1(\tau)}{1+M}. \tag{2.4.3}
$$

Solving these equations is not possible with analytical methods, but it is not really necessary. We will demonstrate by analyzing the associated dynamical system that $V(\tau)$ is a function that always tends to 0 for any initial condition and therefore, its effect in the stationary regime, which is the one we are interested in, can be neglected. To do this, we first calculate the fixed points of the above differential system:

$$
U_1^* = \sqrt{\frac{\pi}{2c_d}}\frac{1-M(2a-1)}{4(1+M)}, \qquad V_1^* = 0,
$$

with U_1^* positive, as we could not expect otherwise being the swimming speed. Actually solving the equation gives an additional fixed point that we do not consider because it leads to an imaginary speed.

The Jacobian matrix associated with the system is:

$$
J = \begin{pmatrix} -\dfrac{4c_d U_1}{\pi M} & \dfrac{V_1}{M} \\[2ex] -\dfrac{V_1}{1+M} & -\dfrac{U_1}{1+M} \end{pmatrix}_{(U_1^*, V_1^*)},
$$

whose eigenvalues are:

$$
\lambda_1 = -\frac{4c_d U_1^*}{\pi M}, \qquad \lambda_2 = \frac{-U_1^*}{1+M},
$$

both negative, showing the stability of the fixed point. For any initial condition, $(U_1(0), V_1(0))$, the horizontal velocity tends to a constant value at the first order approximation. On the other

hand, the term that prevents the vertical velocity from having zero mean over a period tends to 0 in the steady-state and only influences the dynamics in the transient regime. By concentrating specifically on the organism's behavior when it reaches its cruising velocity, we will consider that the initial condition for the vertical velocity is always zero, and therefore, $V_1(\tau)$ is identically zero from the beginning of the motion. This translates into the equation 2.4.2 having as its solution:

$$U_1 = U_1^* \tanh\left[\frac{\tau}{\tau_{sat}} + \tanh^{-1}\left(\frac{U_1^*(0)}{U_1^*}\right)\right],$$

$$U_1^* = \frac{1 + M - 2aM}{4(1 + M)}\sqrt{\frac{\pi}{2c_d}},$$

$$\tau_{sat}^{-1} = \frac{1 + M - 2aM}{2M(1 + M)}\sqrt{\frac{c_d}{2\pi}},$$

with $U_1^*(0)$ the initial condition which can be taken equal to 0 without loss of generality, $U = \varepsilon U_1^*$ is the asymptotic locomotion velocity and τ_{sat} the characteristic transient time. Inserting the expression of $U_1(\tau)$ into the equation of $u_2'(t)$, we derive the equation that determines $u_2(t)$:

$$\frac{d}{dt}u_2(t) = \frac{1 + 2M(1 + 6a) + M^2(1 + 4a(a + 3))}{32M(1 + M)^2}e^{2it} + \text{c.c.}.$$

We obtain by integrating:

$$u_2(t) = K_{u_2} - i\frac{1 + 2M(1 + 6a) + M^2(1 + 4a(a + 3))}{64M(1 + M)^2}e^{2it} + \text{c.c.}.$$

The equation $v_2(t)$ is deduced from the second order of the vertical momentum balance:

$$\frac{d}{dt}v_2(t) = \frac{2a - 3}{4(1 + M)}U_1(\tau) - \frac{U_1(\tau)}{1 + M}v_1(t),$$

and we solve it:

$$v_2(t) = K_{v_2} + i\frac{3 + (3 - 2a)M}{4(1 + M)^2}U_1(\tau)e^{it} + \text{c.c.}.$$

Again the integration constant K_{v_2} is set to zero to remove any vertical drift.

At third order in perturbation theory, the expression becomes very lengthy, but the equation for u_3 presents the same form as that of u_2:

$$\frac{d}{dt}u_3(t) = K_{u_3} + \text{oscillating terms},$$

with K_{u_3} a constant. By invoking the solvability condition to maintain the validity of the expansion, the constant K_{u_3} is set to zero and we finally get:

$$K_{u_2} = 0.$$

Then the solution up to second order of the problem can be written as:

$$u(t) = \varepsilon U_1^* \tanh\left[\frac{\tau}{\tau_{sat}}\right] + \varepsilon^2 \frac{1 + 2M(1 + 6a) + M^2(1 + 4a(a + 3))}{32M(1 + M)^2}\sin(2t),$$

$$v(t) = \varepsilon\frac{a}{1 + M}\cos(t) + \varepsilon^2 U_1 \frac{M(2a - 3) - 3}{2(1 + M)^2}\sin(t).$$

To compute the phase angle between pitch and heave in the steady state, we first rewrite the expression of the lateral velocity at the second-order:

$$v(t) = \varepsilon\frac{a}{1 + M}\cos(t) + \varepsilon^2 U_1^* \frac{M(2a - 3) - 3}{2(1 + M)^2}\sin(t).$$

In order to compare the heave and the pitch, we decompose this expression using only one trigonometric function:

$$v(t) = -\frac{a\varepsilon}{1+M}\sqrt{1 + \varepsilon^2\left(U_1^*\frac{M(2a-3)-3}{2(1+M)^2}\right)}\sin(t - \phi_v),$$

$$\phi_v = \arctan\left[\frac{2a(1+M)}{\varepsilon U_1^*(3 - M(2a-3))}\right],$$

which gives the position of the center of mass after integration:

$$y_{cm}(t) = \frac{a\varepsilon}{1+M}\sqrt{1 + \varepsilon^2\left(U_1^*\frac{M(2a-3)-3}{2(1+M)^2}\right)}\cos(t - \phi_v).$$

By comparing the above expression of $y_{cm}(t)$ with respect to $\alpha(t) = \varepsilon\cos(t - \pi/2)$ we finally deduce the phase shifting in the heave-pitch motion:

$$\phi = -\frac{\pi}{2} + \phi_v = -\frac{\pi}{2} + \arctan\left[\frac{2a(1+M)}{\varepsilon U_1^*(3 - M(2a-3))}\right].$$

Up to now, we have exposed the general method and calculated without making any hypothesis with respect to the parameters, reason why the expressions that appear are, on certain occasions, long and cumbersome. From now on, in the analysis that we will do, we will consider the limit of small M. Recall that this parameter, the dimensionless mass of the swimmer, is the quotient between the swimmer's mass per unit length and the mass per unit length of a circle of water of diameter the length of the swimmer:

$$M = \frac{4m}{\pi\rho_{water}L^2} \sim \frac{4\rho_{fish}Ld}{\pi\rho_{water}L^2} \sim \frac{d}{L} \ll 1,$$

where d is the swimmer's width, but since we are considering very thin swimmers, this parameter will be much smaller than the length L. In the approximate calculation of this quantity we have taken $\rho_{fish} \sim \rho_{water}$ [134]. Although we have wanted to be general in our perturbative treatment, the parameter M represents a quantity that is also of order ε or lower and therefore, we will take the limit $M \ll 1$ from now on. In this limit, the velocities in the steady-state write:

$$u(t) = \varepsilon\sqrt{\frac{\pi}{32c_d}} + \varepsilon^2\left[\frac{1}{32M}\sin(2t)\right] + \mathcal{O}(\varepsilon^3), \tag{2.4.4}$$

$$v(t) = \varepsilon a\cos(t) - \varepsilon^2\frac{3}{2}\sqrt{\frac{\pi}{32c_d}}\sin(t) + \mathcal{O}(\varepsilon^3). \tag{2.4.5}$$

$u(t)$ and $v(t)$ reach their steady state values after a transient time $t \sim M/\varepsilon\sqrt{c_d}$: this reflects that a heavy swimmer will need time to reach its cruising velocity. An oscillatory function, whose frequency is doubled as compared to the driving angle, is superposed to the mean swimming velocity. We remark here that this expansion in terms of the small parameter ε is formal and might break the assumption of a small transverse velocity in comparison to the longitudinal velocity. Nevertheless, on one hand, we recall that the pressure drag coefficient is quite small, of order 0.01, as we will later justify, and this value permits to finally verify that the locomotion velocity is larger than the transverse velocity. On the other hand, experimental data suggest that the thrust derived from the linear theory likely extends beyond the small amplitude regime [135, 136]. The dimensionless swimming velocity $U = \langle u(t)\rangle$ is given by

$$U = \varepsilon\sqrt{\frac{\pi}{32c_d}} + \mathcal{O}(\varepsilon^3). \tag{2.4.6}$$

The steady state transverse velocity $v(t)$ is a harmonic function of time. By integrating this velocity, the dimensionless y-position of the center of mass is given by

$$y_{cm}(t) = \varepsilon a \sin(t) + \varepsilon^2 \frac{3}{2}\sqrt{\frac{\pi}{32c_d}}\cos(t) = \sqrt{\varepsilon^2 a^2 + \varepsilon^4 \frac{9}{4}\frac{\pi}{32c_d}}\sin(t-\phi).$$

From this expression we can infer the phase angle ϕ between the oscillations of the position of the mass center and the driving angle α:

$$\phi = -\frac{\pi}{2} + \arctan\left[\frac{8a}{3\varepsilon}\sqrt{\frac{2c_d}{\pi}}\right]. \tag{2.4.7}$$

Still in the small angle limit, the dimensionless y-position of the tip of the tail is given by

$$y_t = y_{cm} + (1-a)\alpha = \varepsilon \sin(t) + \varepsilon^2 \frac{3}{2}\sqrt{\frac{\pi}{32c_d}}\cos(t).$$

The dimensionless tail beat amplitude A_d is thus given by:

$$A_d = 2\varepsilon\sqrt{1 + \left(\varepsilon\frac{3}{2}\sqrt{\frac{\pi}{32c_d}}\right)^2} + \mathcal{O}(\varepsilon^3) = 2\varepsilon + \mathcal{O}(\varepsilon^3). \tag{2.4.8}$$

As a consequence the physical tail beat amplitude A is given by $2\varepsilon L/2$ and $A/L = \alpha_0$. The position of the tail is in phase with the driving angle, while the phase of the position of the center of mass depends on a: it is in phase if $a \to 1$ and the phase shift equals $-\pi$ if $a \to -1$. Given that U and A_d are calculated up to the second order in ε, the Strouhal number St can be calculated up to the first order in ε:

$$St = \frac{\sqrt{32c_d}}{\pi^{3/2}} + \mathcal{O}(\varepsilon^2). \tag{2.4.9}$$

In this first-order approximation, only the constant term is nonzero. Remarkably, it emphasizes that the Strouhal number is strongly correlated to the drag coefficient and barely depends on the other parameters.

2.4.2 Numerical approach

The equations are solved numerically with a Runge–Kutta method at the fourth-order approximation [137]. We impose as initial conditions $u(0) = v(0) = 0$, although, as we have already shown, the same steady-state will be reached for any set of positive initial conditions, and let our model evolves towards the cruising locomotion regime, which is reached after the aforementioned transient time $M/\alpha_0\sqrt{c_d}$.
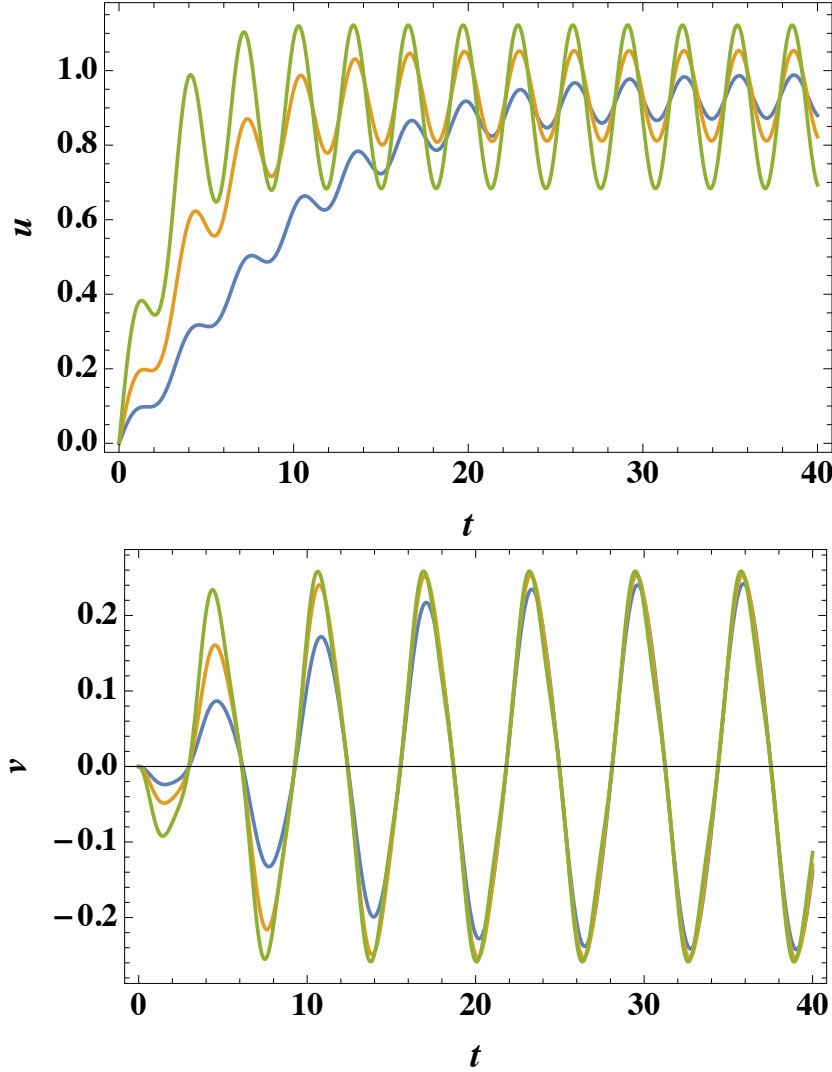
Figure 2.10: u and v as functions of t for the set of parameters $[\alpha_0 = 0.2, a = 0, c_d = 0.01]$ and $M = 0.01, 0.02$ and 0.04 represented by the green, orange and blue lines respectively.

In all our simulations, the forcing in the pitch results in a cruising self propelled swimmer, for physically acceptable dimensionless parameters. In figure 2.10, we show a typical time evolution of the velocities u and v: as expected after a transient time which depends on M, the swimmer cruises in the steady state regime. Theodorsen's approach has been designed for a finite stream velocity. The model is robust with respect to the unsteadiness but is expected to be less precise in the transient regime or at least during the very beginning of the motion, in particular if the swimmer starts from rest. In addition, for very low velocities, it would be necessary to add the skin friction drag, or even a Stokes' drag if the velocity tends to zero. As stated above, we focus on the steady state regime and we assume the Reynolds number to be larger than $10^3 - 10^4$ so that pressure drag is the relevant drag at play.

We remark here that the horizontal component of the locomotion oscillates around the steady value given by equation 2.4.6, with a frequency doubled with respect to the pitch forcing. We present the numerical simulations of the dynamics of the angle α, the y-position of the center of mass y_{cm} and the x-component of the velocity, obtained after the transient regime in figure 2.11. $u(t)$ oscillates twice faster than α and y_{cm}, as predicted by the asymptotics, equations 2.4.4 and 2.4.5.

2.4.3 Results

The model depends on four dimensionless numbers and it is necessary to explore the parameter space in order to gain a complete outlook of the predictions of the system. In this part, we systematically study the effects of varying the values of α_0, a, M and c_d. We then vary most of these parameters while maintaining some of them fixed.
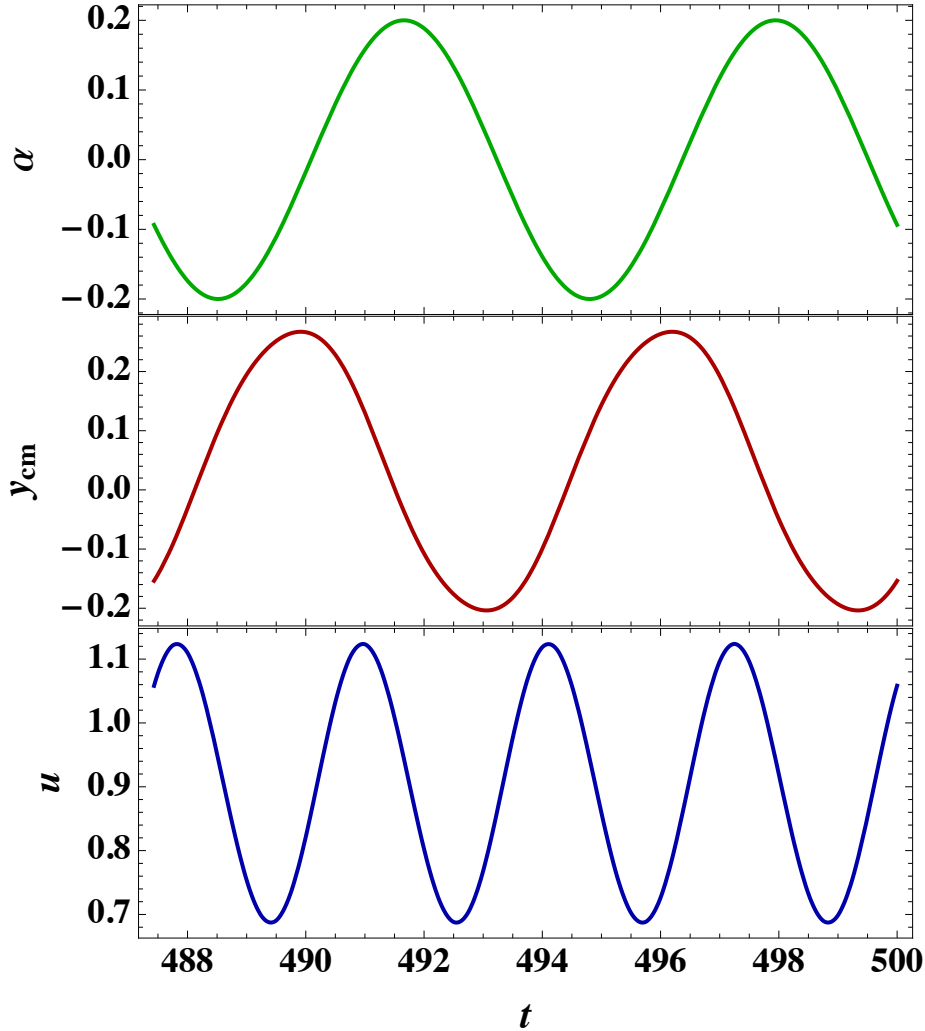
Figure 2.11: α, y_{cm} and u as functions of t in the steady state for the set of parameters $[\alpha_0 = 0.2, a = 0, M = 0.01, c_d = 0.01]$.

The perturbative analysis shows that $\alpha_0 \approx A/L$. Consequently, we have chosen as reference value $\alpha_0 = 0.2$, which is typical for fish [21, 25, 38, 133]. $a = -1/2$ corresponds to the particular case, where the center of mass is situated in the middle of the leading part of the fish. Since the swimmer is considered as a thin body, we expect $M \ll 1$. $M = 0.01$ is taken quite arbitrarily since we will show that in this limit, M does not have a significant effect on the measured quantities in the steady state. Values of the drag coefficient c_d are more difficult to infer from experiments since they require measurements when fish do not make any movement. Nevertheless some data were collected either with dead fish or during gliding deceleration. Lighthill reviewed data obtained with salmon, herring and trout and emphasized coefficients around 0.01 [91]. Cods exhibit value around 0.011–0.015 [127], bluegill around 0.015 [129] and dolphins between 0.003 and 0.03 [128, 130]. The drag coefficient seems to depend on

the experimental procedure, but in most cases the coefficients range between 0.01 and 0.1 for Reynolds numbers ranging between 10^3 and $3 \cdot 10^6$ [129]. In the light of these measurements, we take $c_d = 0.01$ as the reference value.

We tune our controlling parameters to the typical values measured in underwater swimming animals. The reference values are set to:

$$\alpha_0 = 0.2, \quad a = -\frac{1}{2}, \quad M = 0.01, \quad c_d = 0.01.$$

Strouhal number

The Strouhal number is assessed from the steady state values of U and A_d in simulation. In figure 2.12, color plots represent St as a function of c_d (from 10^{-3} to 10^{-1}) and another parameters among α_0 (from 0.003 to 0.3), a (from -1 to 1) and M (from 10^{-3} to 10^{-1}). This choice follows the observation that St is strongly correlated to c_d around the reference values, independently of the other parameters. This is consistent with the first-order approximation obtained theoretically (see equation 2.4.9).

The perturbative approach and the numerical simulations are compared in figure 2.13. They are in very good agreement with each other and support the trend $St \propto \sqrt{c_d}$. More quantitatively, using the analytical expression of the Strouhal number at the first-order approximation, 2.4.9, with values of the drag coefficient measured with fish (0.01–0.1), we obtain values of St between 0.1 and 0.3. It is remarkable that our simple model recovers quantitatively the values measured in biological swimmers.
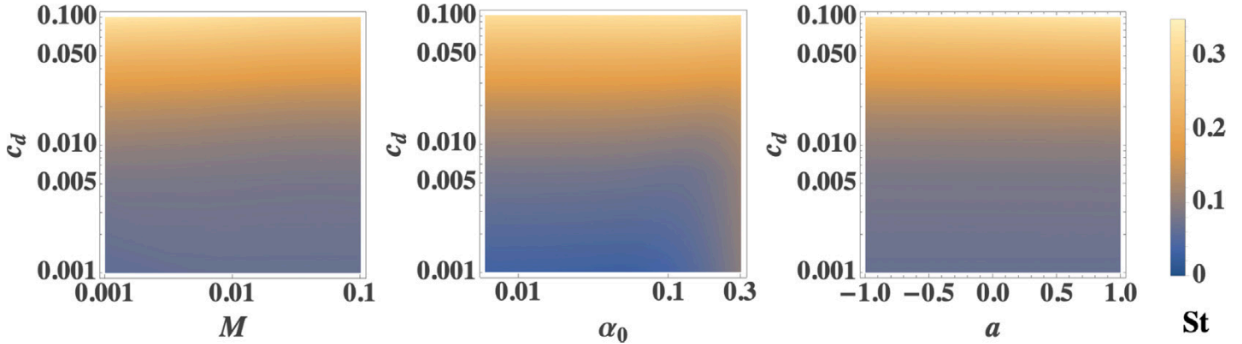
Figure 2.12: Variation of the Strouhal number, as the dimensionless numbers M, c_d, α_0 and a are varied. From left to right: $[a = -1/2$ and $\alpha_0 = 0.2]$, $[M = 0.01$ and $a = -1/2]$ and $[M = 0.01$ and $\alpha_0 = 0.2]$.

The study emphasizes that St barely vary with α_0, a or M, but we recall that M and α_0 play a role in the transient state since the cruising swimming velocity U is reached after a typical time $t \sim M/\alpha_0\sqrt{c_d}$. When the swimmer has reached a nearly constant velocity in the steady state, shown in figure 2.11, the inertia terms (closely related to the parameter M) become negligible and do not play any important role in the final swimming velocity, because this quantity is only determined by the equilibrium between thrust and drag forces as proved by [24].
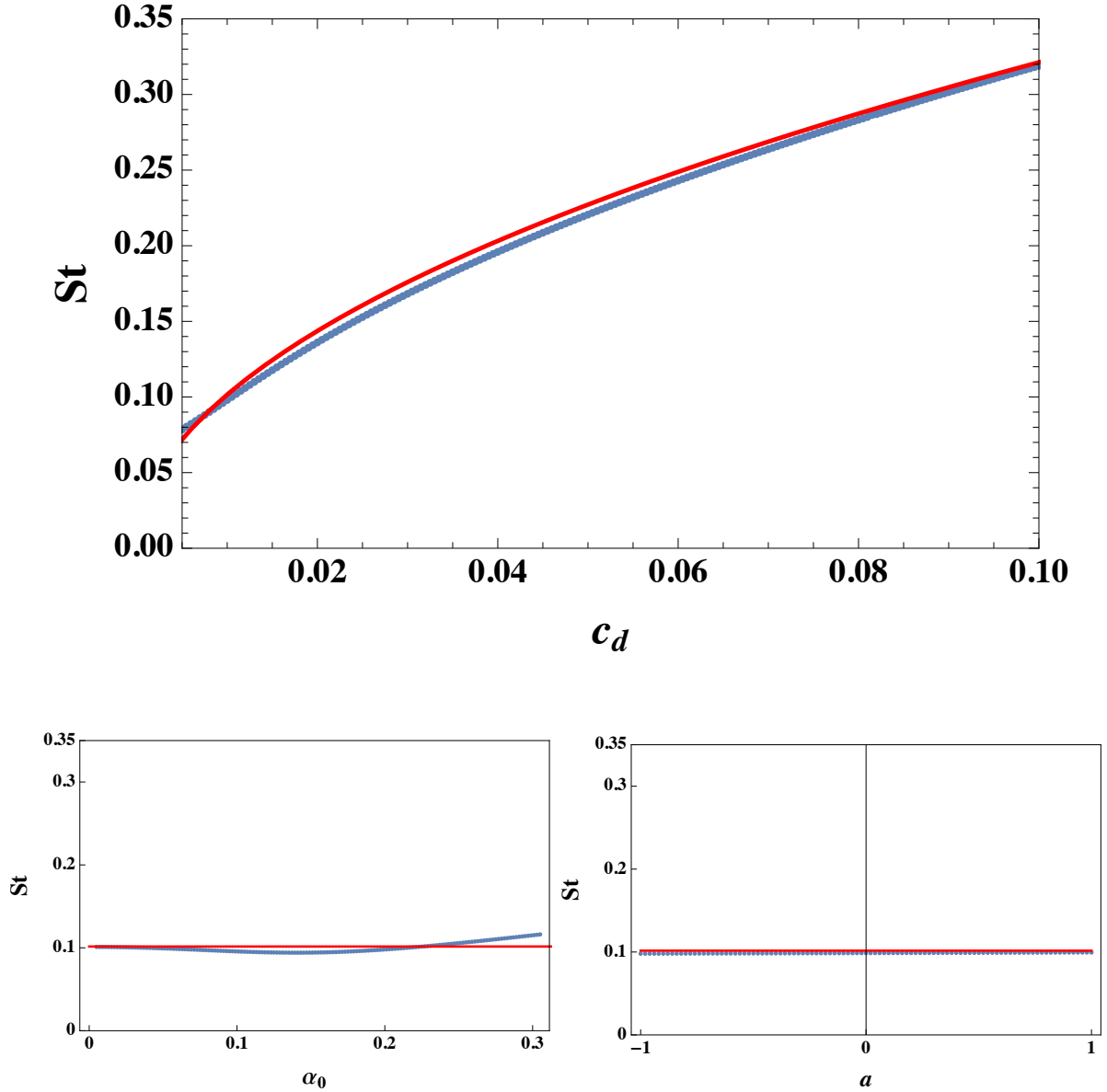
Figure 2.13: Top figure. Strouhal number St as a function of the drag coefficient c_d [$\alpha_0 = 0.2$, $a = -1/2$ and $M = 0.01$]. The blue thick curve is obtained numerically, while the red curve corresponds to the prediction, equation 2.4.9. From left to right at the bottom we display St as a function of α_0 [$a = -1/2$, $M = 0.01$ and $c_d = 0.01$] and a [$\alpha_0 = 0.2$, $M = 0.01$ and $c_d = 0.01$].

Tail beat amplitude

In figure 2.14, A/L is represented as a function of α_0, both in simulations with the parameters [$a = -1/2, M = 0.01, c_d = 0.01$] and in theory with the second-order approximation ($A/L = A_d/2$ in equation 2.4.8). We see that $A/L \simeq \alpha_0$ is a very good approximation in the small angle limit. For $A/L = 0.2$ ($\alpha_0 = 0.17$), there is a 15% difference between what is obtained in simulation and in theory. This means that we probe the limit of the small angle regime (and the validity of our equations as well) and it is remarkable that natural fish are found there, at the onset of a strongly nonlinear regime where a third-order approximation would be required. Saadat et al [25] have shown that a criterion on the minimal energy assumption sets $A/L \sim 0.2$, which would emphasizes that higher order terms become rapidly inefficient. The same argument would hold in the study performed by Florian et al. [31] since they find that the St number at maximal efficiency is still very close to the one obtained in the small angle limit.
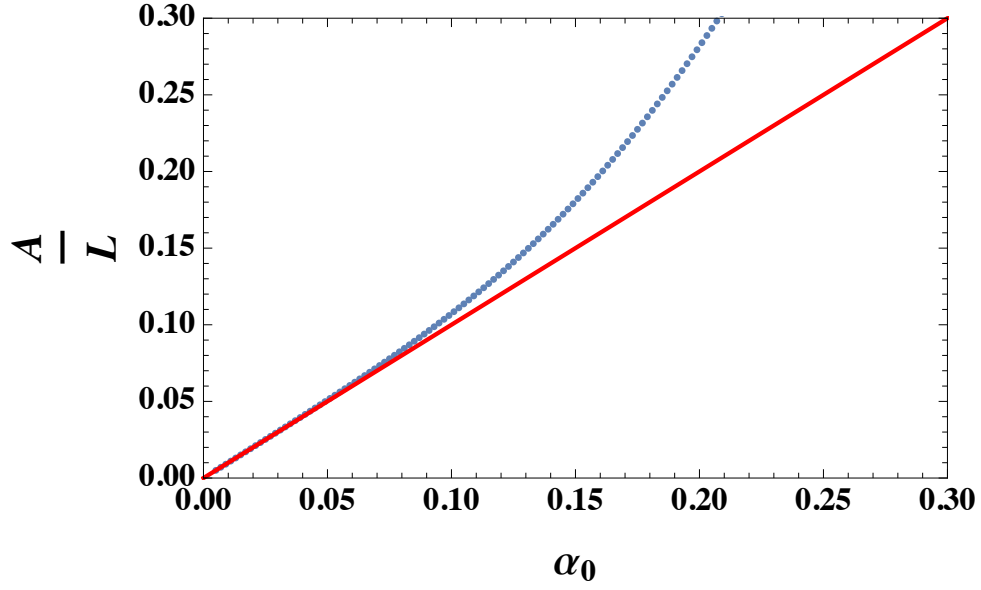
Figure 2.14: Tail beat amplitude A/L as a function of the driving angle α_0. The blue symbols are obtained numerically, while the red curve corresponds to the prediction from equation 2.4.8.
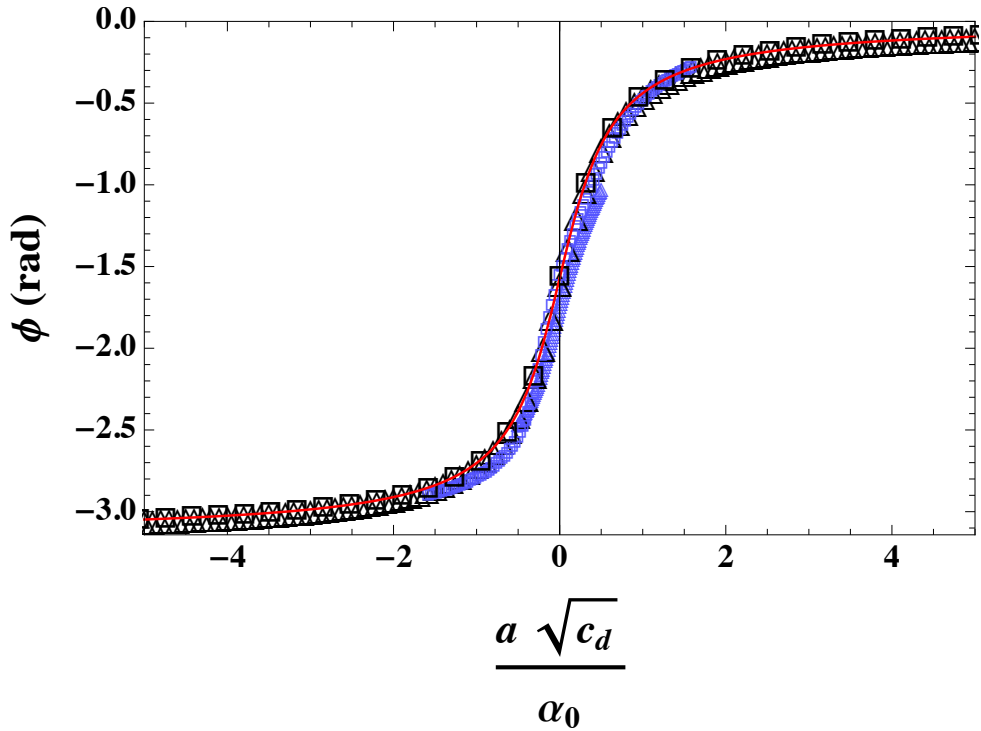
Figure 2.15: ϕ as a function of $\frac{a\sqrt{c_d}}{\alpha_0}$. The red curve is the analytical prediction of equation 2.4.7, $\phi(x) = -\pi/2 + \arctan\left(\frac{8}{3}\sqrt{\frac{2}{\pi}}x\right)$.   In all the simulations we vary a and use the value $M = 0.01$, and the results are displayed for several values of c_d and α_0. Triangles and squares correspond to $c_d = 0.01$ and 0.1, respectively, and large black and small blue symbols correspond to $\alpha_0 = 0.02$ and 0.2, respectively.

Phase angle between heave and pitch

Our asymptotics computations conjecture through equation 2.4.7 the existence of a master curve for the phase ϕ as a function of $\frac{a\sqrt{c_d}}{\alpha_0}$. We have collapsed various results of numerical computations onto this sigmoid curve in figure 2.15: it appears that our small angle approximation successfully predicts the phase angle between pitch and heave, and ϕ takes value in the ranges $[-\pi, \pi/2]$ and $[-\pi/2, 0]$ for $a < 0$ and $a > 0$, respectively.

Thanks to pioneering studies in driving a NACA airfoil, there exist some measurements with respect to the synchronization of the pitch and heave undulations [13, 138]. To compare our results with these studies, we define $\psi = \phi + \pi$ the phase angle between pitch and heave with angles α counted positively counterclockwise (all along our study we have used the clockwise definition taken by [100]). The aforementioned studies demonstrate that the best thrust performance is reached as the phase angle ψ is close to $90°$ for a driven airfoil, or equivalently ϕ close to $-90°$, following our notation. In the light of our results, this suggests that the best thrust performance is obtained as $a\sqrt{c_d}/\alpha_0 \to 0$ or $|a| \ll \alpha_0/\sqrt{c_d}$. We remark here that if $a < 0$, ψ tends to 0, for very low amplitude of the tail $\alpha_0 \to 0$. We also emphasize that the phase ψ is equal to $90°$, independently of any controlling parameter if $a = 0$. All these arguments indicates that the location of the mass center should have an impact on the thrust performance.

2.5   Discussion and conclusions

The most important models and approaches to treat the swimming problem mathematically have been introduced, and the expression of the thrust force was derived in function of the imposed deformation. Then, we proposed our minimal model of self propelled locomotion by using Theodorsen and Garrick's formalism [100, 101].

First, with our set of equations we expect St to be a function of the dimensionless quantities α_0, c_d, a and M. None of them is a function of the tail beat frequency f. This means that the Strouhal number of a free-swimming, airfoil-shaped, rigid body does not depend on the frequency. This behavior is different from the one of the same kind of bodies performing pitching and heaving motions in classical water tunnel experiments [125, 139]. In this case, the body is not free to move since the longitudinal position is fixed and the transverse motion is imposed. These constraints allow pitching and heaving motions to be set independently, which is accounted for by an additional dimensionless number that includes the tail beat frequency. With a free-swimming body, pitching and heaving motions cannot be dissociated and the tail beat frequency is not relevant in determining the Strouhal number. Second, the model makes explicit the trend $St \propto \sqrt{c_d}$ expected from a simple thrust–drag balance [15, 24]. This result obtained with a free-swimming body in the small amplitude regime stems from a thrust scaling as $A^2 f^2$. This scaling seems to be validated beyond the small amplitude regime with constrained systems such as heaving foils [30], pitching foils [139], foils combining both of them [31] and flexible robotic fish [15]. We have studied a minimal model of fish locomotion. Our model is a 2D thin airfoil-shaped body which performs an oscillating motion; its cruising swimming velocity is predicted both numerically and theoretically in the small amplitude regime as a function of several parameters: the body length, the amplitude and frequency of the tail motion, the dimensionless mass, the position of the center of mass and the drag coefficient. We show that the Strouhal number is strongly correlated to the drag coefficient, while the effect of the other parameters can be neglected at the first order approximation. Given that natural fish exhibit values of c_d about $0.01 - 0.1$, we find an almost constant Strouhal number, around $0.1 - 0.3$, in very good agreement with values measured in biological swimmers. This study has been extended by Gross et al. [140], who shows that St is also a constant quantity when the oscillation amplitude is bigger and vortex-induced drag is considered. In addition, we uncover that the position of the center of mass has an effect on the phase angle between pitch and

heave, and should consequently influence the thrust performance. Our simple model accurately predicts the cruising motion of swimmers, but it remains dependent on the choice of the tail dynamics. It would be engaging to implement a mechanism that automatically selects the kinetics of the tail, without imposing either the amplitude α_0 or the beat frequency. We believe that a proprioceptive approach, like those proposed in [141], would be a good research direction and this idea is developped in the next chapter.

These results are published in the Journal of Fluids and Structures [142].

Chapter 3

Swimming gait driven by proprioceptive feedback

3.1 Introduction

The problem of aquatic locomotion is seen under two main visions: one in which the animal's movements are prescribed, and the solution of the problem consists in finding the forces applied on the system for the generation or not of an effective thrust. In this approach, which is the one presented in the previous chapter, no reaction of the swimmer in function of the surrounding fluid is assumed, and the animal dynamics, already fixed, do not consider what is happening around it. Although effective in a dynamic treatment where the forces exerted on the system are calculated, this vision is somewhat simplistic and unambitious for giving the swimming problem a global treatment where factors that are not purely physical (in the context of fluid mechanics) are added and taken into account. The characterization of the organism as a being capable of sensing what is happening around it, processing this information, and sending orders to the motor units to carry out one instruction or another according to the information received is undoubtedly a natural projection in understanding the problem.

Aquatic animals sense the environment and interact with it [143], a fact shared with the rest of living beings and that evolution has been in charge of perfecting in order to be able to detect pressures or forces around them, as well as the direction of currents to orient themselves and migrate, or the detection of chemical in water through chemoreceptors, among other capabilities [144–146]. The existing hydrodynamic feedback also allows fish to adjust their gait according to the flow around them. It is in the work of Liao and Beal [147–149], where they show the change of fish behavior in response to the environment. They placed a trout *Oncorhynchus mykiss* in a water tunnel where they analyzed its movement and then immediately compared it to the movement produced by the trout when an obstacle was placed directly in front of the exit of the flow in the water tunnel. The flow produced in this configuration is called Kármán vortex street [150], and is characterized by being composed of a set of columnar vortices of opposite sign, which are shed periodically and are equally spaced. The motion patterns of the animal in both scenarios turned out to be completely different; see the comparison between B and C in figure 3.1. The amplitudes and body curvatures are much more significant in swimming with obstacles than those found in the absence of the cylinder.

Nevertheless, it is not only the body undulations of the animals that are altered but also the frequency of movement of the tail, which matches the vortex shedding frequency of the cylinder. Therefore, trout are also altering their body kinematics to synchronize with the shed vortices using a mechanism that may not involve propulsive locomotion [147]. The conjecture employed to explain this behavior suggests that the fish may be able to reduce locomotor costs by altering their body kinematics to capture energy from the high-vorticity regions of the wake [147].

To test this hypothesis, Liao performed measurements of muscle activity [148] and oxygen

consumption [151]. The results on muscle activity showed that the fish was using its muscle power to stabilize and control position rather than generate effective propulsion. Measurements of oxygen consumption also showed that this gait was energetically more favorable than steady swimming since the amount of oxygen consumed by the animal was considerably less.
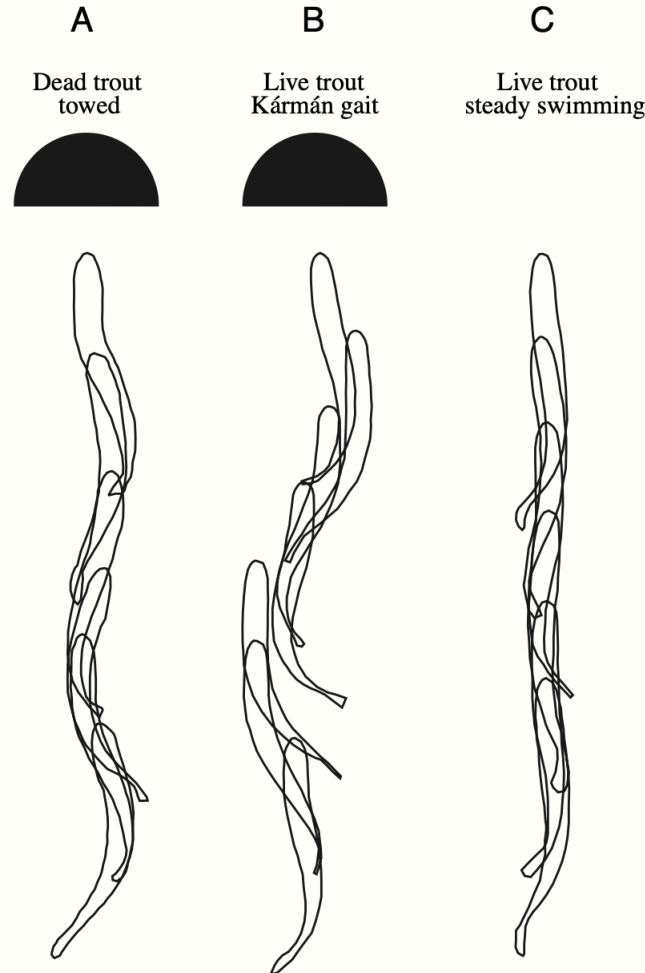
Figure 3.1: Body outlines of a *Oncorhynchus mykiss* for three different configurations: (A) A dead (B) and live trout behind a cylinder and (C) a live trout with no obstacle. From Liao [148].

One of the unknowns about this behavior is whether it was active or passive, that is, if the animal was acting deliberately to take advantage of the environment's energy. The same experiment of analyzing the trout's gait was performed, but this time with a particularity: the animal had been euthanized shortly before the experiment in order to avoid the rigidity typical of lifeless bodies. They attached a thin line into the trout's mouth and placed it in the water tunnel after the obstacle. Surprisingly, the gait of the dead animal maintained many similarities with the movement when it was alive, the body oscillated with amplitudes and frequencies not too far apart and advanced towards the obstacle [148], although when it approached it lost stability and returned to its original position, see A in figure 3.1. This demonstrates, then, that passively, the fish body is able to extract energy from the environment and use it to reduce the energy expended by the fish, showing the existence of an interaction between organism and environment.

However, in order for them to interact with this environment, they must be able to detect changes and act on it to influence it. Fish possess sensors that allow them to analyze the changes they encounter in the environment. They rely on vision as an essential source of

sensory information, which allows them to recognize obstacles around them and their position as well as to detect disturbances created by the flow. Most fish have well-developed eyes. The specific movements and variety of colors available to them allow comparison even with visually advanced species of mammals or birds, which gives a clue to the importance of vision in these animals [152]. Not only does vision constitute one of the significant sensory sources in these organisms, but fish also possess a highly refined organ called lateral line, which allows them to detect movements in the water, changes in pressure, or both [153]. The lateral line consists of two types of neurons, some distributed along the animal's skin and sensitive to flow velocity, and others also present along the body but concentrated near the head that would be responsible for sensing pressure variations [154, 155].
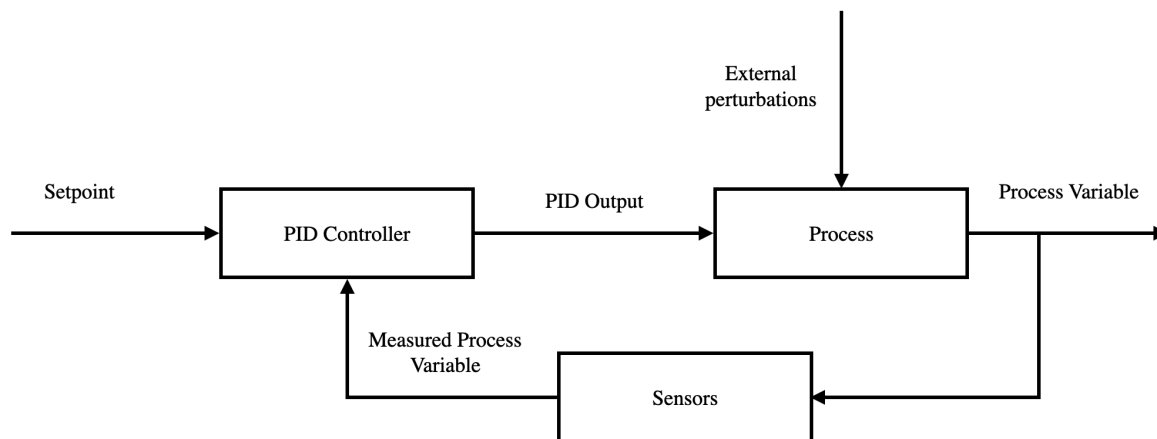
Figure 3.2: Block diagram of a PID control.

These sensory mechanisms must therefore be coordinated with the movement-generating mechanisms to generate harmonious and efficient movements. For most animals, this process is carried out by the central nervous system: complex neural circuits in the brain initiate locomotion and control the speed of movements by exciting neural networks located in the spinal cord. These local networks are responsible for starting and stopping muscle contractions that generate sufficient force to initiate movement. They are of vital importance and are called Central Pattern Generators (CPG). A CPG is a neural network capable of producing coordinate patterns of rhythmic activity without any inputs from sensory feedback or higher control centers [156]. Almost all known vertebrates are equipped with CPG [157, 158]. Even if they do not require any external driving, CPG are affected by sensory feedback because the motion must be obviously adapted to the environment of the moving organism [159–162]. Sensory information encompasses the traditional five senses as well as proprioception. Proprioception, although not one of the five senses traditionally stipulated by the human being (sight, smell, touch, taste, hearing), is taken as an acute sixth sense in the relationship of living beings with their environment: proprioception is the capacity of our brain to know the exact position of all the parts of our body at any given moment. The proprioceptive system "processes" the signals received from joints and muscles to accomplish this task. This system then interprets whether it is necessary to react immediately by activating other muscle groups in response to disturbances that interfere with the desired movement of the body or that could lead to a harmful situation. For example, if somebody tries to balance on one leg and is pushed, his body will immediately send a signal to the leg suspended in the air to brace itself on the ground and avoid a fall. This command occurs before one is aware that one must move to ensure stability. This sense is thus responsible for regulating balance and coordinating movements, as well as maintaining the alertness levels of the nervous system, from receptors included in muscles, joints, ligaments

or tendons [163, 164]. This last class of sensing is usually responsible for the adaptation of the rhythmic driving of the muscles [165, 166], and suggests that locomotion is driven through proprioceptive feedback. In fact, several types of fish have been found to possess proprioceptive feedback of their fins [167–170], specialized mechanoreceptors along their spinal cord providing feedback and modulating the CPG behavior [171, 172], or specialized sensory endings in the subcutaneous tissue, exterior to muscles [159].

Feedback from the environment on the organism configures what is known as a closed-loop controller in control theory. Within this field, there are several techniques and methods to explain and model the behavior of closed-loop systems. Among them, the Proportional-Integral-Derivative (PID) controllers, widely used for their more than satisfactory performance given the simplicity of the elements that compose it, stand out. A prototypical feedback control system is shown in the figure 3.2. The value of the setpoint, or the desired target is continuously adjusted to match the measured process variable, representing the current state of the system. The control is disturbed by the environment, which acts on the system and modifies the process variable. Through the feedback provided by the sensors, once the control is applied, the outgoing signal changes acting on the process.

The control device aims to reduce the error between the desired signal or setpoint and the output signal or process variable. We write this error as:

$$e(t) = r(t) - y(t),$$

where $r(t)$ and $y(t)$ are the reference signal and process variable, respectively.
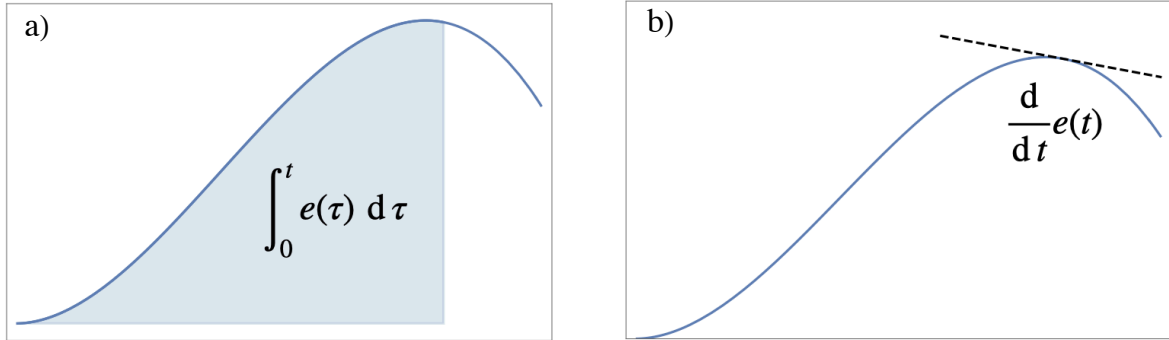
Figure 3.3: Graphic representation of the mechanism underlying integral a) and derivative b) control in PID systems.

If we call $u(t)$ the function that controls the current error, we have that a PID controller is represented mathematically by these three terms:

$$u(t) = K_p e(t) + K_i \int_0^t e(\tau)d\tau + K_d \frac{de(t)}{dt},$$

where K_p, K_i and K_d are just proportionality coefficients for each actuator.

PID control is so named because it is based on three operations to reduce the error between the desired and output signals. The corrections applied belong to three categories: proportional, integral, and derivative, corresponding to the first, second, and third terms of the equation, respectively. The term proportional to the error considers the control process's present; if the error is large, the output control will also be large to ensure the convergence of the control. The integral term somehow regroups the effect of the past on the control, as we see in the figure 3.3a, thanks to the geometrical interpretation of the integral, that is, the area under the curve of a given function. This term gives us an indication of the residual error that has been made throughout the control. Finally, we see the meaning of the derivative control, in the same

figure 3.3b. The geometric interpretation of the derivative is the slope of the tangent line to the curve at a given point. This term gives us information about the "future" of the control, the foreseeable trend of the error, and whether we can anticipate the growth of the error. The choice of the proportionality constants and the importance of each of the terms will depend on the specific system to be controlled and the level of complexity required of the control device [173].

3.2 A proprioceptive hypothesis
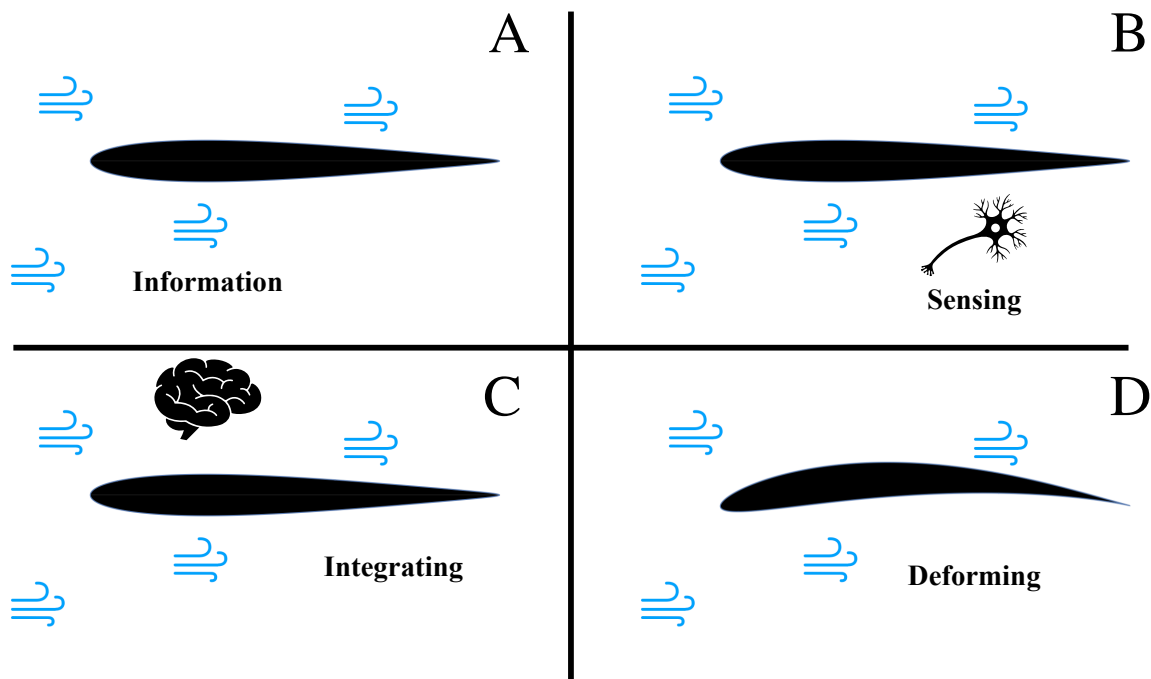
Figure 3.4: Phases of proprioceptive swimming. A) The swimmer lives in an environment from where it can extract information. B) In a state of constant information exchange, the organism detects certain information that can alter its current state and change its locomotion regime. C) The signal is perceived by the animal and passes to the central nervous system, which processes and integrates the signal. D) The integration of the signal sends an order to the muscles and motor systems that produce a deformation in the animal and initiate a different state of locomotion.

Therefore, the motivation of the problem is clear: we want to relate in a general way the neural dynamics of the organism itself with the muscular activity and its perception of the environment. However, formulating a general theory requires taking into account the tremendous diversity in physiology and shape that multicellular organisms exhibit. This variety is usually rationalized by the adaption to their environment within the Darwinian evolution but also by the functions needed by the animals to live [174]. Among these functions, there is lomocotion, which is the function motivating us, as motions result from a mechanical interaction of the organism with its environment. Thus, despite the vast variations of gaits in animals for achieving locomotion [175] we expect general mechanisms to be at play because all the movements result from mechanical principles.

Gazzola et al. [141] already showed how a simple form of proprioceptive feedback was suf-

ficient to drive elastic instabilities associated with thrust production and led to a spontaneous swimming gait without the need for a central pattern generator. Their swimmer is considered as a slender and elastic sheet for which a dynamical analysis is carried on by prescribing expressions for the organism internal stresses, decomposing it into different contributions and highlighting two of them. An active torque in the form of a traveling wave [83], and a torque due to proprioceptive feedback. The reason for adding these two is that, by itself, the introduction of only an active torque is not fully satisfactory because it does not provide any insight into the mechanisms that lead to such a wave. Nevertheless, the muscle torques can be related to the neural network's response driven by the proprioception of the fish shape. Biologically, this finds an explanation in that deformations of the animal's body are sensed by receptor neurons in some organisms such as lampreys, and it has been shown how variations in their curvature can affect muscle activity [162]. Proprioceptive feedback then enters through the swimmer's equations of motion by modeling the force moments.
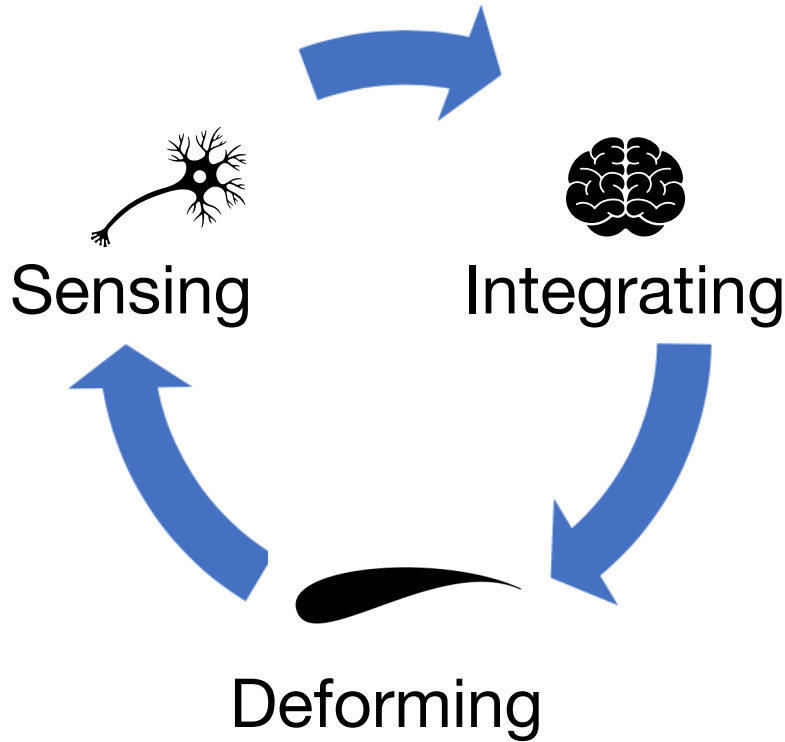
Figure 3.5: Proprioception scheme: the extension of the muscles providing the deformation is moderated by the integration of the information from the proprioceptive sensors.

Following this spirit, our proprioceptive swimmer is a system that interacts with the environment by exchanging information of various kinds but selecting only those that are relevant for locomotion, as explained in figure 3.4. This scheme can be generalized as shown in figure 3.5. We propose the first demonstration of swimming following the simple scheme shown in figure 3.5 using a robotic fish that undulates in a thunniform way. This proprioceptive robot swims without any input from an operator, i.e., where before we needed imperatively to choose by ourselves a given amplitude and frequency to describe the locomotion, now these parameters are not selected by us. However, the swimmer itself selects them according to the interaction strength of the proprioceptive feedback, which now becomes the only control parameter. Furthermore, we show that the activation of the robot is ensured by an oscillatory instability whose threshold matches the environment: the robot does not move in air as it does in water.

The information collected in our setup is carried out through a force sensor described in

Appendix A, capable of measuring the two components F_x and F_y of the force exerted by the fluid on the swimmer, respectively aligned and normal to the swimming direction. We use F_y as the proprioceptive information to trigger locomotion. The choice of the normal force as proprioceptive input is motivated by the biological character of the sensors in fish, mainly by the existence of the lateral line, a mechanism that is supposed to be responsible for detecting pressure changes in the environment [153]. The normal force corresponds to the integration of the pressure variations around the swimmer, which motivates our choice of sensory information. As done by Gazzola et al. [141], we want to relate the hydrodynamic information to the muscular mechanisms and the deformation produced by them in the animal's body. In an attempt to make a simple model and based on the rigid airfoil theory formulation of Theodorsen and Garrick [100, 101], we neglect in a first approximation elastic effects and consider that the deformation is equal throughout the airfoil and depends only on the pitch angle, α. In order to match this approximation with our experimental system, in which obviously the deformation is not homogeneous, we will reduce the reference deformation to a point located in the middle of the tail, as we can see in figure 3.6. A possible relation between the deformation and the normal force could be given by the PID control algorithm, with the target angle α_c being proportional to F_y and the integral and derivative of the force. Apart from a relative increasing complexity, nothing prevents us from implementing this formalism, especially for the proportional and integral terms. Nevertheless, for the sake of simplicity, we keep just the proportional term as a first approximation. The relation we are looking for is then:

$$\alpha_c \propto F_y.$$
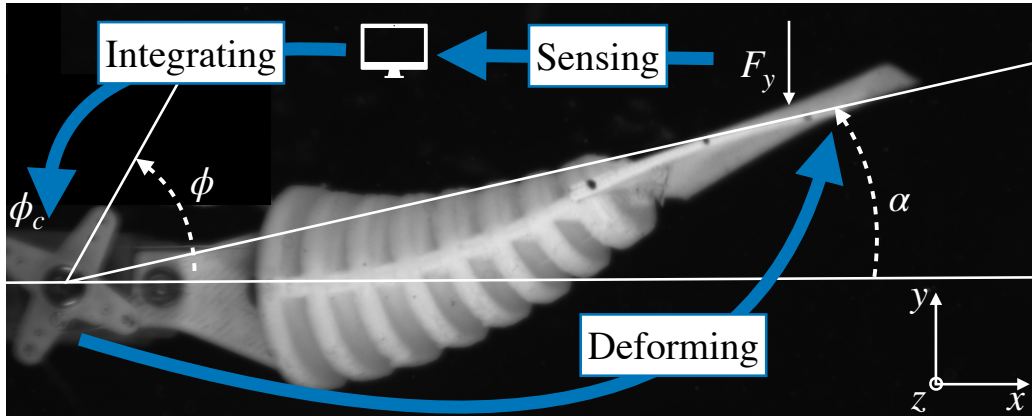
Figure 3.6: Top view of the fishlike robotic system: the white material is 3D printed using soft polymers. The tail is driven by two cables attached to a waterproof servomotor.

However, the access to the oscillations of the swimmer's tail is not direct. Still, it is done through a servomotor controlled by an Arduino Mega micro-controller, whose movement is transmitted to the tail by two wires. This can be seen in the figure 3.7, where the servomotor reacts when the force sensor is touched in any direction, thus moving the tail of the robotic fish.

Therefore, the actual relationship that we formulate as a proprioceptive hypothesis is the following:

$$\phi_c = -\gamma F_y,$$

where ϕ_c is the instruction angle as defined in the Appendix A, and γ is here the control parameter of the proprioceptive driving.

Note that we will focus on positive values of γ in what follows since negative values do not induce locomotion and lead the system to a stable steady-state. Let us take as an example the

figure 3.6, where the tail is moving by increasing the angle α. We see how, according to the action-reaction principle, the fluid exerts a normal force directed in the negative direction of y. According to a proprioceptive hypothesis of opposite sign, the instruction angle ϕ_c would be negative, inducing a movement in the servomotor that would lead the tail to descend in order to decrease the angle α. In this process, however, as the tail moves in the opposite direction, the force that the fluid would exert on it would now be positive, leading ϕ_c to be positive. Therefore it would continue again the path it took before, repeating this endless loop, and thus leading it to a state of no movement and stability.
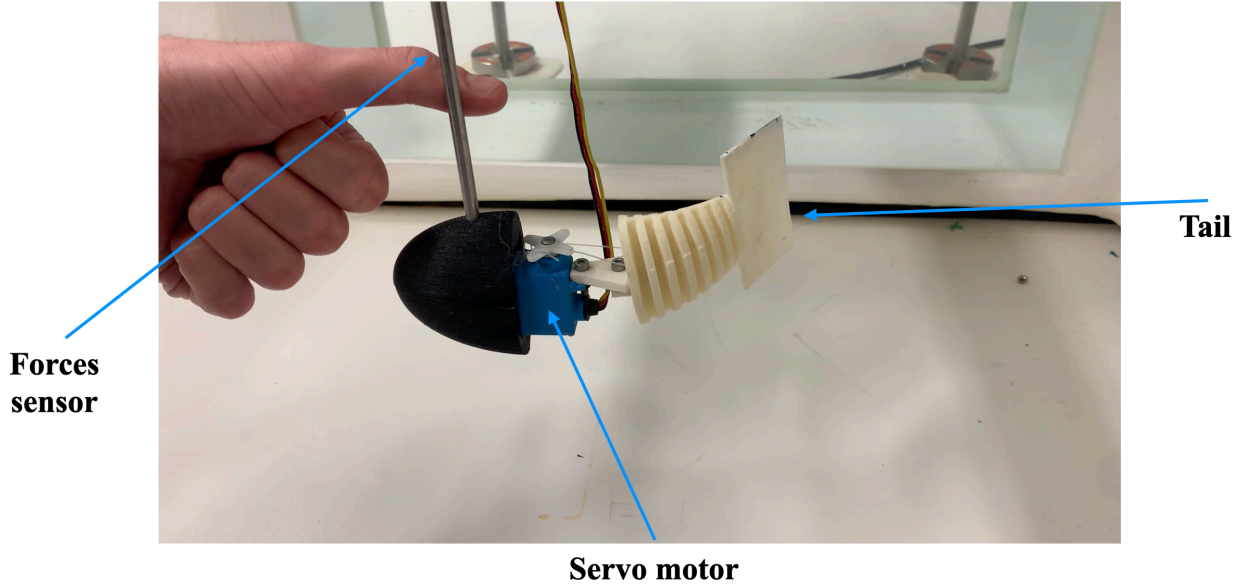
Figure 3.7: Application example of the proprioceptive robotic fish: touching the forces sensor induces a proportional motion on the servomotor and consequently on the tail.

3.3 Experimental validation

First, we show that the proposed hypothesis actually induces a movement of the robotic fish without the need to set amplitude and frequency a priori. The only parameter that is varied systematically is the intensity of the interaction γ. To obtain the amplitude and frequency as functions of γ, we introduce the robotic fish into the water tunnel without imposing a flow velocity. First, we impose $\gamma = 0$ to calibrate the force sensor and get rid of any offset in F_x or F_y. Just after that, the desired value of γ is imposed. The robotic tail is then allowed to oscillate for a sufficient time to ensure that the system converges to its steady-state, which we take to be about twenty periods of robot tail oscillation. Once this time has elapsed, we measure the forces on the sensor and film the oscillations. From the images, we compute the peak-to-peak amplitude α_0 and frequency ω of the signal $\alpha(t)$ (figure 3.8). The experimental points do not correspond to a single experience but result from an average over several experiences. Likewise, the error bars have been obtained by calculating the standard deviation of the data set, taking into account the different experiences.

According to these graphs, we can distinguish three clearly delimited zones:

1. For values of γ smaller than a certain critical value, $\gamma_{c,\exp} \sim 0.72$ rad.N^{-1}, the system relaxes toward the equilibrium state characterized by $\alpha = \alpha' = 0$. For any initial perturbation, the system tends to equilibrium with a relaxation time that is strongly related to

the closeness of the control parameter to its critical value. The closer we are to $\gamma_{c,\exp}$ the longer we have to wait to obtain the equilibrium state, typical behavior of the dynamics near a bifurcation point.

2. In this second phase, already above $\gamma_{c,\exp}$, the robotic tail undergoes spontaneous oscillations with a well-defined angular peak-to-peak amplitude α_0 and frequency ω. The amplitude takes off smoothly from the no-motion regime and increases as γ grows proportional to $\sqrt{\gamma - \gamma_{c,\exp}}$ for γ close to $\gamma_{c,\exp}$, typical of Hopf bifurcations, as explained in the Appendix C. On the other hand, the frequency takes a finite value at the birth of the bifurcation and then decreases as the control parameter increases. Before the bifurcation, the system is stable and relaxes to the motionless regime where the frequency is not defined.

3. Finally, when $\gamma \sim 2$ rad.N^{-1} the system saturates, and both amplitude and frequency values are not altered no matter how much we vary γ. This zone is given by the physical limitation of the system: the maximum amplitude and operating speed of the servomotor.
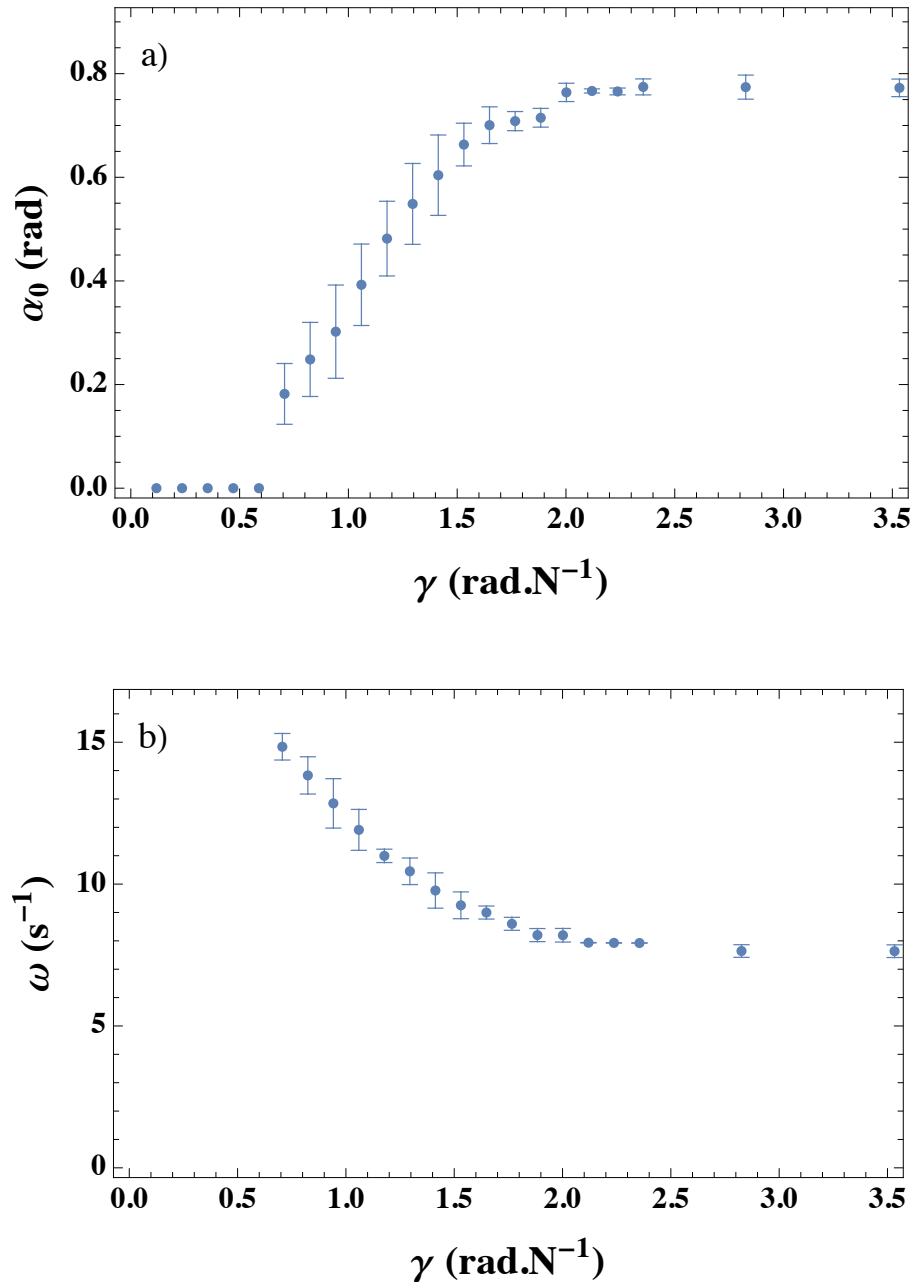
Figure 3.8: Experimental values and error bars of amplitude, α_0, and frequency, ω, as functions of the control parameter γ.
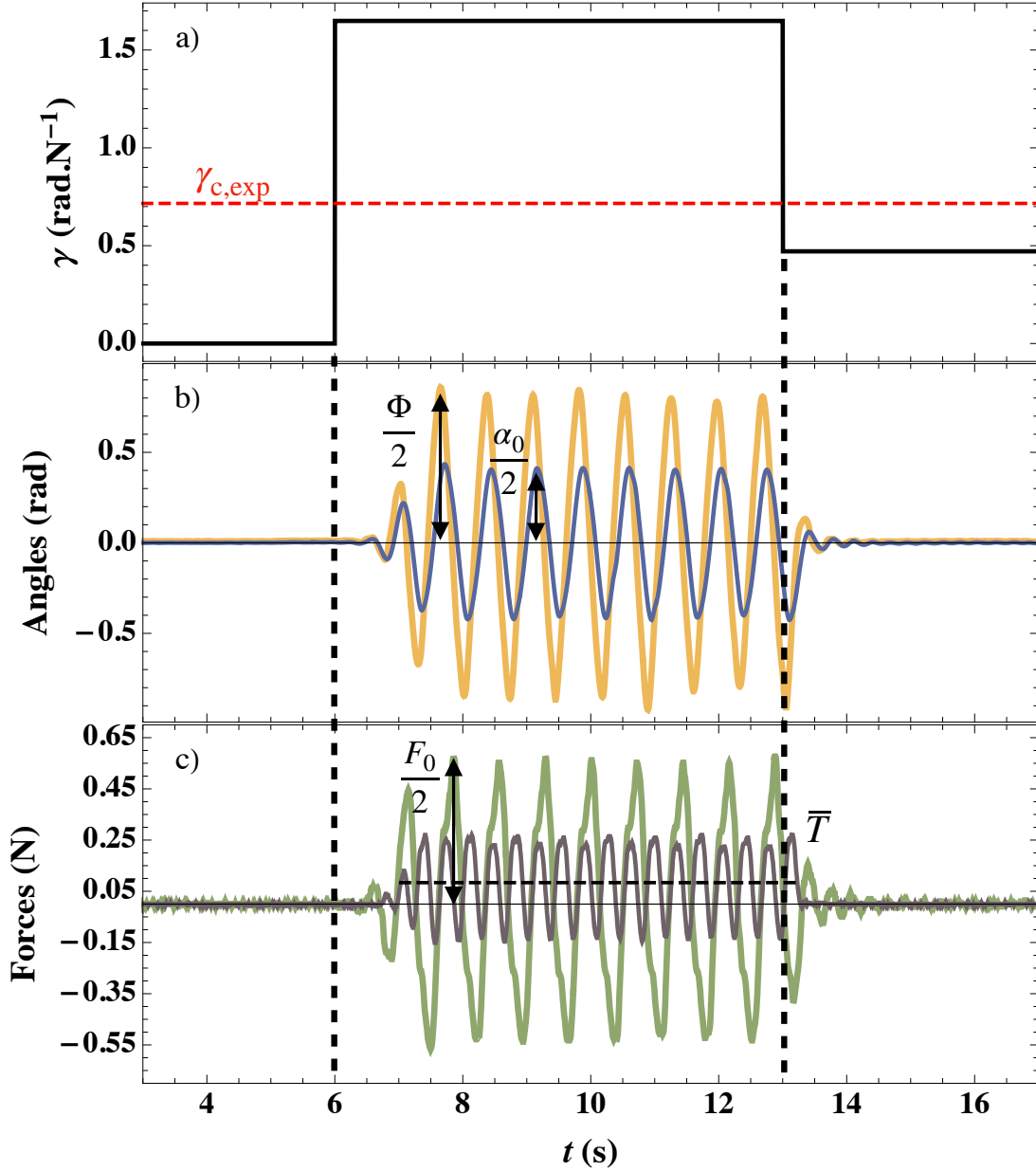
Figure 3.9: a) A typical temporal variation on the feedback parameter γ. b) The dynamics of the angles α (blue) and ϕ (orange) as the controlling parameter γ is varied. The angular frequency ω is deduced from the period $2\pi/\omega$. c) Temporal evolution of the lateral force F_y (green) and of the thrust $T = -F_x$ (gray) with F_x the longitudinal force. We also show the mean thrust $\overline{T}$ in steady state for $\gamma = 1.65$ rad.N^{-1} (dashed horizontal line). α_0, Φ, and F_0 denote the peak-to-peak amplitudes of $\alpha(t)$, $\phi(t)$, and $F_y(t)$, respectively.

In figure 3.9, we present the typical temporal evolution of the angles (ϕ and α) and forces ($T = -F_x$ and F_y) as the controlling parameter γ is varied. Summing up, for $\gamma < \gamma_{c,\exp}$, the system is stable, and no locomotion is expected: for any initial condition the system decays to the equilibrium characterized by $\alpha = \alpha' = 0$. Nevertheless, as $\gamma > \gamma_{c,\exp}$, an instability occurs and leads to a periodic undulation of the tail. This oscillation produces a nonzero mean thrust $\overline{T} = -\overline{F_x} > 0$, which indicates the capacity of the proprioceptive loop to induce a propulsion motion.

3.4 Theoretical characterization

Having demonstrated the efficiency of the loop to induce locomotion, we propose a simple, yet generic, model to shed light on the instability and discuss how it relies on the feedback loop depicted in figure 3.5. According to such scheme, it is necessary to understand the interactions between the different stages. Each step of the proprioceptive loop is associated with a relevant magnitude within the system, and our objective is to relate them to each other. The integrating stage has already been defined when we have proposed the proprioceptive hypothesis, and we have remarked as a reference variable for this stage the angle instruction ϕ_c, which we have related to the normal force. As this information is related to the normal force, F_y is the significant magnitude and relates to the deformation stage. The latter is represented by the angle α, and it also involves the dynamics of the servomotor, which we also model appropriately.

3.4.1 Integration stage

It is the only phase that is not motivated by physical criteria. In this phase, we impose the relationship between normal force and instruction angle:

$$\phi_c(t) = -\gamma F_y(t).$$

In this case, unlike Gazzola et al. [141], we do not consider any temporal delay between the force signal and force integration. Gazzola et al. justifiably choose a time lag between the proprioceptive force moment and the deformation of the animal to account for the inherent delays in biological feedback loops [176, 177]. In our case, the situation is somewhat different. The temporal delay does not come from the dynamics of the excitatory-inhibitory neural network but from the response time that the Arduino takes between detecting the force signal and transmitting it to the servomotor. This time turns out to be about 20 ms. The times we are dealing with in our system, however, are much longer than the force transmission time, so that this time can be neglected assuming that the signal is instantaneous, facilitating the theoretical and numerical resolution of the system and without having to resort to the formalism of the delay differential equations [178].

3.4.2 Sensing stage

At this stage, we are interested in finding out the relationship of the normal force to the tail dynamics. An exhaustive calculation of these forces is entirely beyond our scope. In an attempt to simplify the problem but highlighting the underlying physical mechanisms, our approach relies on Theodorsen formalism [100]. The computation of the forces generated by a hydrofoil oscillating with a relatively small amplitude, $\alpha \ll 1$, within a perfect fluid takes the following expression, which we already deduced in the previous chapter:

$$F_y = -K_{\alpha''}\alpha'' - K_{\alpha'}\alpha' - K_\alpha\alpha.$$

where $K_{\alpha''}$, $K_{\alpha'}$ and K_α are parameters characterizing the medium, the material, or the substrate with which the swimmer interacts and could by construction account for inertial, viscous,

and elastic effects. According to the dimensional analysis, the dimensions of these terms must be:

$$[K_{\alpha''}] = \mathsf{ML}, \qquad [K_{\alpha'}] = \mathsf{MLT}^{-1}, \qquad [K_{\alpha}] = \mathsf{MLT}^{-2}.$$

Where [...] represent the dimension of a quantity and M, L, and T are the dimensions of the fundamental magnitudes mass, length and time, respectively. During the motion of a fish of length L in a fluid of density ρ at velocity U, a simple scaling analysis recovers the terms found by Theodorsen in his theory of oscillating airfoils, assuming that inertia is dominant [100].

$$K_{\alpha''} \sim \rho L^4, \qquad K_{\alpha'} \sim \rho U L^3, \qquad K_{\alpha} \sim \rho U^2 L^2,$$

where ρ takes the value 1000 kg.m^{-3} for water, and $L \sim 10$ cm, the typical length of the fish. The first term $K_{\alpha''}$ accounts for the added mass due to the bolus of water accelerated during the tail oscillation, while the last two terms account for the lift of a moving and inclined airfoil in a flow. To guess which term is dominant, we compute the ratios

$$\frac{K_{\alpha''}\alpha''}{K_{\alpha'}\alpha'} \sim \omega^{\star} \qquad \text{and} \qquad \frac{K_{\alpha''}\alpha''}{K_{\alpha}\alpha} \sim \omega^{\star 2},$$

where we have introduced the dimensionless number

$$\omega^{\star} = \frac{\omega L}{U}.$$

This parameter is usually called reduced frequency [25, 30] and it appears that, for biological swimmers, this dimensionless parameter is large [25], $\omega^{\star} \sim 10$. However, at first, our experiments run with zero flow velocity, so our first impression is that the terms proportional to α' and α do not play any vital role. To verify this assumption and obtain the coefficients' experimental values, we impose a known dynamic on the servomotor and measure the forces arising as a function of the tail behavior. In all the situations where we try to obtain an experimental characterization of the system, we always impose a harmonic response on the servomotor. The reason is that the tail angle, as we have defined it, reproduces harmonic behavior exceptionally well if it is forced in the same way by the servomotor. Furthermore, we prototypically expect the swimmers to exhibit periodic behavior with fixed values of amplitudes and frequencies, which we recover by assuming harmonic forcings. If we then take an oscillation of the following form

$$\alpha(t) = \frac{\alpha_0}{2}\sin(\omega t),$$

the normal force in the limit of small amplitudes reads:

$$F_y(t) = -\frac{1}{2}\alpha_0 K_{\alpha'}\cos(\omega t) - \frac{1}{2}\alpha_0(K_{\alpha} - K_{\alpha''}\omega^2)\sin(\omega t),$$

which may be expressed more compactly as:

$$F_y(t) = \frac{F_0}{2}\sin(\omega t + \psi),$$

with F_0 as the amplitude of the force and ψ the phase shift, expressed by:

$$F_0 = K_{\alpha''}\alpha_0\omega\sqrt{\left(\frac{K_{\alpha} - \omega^2 K_{\alpha''}}{\omega K_{\alpha''}}\right)^2 + \left(\frac{K_{\alpha'}}{K_{\alpha''}}\right)^2} \qquad (3.4.1)$$

$$\psi = \frac{\omega K_{\alpha'}}{\omega^2 K_{\alpha''} - K_{\alpha}} \qquad (3.4.2)$$

Thus, to determine the coefficients appearing in the force expression, we measure the amplitude F_0 and the phase shift ψ of the force as a function of α_0 and ω. We impose harmonic oscillations of the servomotor wheel following the equation:

$$\phi_c = \frac{\Phi}{2}\sin(\omega t), \tag{3.4.3}$$

with Φ ranging between 0 and 1.9 rad and f between 0 and 1.4 Hz. In all cases, we record $\alpha(t)$ and $F_y(t)$ in steady state and measure α_0 and F_0. In the setting where these experiments were performed, the measurement of ψ was not entirely satisfactory and could be misleading, which led us to erase it from the experimental procedure.
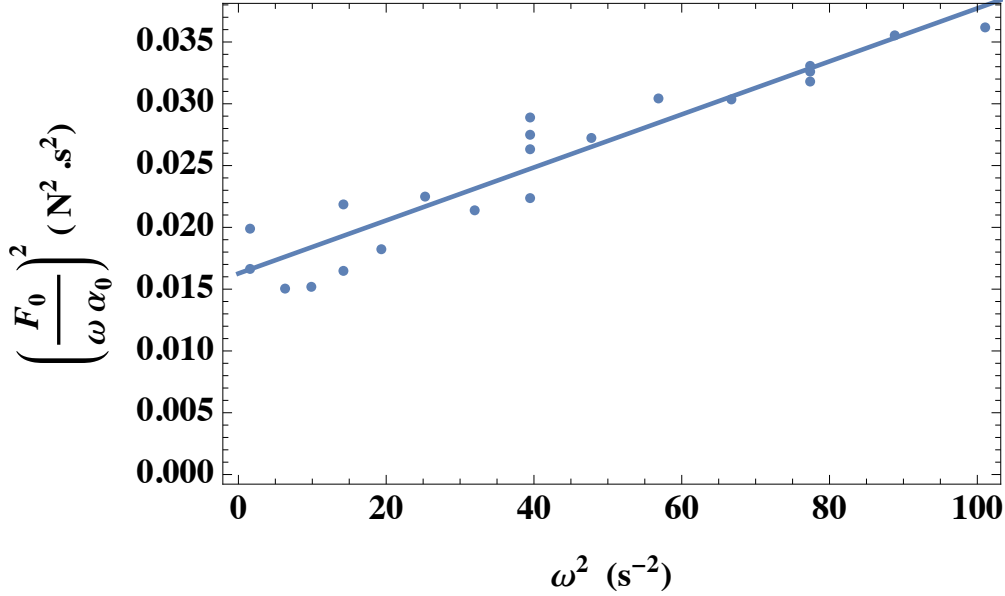
Figure 3.10: $(F_0/\alpha_0\omega)^2$ is plotted as a function of ω^2. The solid line is a linear function, which comparison with the model gives a slope $K^2_{\alpha''}$ and an intercept $K^2_{\alpha'}$.

Given the form of the equation 3.4.1, we plot in figure 3.10 the quantity $(F_0/\alpha_0\omega)^2$ as a function of ω^2. Developing the expression $(F_0/\alpha_0\omega)^2$:

$$\left(\frac{F_0}{\alpha_0\omega}\right)^2 = K^2_{\alpha''}\left[\omega^2 + \left(\frac{K_\alpha}{\omega K_{\alpha'}}\right)^2 - \frac{2K_\alpha}{K_{\alpha'}} + \left(\frac{K_{\alpha'}}{K_{\alpha''}}\right)^2\right],$$

we realize that considering a linear dependence on α disagrees with what we see in the figure 3.10, where we should see higher values near the origin. This leads us to consider $K_\alpha = 0$, as we predicted. According to our initial hypothesis, however, we expect only one dominant term, the one corresponding to the added mass, $K_{\alpha''}$. The problem is then in the starting hypothesis since if we only consider this term, our experimental curve should pass through the origin and not have such an important intercept as we see in the figure. Keeping the terms $K_{\alpha''}$ and $K_{\alpha'}$ we have:

$$\left(\frac{F_0}{\alpha_0\omega}\right)^2 = K^2_{\alpha''}\left[\omega^2 + \left(\frac{K_{\alpha'}}{K_{\alpha''}}\right)^2\right].$$

So we can identify the slope of the line with the parameter $K^2_{\alpha''}$ and the intercept with $K^2_{\alpha'}$. This validates the force expression and, from the best interpolation, we measure $K_{\alpha''} = (14.7 \pm 0.6)$ mN.rad^{-1}.s^2 and $K_{\alpha'}/K_{\alpha''} = (8.7 \pm 0.4)$ s^{-1}. As a consequence:

$$\frac{K_{\alpha''}\alpha''}{K_{\alpha'}\alpha'} \simeq \frac{\omega K_{\alpha''}}{K_{\alpha'}} \sim 1,$$

around $\omega \sim 10$ s^{-1}. This implies that $K_{\alpha'}\alpha'$ cannot be discarded in the force expression even if $U \neq 0$. We interpret this term as a viscous force due to the oscillation of the tail inside a fluid of viscosity $\eta \sim 1$ mPa.s for water. As an example, the case of a cylinder of radius and length L [69] leads to a rough estimate of $K_{\alpha'} \sim 2\pi L^3 \sqrt{2\rho\eta\omega} \sim 30$ mN.rad^{-1}.s, which is in agreement with the precise measurement mentioned. As discussed in Landau and Lifshitz [69], convective terms in the Navier-Stokes equation can be dominated by unsteady terms in oscillatory flow. This could explain the prevalence of the linear term in α'. Still, the origin of this term is not completely clear because studies on swimming obviously presuppose a non-zero flow velocity, with which we can justify the terms arising from Theodorsen's inviscid flow theory [100]. The term is measured anyway, so we consider it in the treatment of the problem at all times. A detailed study is being carried out to understand the origin of this force.

Even if we remain in the linear approximation, nonlinear terms could be expected as a transverse pressure drag force writing

$$-c_y \rho L^4 \alpha' |\alpha'|,$$

with c_y a dimensionless coefficient. However, experimentally we expect this coefficient to be minimal, $c_y \ll 1$ for the following reasons:

1. We do not observe any significant change of frequency in the temporal signal of the transverse force F_y (figure 3.9). In fact, if we developed in Fourier series the term in pressure drag, we would obtain:

$$\cos(\omega t)|\cos(\omega t)| \sim \frac{8}{3\pi}\cos(\omega t) + \frac{8}{15\pi}\cos(3\omega t),$$

   where we see how the term with triple frequency accounts for just over 15% of the total term contribution.

2. As shown later in figure 3.15, the amplitude of the force is proportional to the amplitude of the harmonic forcing since we do not observe any quadratic tendance when we vary α_0.

Additionally, if we did not consider the term in α' but the quadratic term in $\alpha'|\alpha'|$, we would also observe a zero intercept in the figure 3.10 as there would exist a ω^2 term in front of $\alpha'|\alpha'|$. Nevertheless, accounting for this nonlinear term improves the matching between the model and the experimental data at high α_0 values, as we will show in the section 3.5.2.

For consistency with what follows, we rewrite

$$F_y = -K_{\alpha''}\left(\alpha'' + \xi\omega_0\alpha'\right), \qquad (3.4.4)$$

with ξ a dimensionless factor and ω_0 a quantity that has the dimension of a frequency and that we will properly justify later.

3.4.3   Deforming stage

At this stage, we study the phenomenon of tail deformation as a function of the external forcing and bring out the essential parameters characterizing the structure's response. In the first step, the flexibility effects are neglected, and the deformation of the robot fish is quantified by the tail angle $\alpha(t)$. The motion of the servomotor wheel imposes a deformation of the tail through the tension of cables inside the soft structure, as we explain in the section A.4 of the Appendix A. In the quasistatic regime, there is a monotonic relation between the two quantities, as shown in figure 3.11. This relation is well fitted by a linear relation $\alpha = K_1\phi$ with $K_1 = 0.549 \pm 0.007$.
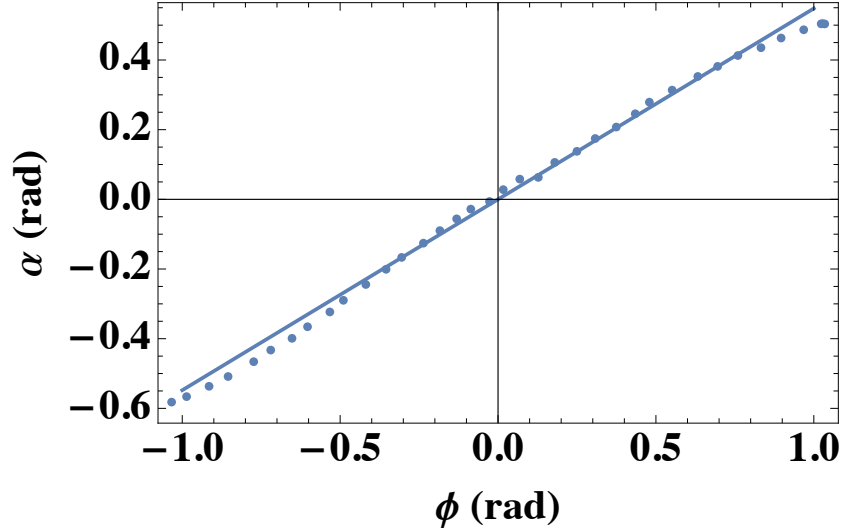
Figure 3.11: α as a function of ϕ in the quasistatic regime. The linear behaviour $\alpha = K_1\phi$ is represented by the blue line, with $K_1 = 0.549$.

To predict the dynamic behavior of the angle α, we apply Newton's second law on the tail, taking into account that mainly two forces act on the system: F_y which is the fluid-structure interaction force that we have already characterized previously in equation 3.4.4, and F_d the driving force in the y direction. This force has a restoring nature and arises from the arrangement of the wires connecting the servomotor wheels to the tail to align α and ϕ at all times. This force fulfills two conditions:

- First, it drives the angle α with respect to the control angle

$$\alpha^* = K_1\phi.$$

- Second, at the leading order deformation, F_d is modeled by a polynomial function of

$$\delta\alpha = \alpha - \alpha^*.$$

We consider a linear term proportional to $\delta\alpha$ to account for the linear elastic response without a quadratic monomial due to the symmetry of the problem. A linear response might seem satisfactory at first, however, experimental data performed with the same robotic fish model [15] or flexible panels in other setups [30, 179–181] show a shift of the resonant frequency as a function of the oscillation amplitude. In figure 3.12a, we show the data corresponding to the study of Gibouin et al. [15], where the oscillation amplitude of the tail A as a function of the servomotor forcing frequency, f, for different servomotor forcing amplitudes is shown. In this image, we observe how the resonant frequency shifts toward the left of the graph as the servomotor amplitude increases. This effect is typical behavior of the Duffing oscillator, a forced oscillator with a cubic nonlinear term, which can be rewritten in dimensionless form as:

$$\alpha'' + p_1\alpha' + \alpha + p_2\alpha^3 = \cos(ft),$$

with p_1 and p_2 dimensionless parameter characterizing the strengh of the dissipation and nonlinear terms, respectively.

The parameter p_2 is responsible for causing the resonant frequency to shift towards lower frequencies if $p_2 < 0$ and vice versa if $p_2 > 0$. The typical behavior of this nonlinear oscillator with negative p_2 is shown in figure 3.12b, compared together with an oscillator

without a cubic term. An increase in forcing creates a shift toward lower resonant frequencies than those obtained with small forcings, unlike linear oscillators, in which the maximum frequency of the system always lies at the same value of f [182].
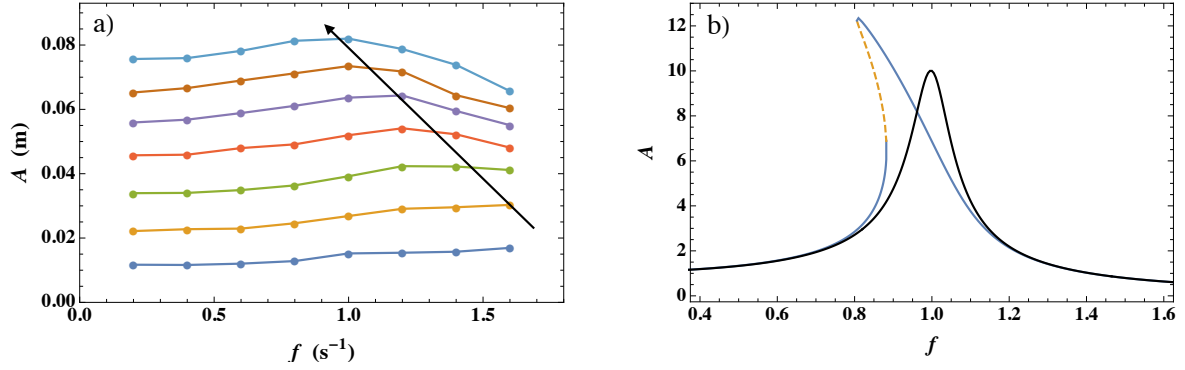
Figure 3.12: a) A as a function of f for several Φ (20, 40, 60, 80, 100, 120 and 140 ° from bottom to top). The black arrow shows the shift of the resonant frecuency. Adaptation from Gibouin et al. [15]. b) Frequency response for a linear, damped, harmonic oscillator in black and for a Duffing oscillator in blue and orange. Orange dashed line corresponds to the unstable frequency response.

Consequently, we write

$$F_d(t) \propto -\delta\alpha(t) \left[1 - K_2 \delta\alpha(t)^2\right], \tag{3.4.5}$$

with K_2 a positive parameter that weights the nonlinear term with respect to the linear one.

The tail angle then, can be predicted by the dynamics of a weakly nonlinear oscillator driven by the servomotor. By exploiting the momentum balance applied to the tail along the y axis, we write

$$m_t L \alpha'' = F_y + F_d,$$

with m_t the mass of the tail and F_y and F_d defined in equations 3.4.4 and 3.4.5, respectively.

Given that $K_{\alpha''} \sim \rho L^4$ and that fish in general, and the robotic fish in particular, are slender objects [142], we expect $m_t \ll \rho L^3$ and the dynamical equation becomes

$$\alpha'' + \xi\omega_0\alpha' + \omega_0^2 \left(\alpha - K_1\phi\right) \left[1 - K_2 \left(\alpha - K_1\phi\right)^2\right] = 0, \tag{3.4.6}$$

with ω_0 now interpreted as the linear regime oscillation frequency of the tail around its equilibrium value $K_1\phi$. In addition, ξ is interpreted as the damping factor of the oscillator. In order to quantitatively compare the dynamics of the experiments with those of the model, it is necessary to accurately measure the value of ω_0, ξ and K_2 in the last equation. To achieve this objective, we measure the tip-to-tip angular response of the robotic tail, α_0, for the harmonic forcing described in equation 3.4.3. Several values of Φ and f were probed as shown in figure 3.13. We have numerically integrated the system and compare the predicted $\alpha_0(\Phi, f, \omega_0, \xi, K_2)$ to the experimental measurements $\alpha_0(\Phi, f)$.
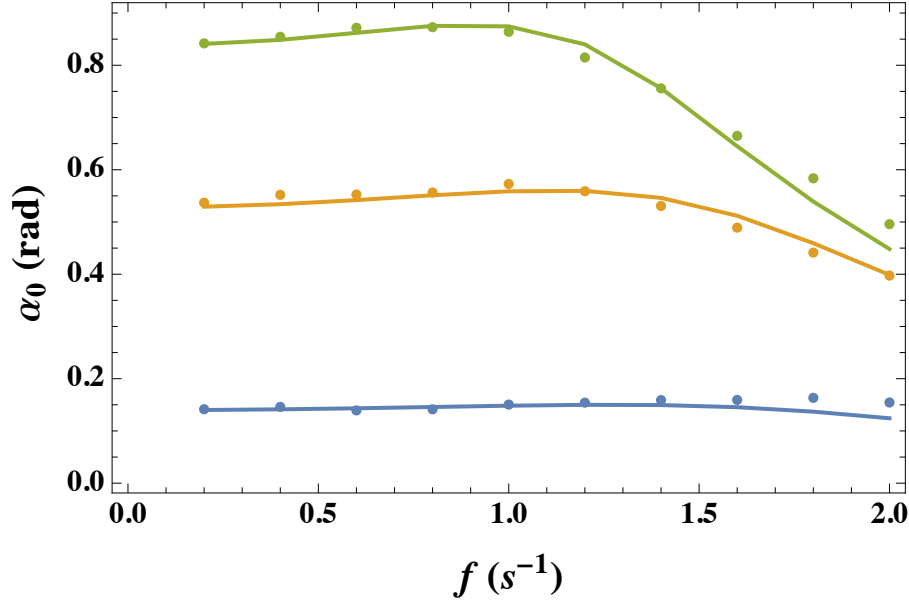
Figure 3.13: α_0 as a function of f for three values of Φ (0.24, 0.94 and 1.65 rad from bottom to top). The solid lines are the prediction of the model with the parameters $\omega_0 = 13$ s^{-1}, $\xi = 1.0$ and $K_2 = 1.6$.

We have constructed an error function $e(\omega_0, \xi, K_2)$ that measures the absolute error between the numerical prediction and the experimental data for each set of parameters ω_0, ξ and K_2. The three parameters are systematically varied and a minimum of the error function is found around $\omega_0 = 13$ s^{-1}, $\xi = 1.0$ and $K_2 = 1.6$ (solid lines in figure 3.13). Uncertainties are quantified by 10% of the error function. This leads to an acceptable domain in the parameter space (figure 3.14), with the typical range given by:

$$12.75 < \omega_0 < 13.50, \qquad 0.97 < \xi < 1.05, \qquad 1.55 < K_2 < 1.65$$
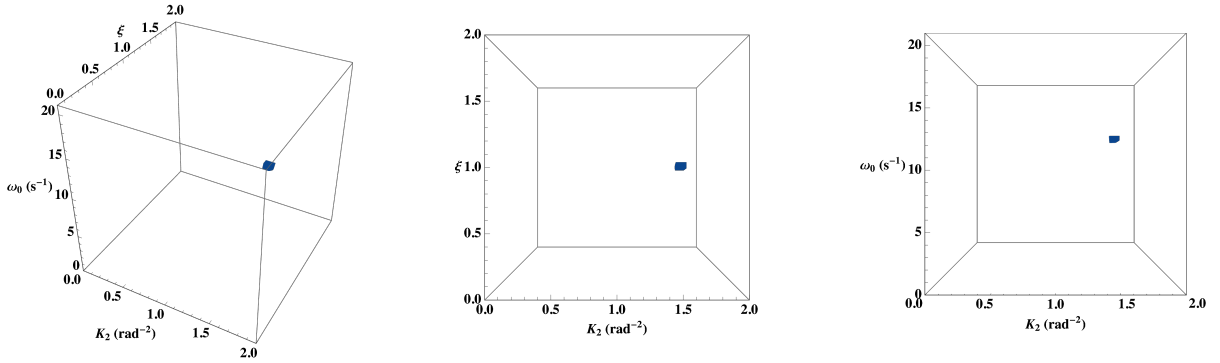
Figure 3.14: Location of the minimum of the error function and its acceptable domain in the parameter space of ω_0, ξ and K_2.

The force expression we derived in the previous section (equation 3.4.4) has been introduced into the oscillator equation 3.4.6 by redefining the parameter proportional to α' as:

$$K_{\alpha'} = K_{\alpha''} \xi \omega_0.$$

Depending on the sensing and deforming stage, we have two ways to calculate this term. Either by doing a fit of the data in figure 3.10 or by calculating ξ and ω_0 directly from figure 3.13. We

observe that by carrying out the second option, the best parameters are $\xi = 1$ and $\omega_0 = 13$, which results in

$$\frac{K_{\alpha'}}{K_{\alpha''}} = 13 \text{ s}^{-1}.$$

However, a fit of the data in the figure 3.10 results

$$\frac{K_{\alpha'}}{K_{\alpha''}} = 8.7 \text{ s}^{-1}.$$

Both values are, in fact, very close, which supports the model. To be consistent with the determination of the nonlinear oscillator parameters, we fix $K_{\alpha'}/K_{\alpha''} = 13 \text{ s}^{-1}$ since the value obtained by the other technique does not allow us to get a good representation of the oscillator dynamics. We then determine the parameter $K_{\alpha''}$ by plotting F_0 as a function of $\alpha_0\omega\sqrt{\omega^2 + (\xi\omega_0)^2}$. Both quantities are proportional as expected (figure 3.15) and the proportionality ratio equals $K_{\alpha''} = (11.3 \pm 0.1) \text{ mN.rad}^{-1}.\text{s}^2$ from the best interpolation. We keep this value for the rest of the study.
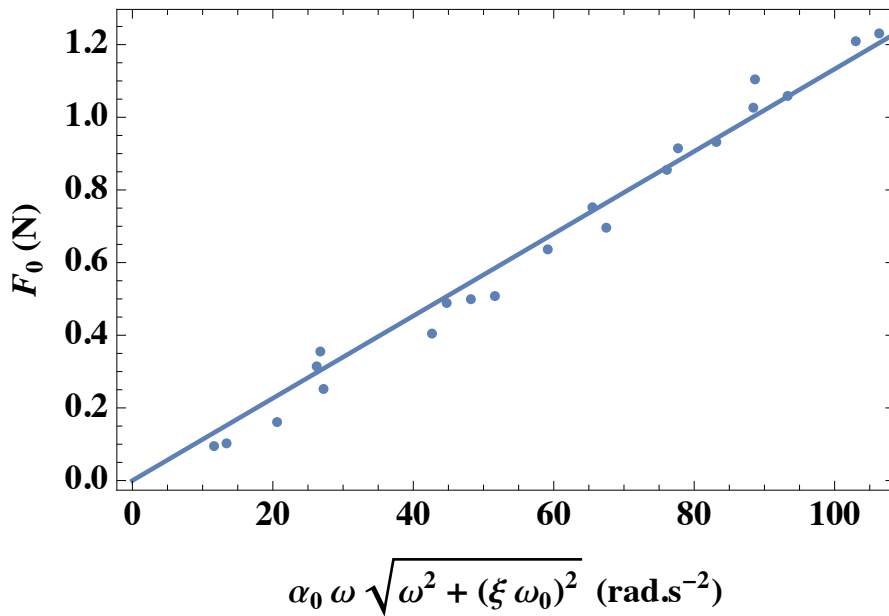
Figure 3.15: F_0 is plotted as a function of $\alpha_0\omega\sqrt{\omega^2 + (\xi\omega_0)^2}$. The solid line is the best relation of proportionality with $K_{\alpha''}$ as the proportionality constant.

3.4.4 Modeling the servomotor internal dynamics

To close the system, we now model the response of the servomotor to account for the error between the instruction angle ϕ_c and the output angle ϕ associated with this element in the proprioceptive loop. We model the response of the servomotor driven by a reference value; more precisely the angle of the steering wheel $\phi(t)$ in response to the instruction angle $\phi_c(t)$. As a simple benchmarking of the servomotor, we study its dynamics as we harmonically force it with the the instruction angle defined in equation 3.4.3 with amplitude $\Phi/2$ and frequency $\omega = 2\pi f$. For small amplitude Φ and frequency f, we expect the servomotor to have a low load and the wheel angle ϕ to instantaneously follow the instruction ϕ_c, such that $\phi(t) = \phi_c(t)$. For larger amplitude Φ and frequency f, the servomotor might not be fast enough, and we expect a difference between the requested angle ϕ_c and the real wheel angle ϕ.
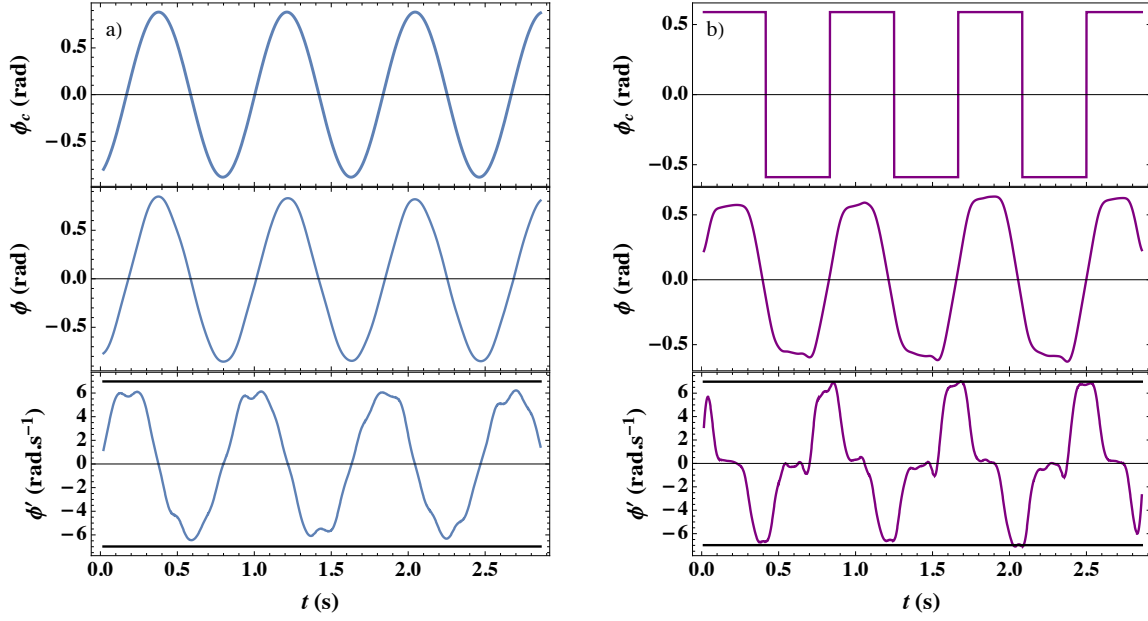
Figure 3.16: ϕ_c, ϕ and ϕ' as functions of time for two different driving signals. a) A sinusoidal signal with amplitude $\Phi = 1.77$ rad and frequency $f = 1.2$ Hz. b) A rectangular signal with amplitude $\Phi = 1.18$ rad and frequency $f = 1.2$ Hz. The black lines represent the maximum angular velocity of the servomotor, $\Omega = 7.0 \pm 0.1$ rad.s^{-1}.
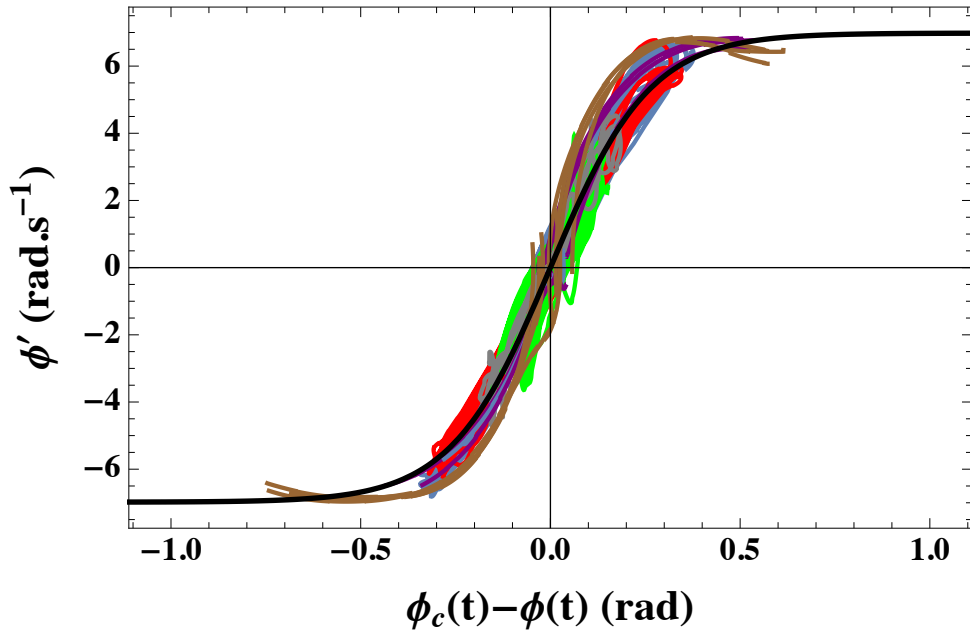
Figure 3.17: $\phi'(t)$ as a function of $\phi_c(t) - \phi(t)$ for six different experiments. For harmonic signals we show: in red $\Phi = 1.18$ rad, $f = 2.2$ Hz, in blue $\Phi = 1.77$ rad, $f = 1.2$ Hz, in green $\Phi = 0.59$ rad, $f = 2.2$ Hz and in grey $\Phi = 1.18$ rad, $f = 1.2$ Hz. For rectangular signals we have: in purple $\Phi = 1.18$ rad, $f = 1.2$ Hz and in brown $\Phi = 1.18$ rad, $f = 2.2$ Hz. The black curve represents the function $\Omega \tanh((\phi_c - \phi)/\Delta\phi)$, with $\Omega = 7.0$ rad.s^{-1} and $\Delta\phi = 0.26$ rad.

In figure 3.16a, we plot ϕ_c, ϕ and ϕ' as functions of time for typical experiments. ϕ' saturates as it approaches the maximal value Ω that the servomotor can deliver; the manufacturer's

technical manual estimates it at approximately 7 rad.s^{-1}. This limitation is confirmed by imposing rectangular signals (figure 3.16b), and we measure $\Omega = 7.0 \pm 0.1$ rad.s^{-1} in agreement with the data provided by the manufacturer.

In figure 3.17, ϕ' is plotted as a function of the tracking error $\phi_c(t) - \phi(t)$ and all the data collapse on a single master curve whatever the amplitude, the frequency and the shape of the forcing signal. Given the shape of the master curve, we fit the data with the following expression:

$$\phi' = \Omega \tanh\left(\frac{\phi_c - \phi}{\Delta\phi}\right),$$

where $\Delta\phi = 0.26 \pm 0.05$ rad is obtained from the best interpolation over all the data and represents the typical angle difference between the instruction and the wheel angle at which the servomotor achieves maximum velocity. This equation is used to model the servomotor inside the proprioceptive loop. We have chosen to model the saturation with a hyperbolic tangent for simplicity among other sigmoid functions.

3.4.5 Theoretical computation of the weakly nonlinear dynamics of the swimmer

In the previous sections, we have measured all the relevant parameters, shown in the table 3.1, which we now use for the application of the model.

ω_0	ξ	Ω	$\Delta\phi$	K_1	K_2	$K_{\alpha''}$
13.0 s^{-1}	1.0	7.0 rad.s^{-1}	0.26 rad	0.55	1.6 rad^{-2}	11.3 mN.rad^{-1}.s^2

Table 3.1: Measured parameters.

Our complete system is mathematically described by the following four algebraic-differential equations, where the first three characterize the integration, sensing and deforming stages and the last one models the servomotor:

$$\phi_c = -\gamma F_y,$$
$$F_y = -K_{\alpha''}\left(\alpha'' + \xi\omega_0\alpha'\right),$$
$$\alpha'' = -\xi\omega_0\alpha' - \omega_0^2\left(\alpha - K_1\phi\right)\left[1 - K_2\left(\alpha - K_1\phi\right)^2\right],$$
$$\phi' = \tanh\left(\frac{\phi_c - \phi}{\Delta\phi}\right).$$

If we group the first two equations and introduce them in the last one, we finally obtain the differential system that we have to solve:

$$\alpha'' = -\xi\omega_0\alpha' - \omega_0^2\left(\alpha - K_1\phi\right)\left[1 - K_2\left(\alpha - K_1\phi\right)^2\right],$$
$$\phi' = \tanh\left(\frac{\gamma K_{\alpha''}(\alpha'' + \xi\omega_0\alpha') - \phi}{\Delta\phi}\right).$$

This set of equations constitutes a generic model for proprioceptive locomotion. This system has a steady solution $\alpha = \phi = 0$, which corresponds to a nonmoving swimmer. Our conjecture is that an oscillatory instability is responsible for the proprioceptive locomotion. Following this idea, we perform a standard linear stability analysis around the stationary state ($\alpha = \alpha' = \phi = 0$). We aim to carry out a weakly nonlinear analysis for characterizing the bifurcation. As usual, near the instability, the dynamics of the system undergoes slow temporal evolution. In order to properly describe the transition to the slow dynamics, we rewrite the full system as:

$$\partial_t \boldsymbol{u} = L\boldsymbol{u} + \boldsymbol{N}(\boldsymbol{u})$$

with:

$$
\boldsymbol{u} = \begin{pmatrix} \alpha \\ \alpha' \\ \phi \end{pmatrix}, \quad L = \begin{pmatrix} 0 & 1 & 0 \\ -\omega_0^2 & -\xi\omega_0 & K_1\omega_0^2 \\ -\frac{K_3\gamma\Omega\omega_0^2}{\Delta\phi} & 0 & -\frac{\Omega}{\Delta\phi} + \frac{K_1K_3\gamma\Omega\omega_0^2}{\Delta\phi} \end{pmatrix},
$$

$$
\boldsymbol{N}(\boldsymbol{u}) = \begin{pmatrix} 0 \\ \omega_0^2 K_2 \left(\alpha - K_1\phi\right)^3 \\ \frac{\Omega}{\Delta\phi}\left[K_2K_3\gamma\omega_0^2(\alpha - K_1\phi)^3\right] + \frac{\Omega}{3\Delta\phi^3}\left[\phi + K_3\gamma\omega_0^2\left(\alpha - K_1\phi\right)\right]^3 \end{pmatrix},
$$

where we have separated the linear part $L\boldsymbol{u}$ from the nonlinear one $\boldsymbol{N}(\boldsymbol{u})$. We assume a small parameter $\gamma - \gamma_c \ll 1$, where γ_c is the critical value at which the bifurcation appears, and we propose, as it is standard in asymptotic analysis for bifurcations, described in the Appendix C, the following ansatz:

$$
\begin{aligned}
\gamma &= \gamma_c + \varepsilon^2\gamma_2, \\
\boldsymbol{u} &= \varepsilon\boldsymbol{u}_1(t, t_2) + \varepsilon^3\boldsymbol{u}_3(t, t_2) + O(\varepsilon^4), \\
L &= L_0 + \varepsilon^2 L_2, \\
t_2 &= \varepsilon^2 t,
\end{aligned}
$$

where the parameter ε controls the distance to the bifurcation threshold. The variable t_2 has been introduced to represent the slow dynamics of the oscillation amplitude, as explained in Appendix B.

At order ϵ, the system to solve takes the form of a linear ODE :

$$
\partial_t \boldsymbol{u}_1 = L_0 \boldsymbol{u}_1,
$$

with

$$
L_0 = \begin{pmatrix} 0 & 1 & 0 \\ -\omega_0^2 & -\xi\omega_0 & K_1\omega_0^2 \\ -\frac{K_3\gamma_c\Omega\omega_0^2}{\Delta\phi} & 0 & -\frac{\Omega}{\Delta\phi} + \frac{K_1K_3\gamma_c\Omega\omega_0^2}{\Delta\phi} \end{pmatrix}.
$$
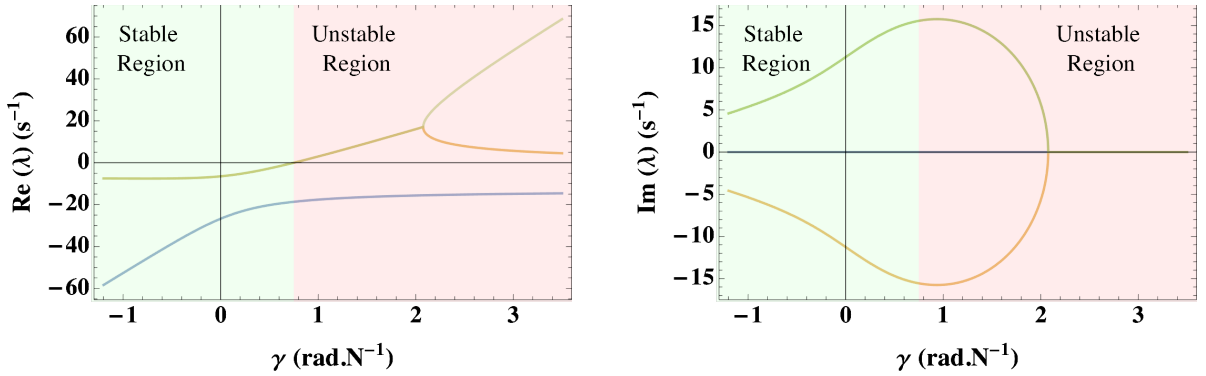
Figure 3.18: Real and imaginary parts of the eigenvalues, λ, in function of the control parameter for the proprioceptive system. We show the dependence of the real and imaginary parts of the three eigenvalues in blue, orange and green. A Hopf bifurcation occurs at $\gamma_c \sim 0.75$ rad.N^{-1}, characterized by the cancellation of the real part of the orange and green eigenvalues. The green and red zones correspond to the stable and unstable regions, respectively.

Where we have assumed $L_0 = L_{\gamma=\gamma_c}$. Following the main text definitions, γ_c is the value of the feedback parameter for which the matrix L has three different eigenvalues that we denote

as λ. These eigenvalues are $i\omega_c$, $-i\omega_c$ and one negative. We show the behavior of the three eigenvalues of the system as function of γ in figure 3.18, where we recognize the point γ_c characterized by two eigenvalues with zero real parts and one being negative. This occurs as

$$\omega_c = \omega_0 \frac{\sqrt{2(1-\xi^2)}}{2} \sqrt{1 + \sqrt{1 + 4\frac{\xi\Omega}{\Delta\phi\omega_0(1-\xi^2)^2}}}, \tag{3.4.7}$$

$$\gamma_c = \frac{2\xi + \frac{\omega_0\Delta\Phi}{\Omega}\left(1 + \xi^2 - \sqrt{1 + 4\xi\frac{\Omega}{\omega_0\Delta\Phi} - 2\xi^2 + \xi^4}\right)}{2K_1 K_{\alpha''}\xi\omega_0^2}. \tag{3.4.8}$$

Consequently, we propose as solution for the unknown $\boldsymbol{u}_1(t, t_2)$:

$$\boldsymbol{u}_1 = A(t_2)e^{i\omega_c t}\boldsymbol{\zeta} + \overline{A(t_2)}e^{-i\omega_c t}\overline{\boldsymbol{\zeta}}, \tag{3.4.9}$$

$$i\omega_c\boldsymbol{\zeta} = L_0\boldsymbol{\zeta}, \tag{3.4.10}$$

where $\boldsymbol{\zeta}$ is the eigenvector of L_0 associated to $\lambda = i\omega_c$:

$$\boldsymbol{\zeta} = \begin{pmatrix} 1 \\ i\omega_c \\ \frac{\omega_0^2 + i\xi\omega_0\omega_c - \omega_c^2}{K_1\omega_0^2} \end{pmatrix}.$$

We note here that the oscillation amplitude $A(t_2)$ varies slowly in time. We use the previous result $\mathcal{L}_0\boldsymbol{u}_1 = 0$ to obtain:

$$\mathcal{L}_0 = \partial_t - L_0,$$

$$\mathcal{L}_0\boldsymbol{\zeta}e^{i\omega_c t} = 0.$$

Because of the symmetry and the ansatz, no terms need to be balanced at this order so we can immediately get to order ϵ^3, for which we get the following equation for the unknown $\boldsymbol{u}_3$.

$$\partial_t\boldsymbol{u}_3 - L_0\boldsymbol{u}_3 = -\partial_{t_2}\boldsymbol{u}_1 + L_2\boldsymbol{u}_1 + \boldsymbol{N}(\boldsymbol{u}_1).$$

Here we recognize an equation which takes the form $\mathcal{L}_0\boldsymbol{u}_3 = \boldsymbol{R}_3$. This equation has no solution in general, because the operator $\mathcal{L}_0$ has one element in its kernel: $\mathcal{L}_0\boldsymbol{\zeta}e^{i\omega_c t} = 0$, as shown in equation 3.4.10. In such cases, the only technique to compute $\boldsymbol{u}_3$ is to apply the Fredholm alternative: $\boldsymbol{R}_3$ must be orthogonal to the elements of the kernel of the adjoint operator, as derived in the Appendix B. In order to apply this compatibility condition, we define the following scalar product:

$$\langle \boldsymbol{u}|\boldsymbol{v}\rangle = \int_0^{2\pi/\omega_c} \boldsymbol{u} \cdot \overline{\boldsymbol{v}}dt,$$

where $2\pi/\omega_c$ is the period at the onset of the limit cycle. The adjoint operator $\mathcal{L}_0^\dagger$ of the operator $\mathcal{L}_0$ under the above scalar product is written as:

$$\mathcal{L}_0^\dagger = -\partial_t - L_0^t,$$

This operator has two elements in its kernel:

$$\text{Ker}(\mathcal{L}_0^\dagger) = \{e^{i\omega_c t}\boldsymbol{\zeta}^\dagger, e^{-i\omega_c t}\overline{\boldsymbol{\zeta}^\dagger}\},$$

with

$$\boldsymbol{\zeta}^\dagger = \begin{pmatrix} 1 \\ \frac{1}{\xi\omega_0 - i\omega_c} \\ \frac{\Delta\phi}{K_3\Omega\omega_0^2\gamma_c}\left(i\omega_c - \frac{\omega_0^2}{\xi\omega_0 - i\omega_c}\right) \end{pmatrix}.$$

Consequently, the Fredholm alternative is written:

$$\int_0^{2\pi/\omega_c} \left(-\partial_{t_2}\boldsymbol{u}_1 + L_2\boldsymbol{u}_1 + \boldsymbol{N}(\boldsymbol{u}_1) \right) e^{-i\omega_c t}\,\overline{\boldsymbol{\zeta}^\dagger}\,dt = 0,$$

which determines the equation for the slowly varying amplitude of the oscillations:

$$\partial_{t_2} A = (\mu_r + i\mu_i)\gamma_2 A - (\alpha_r + i\alpha_i)|A|^2 A,$$

where the parameters μ_r, μ_i, α_r and α_i are computed by evaluating the previous integral. This equation is the amplitude equation of the oscillation, as in equation C.0.8, and it corresponds to the normal form of the Hopf bifurcation. By setting $A = Re^{i\theta}$, we determine the oscillation dynamics:

$$\partial_{t_2} R = \mu_r \gamma_2 R - \alpha_r R^3,$$
$$\partial_{t_2}\theta = \mu_i \gamma_2 - \alpha_i R^2.$$

Hence after a transient regime, the amplitude of the oscillation becomes steady and a detuning in frequency $\alpha_i\,(\gamma - \gamma_c)$ appears because of the weakly nonlinear corrections.

$$R = 4\sqrt{\mu_r/\alpha_r}\sqrt{\gamma - \gamma_c} = 4\Theta\sqrt{\gamma - \gamma_c},$$
$$\omega = \omega_c - (\gamma - \gamma_c)\left(\mu_r\frac{\alpha_i}{\alpha_r} - \mu_i\right) = \omega_c - (\gamma - \gamma_c)\,\omega_2,$$

where we define:

$$\Theta = \left(\frac{2K_1^3 K_3 x^3 y (1 + \Xi)\Omega^2}{\text{den}_\Theta} \right)^{1/2},$$

and the expression of the Θ denominator, den_Θ, reads:

$$\text{den}_\Theta = 3K_1^2 K_2 \Delta\phi^2 (2(1 + y) + x(1 + \Xi)(2 + x\Xi(\Xi - y))) - x^2(1 + \Xi)\,(y$$
$$-3(2 + \Xi) + x(y(3 + \Xi(3 + \Xi + x(1 + \Xi)^2)) - \Xi(7 + \Xi(5 + \Xi + x(1 + \Xi)^2)) - 4))$$

where we have introduced the additional parameters:

$$y = \sqrt{(\xi^2 - 1)^2 + \frac{4}{x}}, \qquad x = \frac{\omega_0 \Delta\phi}{\xi\Omega}, \qquad \Xi = \xi^2 - 1.$$

This relation predicts that the oscillation amplitude grows as the square root of the distance to the threshold.

Concerning the nonlinear corrections to the oscillation frequency, we obtain:

$$\omega_2 = \omega_c \left(\Theta^2 \frac{\text{num}_{\omega_2}}{2K_1^2 x^2 \Delta\phi^2 (2 + y - xy\Xi(1 + \Xi) + \Xi(3 + x\Xi(1 + \Xi)))} \right.$$
$$\left. + \frac{K_1 K_3 x^2 (1 + \Xi)(2 - y + \Xi)\Omega^2}{2\Delta\phi^2 (2 + x(y - \Xi + 2y\Xi))} \right),$$

with the expression of the ω_2 numerator, num_{ω_2}, is defined as:

$$\text{num}_{\omega_2} = 3K_1^2 K_2 \Delta\phi^2 (2 + x(2 + 2x(y - 2\Xi)(1 + \Xi) + x^2(y - \Xi)\Xi^2(1 + \Xi) + \Xi(2 - y + \Xi)))$$
$$- x^3(1 + \Xi)^2(6 - 2y + 4\Xi + x(1 + \Xi)(2 - y(3 + \Xi(1 + x + x\Xi)) + \Xi(5 + \Xi(1 + x + x\Xi)))).$$

These calculations determine the first-order amplitude and frequency corrections as a function of γ and predict the behavior of the system in a neighborhood of the bifurcation point γ_c.

3.5   Results

From the values of the parameters (table 3.1), we found from equations 3.4.7 and 3.4.8 the predicted threshold value for γ to be $\gamma_c = 0.75$ rad N^{-1} and the oscillation frequency to be $\omega_c = 15.6$ rad s^{-1}, while the experimental values are $\gamma_{c,\exp} \sim 0.72$ rad N^{-1} and $\omega_{c,\exp} \sim 14.8$ rad s^{-1}. The agreement is very satisfactory given there is no free parameter once the physical model parameters are measured, as we show in figure 3.19, where we compare the numerical predictions of our model with the experimental values.
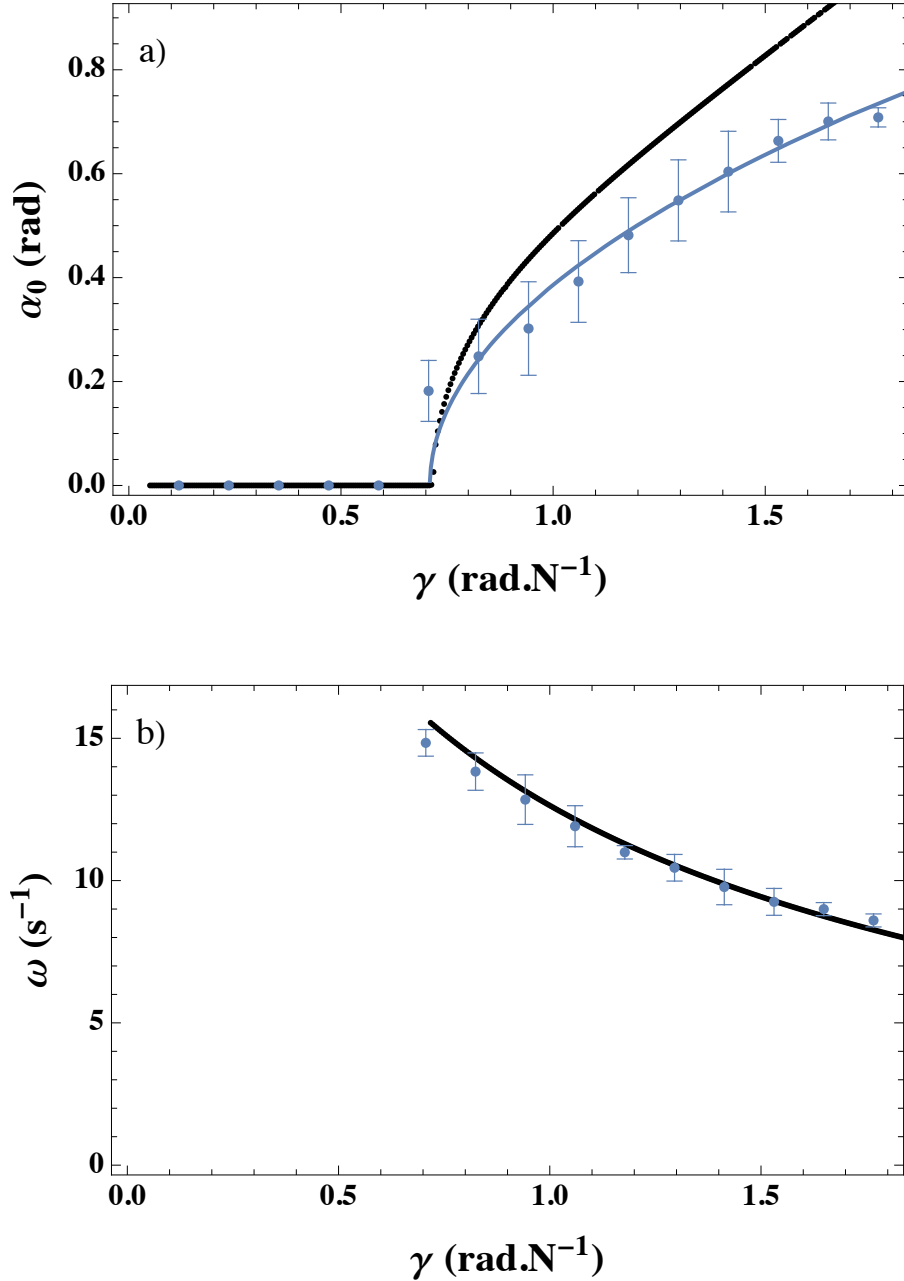
Figure 3.19: Oscillatory characteristics of the proprioceptive loop. a) Angular amplitude of the tail oscillation α_0 as a function of γ. b) Angular frequency ω as a function of γ. The experimental measurements and their error bars are drawn in blue. In a), the blue curve passing through the data is an interpolation with the function $\alpha_0 = \Theta_{\exp}\sqrt{\gamma - \gamma_{c,\exp}}$ with $\gamma_{c,\exp} \sim 0.72$ rad N^{-1} and $\Theta_{\exp} = 0.72$ $\text{rad}^{1/2}$ $N^{1/2}$. The numerical predictions are represented by thick black lines.

Using a fourth-order Runge-Kutta algorithm, we have numerically integrated the complete nonlinear system, and we compare the model prediction to the experimental measurements. It appears that both the oscillation angular amplitude and frequency in experiments are well captured by the simple model, taking into account again that there is no free parameter. We note here the square root behavior for the amplitude, which is characteristic of Hopf bifurcation, and we show by using the calculations of the precedent section that

$$\alpha_0 = \Theta\sqrt{\gamma - \gamma_c},$$

where $\Theta = 0.97$ rad$^{1/2}$ N$^{1/2}$. In experiments, Θ is evaluated to $\Theta_{\exp} = 0.72$ rad$^{1/2}$ N$^{1/2}$, and the agreement is again very satisfactory.

3.5.1   Long tail analysis and saturation effect

To check the robustness of our approach we proceed by modifying the structure of the robotic fish with a longer and more rigid tail (figure 3.20). The coefficients K_1, Ω and $\Delta\phi$ remain the same since they characterize the servomotor only, but ω_0, ξ, K_2 and $K_{\alpha''}$ are expected to vary due to a change of the fluid-structure interaction.
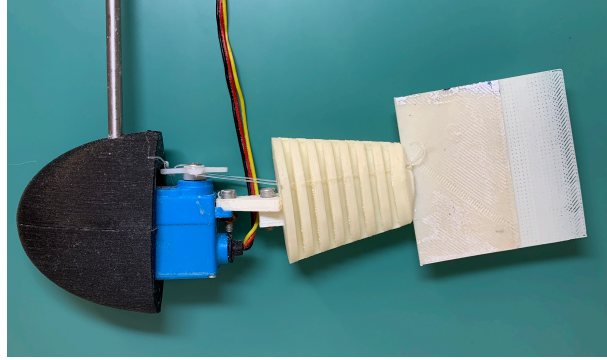
Figure 3.20: Robotic fish with a longer and more rigid tail.

We follow the same procedure to find the coefficients (figure 3.21) and we obtain $\omega_0 = 7$ s^{-1}, $\xi = 1.3$, $K_2 = 0.7$ and $K_{\alpha''} = 0.020$ N.rad^{-1}.s^2.
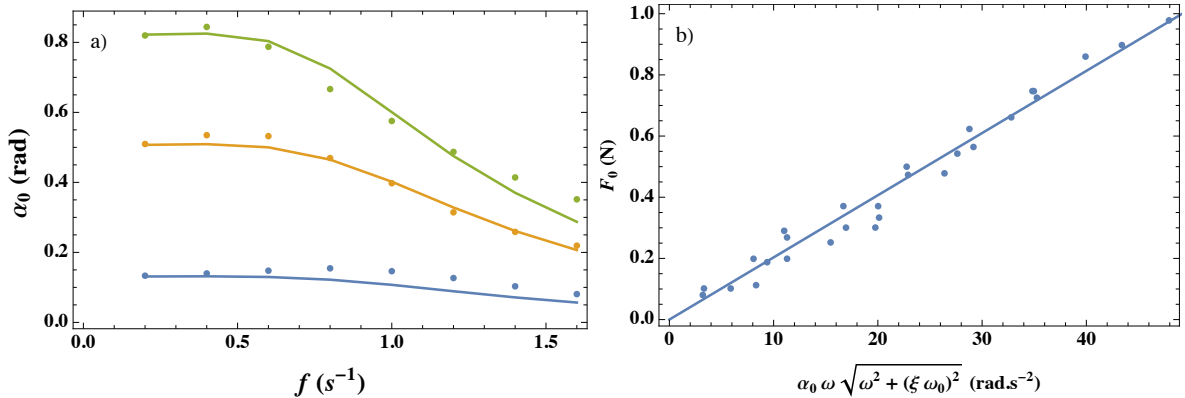
Figure 3.21: Long tail analysis. a) α_0 as a function of f for three values of Φ (0.24, 0.94 and 1.65 rad from bottom to top). The solid lines are the prediction of the model with the parameters $\omega_0 = 7$ s^{-1}, $\xi = 1.3$ and $K_2 = 0.7$. b) F_0 as a function of $\alpha_0\omega\sqrt{\omega^2 + (\xi\omega_0)^2}$. The solid line is the line of best fit with $K_{\alpha''} = (20.3 \pm 0.3) \cdot 10^{-3}$ N.rad^{-1}.s^2 as the proportionality constant.

The results of the experiments performed with both the regular and long tails are reported in figure 3.22. We observe that γ_c is higher and ω_c is smaller for the long tail. For the long tail, comparison with the model again gives a very good agreement, at least up to $\gamma = 2.5$ rad.N^{-1}. Beyond that, both α_0 and ω seem to saturate. Actually this feature had already been observed for the regular tail and $\gamma > 1.8$ rad.N^{-1}. To describe this feature we need to account for another limitation of the servomotor: the angle ϕ is restricted to the range $[-\pi/3\,\text{rad}, \pi/3\,\text{rad}]$. We can account for this limitation in the model and achieve a better match between the model and experiments.
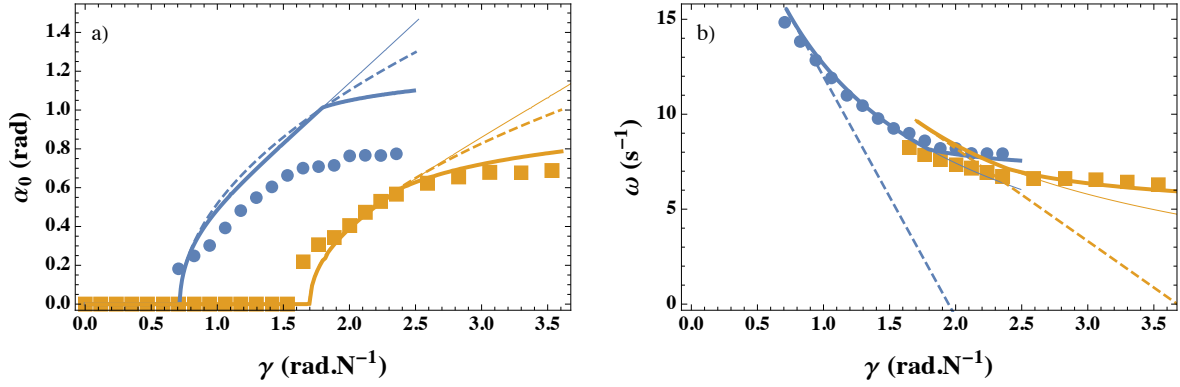
Figure 3.22: Comparison of the angular amplitude, a), and frequency, b), as functions of γ for the two tails. Blue circles and orange squares represent the regular and long tails, respectively. Solid lines hold for the model with (thick) and without (thin) saturation. The perturbative approach is represented by the dashed lines.
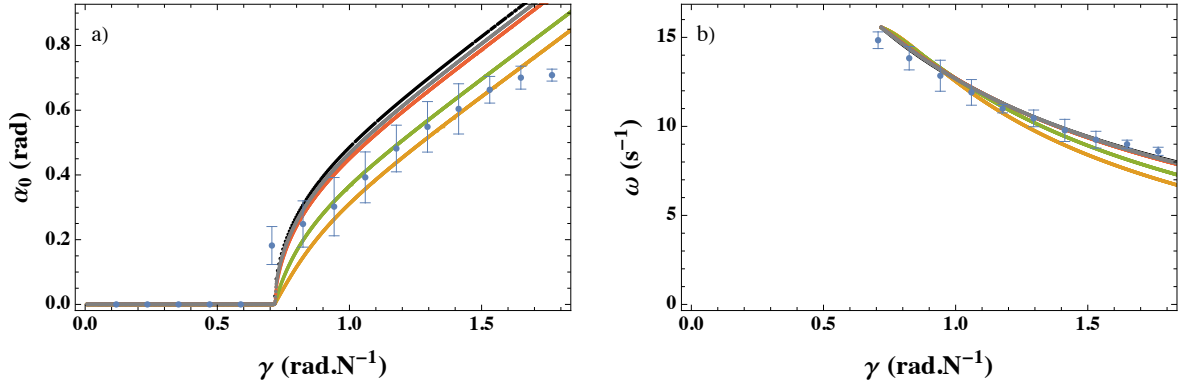
Figure 3.23: Comparison of the angular amplitude, a), and frequency, b), as functions of γ for different values of the coefficient c_y. Blue circles correspond to experiments. The model is calculated with $c_y = 0$ (black), 0.005 (gray), 0.01 (red), 0.05 (green) and 0.1 (orange).

3.5.2 Effect of the quadratic drag in the transverse force expression

As discussed above, a nonlinear term accounting for the transverse pressure drag might be expected in the sensing stage 3.4.4 because of the high value of the Reynolds number characterizing the lateral oscillations. This term writes $-c_y \rho L^4 \alpha' |\alpha'|$ with $\rho = 1000$ kg.m^{-3}, $L = 10$

cm and c_y a dimensionless coefficient we expect to be small. The comparison between the experimental data, the model without quadratic drag and several simulations with small values of the coefficients c_y is shown in figure 3.23. The introduction of this nonlinear drag does not change the threshold nor the angular frequency at γ_c, as these quantities are issued of a linear stability analysis. Taking $c_y \sim 0.05$ slightly improves the matching between the model and the experimental data at high α_0 values.

3.6   Swimming driven by the proprioceptive loop

To conclude on the capacity of the proprioceptive loop to induce locomotion, we have submitted the robotic fish to an imposed fixed velocity flow into the water tunnel. Following Garrick [101] we expect the thrust T to scale as $F_y \cdot \alpha$ in the small amplitude regime. For a harmonic signal $\alpha = \alpha_0 \sin(\omega t)$, we expect the mean thrust $\overline{T} = -\overline{F_x}(t)$ to be positive and proportional to $\alpha_0^2 \omega^2$ from equation 3.4.4. Note that the α' term in this equation is $\pi/2$-shifted so that $\overline{\alpha'(t)\alpha(t)} = 0$. The proportionality between T and $\alpha_0^2 \omega^2$ is tested experimentally by imposing a harmonic signal to ϕ_c, as in equation 3.4.3. Several values of Φ and ω, in the ranges $[0, 1.9]$ rad and $[0, 8.8]$ s^{-1} respectively, were tested and results are given in figure 3.24. There is a very good linear relation between both quantities. This result is in agreement with previous measurements performed in a former study [15] as well as data obtained with foils [30, 31, 139].
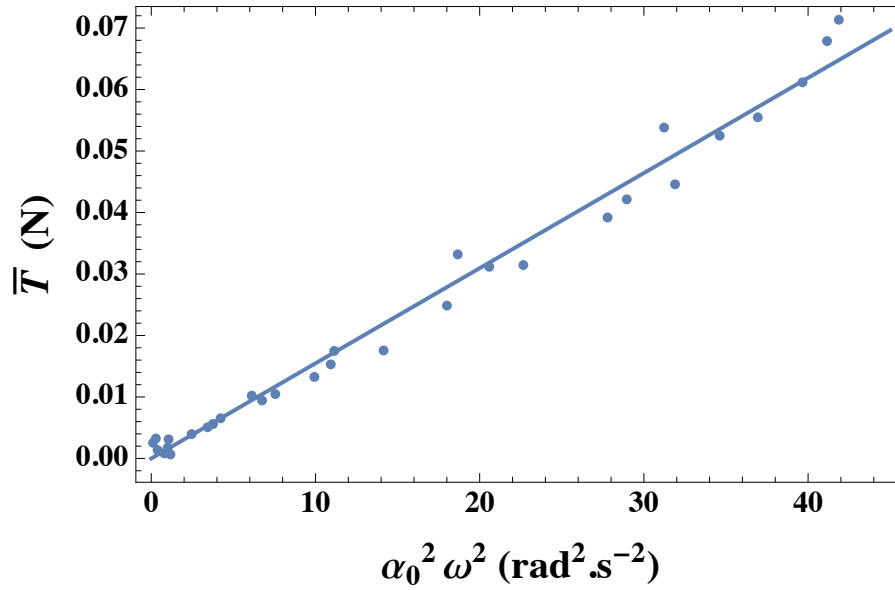
Figure 3.24: Measurement of the mean thrust T for a harmonic forcing of the wheel angle at amplitude Φ and frequency ω. The angle α_0 is directly measured in the images. The experimental points are shown as disks, and the linear fit is the thick line.

To determine the drag coefficient of the robotic fish, we measure the mean longitudinal force F_x felt by the sensor keeping the fish at rest, $\alpha = 0$, during this set of experiments. We then impose a flow in the water tunnel varying the velocity U from 0 to 0.11 m.s^{-1}. Given the orientation of the x-axis, F_x is positive in this case. As we are dealing with high Reynolds numbers we expect this drag force to be proportional to U^2, a tendency which is confirmed in figure 3.25. Assuming that the pressure drag is:

$$F_x = \rho C_d L^2 U^2,$$

the best interpolation gives $C_d = 0.254 \pm 0.004$ with $\rho = 1000$ kg.m^{-3} and $L = 10$ cm.
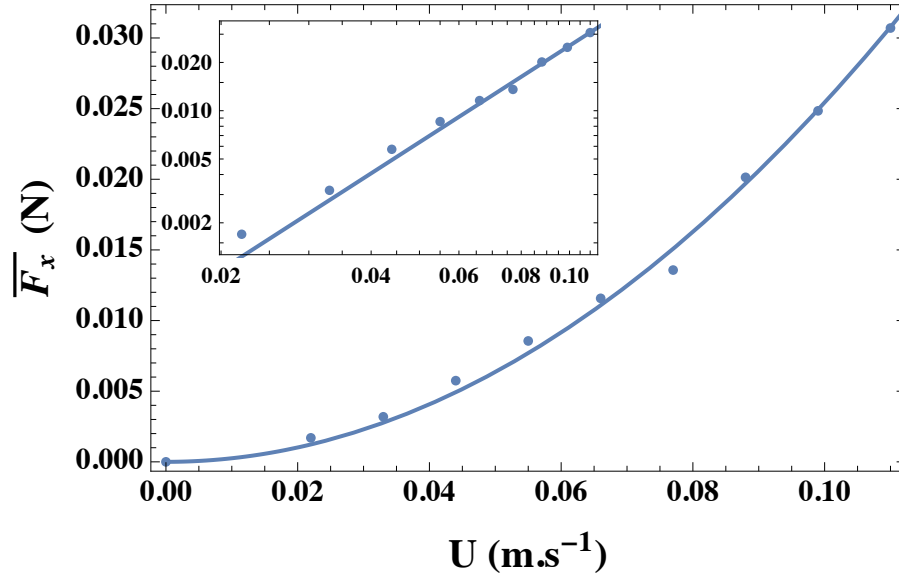
Figure 3.25: Mean longitudinal force, F_x, as a function of the water tunnel velocity, U, for $\alpha = 0$. Inset: log-log plot of the same data.
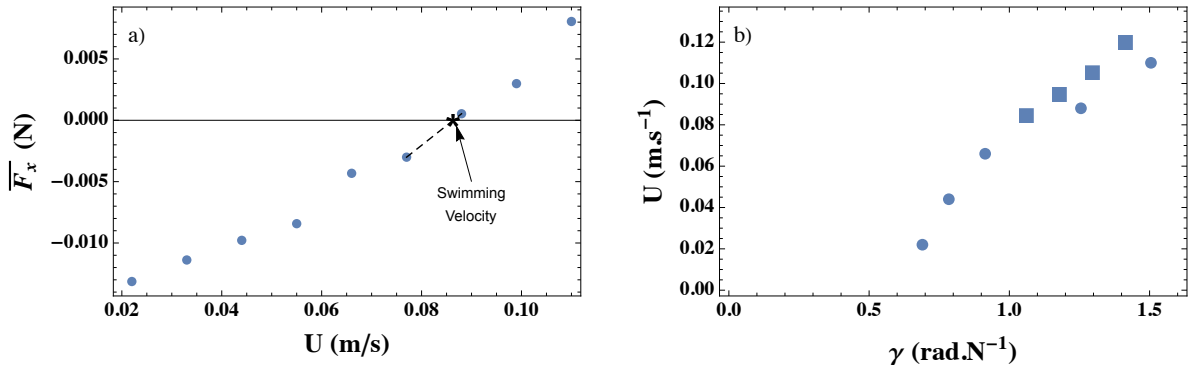
Figure 3.26: a) F_x as a function of U for $\gamma = 1.06 \, \text{rad.N}^{-1}$ following the first protocol. The swimming velocity for this particular value of γ is indicated with the horizontal line. b) Swimming velocity U as a function of γ obtained with the first (squares) and second (circles) protocols. See the main text for the protocols definition.

As the device is attached to the force sensor, the cruising velocity of the swimmer can be measured by zeroing the value of the longitudinal force F_x with the tuning of the inflow velocity. For a swimmer in motion, the locomotion velocity is reached when the propulsive and resistive components of the total force applied on the swimmer compensate each other. For $\gamma > \gamma_c$, the oscillation of the tail triggers a net thrust. At the same time the robotic fish is immersed in a water channel, the velocity of which can be varied between 0 and 0.11 m.s^{-1}, and is subject to a net drag force. The swimming velocity is measured with either of two protocols. In the first protocol, γ is fixed to a given value and the velocity of the water tunnel is increased progressively. The average longitudinal force F_x probed by the sensor is initially negative, increases with the velocity U and finally becomes positive. The swimming velocity corresponds to the transition from negative to positive values (figure 3.26a). In the second protocol, U is fixed and the initial force is positive. γ is increased and the force transits from positive to negative values. In that case, the γ that corresponds to this transition is associated with the swimming velocity U. Both

protocols give coherent results that are summarized in figure 3.26b.
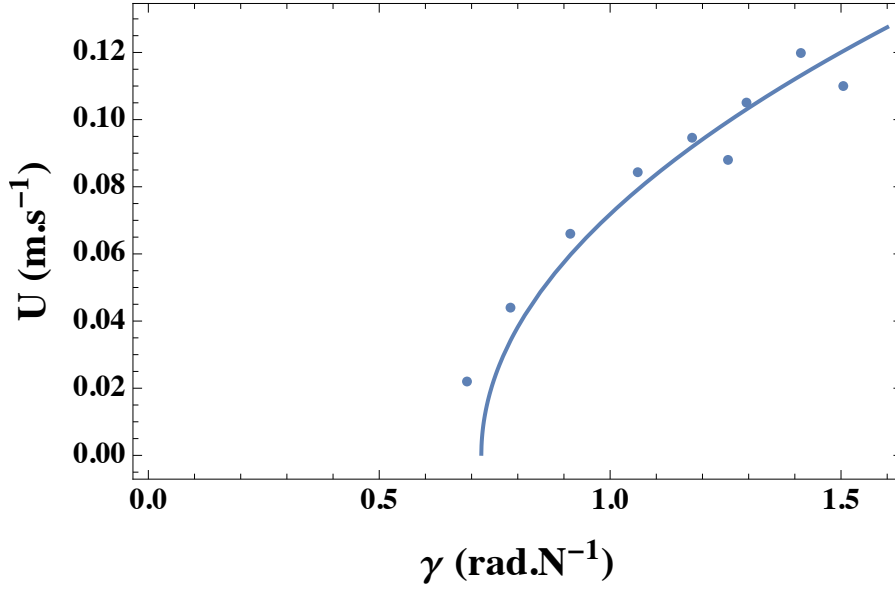
Figure 3.27: Swimming velocity U as a function of the proprioceptive feedback parameter γ. The experimental points are shown. The curve represents the fit $U \sim 0.14\sqrt{\gamma - \gamma_c}$ in SI units.

In figure 3.27, we show the swimming velocity dependence as a function of the feedback parameter γ. We now compute a first-order approximation for the thrust. This quantity results from the projection of the normal force to the fin toward the x axis [101]. Assuming a harmonic motion, α and α' are $\pi/2$ phase shifted and the term in α' does not contribute to the thrust. Only added mass effects are relevant and the average thrust equals

$$\overline{\alpha(t)F_y(t)} \simeq \frac{K_{\alpha''}\omega^2\alpha_0^2}{8} \simeq \frac{K_{\alpha''}\omega^2\Theta^2}{8}(\gamma - \gamma_c).$$

By balancing the thrust with the typical drag, which is dominated by the pressure drag $C_d\rho U^2 L^2$ we determine that the velocity scales as

$$U \sim \sqrt{\frac{K_{\alpha''}}{8C_d\rho L^4}}\omega L\Theta\sqrt{\gamma - \gamma_c} \sim 0.17\sqrt{\gamma - \gamma_c},$$

with SI units, and the order of magnitude of the proportionality constant is in good agreement with that obtained in experiments. This relation is a consequence of the simple force balance and consequently retrieves the constancy of the Strouhal number $\omega L\alpha_0/(2\pi U)$, around 0.3 for Reynolds numbers larger than 3000 [12, 24, 140]. The fact that both α_0 and ω are functions of γ does not modify this balance, so that tuning γ gives a direct control over the swimming velocity.

3.7   Conclusions

Sensing the environment and the sense of proprioception result to be very important in the locomotion of swimmers. Therefore, we have hypothesized that a feedback closed-loop system relating information from the environment to the swimmer's deformation is a fundamental element to consider in swimming.

We have proposed a mechanism for driving bioinspired fish swimming locomotion based on proprioceptive sensing. Proprioception provides information about and representation of a

body's position, motion, and acceleration in addition to the usual five senses. We hypothesize that a feedback loop based on this "sixth" sense results in an instability, starting the locomotion. In order to test our assumptions, we have introduced a generic model for describing swimming driven by proprioception. Beside the general framework we have introduced, we have developed a simple experiment that enabled us to validate the idea that underwater swimmers might select their amplitude and beating frequency using mechanical sensors. Our simple model permits the realization of a tractable experiment; beside its simplicity, it is shown to have excellent predictive capabilities.

These results are published in Physical Review Letters [183].

Chapter 4

Optimization of oscillatory gaits

4.1 Introduction

In the previous chapters, we have extensively characterized and discussed the fluid-structure interaction that appears between the swimmer and its environment. In fact, in chapter 2, we calculated the forces exerted by the fluid on the swimmer within a linear framework for any movement of the swimmer. The calculation of forces allows the knowledge of the swimming velocity as a function of the system's physical parameters via the solution of Newton's equations. However, for an organism, the swimming speed is nothing more than a response to the complex situations it has to face: mating, migrating, escaping from a predator, hunting for food. In each of these situations and many others, the animal's behavior is different and is manifested by choosing different body dynamics to achieve different objectives. An activity such as migrating is not comparable to another, such as hunting. At the same time, in the former, the animal must travel long distances without faltering; in the latter, it is expected to move quickly, during a short time, with which it can surprise and catch its prey. In these two situations, the aim is to optimize a different quantity: in the first, the objective is to keep energy expenditure as low as possible [184–186] while in the second, an explosive movement with the fastest possible speed is expected.

Both magnitudes (velocity and energy) are closely related, and therefore it is of interest to know how they behave as a function of each other. One way to observe how close this relationship is consists in identifying the activity levels of a specimen. Unfortunately, activity levels in swimming fish are often difficult to characterize [187–189] due to the number of external factors that can affect a swimmer's performance, as well as the individual's own preparation and the variety of experimental devices, which only complicates the comparison between the different results obtained [21, 190–194].

However, in some species, it has been possible to establish a clear pattern and differentiated performance levels, as in the case of salmon [189, 195, 196]. Brett found three different scenarios by measuring how long the animals were able to maintain a given swimming speed before becoming fatigued and stopping completely, which are depicted in figure 4.1. These three regimes are defined by the time the organisms are able to maintain a given speed. For reduced speeds, the animal develops a sustained activity and can swim at these speeds for extended periods (on the order of several hours). In prolonged exercise, characterized by a higher range of speeds, the animal can maintain its performance for one or two hours but eventually becomes fatigued. Finally, the animal may develop an explosive phase, burst activity, at very high speeds at the cost of maximum effort for a minimal amount of time (about 30 seconds).
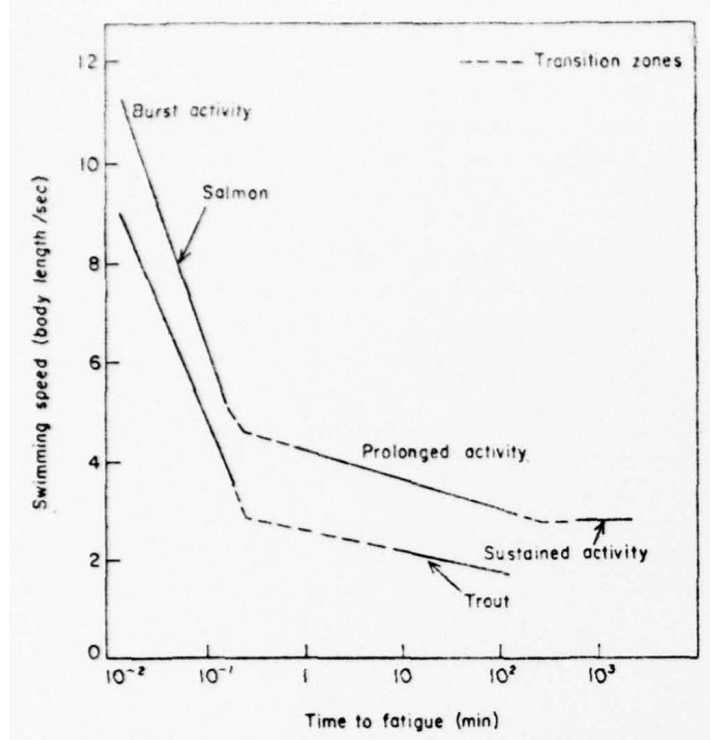
Figure 4.1: Activity levels of sockeye salmon and rainbow trout. Transition zones are represented by broken lines. From Wu [33].

A higher swimming speed leads to faster fatigue, which needs no remarkable intuition: anaerobic exercises are more intense and shorter in duration than aerobic ones [197]. However, in addition to qualitative deductions, it is necessary to mathematically relate the swimmer's energetic variables to the swimming speed and the forces they are able to exert. One of the measures that allows us to establish a relationship between the conversion of total energy into kinetic energy of the swimmer is the Froude efficiency, η [31, 33, 87]:

$$\eta = \frac{\overline{U}\,\overline{T}}{\overline{P}},$$

where $\overline{T}$ is the mean net thrust that propels the animal, $\overline{U}$ is the mean swimming velocity and $\overline{P}$ is the mean power input required to create the thrust. Certain definitions use the drag force D instead of T, since in the animal's stationary swimming regime, both forces are assumed to balance and therefore $T = D$. A similar definition contemplates expressing the numerator as $\overline{UT}$, the average of the propulsive power. However, considering that the swimming velocity is usually a constant quantity perturbed by small terms, both definitions give similar estimates. Power, in this case, might be taken as the mechanical power to produce the oscillations or the metabolic power of the organism. However, both quantities are not equal since the mechanical power to create the lateral oscillations will depend on the animal's muscular power, which, in turn, depends on the power given by the metabolism. The measurements of the metabolic rate of an aquatic animal are based mainly on the consumption of oxygen when it develops an activity [76]. Furthermore, metabolic power is strongly influenced by a myriad of factors such as sex and age of the specimen, preparation prior to the experiment, environmental factors, etc. [198]. There exist, however, scaling laws relating metabolic expenditure to swimmer mass (or length). Kleiber's law is one of the most representative, showing that for the majority of animals, the metabolic rate scales as $W^{3/4}$, being W the mass of the animal [199]. Explanations about this exponent rely on the transport of essential materials through fractal networks of branching tubes [200].

Another widely used measure of the energy expenditure of an organism is the so-called cost of transport, COT, defined as the energy used to move an animal over a distance d and which can be expressed as [32, 34]:

$$COT = \frac{E}{d} = \frac{P}{U},$$

where E, d, P and U correspond to the variables metabolic energy, distance, metabolic power and velocity, respectively. Analogous definitions include in the denominator of the expression the mass of the animal [201], or the acceleration of gravity, $g = 9.81$ m.s^{-2}, to make the quantity dimensionless [33]. This quantity is more convenient to represent the swimmer's energy expenditure as it does not involve the animal's thrust, a magnitude that may be ambiguous as there is no single method to determine it [202].
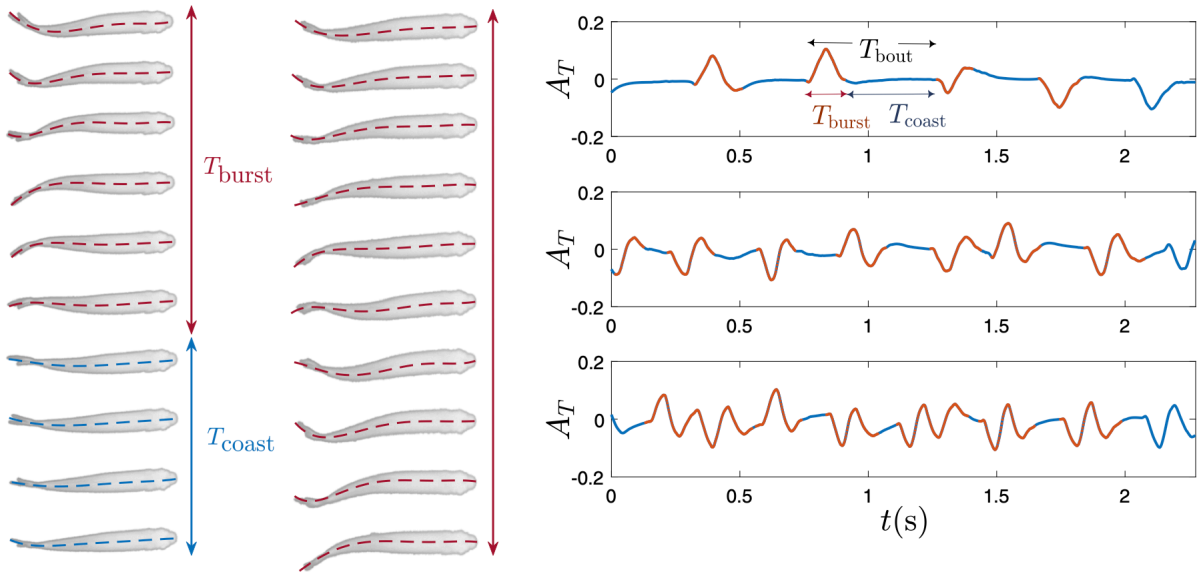
Figure 4.2:   Left: snapshots of two swimming dynamics for two different swimming speeds. Right: three tail-tip kinematics extracted from actual swimmers. From Li et al. [201].

The COT turns out to be a very interesting quantity because, by examining the energetic expenditures of a swimmer, it can give us some insights on what should be its optimal speed to perform this [203]. Although we can determine the speed that optimizes the COT, we still lack essential information about the dynamics of the fish itself, i.e., the body movements it performs to obtain this speed. Considering that the scaling law of the swimming speed depends on the tail beat amplitude and frequency, calculating an optimal speed does not adjust both parameters, and we have an endless number of possibilities. However, understanding the behavior of the COT could make us go further; the measurement of energetic efficiency could also give us clues to determine which are the most efficient gaits in biological swimmers. Or even proceeding backward, choosing the speed and power produced by one type of oscillation could give us clues to investigate how a given gait is energetically desirable compared to others.

It is, in fact, the latter strategy that is used to explain why certain fish choose an intermittent swimming dynamics, known as burst-and-coast (or kick-and-glide), which consists of cyclic bursts of swimming movements followed by a coast phase in which the body is kept motionless and straight [203]. An example of this swimming dynamic can be seen in the first sequence of the figure 4.2, where the swimmer oscillates its tail for a time T_{burst} and then keeps its tail totally immobile during another phase of duration T_{coast} [201]. Intermittent swimming predicts an energy savings of 50% if this strategy is used instead of steady swimming with the same

average velocity [204–206], verifying that for a given swimming velocity, the burst-and-coast strategy corresponds to a gait that minimizes the global cost of transport [201]. Therefore, it is essential to establish the relationship between the different body movements that a swimmer can perform and the speeds derived to compare and judge which of them is more efficient.

4.2 Setting the model up

Since our objective now is not to perform a thorough characterization of the existing fluid-structure interaction but rather to develop simple models where we characterize the swimming speed as a function of the tail behavior, we will oversimplify the fluid-structure interaction and write that thrust or propulsive force of the animal is dominated by the added mass acceleration:

$$T = -C_{Th}\alpha(t)\alpha''(t),$$

with C_{Th} the dimensional thrust coefficient. This simplification assumes that swimming velocities might be considered small in order to neglect the terms α^2 and $\alpha\alpha'$ in equation 2.4.1 [100, 101].

Considering again Reynolds numbers greater than $Re_c \sim 3000$, where pressure drag dominates skin friction [24], the modulus of the drag force reads:

$$D = C_D u(t)|u(t)|,$$

with C_D the dimensional drag coefficient.

Newton's second law, in this case, is written as:

$$mu'(t) = T - D = -C_{Th}\alpha(t)\alpha''(t) - C_D u(t)|u(t)|, \tag{4.2.1}$$

where m is the animal's mass.

This equation is specially adapted to describe swimming in the steady-state since Theodorsen's approach has been designed for a finite stream velocity. The model is robust with respect to the unsteadiness but is expected to be less precise in the transient regime. The system is written in a single dimension; we consider at all times that the swimmer can only move in a straight line. The equation 4.2.1 is made dimensionless if we introduce a time, t_c, and a characteristic length, l_c. We note:

$$x = l_c \tilde{x}, \qquad t = t_c \tilde{t}, \qquad u = \frac{l_c}{t_c}\tilde{u},$$

where $\widetilde{\cdots}$ denotes the dimensionless variables and we write:

$$m l_c \tilde{u}'(\tilde{t}) = -C_{Th}\alpha(\tilde{t})\alpha''(\tilde{t}) - C_D l_c^2 \tilde{u}(\tilde{t})|\tilde{u}(\tilde{t})|.$$

By writing the characteristic length as:

$$l_c = \sqrt{\frac{C_{Th}}{C_D}},$$

we write equation 4.2.1 in which only one parameter appears:

$$M\tilde{u}'(\tilde{t}) = -\alpha(\tilde{t})\alpha''(\tilde{t}) - \tilde{u}(\tilde{t})|\tilde{u}(\tilde{t})|.$$

with M a parameter that weights the inertia of the system and is expressed as:

$$M = \frac{m}{\sqrt{C_{Th}C_d}}$$

To set up the differential equation, we need the expression of $\alpha(t)$ and its second derivative. This is precisely what we will seek next; we will characterize the swimmer's swimming speed

from these already prescribed quantities. We distinguish from now on two possible ways of controlling the swimmer's dynamics: one of them, somewhat idealized in which we assume that all or some of the dynamical variables only take discrete values and which corresponds to discrete control, and the other we will call continuous control, where the continuity of all the variables is mandatorily required.

4.2.1 Acceleration control by impulses

Here we investigate the control over a quantity that can only take discrete values. In the first place, the control hypothesis is made on the angular acceleration, α'', since the simplest case of control of the dynamics of a swimmer might be seen as one where there are only three possible actions to take: a positive angular force, a negative one and a zero one. Consequently, the variables α and α'' are not always differentiable quantities in the classical sense. Therefore, the applied angular acceleration, not dimensionless, in this framework is written as:

$$\alpha''(t) = \Gamma \sum_{i=0} \epsilon_i \delta(t - i\Delta t),$$

with $\epsilon_i = 0, +1, -1$ corresponding to standing by, adding or retrieving an elementary angular force Γ, respectively. $\delta(t)$ corresponds to Dirac delta function, which is applied at every interval of time Δt.

The function $\delta(t)$ represents what is known as a distribution or generalized function [207], which takes the value 0 at all t except at the value $t = 0$ and whose integral over an interval that includes the origin is worth unity. Such a function can be approximated by taking the limit of specific functions that we easily construct:

$$\delta(t) \equiv \lim_{\sigma \to 0} \frac{1}{\sigma\sqrt{2\pi}} e^{-\frac{t^2}{2\sigma^2}}.$$

Appropriately choosing the characteristic time defined above, $t_c = \Gamma^{-1/2}$, the control equation of α'' is:

$$\alpha''(\tilde{t}) = \sum_{i=0} \epsilon_i \delta(\tilde{t} - i\widetilde{\Delta t}).$$

To lighten the notation, we get rid of the variables with a tilde. So from now on, all the variables we deal with in the discrete case are dimensionless.

First, since accelerations occur discontinuously with positive, negative, or zero unitary pulses, we think that a first model of dynamics is one where negative and positive pulses alternate in time, to establish a periodical structure in the acceleration, that is to say:

$$\alpha''(t) = \sum_{i=0}^{n} (-1)^{\lfloor \frac{t - \Delta t/2}{\Delta t} \rfloor} \delta(t - i\Delta t) \tag{4.2.2}$$

where $\lfloor t \rfloor$ is the floor function which takes as input a real number t and gives as output the greatest integer less than or equal to t and Δt is the time between two consecutive δ.

Being interested in the average velocity and in the variations of the velocity over time, we will solve the equation in the steady-state. This means that the transient regime where the speed starts from any value until it converges to a state where the variable becomes periodic is not solved. This greatly simplifies our calculations, and in addition, we lose little information since we also know that the behavior of the swimming is not as well described in the transient regime as in the steady-state [142].

For the calculation of velocities, we discretize the system. We assume that all variables can be labeled at the points $i\Delta t$ where the function δ acts, as depicted in the figure 4.3. At each of these points, the velocity, displacement, and angular velocity are represented by u_i, α_i, and α'_i,

respectively. The green line indicates all the instants in which the angular acceleration is zero; therefore, $\alpha\alpha'' = 0$.
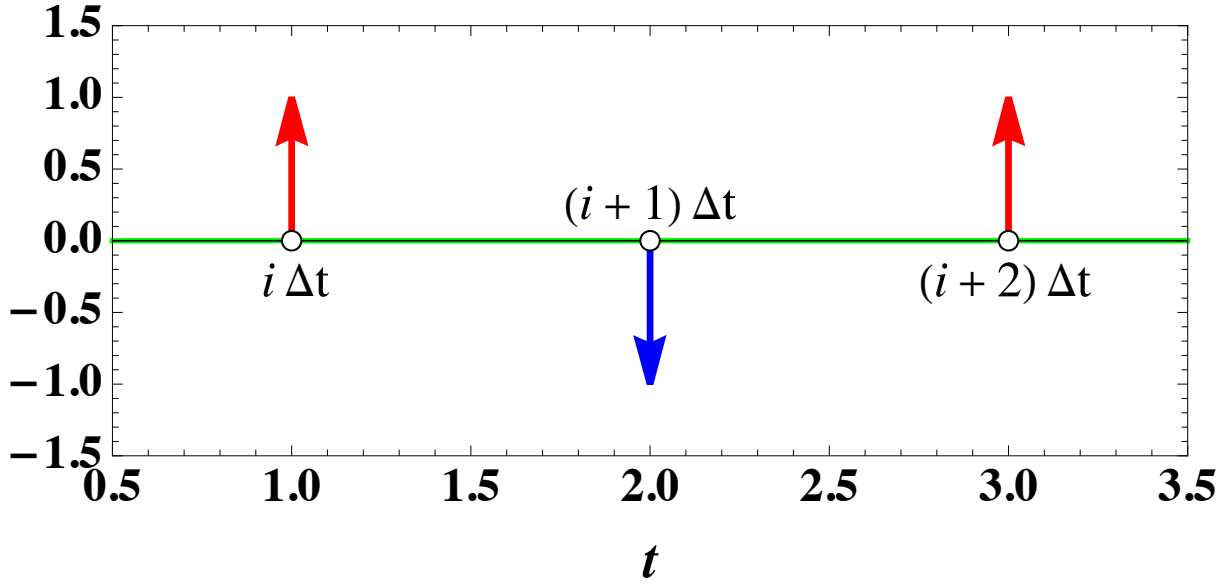
Figure 4.3: Scheme of the discretized forcing. The red arrows represent positive impulses, while the blue one corresponds to a negative impulse. The green line corresponds to times where the thrust force is 0.

Between two consecutive Δt, the equation we have to solve for the velocity is:

$$Mu'(t) = -u(t)^2,$$

with the initial condition $u(i\Delta t) = u_i$. We find that the solution of the equation is:

$$u(t) = \frac{Mu_i}{M + u_i\,(t - i\Delta t)}. \tag{4.2.3}$$

Likewise, since the angular acceleration is zero in this space, the angular variable reads:

$$\alpha(t) = \alpha_i + \alpha_i'\,(t - i\Delta t)\,.$$

We observe that the tail movement describes triangular signals with period $2\Delta t$, as it could not be otherwise. The angular velocity, on the other hand, is a square signal of the same period. Both functions are not derivable in the usual sense, but they are in the sense of the distributions. Actually, we show that the values of α_i' are already prescribed and this is not a variable parameter of the system. If we integrate the angular acceleration in a neighborhood of a point $i\Delta t$:

$$\int_{i\Delta t - \varepsilon}^{i\Delta t + \varepsilon} \alpha''(t)dt = \alpha'(i\Delta t + \varepsilon) - \alpha'(i\Delta t - \varepsilon) = \epsilon_i$$

because $\alpha''(t) = \epsilon_i\delta(t - i\Delta t)$. ϵ_i is, as we defined previously, a parameter taking the values $+1$ or -1 depending on how we defined the sequence of impulses in equation 4.2.2:

$$\epsilon_i = \begin{cases} -1, & \text{if } 0 < \mathrm{mod}(t, 2\Delta t) < \Delta t \\ 1, & \text{if } \Delta t < \mathrm{mod}(t, 2\Delta t) < 2\Delta t \end{cases} = \begin{cases} -1, & \text{if } i = 2m \\ 1, & \text{if } i = 2m + 1 \end{cases},$$

with $m \in \mathbb{N}_0$, representing the ensemble of natural numbers including 0.

This calculation shows that the angular velocity is a discontinuous quantity and that the difference between values when an impulse is applied may be 1 or -1:

$$\alpha'_i - \alpha'_{i-1} = \epsilon_i.$$

For symmetry arguments (intervals between impulses are constant in time) and keeping in mind that the average of the angular velocity should always be 0 (otherwise we would have a drift in α and it would no longer be periodic) the natural condition α'_i has to fulfill is:

$$\alpha'_i = -\alpha'_{i-1},$$

which implies:

$$\alpha'_i = \epsilon_i \frac{1}{2}.$$

α_i is shown to have a relationship with α'_i. Actually, if we suppose that α is a periodic function with zero average, taking $\alpha(i\Delta t) = \alpha_i$ it is clear that for $\alpha((i+1)\Delta t)$ we must find the same value α_i but with opposite sign. That is, we have:

$$\alpha((i+1)\Delta t) = \alpha_{i+1} = \alpha_i + \alpha'_i \Delta t = -\alpha_i,$$

which gives us a relation between α_i and α'_i:

$$\alpha_i = -\frac{\alpha'_i \Delta t}{2} = -\frac{\epsilon_i \Delta t}{4}. \tag{4.2.4}$$

A typical evolution of the angle and angular velocity is shown in figure 4.4.
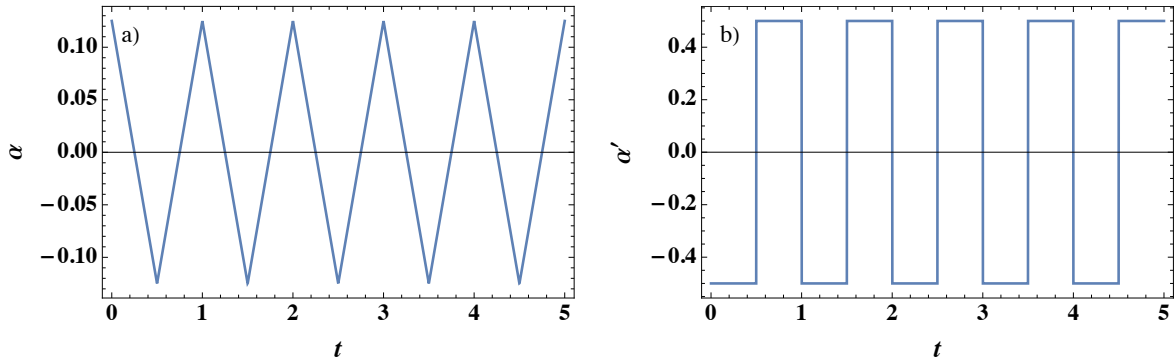
Figure 4.4: Dynamics of a) the tail angle α and b) angular velocity α' for a period $2\Delta t = 1$.

To compute the maximum velocity, which appears just after applying a unit impulse in the acceleration, it may be convenient to rewrite the equation of motion:

$$Mu'(t) = -\alpha(t)\alpha''(t) - u(t)^2.$$

And integrate in a neighborhood of a point $i\Delta t$:

$$M \int_{i\Delta t - \varepsilon}^{i\Delta t + \varepsilon} u'(t)dt = -\int_{i\Delta t - \varepsilon}^{i\Delta t + \varepsilon} \alpha(t)\alpha''(t)dt - \int_{i\Delta t - \varepsilon}^{i\Delta t + \varepsilon} u(t)^2 dt,$$

with $\varepsilon \ll 1$.

The first of the integrals is immediate and its result is:

$$M \int_{i\Delta t - \varepsilon}^{i\Delta t + \varepsilon} u'(t)dt = M\left(u(i\Delta t + \varepsilon) - u(i\Delta t - \varepsilon)\right) = M\Delta u(i\Delta t),$$

where Δu is the velocity jump, this is, the difference between the velocity values before and after applying the acceleration impulse, which shows that u may be potentially discontinuous. The second integral is easily performed, taking into account one of the fundamental properties of the Dirac delta function:

$$-\int_{i\Delta t-\varepsilon}^{i\Delta t+\varepsilon} \alpha(t)\alpha''(t)dt = -\epsilon_i\alpha(i\Delta t) = -\epsilon_i\alpha_i,$$

because $\alpha''(t) = \epsilon_i\delta(t - i\Delta t)$.

Finally, the third integral is solved directly and gives:

$$-\int_{i\Delta t-\varepsilon}^{i\Delta t+\varepsilon} u(t)^2 dt = -\frac{2M^2u_i^2\varepsilon}{(M - u_i\varepsilon)(M + u_i\varepsilon)},$$

that vanishes in the limit $\varepsilon \to 0$.

Therefore, in this limit, the equation of motion reduces to:

$$M\left[\lim_{t\to i\Delta t^+} u(t) - \lim_{t\to i\Delta t^-} u(t)\right] = M\Delta u_i = -\epsilon_i\alpha_i.$$

We rewrite the velocity jump, Δu_i, using the equation 4.2.3:

$$M\left(u_i - \frac{Mu_i}{M + u_i\Delta t}\right) = -\epsilon_i\alpha_i.$$

And taking the expression 4.2.4 for α_i we obtain for the maximum velocity:

$$u_i = u_{\max} = \frac{\Delta t + \sqrt{16M^2 + \Delta t^2}}{8M}.$$

The minimum velocity is defined as the speed of the swimmer just before applying the δ function. Again using the equation 4.2.3, this quantity is easily computed:

$$u_{\min} = \frac{Mu_{\max}}{M + u_{\max}\Delta t}.$$

The average velocity in this formalism is obtained by integrating the solution over one period:

$$U = \frac{1}{\Delta t}\int_{i\Delta t}^{(i+1)\Delta t} \frac{Mu_{\max}}{M + u_{\max}(t - i\Delta t)}dt = \frac{1}{\Delta t}M\log\left[M + u_{\max}(t - i\Delta t)\right]\Big|_{i\Delta t}^{(i+1)\Delta t}$$

$$= \frac{M}{\Delta t}\log\left[\frac{M + u_{\max}\Delta t}{M}\right] = \frac{M}{\Delta t}\log\left[\frac{1 + 8\left(\frac{M}{\Delta t}\right)^2 + \sqrt{1 + 16\left(\frac{M}{\Delta t}\right)^2}}{8\left(\frac{M}{\Delta t}\right)^2}\right].$$

There is only one fundamental parameter in this expression, the ratio between M and Δt. The mean swimming velocity is plotted as a function of the parameter $M/\Delta t$ in figure 4.5. The maximization of the swimming velocity is obtained when $M/\Delta t$ tends to ∞, which, if we fix the swimmer's inertia M, might only be accomplished if the duration Δt between two impulses is negligible. In this limit, $\Delta t \to 0$, the three speeds coincide and are equal to a finite value (figure 4.5):

$$\lim_{\Delta t\to 0} U = u_{\max}(0) = u_{\min}(0) = \frac{1}{2}.$$
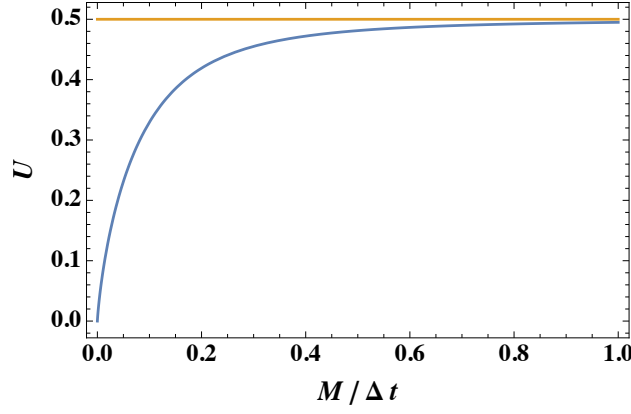
Figure 4.5: Mean swimming velocity as a function of the ratio $M/\Delta t$. The orange line corresponds to the asymptotic limit of the mean velocity $\dfrac{1}{2}$.

Taking the opposite limit, i.e., the one where the time interval between two pulses is very long, $\Delta t \to \infty$, we find a different and unphysical situation: maximum velocity diverges and minimum and mean velocity tend to 0. Furthermore, we may find huge values of α_i. According to equation 4.2.4, there exists a linear relation between α_i and Δt, so larger Δt will cause the divergence of α_i, which is not physical since the amplitude of oscillations must remain bounded below a biological limit, $\alpha_{i,\max}$. The relation between this limit and the maximum period is:

$$\Delta t_{\max} = 4\alpha_{i,\max},$$

so Δt should always be smaller than this maximum value $4\alpha_{i,\max}$.
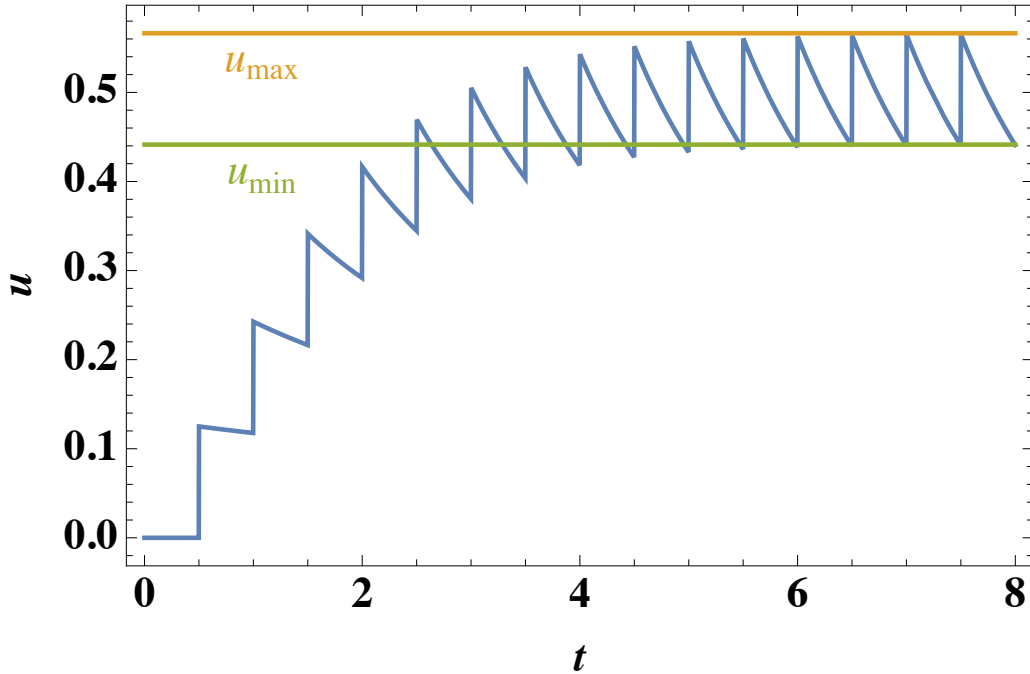
Figure 4.6: Numerical simulations of the swimming velocity u, in blue, as a function of time t. Time between pulses is $\Delta t = 0.5$. The theoretical maximum and minimum velocities are in orange and green, respectively, which characterize the steady-state of the swimming velocity. We also show the predicted transient regime.

Let us suppose that the swimmer's aim is to maximize the average velocity. In that case, we show that the best option is to perform movements very close together, without allowing much time to pass between two, as we might intuitively think. An example of locomotion with this tail dynamics is shown in figure 4.6, where we present the temporal evolution of the velocity until it reaches its stationary state, as well as the maximum and minimum velocities expected in this regime.

4.2.2 Acceleration control by constant piecewise functions

Although it is easily tractable and gives rise to non-zero locomotion velocities, this first model is somewhat inaccurate for certain limits, especially that of $\Delta t \to \infty$, showing a divergent velocity and zero average velocities. In order to make it more realistic, we will increase the complexity level by giving more freedom to the system. In our previous framework, accelerations could only be applied at particular times marked by the Δt parameter. As we have shown, setting this parameter to 0 maximizes the average velocity, an objective that can be very desirable in some situations. To incorporate this fact, let us assume that now the accelerations only take the same three values, one positive, one negative, and one null. Still, now they extend continuously in time (technically, what happens is that the mean time between two accelerations is negligible compared to the order of magnitude of the time of the oscillation) arbitrarily. To illustrate this behavior, we proceed as in figure 4.7, where the acceleration of the swimmer can be written dimensionless by choosing the same characteristic time, $t_c = \Gamma^{-1/2}$, that in the previous subsection:

$$\alpha''(t) = \begin{cases} -1, & \text{if } 0 < \mathrm{mod}(t, \tau) < a_1 \tau, \\ 1, & \text{if } a_1 \tau < \mathrm{mod}(t, \tau) < a_2 \tau, \\ 0, & \text{if } a_2 \tau < \mathrm{mod}(t, \tau) < \tau, \end{cases}$$

with τ the period of the motion and a_1, a_2 two parameters less or equal than unity which are used to model what fraction of the period is occupied by one of the accelerations and which satisfy $a_1 \leq a_2$.

Figure 4.7: Discontinuous angular acceleration over an oscillation period τ.

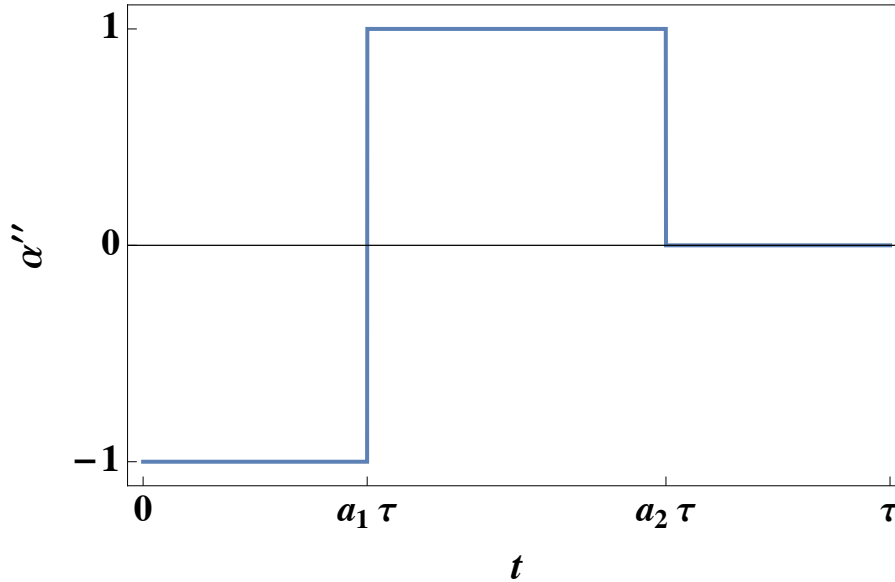Note that the order of the acceleration signs in the configuration has been chosen randomly, and the ordering could have been different. Our only interest is to show that each of the piecewise accelerations acts on the system for a particular non-zero time which is a fraction of the total period of the motion. Of course, more complicated configurations could have been proposed by adding more stages; however, for the sake of simplicity, we chose the most straightforward model where each step appears only once.

If we integrate $\alpha''(t)$ in one period, the solution writes:

$$\alpha(t) = \begin{cases} \alpha_1(t) = -\frac{1}{2}t^2 + C_1 t + C_2, & \text{if } 0 < \mathrm{mod}(t,\tau) < a_1\tau, \\ \alpha_2(t) = \frac{1}{2}t^2 + C_3 t + C_4, & \text{if } a_1\tau < \mathrm{mod}(t,\tau) < a_2\tau, \\ \alpha_3(t) = C_5 t + C_6, & \text{if } a_2\tau < \mathrm{mod}(t,\tau) < \tau, \end{cases} \tag{4.2.5}$$

with C_1, C_2, C_3, C_4, C_5 and C_6 integration constants determined by the conditions that we now settle.

Since we describe the period dynamics of the tail of a swimmer, we need on the one hand to impose the continuity of α over the whole period, that is:

$$\alpha_1(a_1\tau) = \alpha_2(a_1\tau), \qquad \alpha_2(a_2\tau) = \alpha_3(a_2\tau).$$

Likewise, the angular velocity must be continuous as well:

$$\alpha_1'(a_1\tau) = \alpha_2'(a_1\tau), \qquad \alpha_2'(a_2\tau) = \alpha_3'(a_2\tau).$$

If we also require periodicity in α and α' we must demand:

$$\alpha_1(0) = \alpha_3(\tau), \qquad \alpha_1'(0) = \alpha_3'(\tau).$$

In matrix form the system is written as:

$$\begin{pmatrix} a_1\tau & 1 & -a_1\tau & -1 & 0 & 0 \\ 1 & 0 & -1 & 0 & 0 & 0 \\ 0 & 0 & a_2\tau & 1 & -a_2\tau & -1 \\ 0 & 0 & 1 & 0 & -1 & 0 \\ 0 & 1 & 0 & 0 & -\tau & -1 \\ 1 & 0 & 0 & 0 & -1 & 0 \end{pmatrix} \begin{pmatrix} C_1 \\ C_2 \\ C_3 \\ C_4 \\ C_5 \\ C_6 \end{pmatrix} = \begin{pmatrix} a_1^2\tau^2 \\ 2a_1\tau \\ -\frac{a_2^2\tau^2}{2} \\ -a_2\tau \\ 0 \\ 0 \end{pmatrix}.$$

However, this system is inconsistent, i.e., there is no solution for any value of the parameters. In fact, if we calculate the rank of the coefficient matrix and the augmented matrix, we see that these values are 5 and 6, respectively, making it impossible to solve the system. The row echelon form of the augmented matrix is:

$$\begin{pmatrix} a_1\tau & 1 & -a_1\tau & -1 & 0 & 0 & a_1^2\tau^2 \\ 0 & -1 & 0 & 1 & 0 & 0 & a_1^2\tau^2 \\ 0 & 0 & a_2\tau & 1 & -a_2\tau & -1 & -\frac{a_2^2\tau^2}{2} \\ 0 & 0 & 0 & -1 & 0 & 1 & -\frac{a_2^2\tau^2}{2} \\ 0 & 0 & 0 & 0 & -\tau & 0 & a_1^2\tau^2 - \frac{a_2^2\tau^2}{2} \\ 0 & 0 & 0 & 0 & 0 & 0 & a_2^2\tau^2 - 2a_1a_2\tau^2 \end{pmatrix}.$$

Then the ranks of both matrices (and therefore the possibility that at least one solution exists) are equal if and only if:

$$a_2 = 2a_1.$$

The solution $a_2 = 0$ is automatically discarded as this would imply $a_1 = a_2 = 0$ and therefore zero acceleration over the whole period, giving rise to no thrust force.

Surprisingly, a discontinuous acceleration as shown in the figure 4.7 is possible if and only if each of the discontinuous stages has exactly the same duration. The values of a_1 and a_2 cannot be arbitrary if we require the displacement and velocity to be continuous and periodic. The solution of the system with $a_2 = 2a_1$ is:

$$C_1 = a_1^2\tau, \qquad C_3 = (a_1 - 2)a_1\tau, \qquad C_4 = C_2 + a_1^2\tau^2,$$
$$C_5 = a_1^2\tau, \qquad C_6 = C_2 - a_1^2\tau^2.$$

The system has infinite solutions as we present it here; the solutions of the coefficients $C_{i\neq 2}$ depend on the parameter C_2 and, a priori, this can take any value since we do not have an additional bound. In order to resemble a little more to the biological swimmers and taking into account that the locomotion is performed only in one direction, we will impose as a constraint that the average of α in one period must be zero, otherwise the fish could turn and explore a two-dimensional space that is not defined in our equations. Representing the average of a quantity as:

$$\langle X(t) \rangle = \frac{1}{\tau} \int_t^{t+\tau} X(t)dt,$$

the condition we add is $\langle \alpha(t) \rangle = 0$, which implies that C_2 must obey the following equation:

$$C_2 = \frac{1}{2}a_1^2 \left(1 - 2a_1\right)\tau^2.$$

The condition $\langle \alpha(t) \rangle = 0$ is not critical in the sense that it does not affect the calculation of the mean velocity, as we will see later. Typical oscillations are shown in figure 4.8. Here we also calculate the maximum values of the oscillation as a function of the parameter a_1:

$$\alpha_{\max} = \frac{1}{2}(a_1 - 1)^2 a_1^2\tau^2. \tag{4.2.6}$$

For fixed τ oscillation periods, this amplitude is maximized at $a_1 = 0.5$. However, the value $\alpha_{\max}$ does not take any values because there are biological limits. The value at which most biological swimmers swim is usually around 0.1 [21, 25, 38, 133]. This limit imposes a relation between the period τ and the fraction time a_1:

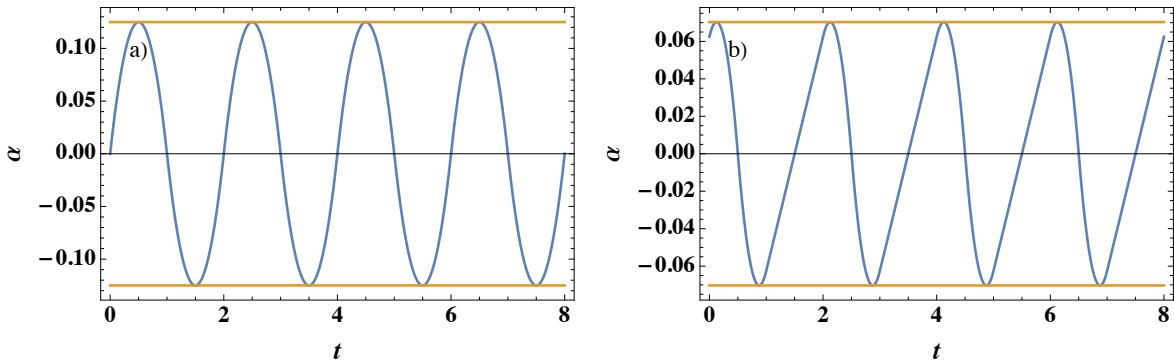$$\tau = \frac{\sqrt{2\alpha_{\max}}}{|(a_1 - 1)a_1|}. \tag{4.2.7}$$

Figure 4.8: Angular amplitude as a function of time. a) For $a_1 = 0.5$ and $\tau = 2$. b) For $a_1 = 0.25$ and $\tau = 2$. Orange lines represent $\pm\alpha_{\max}$.

With all the integration constants calculated, we finally proceed to compute the swimming speed:

$$Mu'(t) = -\alpha(t)\alpha''(t) - u^2(t).$$

However, solving this differential equation with the dynamics prescribed by 4.2.5 is not straightforward and, although it can be solved analytically, the solution overshadows the correct physical interpretation of the results. Therefore, instead of solving for the whole time interval and since we are mainly interested in the behavior of the average locomotion velocity in the stationary regime, we proceed to calculate the average speed in this framework. For this purpose, we assume that in the stationary regime, $u(t)$ can be decomposed as follows:

$$u(t) = U + \delta u(t), \tag{4.2.8}$$

with U the average velocity we intend to calculate and $\delta u(t)$ the fluctuations around this equilibrium state which also satisfy:

$$\delta u(t) \ll U, \qquad \langle \delta u(t) \rangle = 0.$$

The requirements for this hypothesis to be valid rely on the values of τ and M: increasing the period τ implies increasing the amplitude of the oscillations according to the equation 4.2.6. The larger the period is, the more significant the fluctuations will be due to the relation between amplitude and period. For the parameter M, a small value will give rise to big fluctuations because we will almost have $u(t)^2 \sim -\alpha(t)\alpha(t)''$ and so the velocity will oscillate as the product $\alpha(t)\alpha(t)''$. Introducing the above decomposition 4.2.8 in the equation of motion, we obtain:

$$M\delta u'(t) = -\alpha(t)\alpha''(t) - U^2 - 2U\delta u(t) - \delta u(t)^2.$$

If we average the whole equation, taking into account that the average velocity fluctuations are zero and that this quantity is also small compared to the velocity, we find that the average speed reads:

$$U^2 = \langle -\alpha(t)\alpha''(t) \rangle.$$

Here we see that if we replace $\alpha(t)$ by $\alpha(t) + \alpha_0$, with α_0 a constant, the average velocity does not change because:

$$\langle -(\alpha(t) + \alpha_0)\alpha''(t) \rangle = \langle -\alpha(t)\alpha''(t) \rangle - \alpha_0 \langle \alpha''(t) \rangle,$$

and the average of $\alpha''(t)$ is identically 0. Injecting the expression of α and α'' in U^2 we finally get:

$$U^2 = \frac{1}{3}(2 - 3a_1)a_1^3\tau^2. \tag{4.2.9}$$

The numerical solution of the motion equation for two different values of a_1 is shown in figure 4.9, as well as the value of the mean velocity predicted by equation 4.2.9, exhibiting an excellent agreement. It is easy to show that the mean velocity reaches a maximum when $a_1 = 0.5$, which may be somewhat intuitive since this parameter cancels the null acceleration zone of the formalism, allowing there to be a thrust force $-\alpha\alpha''$ throughout the whole period of oscillation. The maximum value of the average velocity is:

$$U = \frac{1}{4\sqrt{3}}\tau.$$

The last calculation considered that both τ and a_1 are independent quantities. If we consider the constraint imposed by equation 4.2.7, the expression 4.2.9 may be written as:

$$U^2 = \alpha_{\max}\frac{2(2 - 3a_1)a_1}{3(a_1 - 1)^2},$$

where we have decided to explicit the dependence on a_1 and the constant value $\alpha_{\max}$. An analogous expression with τ instead of a_1 may also be considered if we already know the maximum amplitude value.
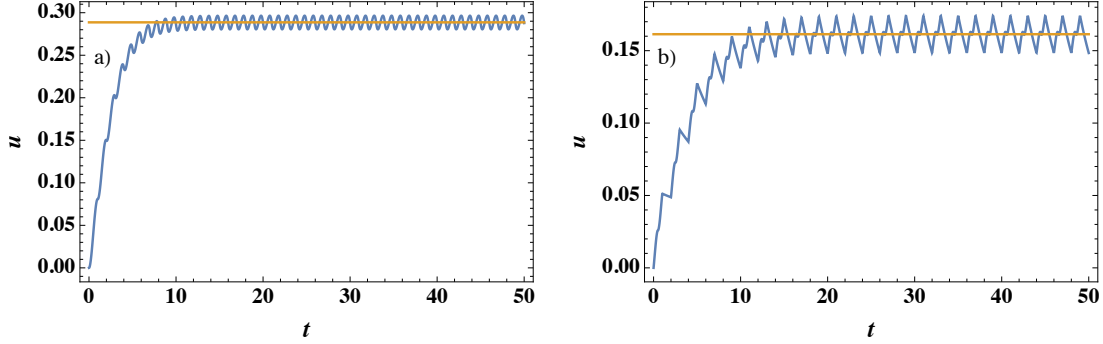

Figure 4.9: Numerical solution of the swimming velocity in function of time. a) For $a_1 = 0.5$ and $\tau = 2$. b) For $a_1 = 0.25$ and $\tau = 2$. In both simulations $M = 1$ and the initial condition is $u(0) = 0$. We plot in orange the theoretical prediction of the mean swimming velocity.

4.2.3   Amplitude control in a relaxation dynamics

A control in torques (via choosing the values of the angular acceleration) has proved fruitful in allowing us to calculate all the kinematic variables of the swimmer, as well as its average propulsive velocity, which we have optimized thanks to handling the expressions that we have derived. This type of control is very suitable for a theoretical treatment since, assuming instantaneous and perfectly characterized accelerations, it is possible to proceed backward integrating to know the other variables of interest. Another alternative, much more realistic and more adapted to experimental devices' control, is to directly regulate the angular motion that we want the swimmer to follow. Again, we could assume an instantaneous α angle and know the other variables by derivation; however, at a practical level, this can be complicated if we do not have full access to the motion of the prototype. Furthermore, it is also necessary to describe the device's behavior as a function of the controller input. That is, to solve the system, we must be able to relate the equation of motion that associates the control variables (input) with the actual movement we want to study (output), which in this case is the dynamics of the tail of a fish-like system.

As a practical example, we are interested in the control of the robotic fish described in Appendix A, which we have already characterized in chapter 3. The equation of motion of the tail was described as a nonlinear damped oscillator forced by the servomotor. Removing the nonlinear dependence completely and calling α_c the external forcing, we write the equation of motion of α as:

$$\alpha''(t) + 2\xi\omega_0\alpha'(t) + \omega_0^2\left(\alpha(t) - \alpha_c\right) = 0.$$

The coefficient 2 in front of the dissipative term, which did not appear in the previous characterization, has been added for ease of use in the equations below.

In this discrete formalism, the amplitude control can only command the instruction to send the tail to specific amplitude values. To keep the treatment simple, we choose a rule such that the desired control is to bring the tail to a maximum angle $\alpha_{\max}$, a minimum angle $-\alpha_{\max}$ or zero amplitude:

$$\alpha_c = +\alpha_{\max}, -\alpha_{\max}, 0.$$

We render t dimensionless and we scale α taking the following characteristic quantities:

$$\tilde{t} = \omega_0 t, \qquad \tilde{\alpha} = \frac{\alpha}{\alpha_{\max}},$$

and the oscillator equation can be written in dimensionless form as:

$$\tilde{\alpha}''(\tilde{t}) + 2\xi\tilde{\alpha}'(\tilde{t}) + \big(\tilde{\alpha}(\tilde{t}) - \tilde{\alpha}_c\big) = 0.$$

with the dimensionless control:

$$\tilde{\alpha}_c = +1, -1, 0.$$

Dropping tildes, the solution of the equation (with $\xi \neq 1$) is:

$$\alpha(t) = A e^{t(-\xi-\Xi)} + B e^{t(-\xi+\Xi)} + \alpha_c,$$

with A and B integration constants and $\Xi = \sqrt{\xi^2 - 1}$, which is a imaginary quantity if $\xi < 1$. Suppose a period of oscillation is defined as τ. In this case, we may impose a positive amplitude value a time $a_1\tau$ ($a_1 \leq 1$), then a negative one up to $a_2\tau$ ($a_1 \leq a_2 \leq 1$) and finally a zero amplitude until the end of the period. Under this choice the angular variable reads:

$$\alpha(t) = \begin{cases} \alpha_1(t) = C_1 e^{t(-\xi-\Xi)} + C_2 e^{t(-\xi+\Xi)} + 1, & \text{if } 0 < \mathrm{mod}(t, \tau) < a_1\tau, \\ \alpha_2(t) = C_3 e^{t(-\xi-\Xi)} + C_4 e^{t(-\xi+\Xi)} - 1, & \text{if } a_1\tau < \mathrm{mod}(t, \tau) < a_2\tau, \\ \alpha_3(t) = C_5 e^{t(-\xi-\Xi)} + C_6 e^{t(-\xi+\Xi)}, & \text{if } a_2\tau < \mathrm{mod}(t, \tau) < \tau, \end{cases}$$

where the integrations constants are calculated such that α and α' are continuous and periodic functions:

$$
\begin{aligned}
C_1 &= \frac{e^{\tau(\xi+\Xi)} - 2e^{a_1\tau(\xi+\Xi)} + e^{a_2\tau(\xi+\Xi)}}{2\left(e^{\tau(\xi+\Xi)} - 1\right)\Xi}(\xi - \Xi), \\
C_2 &= \frac{1 - 2e^{(a_1-1)\tau(\xi-\Xi)} + e^{(a_2-1)\tau(\xi-\Xi)}}{2\left(e^{\tau(-\xi+\Xi)} - 1\right)\Xi}(\xi + \Xi), \\
C_3 &= \frac{e^{\tau(\xi+\Xi)} - 2e^{(1+a_1)\tau(\xi+\Xi)} + e^{a_2\tau(\xi+\Xi)}}{2\left(e^{\tau(\xi+\Xi)} - 1\right)\Xi}(\xi - \Xi), \\
C_4 &= \frac{1 - 2e^{a_1\tau(\xi-\Xi)} + e^{(a_2-1)\tau(\xi-\Xi)}}{2\left(e^{\tau(-\xi+\Xi)} - 1\right)\Xi}(\xi + \Xi), \\
C_5 &= \frac{1 - 2e^{a_1\tau(\xi+\Xi)} + e^{a_2\tau(\xi+\Xi)}}{2\left(e^{\tau(\xi+\Xi)} - 1\right)\Xi}e^{\tau(\xi+\Xi)}(\xi - \Xi), \\
C_6 &= \frac{1 - 2e^{a_1\tau(\xi-\Xi)} + e^{a_2\tau(\xi-\Xi)}}{2\left(e^{\tau(-\xi+\Xi)} - 1\right)\Xi}(\xi + \Xi).
\end{aligned}
\tag{4.2.10}
$$

Unlike the previous case, the problem is univocally determined by the conditions of continuity and periodicity. Therefore, it is not necessary to impose any additional equation, which causes that the angle α does not have to be zero on average. In fact, integrating the angular displacement over a period, we obtain that the average is:

$$\langle\alpha\rangle = 2a_1 - a_2,$$

which, surprisingly, depends neither on the period nor on the damping factor, simply on the coefficients a_1 and a_2, which mark the control behavior in time. Figure 4.10 shows two tail dynamics for different a_1 and a_2 period fractions, but satisfying $2a_1 - a_2 = 0$, with the parameters ξ and τ set to 0.8 and 10, respectively. These are completely arbitrary values since what we want to show is how the value of a_2 affects the behavior of α, performing a motion very similar to burst-and-coast (4.10a) or swimming continuously (4.10b). In our discrete formalism this is the first time we see intermittent swimming appear, by letting the system tend for a long time to $\alpha_c = 0$.
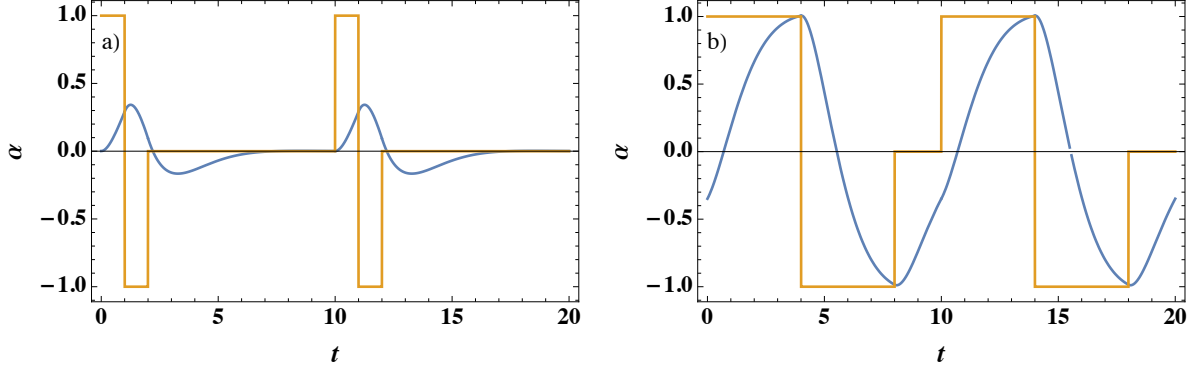
Figure 4.10: Temporal evolution of α. a) For $a_1 = 0.1$ and $a_2 = 0.2$. b) For $a_1 = 0.4$ $a_2 = 0.8$. The values of the parameters are $\xi = 0.8$ and $\tau = 10$. In orange we show the target amplitude as a function of time.

Analogously to our previous approaches, we optimize the average swimming speed. Under the same hypothesis we outlined before, we can get rid of the derivative term of the evolution equation by assuming that the swimming velocity may be decomposed into a mean and a fluctuating part, the latter being much smaller than the former. Under these hypothesis, maximizing the average swimming speed is equivalent to maximize the average thrust force $\langle T \rangle$, except for a multiplicative constant. The average thrust force is calculated as:

$$\langle T \rangle = \frac{1}{\tau} \left(\int_0^{a_1\tau} -\alpha_1 \alpha_1'' dt + \int_{a_1\tau}^{a_2\tau} -\alpha_2 \alpha_2'' dt + \int_{a_2\tau}^{\tau} -\alpha_3 \alpha_3'' dt \right),$$

whose expression is too lenghty to be shown here.

Analytically optimizing this expression is not possible. There are four parameters to vary, and the relationship between them is strongly nonlinear. However, we can always find the values that maximize the force numerically. First, we want to understand what should be the optimal fraction of time that the control should develop to set the values of a_1 and a_2. To do this, we systematically vary the values of ξ and τ in the function $\langle T \rangle (\xi, \tau, a_1, a_2)$ and calculate the values of a_1 and a_2 that maximize $\langle T \rangle$ under the constraints $0 \leq a_1 \leq 1$ and $a_1 \leq a_2 \leq 1$. The intervals of variation of ξ and τ are:

$$\xi \in [0.01, 2.01], \qquad \tau \in [0.1, 20.1].$$

We find the optimal values of a_1 and a_2 with the Mathematica software, using the Differential Evolution method [208], which, although numerically more expensive, gives more robust results. The algorithm sets the value $a_2 = 1$ for all cases since this value overrides the instants where the control wants to bring the tail to 0, which is a phase where the thrust is reduced. The value of a_1, however, is not fixed to 0.5 as would be expected by symmetry arguments, at least not for all parameter values, as we show in figure 4.11. For increasing values of the oscillation period and damping rates always less than unity, the optimal values of a_1 are less than 0.5 4.11. The optimal values are strictly less than 0.5 because there is a symmetry $\langle T(a_1, a_2 = 1) \rangle \rightarrow \langle T(1 - a_1, a_2 = 1) \rangle$; the zones where the control angle is $+\alpha_{\max}$ and $-\alpha_{\max}$ are perfectly interchangeable in the sense that they will give the same thrust average force.
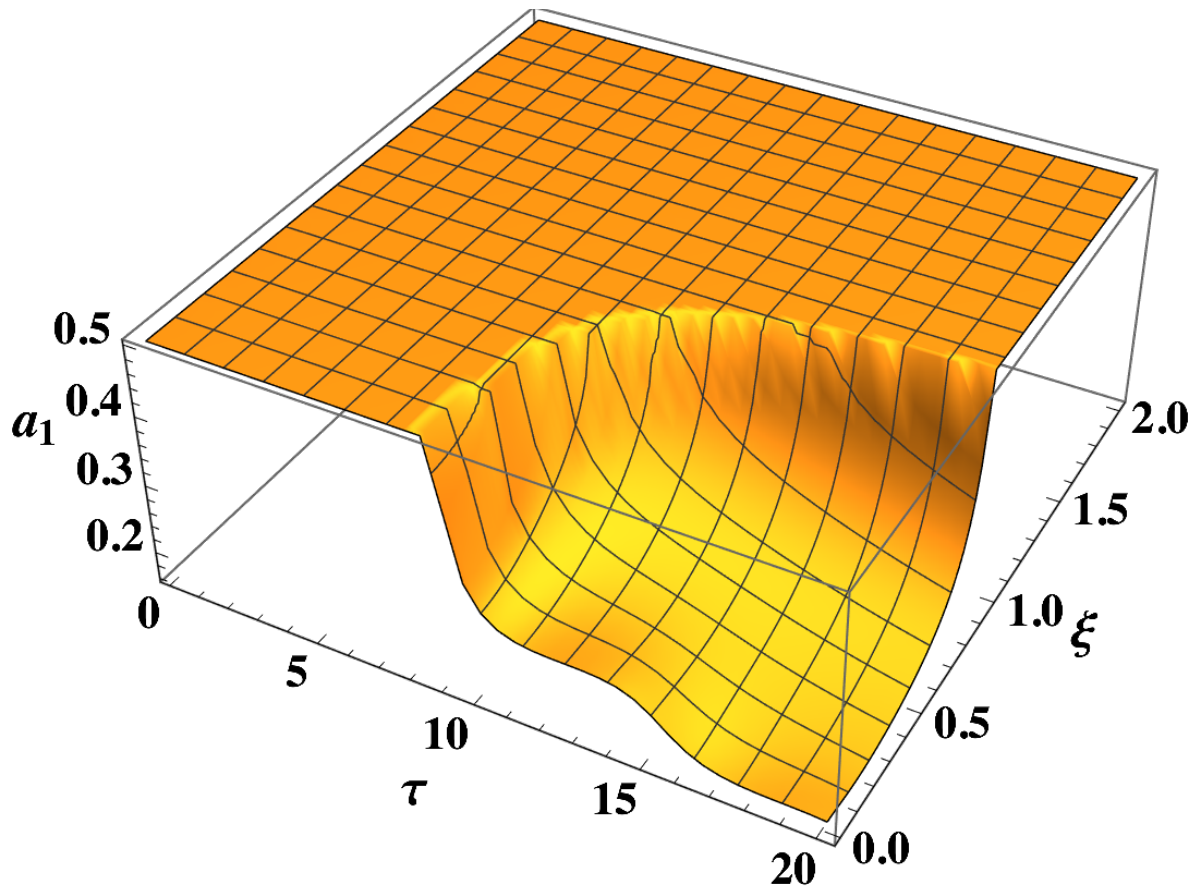
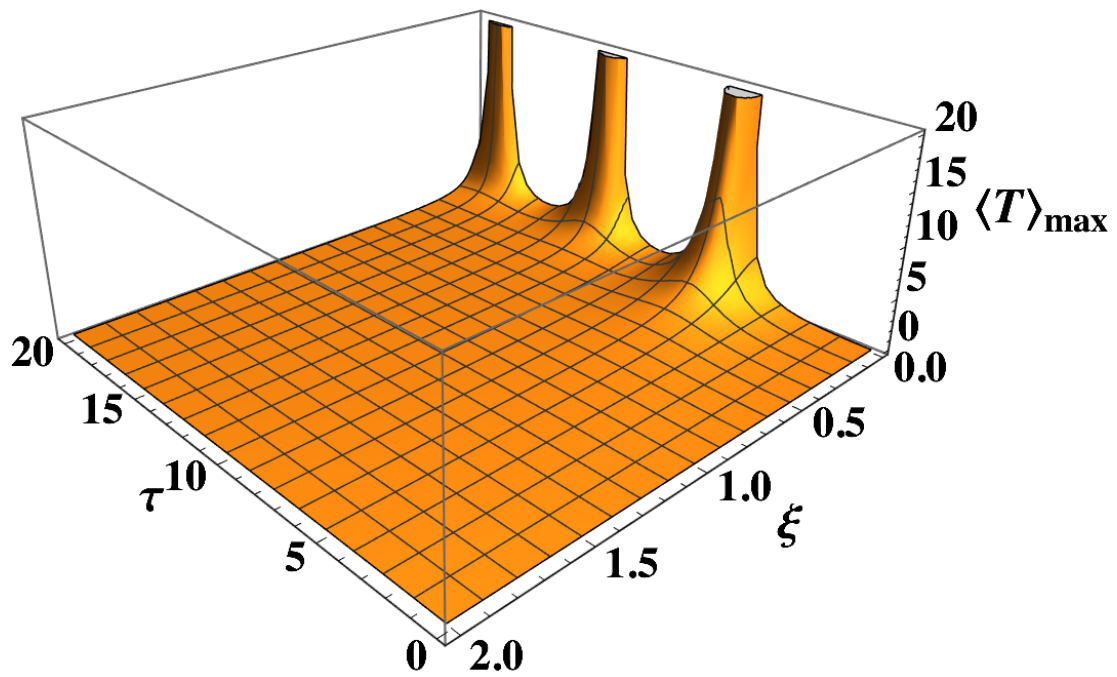Figure 4.11:   Values of a_1 achieving maximum thrust force as a function of ξ and τ.

Figure 4.12: Maximum average thrust as a function of ξ and τ.

Once a_1 and a_2 are fixed, we have to ask ourselves which are the maximum values of thrust $\langle T \rangle_{\max}$ as a function of ξ and τ. By the above simulation, we obtained, in addition to the optimal values of a_1 and a_2, the values of the maxima, which we show in figure 4.12. The maximum values are small for high damping rates and increase progressively as this parameter tends to 0. In addition, we observe three peak-like structures in the limit $\xi \to 0$. These peaks are provoked by a divergence of $\langle T \rangle_{\max}$, caused by a resonance effect on the angle α. Actually, if we examine the integration constants in equation 4.2.10 and look deeper in the denominator of these expressions we see that this term is written as:

$$e^{\tau(\pm\xi+\Xi)} - 1,$$

which, in the limit $\xi \to 0$ is equal to 0 if and only if:

$$\tau = 2\pi m,$$

with $m \in \mathbb{N}$. This explains the occurrence of peaks around 2π, 4π and 6π.

4.2.4 Continuous control

Unlike the previous case, where at least one of the control variables could only take specific discrete values or even only act at certain times, which meant that in general, some of the functions describing the dynamics of the animal were neither continuous nor differentiable in the usual sense, we get rid of that problem henceforth. All the variables we are dealing with now are continuous, differentiable, and there is no a priori limitation on the values that these functions can take. Precisely this is a drawback in our calculations from now on. Moreover, since there are no limitations, the choice between one behavior or another is more complicated.

We may think that a function describing the behavior of the swimmer's tail will be optimal if it is able to optimize some interesting quantity of the organism: the energy to develop economical swimming or the thrust force if it intends to reach high speeds, for example. At first, the animal's energy will be an excellent quantity to optimize (minimize) to observe what should be the temporal evolution of the angle α. The energy expended by the animal to go from point A to point B may be written as:

$$E = \int_0^{t_{AB}} P(t)dt,$$

where t_{AB} is the time took by the swimmer to get from A to B and $P(t)$ is the power supplied, which for the sake of simplicity, we assume is simply the mechanical power.

Focusing only on this quantity, we calculate it utilizing the following expression:

$$P(t) \sim F_y(t)\alpha'(t),$$

with F_y the force applied by the swimmer on the fluid in its normal direction and α' the angular velocity of the tail.

Following Theodorsen's formalism [100] and using the notation we used in chapter 3 we write the normal force as:

$$F_y = K_{\alpha''}\alpha'' + K_{\alpha'}\alpha' + K_\alpha\alpha.$$

Thus, the expression of the energy is written as follows:

$$E \sim \int_0^{t_{AB}} \left(K_{\alpha''}\alpha'' + K_{\alpha'}\alpha' + K_\alpha\alpha\right)\alpha'dt.$$

We realize that this quantity and the COT are defined up to a constant, which is the distance d. To treat the problem simply, we may define it as a constant quantity or one that depends on the length of the animal L but which does not change our optimization problem at all. A final

hypothesis that is fundamental to solving the problem is to assume, without loss of generality actually, that the time taken to travel a distance d that we are taking is an integer multiple of the period of oscillation of the tail.

$$t_{AB} = m\tau,$$

with m a positive integer. Therefore the functions α, α' and α'' are periodic functions with period τ.

The problem is then the optimization of the functional

$$I = \int_0^\tau \left(K_{\alpha''}\alpha'' + K_{\alpha'}\alpha' + K_\alpha\alpha \right) \alpha' dt,$$

where, by hypothesis, the functions are periodic. With this fundamental fact, this functional can be drastically simplified. Let $\alpha(t)$ be a periodic function that can be developed in Fourier series:

$$\alpha(t) = \sum_{n=-\infty}^{n=\infty} c_n e^{i\frac{2\pi}{\tau}nt},$$

being c_n the Fourier coefficients and i the imaginary unit.

Its derivatives are easily identifiable from this expression:

$$\alpha'(t) = \sum_{n=-\infty}^{n=\infty} \left(i\frac{2\pi}{\tau}n \right) c_n e^{i\frac{2\pi}{\tau}nt}, \qquad \alpha''(t) = \sum_{n=-\infty}^{n=\infty} \left(i\frac{2\pi}{\tau}n \right)^2 c_n e^{i\frac{2\pi}{\tau}nt}.$$

Multiplying a function by its derivative, $\alpha \cdot \alpha'$ for example, we have:

$$\alpha\alpha' = \frac{2i\pi}{\tau}e^{\frac{2i\pi}{\tau}t} \sum_{n=1} c_n c_{1-n} + \frac{2i\pi}{\tau}e^{\frac{4i\pi}{\tau}t} \left(c_1^2 + 2\sum_{n=2} c_n c_{2-n} \right) + \cdots + \text{c.c.}.$$

In short, infinitely many terms multiplied by $e^{\pm 2i\pi nt/\tau}$, all terms that integrated over a period yield zero. Thanks to this calculation, the functional can therefore be written simpler getting rid of the terms $\alpha\alpha'$ and $\alpha''\alpha'$:

$$I = \int_0^\tau \alpha'^2 dt.$$

However, finding the minimum of this functional inevitably leads to finding the trivial solution if we require periodicity to the function, as we have assumed, in addition to continuity and differentiability. It is then necessary to solve the Euler-Lagrange equation with certain constraints, which we introduce employing the formalism of the Lagrange multipliers [209]. Since what we want is to find a function that is not zero over the entire interval and that can take a fixed amplitude, the constraint we impose is that the average angular displacement squared is equal to a constant:

$$\frac{1}{\tau} \int_0^\tau \alpha(t)^2 dt = \frac{\alpha_{\text{typ}}^2}{2}, \tag{4.2.11}$$

with α_{typ} a typical amplitude of the motion.

Thus, the functional that we will finally optimize is given by the following expression:

$$I[\alpha] = \int_0^\tau F\left(\alpha(t), \alpha'(t)\right) dt = \int_0^\tau \left(\alpha'^2 + \lambda\alpha^2 \right) dt. \tag{4.2.12}$$

with λ a Lagrange multiplier.

The candidate to extremize this functional has to fulfill that the first variation of the functional I is zero, which implies that the integrand must satisfy the Euler-Lagrange equation [209]:

$$\frac{\partial F}{\partial \alpha} - \frac{d}{dt}\frac{\partial F}{\partial \alpha'} = 0.$$

Which for our system is simply:
$$\alpha''(t) - \lambda\alpha(t) = 0.$$

Equation that only offers periodic solutions if $\lambda < 0$. We write then:

$$\alpha(t) = A\sin(\sqrt{|\lambda|}t + \varphi),$$

with A and φ integration constants.

Surprisingly, the function that extremizes the energy expended by the motion of the swimmer subjected to the above constraint is a sinusoidal function, with period $\tau = 2\pi/\sqrt{|\lambda|}$ and where the integration constants can be chosen appropriately as a function of the initial conditions.

It remains to check whether the function we have found indeed corresponds to an energy minimum or not. Then, proceeding analogously to the calculation of extrema in analysis of one real variable, we have to find the second variation of the functional and study its sign. Without going into details, the second variation, δI^2, of a functional of this type is written as [209]:

$$\delta^2 I = \int_0^\tau \left(Ph'^2 + Qh^2\right) dt,$$

with h a test function and P and Q defined as:

$$P(t) = \frac{1}{2}\frac{\partial^2 F}{\partial \alpha'^2}, \qquad Q(t) = \frac{1}{2}\left(\frac{\partial^2 F}{\partial \alpha^2} - \frac{d}{dt}\frac{\partial^2 F}{\partial \alpha \partial \alpha'}\right).$$

A necessary condition for the functional to have a minimum is that the second variation must be strictly positive, which can be achieved by requiring only that the P term is purely positive, known as Legendre's condition [209]. This condition is satisfied in our system for every instant of time since:

$$P(t) = 1.$$

Another necessary condition is that the interval of definition $t \in (0,\tau)$ has no points conjugate to 0. A point $\bar{t}$ is conjugate to the point $t = 0$ if the equation

$$-\frac{d}{dt}\left[P(t)h'(t)\right] + Q(t)h(t) = 0,$$

with boundary conditions $h(0) = h(\tau) = 0$ has a solution that vanishes at $t = 0$ and at $t = \bar{t}$ but is not identically null [209]. The above equation reads:

$$h''(t) + |\lambda|h(t) = 0,$$

and unfortunately, vanishes at a point $t \in (0,\tau)$, namely at $\tau/2$.

Both conditions are necessary independently, but the set of those two is the sufficient condition that has to be satisfied to ensure the presence of an extremum. Given these results, we could not conclude directly that the sinusoidal function is really a minimum of the functional 4.2.12. However, the existence or not of conjugate points depends on the upper bound of the integral in equation 4.2.12. If it is less than or equal to $\tau/2$, we can say that the solution of the harmonic oscillator is genuinely a local minimum.

Rewriting the functional with the full expression of the power:

$$J[\alpha] = \int_0^{\tau/2} \left(\frac{K_{\alpha''}}{K_{\alpha'}}\alpha''\alpha' + \alpha'^2 + \frac{K_\alpha}{K_{\alpha'}}\alpha\alpha' + \lambda\alpha^2\right) dt,$$

we calculate its Euler-Lagrange equation, which turns out to be the same as for the previous case:

$$\alpha'' - \lambda\alpha = 0$$

And calculate its second variation, which reads:

$$\delta^2 J = \int_0^{\tau/2} \left(h'^2 + |\lambda| h^2 \right) dt.$$

Then for this functional, we can confirm that both the necessary and sufficient condition ensure that the harmonic solution is a minimum of the energy. Although "formally" it is required to change the upper limit of integration to ensure convergence to the local minimum, it is not a situation that sets any problems at physical level. The function that we obtain is the same, and given the properties of the basic trigonometric functions, changing τ by $\tau/2$ in the integral only makes vary our functional a term 2, since the products of functions that we have there are periodic with period $\tau/2$.

In our simple and straightforward formalism, the energy put into play by the organism is minimized by a sinusoidal function, which results in agreement with continuous swimming used by large animals where they regulate their motion by modulating the amplitude and frequency [39, 210]. However, as we mentioned in the introduction, some animals prefer to choose a burst-and-coast strategy to reduce their COT [201], dynamics that we do not find using this optimization. In order not to complicate the expression of the energy to be minimized but to introduce changes in the solution of the Euler-Lagrange equation, we can look at possible constraints to be fulfilled by the angle α. In this way, we will act on the presumed shape desired by a swimmer in general by focusing on its tail angle. Analogously to the definition in probability theory of the characteristics of a probability distribution, we can use the same concepts to define what we want to achieve for our tail position.

In addition to the parameters measuring location, such as the mean, or scale, such as the variance, the higher-order moments give information about the shape of the distribution. The moments of order 3 and 4 are called skewness and kurtosis and provide us information about the form of the function. The skewness is a measure of the asymmetry of the probability distribution; positive skewness values indicate that the right tail of the distribution is longer and the most probable values are concentrated on the left of the distribution, just the opposite for negative skewness, as can be seen in figure 4.13a. On the other hand, kurtosis, although it encounters more complications in its fundamental definition [211], can be understood as the concentration or not of values around the peak and tails of the distribution. A high kurtosis implies values near the peak and tails, while a reduced kurtosis maintains concentrated values at all points of the distribution, including the shoulders, figure 4.13b.
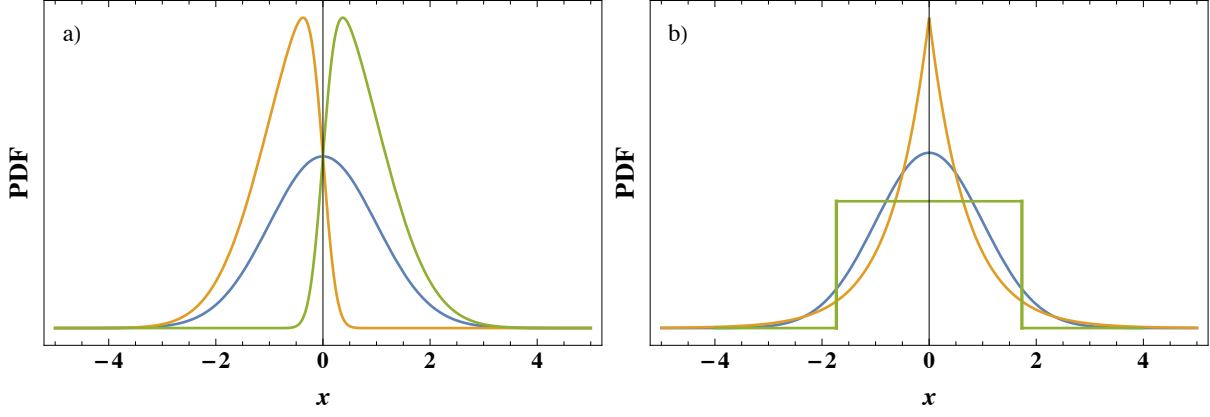
Figure 4.13: Continuous Probability Distribution Functions (PDF) as a function of the random variable x. a) Graphical representation of skewness. The blue line corresponds to zero skewness, while orange and green represent negative and positive skewness, respectively. b) Graphical representation of kurtosis. In blue, a Gaussian PDF with kurtosis equals 3, while orange and green PDFs correspond to kurtosis larger than and smaller than 3, respectively.

So, we add a constraint for each of the different definitions of a probability distribution: mean, variance, skewness, and kurtosis, and require that α satisfies the values we deem convenient. The constraints, in this case, would be:

$$\frac{1}{\tau}\int_0^\tau \alpha(t)dt = \bar{\alpha}, \qquad \frac{1}{\tau}\int_0^\tau \alpha(t)^2 dt = \frac{\alpha_{\text{typ}}^2}{2},$$
$$\frac{1}{\tau}\int_0^\tau \alpha(t)^3 dt = \alpha_{\text{sym}}^3, \qquad \frac{1}{\tau}\int_0^\tau \alpha(t)^4 dt = \alpha_{\text{kur}}^4,$$

with $\bar{\alpha}$, α_{typ}, α_{sym} and α_{kur} the values that we want to assign to these integrals. If we want to write a functional that agglutinates these four constraints, we must write:

$$K[\alpha] = \int_0^\tau \left(\alpha'^2 + \sum_{i=1}^4 \lambda_i \alpha^i \right) dt,$$

where λ_i are all the Lagrange multipliers.

In order to maintain the symmetry $\alpha \to -\alpha$ and for ease of solving the Euler-Lagrange equation, we cancel the coefficients λ_1 and λ_3 and write the equation that gives us the extrema of the above functional:

$$\alpha''(t) - \lambda_2 \alpha(t) - 2\lambda_4 \alpha(t)^3 = 0.$$

Introducing a characteristic time and angular amplitude, we rewrite this equation in dimensionless form as:

$$\alpha'' \pm \alpha \pm \alpha^3 = 0, \tag{4.2.13}$$

the equation of which is a nonlinear oscillator. To determine whether this equation has periodic solutions, it is convenient to rewrite it by making explicit the potential function, V, from which the forces are derived:

$$\alpha'' = -\frac{dV}{d\alpha},$$

with V defined as:

$$V = \pm\frac{1}{2}\alpha^2 \pm \frac{1}{4}\alpha^4,$$

and which we treat individually by defining the potentials that correspond to each of the four existing combinations:

$$V_{++} = \frac{1}{2}\alpha^2 + \frac{1}{4}\alpha^4, \qquad V_{+-} = \frac{1}{2}\alpha^2 - \frac{1}{4}\alpha^4,$$
$$V_{-+} = -\frac{1}{2}\alpha^2 + \frac{1}{4}\alpha^4, \qquad V_{--} = -\frac{1}{2}\alpha^2 - \frac{1}{4}\alpha^4.$$

A confinement of the trajectories is only possible in the cases where the potential is V_{++}, V_{+-} and V_{-+}. Potential V_{--} is shown in figure 4.14 and it corresponds to an entirely repulsive potential where periodic trajectories are not allowed. V_{++} reflects standard oscillatory dynamics while V_{+-} only allows trajectories confined around 0 with amplitudes that cannot exceed ± 1. The possible trajectories of V_{-+} are the most interesting in our study since a particle subjected to this potential could oscillate back and forth in such a way that it would stay an arbitrarily long time at the origin, which in this case turns out to be an unstable point, and roll back and forth on the parabola. This behavior of α can be likened to that of an organism performing intermittent swimming.
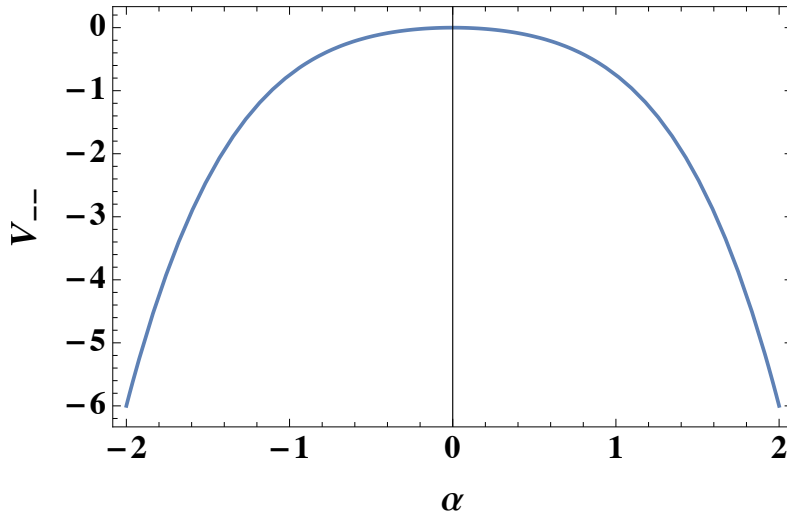
Figure 4.14: Plot of the potential $V_{--} = -1/2\alpha^2 - 1/4\alpha^4$, for which there are no periodic solutions.

The equation 4.2.13 admits analytical solutions [212] in terms of special functions known as Jacobi elliptic functions. The solution of this equation subjected to the initial conditions $\alpha(0) = A_0$ and $\alpha'(0) = 0$ is:

$$\begin{aligned}
\alpha(t) &= A_0 \, \text{cn}\left(t\sqrt{1 + A_0^2}, \frac{A_0^2}{2(1 + A_0^2)}\right), & & & V(\alpha) = V_{++} = \frac{1}{2}\alpha^2 + \frac{1}{4}\alpha^4, \\
\alpha(t) &= A_0 \, \text{cn}\left(t\sqrt{1 - A_0^2}, \frac{-A_0^2}{2(1 - A_0^2)}\right), & \text{if} & & V(\alpha) = V_{+-} = \frac{1}{2}\alpha^2 - \frac{1}{4}\alpha^4, & (4.2.14)\\
\alpha(t) &= A_0 \, \text{cn}\left(t\sqrt{-1 + A_0^2}, \frac{A_0^2}{2(-1 + A_0^2)}\right), & & & V(\alpha) = V_{-+} = -\frac{1}{2}\alpha^2 + \frac{1}{4}\alpha^4,
\end{aligned}$$

where cn is the Jacobi elliptic function cn [117]. The period of the function $\text{cn}(\omega t, k)$ is defined through the following expression:

$$\tau = 4\frac{K(k)}{\omega} = \frac{1}{\omega}F\left(\frac{\pi}{2}, k\right) = \frac{1}{\omega}\int_0^{\frac{\pi}{2}} \frac{d\theta}{\sqrt{1 - k^2 \sin^2\theta}},$$

where K represents the Legendre's complete elliptic integral of the first kind and F the Legendre's incomplete elliptic integral of the first kind [117]. These functions respond differently depending on the potential we use, as can be seen in the figures 4.15, 4.17, 4.18 and 4.19.
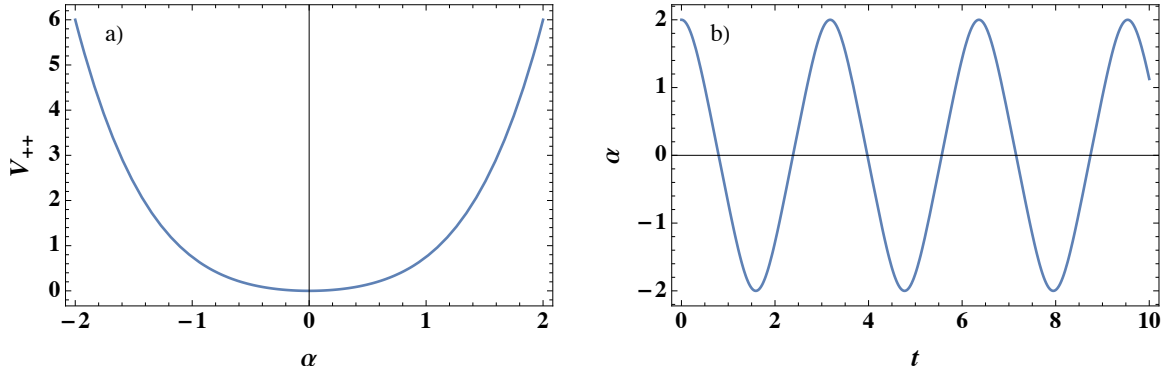
Figure 4.15: a) Plot of the potential $V_{++} = \frac{1}{2}\alpha^2 + \frac{1}{4}\alpha^4$. b) Angular evolution for a potential V_{++} with initial conditions $\alpha(0) = 2$ and $\alpha'(0) = 0$.

A potential of the type $V_{++} = \frac{1}{2}\alpha^2 + \frac{1}{4}\alpha^4$ automatically correlates the period of the oscillations with the amplitude of the oscillations because of adding the nonlinear cubic term to the oscillator equation. In 4.15a we show the plot of this potential V_{++} and in 4.15b the corresponding solution 4.2.14 for this potential with initial condition $\alpha(0) = 2$. Figure 4.16 shows how the oscillation period τ varies as a function of the initial condition.
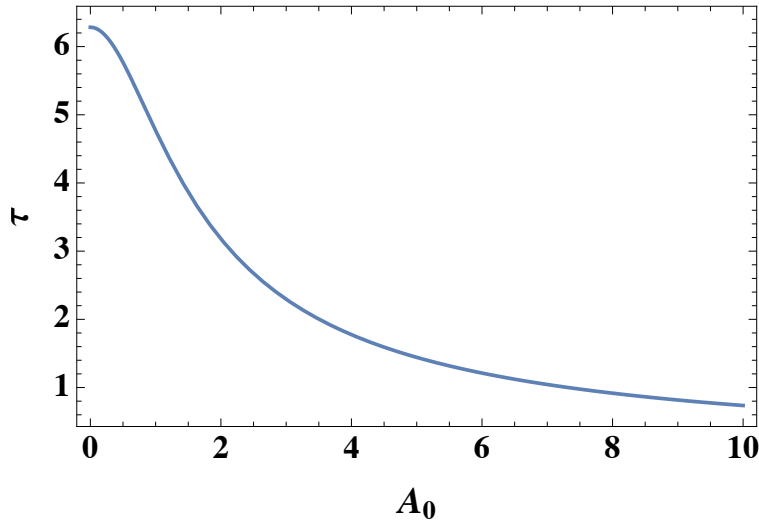
Figure 4.16: Effect of the cuartic potential V_{++}, the period of oscillation, τ, decreases as a function of initial amplitude, A_0.

The potential $V_{+-} = \frac{1}{2}\alpha^2 - \frac{1}{4}\alpha^4$ is very interesting if the initial condition is chosen near one of the two maxima of the graph 4.17a. In this case (figure 4.17b) the tail spends a long time in a neighborhood of this point until it loses stability and moves very quickly to the other maximum.
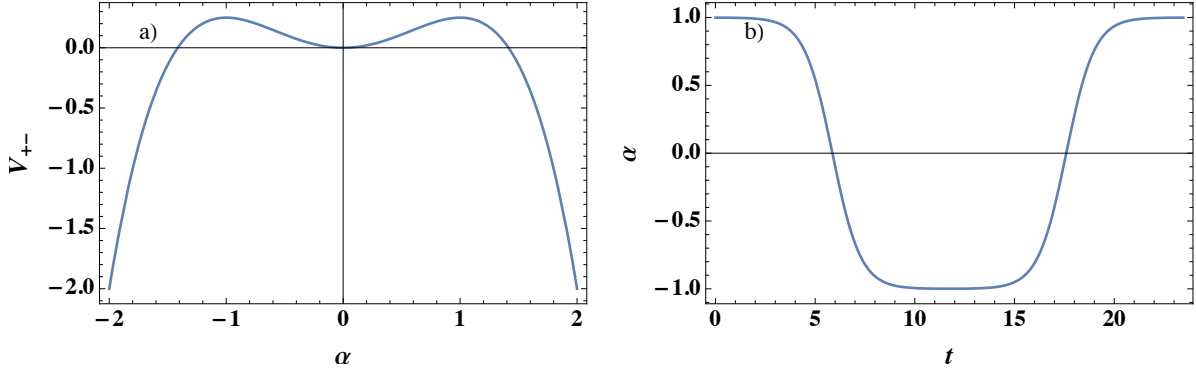
Figure 4.17: a) Plot of the potential $V_{+-} = \frac{1}{2}\alpha^2 - \frac{1}{4}\alpha^4$. b) Angular evolution for the potential V_{+-} with initial conditions $\alpha(0) = 0.999$ and $\alpha'(0) = 0$.
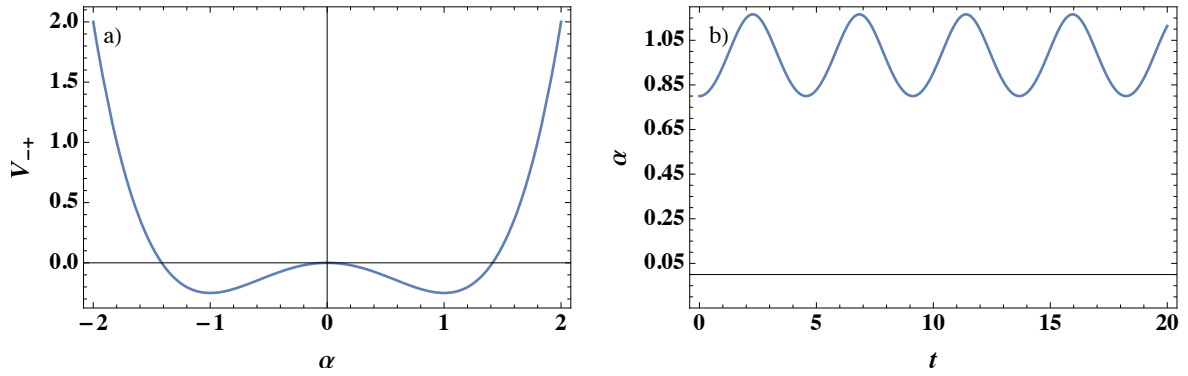
Figure 4.18: a) Plot of the potential $V_{-+} = -\frac{1}{2}\alpha^2 + \frac{1}{4}\alpha^4$. b) Angular evolution for the potential V_{-+} with initial conditions $\alpha(0) = 0.85$ and $\alpha'(0) = 0$.
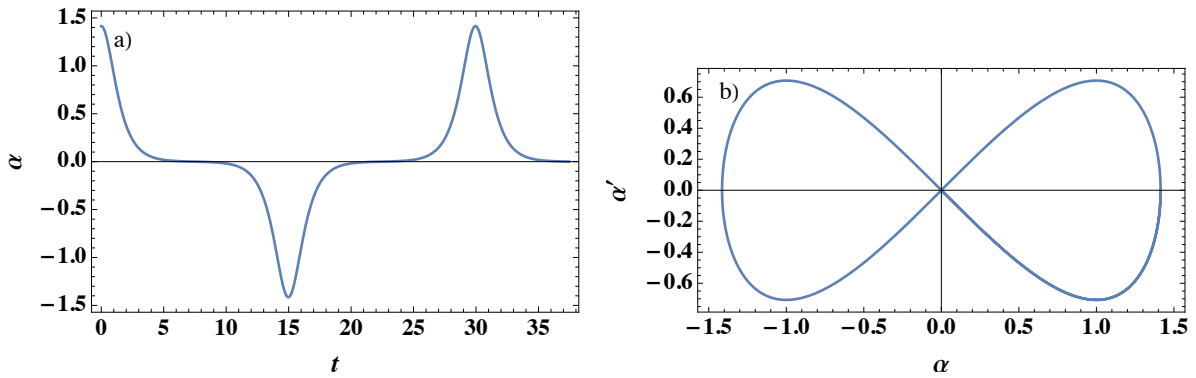
Figure 4.19: Angular evolution for the potential V_{-+} with initial conditions $\alpha(0) = \sqrt{2.00001}$ and $\alpha'(0) = 0$. b) Phase space with same initial conditions.

However, the most interesting case is the one given by the potential $V_{-+} = -\frac{1}{2}\alpha^2 + \frac{1}{4}\alpha^4$, depicted in figure 4.18a. In a first case, oscillations centered around $\alpha = \pm 1$ (figure 4.18b) are

possible if the initial value of α is confined in $(0, \pm\sqrt{2})$. In the limit $A_0 \to 0$ from the right or $A_0 \to \sqrt{2}$ from the left (or equivalently $A_0 \to 0$ from the left or $A_0 \to -\sqrt{2}$ from the right if we consider the oscillation around the other equilibrium point) a homoclinic orbit appears. A homoclinic orbit is a trajectory that starts and ends at the same saddle point and which approach this point as $t \to \infty$ [213]. For values of A_0 larger than $|\sqrt{2}|$ the oscillations occur around the origin passing from one branch to another of the potential. For initial conditions very close to the points where the graph cuts the abscissa axis, $\alpha = \pm\sqrt{2}$, but always greater in absolute value than these numbers, the behavior of the angle performs something that we could resemble intermittent swimming (figure 4.19). α oscillates from one branch to another of the potential, but as it approaches the origin, its velocity decreases, causing the tail to remain with values very close to 0 for a time $\tau^\star$, which is greater the closer the initial value A_0 approaches $|\sqrt{2}|$ for higher values.

Once all the solutions of the Euler-Lagrange equation have been characterized, it remains to verify that the solutions correspond well to the minima of the functional. The Legendre condition is assured without any problem, but it is necessary to confirm if there are conjugate points in the interval $(0, \tau)$, which is known by solving the equation:

$$-\frac{d}{dt}\left[P(t)h'(t)\right] + Q(t)h(t) = 0,$$

with $P(t) = 1$ and $Q(t) = \lambda_1 + 2\lambda_2\alpha(t)^2$.

The equation, in this case, cannot be solved by usual methods. A detailed numerical study must be performed to determine under which conditions the solutions found above constitute true local minima of the functional.

Likewise, as we proceeded with energy as the quantity to optimize, we could have changed the situation and chosen the thrust force to maximize the average speed. So, if the functional chosen is:

$$I_T = \int_0^\tau F_T(\alpha'', \alpha', \alpha)dt = \int_0^\tau \left(-\alpha\alpha'' + \lambda_T\alpha^2\right)dt,$$

where the first term of the integral corresponds to the thrust force of our toy model and the second to the bound given by equation 4.2.11, with λ_T the Lagrange multiplier. We find that the function that extremizes this functional is:

$$\alpha''(t) - \lambda_T\alpha(t) = 0$$

Again, for $\lambda_T < 0$, the solution of this equation are sinusoids, just as in the previous case. To verify the maximum condition, we write its second variation:

$$\delta^2 I_T = \int_0^\tau \left(Ph'^2 + Qh^2\right)dt,$$

with

$$P(t) = \frac{1}{2}\left(\frac{\partial^2 F_T}{\partial\alpha'^2} - \frac{d}{dt}\frac{\partial^2 F_T}{\partial\alpha'\partial\alpha''} - 2\frac{\partial^2 F_T}{\partial\alpha\partial\alpha''}\right),$$

$$Q(t) = \frac{1}{2}\left(\frac{\partial^2 F_T}{\partial\alpha^2} - \frac{d}{dt}\frac{\partial^2 F_T}{\partial\alpha\partial\alpha'} + \frac{d^2}{dt^2}\frac{\partial^2 F_T}{\partial\alpha\partial\alpha''}\right).$$

The terms accompanying h'' have been omitted as they are all null.

The polynomial $P(t)$ in this case reads:

$$P(t) = -\frac{\partial^2 F_T}{\partial\alpha\partial\alpha''} = 1.$$

And does not meet Legendre's condition for a maximum, but rather the opposite. We can actually compare the average thrust force for two different periodic functions and show that

the thrust associated with a sinusoidal function will be smaller. For example, let us take two different periodic functions with the same period:

$$\alpha_1 = A_1 \ \text{sn}\,(t,k)\,,$$
$$\alpha_2 = A_2 \ \sin\left(\frac{2\pi}{\tau}t\right),$$

where sn is the Jacobi elliptic function sn [117] and τ is the period defined by:

$$\tau = 4K(k).$$

In order to compare the resulting thrusts, both functions have to accomplish the condition $\langle \alpha^2 \rangle = \alpha_{\text{typ}}^2/2$ forcing the amplitudes A_1 and A_2 to be:

$$A_1 = \frac{\alpha_{\text{typ}}}{\sqrt{\frac{2}{k} - \frac{2E(k)}{kK(k)}}},$$
$$A_2 = \alpha_{\text{typ}},$$

with $E(k)$ the Legendre's complete elliptic integral of the second kind [117]. Then, we calculate the average thrust corresponding to each function:

$$\langle T_1 \rangle = -\int_0^\tau \alpha_1 \alpha_1'' dt = -\frac{\alpha_{\text{typ}}^2 \left(E(k)(1+k) + K(k)(k-1)\right)}{6\left(E(k) - K(k)\right)},$$
$$\langle T_2 \rangle = -\int_0^\tau \alpha_2 \alpha_2'' dt = \frac{\pi^2 \alpha_{\text{typ}}^2}{8K(k)^2}.$$

The ratio of both integrals $\langle T_1 \rangle / \langle T_2 \rangle$ is represented in figure 4.20 as a function of the parameter k. We observe that the average thrust $\langle T_1 \rangle$ is always bigger than $\langle T_2 \rangle$ except when $k = 0$, in which both functions are identical.
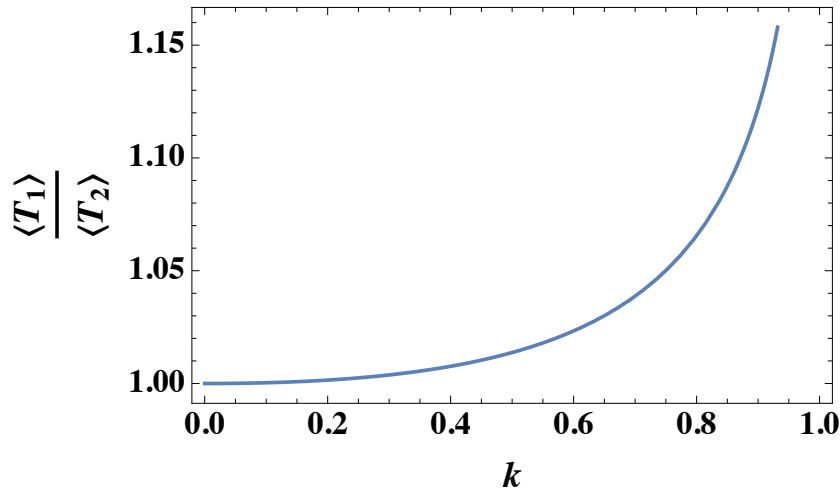
Figure 4.20: Ratio of the averages thrust $\langle T_1 \rangle$ and $\langle T_2 \rangle$ as a function of the parameter k. The average thrust force of the sn function is always bigger than the thrust given by a sinusoidal function except for $k = 0$.

Therefore, this approach cannot find true maxima of the thrust force, which may be motivated by our oversimplification of the fluid-structure interaction or by a lack of more influential constraints of the system.

4.3   Teaching a fish how to swim

This section is part of a collaboration with Li Fu, currently postdoctoral researcher in our group, who has performed the Reinforcement Learning simulations within the framework of a joint project on underwater robotic swimmers.

The theoretical models we have discussed so far are helpful because they allow us to approximate complex situations and understand the influence of the different parameters at play in swimmers' behavior. However, the price to pay is a loss of interesting information necessary to understand the swimming mechanisms. Moreover, the situations we have dealt with are certainly ideal: we have only optimized two quantities in very differentiated frameworks, which is not at all the case for a real animal, which is constantly subjected to external perturbations and by which it must change its dynamics accordingly. Our natural next step is to elaborate a procedure for the swimmer to learn to swim with given constraints, such as avoiding obstacles, performing emergency sequences to move to the water interface, moving efficiently, achieving the best acceleration, or many others. This task is only possible to develop by immersing ourselves in Machine Learning. Machine Learning is a set of techniques that allows the extraction and detection of patterns and the processing of information from a collection of data to learn and make predictions. These algorithms can be classified according to the knowledge and human intervention on this data, as depicted in figure 4.21 [214].
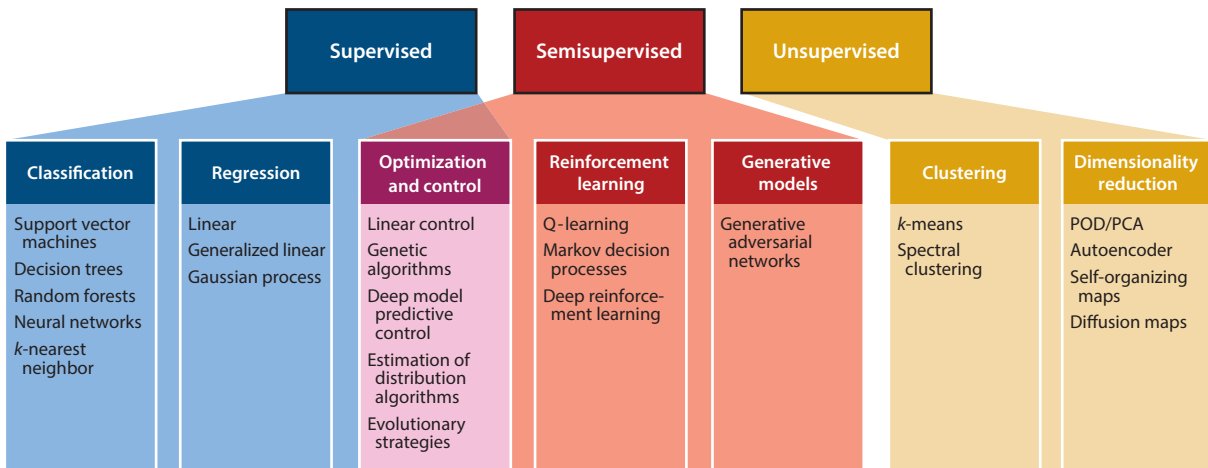
Figure 4.21: Classification of Machine Learning algorithms. From Brunton et al. [214].

Among these algorithms, a particularly exciting approach is Reinforcement Learning (RL). Reinforcement learning is a field of Machine Learning that focuses on how agents perform actions in an environment to maximize some notion of cumulative reward [215]. This framework has become a very practical perspective for dealing with problems in fluid mechanics in general and in bio-inspired locomotion in particular, for example soaring [216], behavior of individual fish or groups of fish [217–220] or the optimization of the movement of microswimmers [221], among others. In this framework, an agent is an individual that lives in an environment with which it interacts and takes an action at each time step. The configuration of an agent at a given time is called state and may change depending on the agent's action. At each time interval, the agent gathers its state from the environment, as well as the reward after having undertaken previously an action. In simple words, the reward basically measures how good or bad it is for the agent to be at a particular state after a given action. The agent's objective is to maximize its return which is the cumulative reward over all the time steps. The concept of reward is of paramount importance, and it is, in fact, what will determine the success of the agent's learning process. The agent's behavior in the environment is defined by a policy $\pi(a|s)$, which gives the

probability to take action a as the agent is in state s. In these algorithms, it is assumed that the agent and its action can be modeled trough a Markov Process [215], and therefore the dynamics of the agent only depends on its state at the previous time interval.

Actually, the two main approaches to train RL agent's policy are the policy optimization [222, 223] and the Q-learning [224]. While the first family of methods work directly on the policy $\pi(a|s)$, the second family of algorithms focuses on the learning action-value function approximation $Q(s,a)$. This function estimates the return of the agent taking an action a being in state s.

Q-Learning is a reinforcement learning algorithm that does not need a model to operate (the agent does not know the dynamics of the environment) and accomplish different tasks. It is based on the "Q-table", tabular representation of the action-value function, that is refreshed as the agent interacts with the environment [225, 226]. The objective of Q-Learning is to optimize the action-values function $Q(s,a)$: it measures the overall expected reward assuming the agent is in state s and performs action a, and then the algorithm follows a greedy policy, which is the strategy trying to maximize the received reward. The update process is:

$$Q\left(s_i, a_i\right) \leftarrow Q\left(s_i, a_i\right) + \alpha_{lr} \left(R(s_i, a_i) + \gamma \max_{a'} Q\left(s_{i+1}, a'\right) - Q\left(s_i, a_i\right) \right), \tag{4.3.1}$$

where $s_i = s(i)$ and $a_i = a(i)$ are the state and action at i-th instant, α_{lr} is the learning rate (a measure of how much of the old value is retained), the function R gives the immediate reward received after the action a_i has been effectuated and $\gamma \in [0,1]$ is the discount factor which determines how valuable is a reward in a future step. Q-Learning uses a greedy policy to estimate the optimal action-value at $i+1$ instant, giving an expression of $\max_{a'} Q\left(S_{i+1}, a'\right)$, with a' the accessible actions in state S_{i+1}. Practically, the learning process can be realized with the following steps. First, we initialize an arbitrary Q-table, covering the whole state space and action space. Then, for each time-step, the agent chooses an action for the current state according to its behavior policy, which usually is an ϵ-greedy policy. At each state, the agent chooses either an action maximizing the reward with probability $1 - \epsilon$ or a random action in order to explore the environment with probability ϵ, with $\epsilon < 1$. It receives the reward $R(s_i, a_i)$ and the Q-table is updated according to equation 4.3.1. We then iterate the process for each time step for N episodes, and the total reward will be evaluated at the end of each episode. The difficulty of this algorithm is that, for an agent with a multitude of spaces and possible actions to take, the representation of this Q function is not simple, and a vast memory capacity is necessary to store all these data. The Q-Learning algorithms use these tables and are consequently restricted to low dimensional state and action space. In order to better represent the return function, neuronal networks can be used, but the Q-learning has to be upgraded, and the resulting RL technique is called Deep Q-Learning (DQN) [224].

DQN, on the other hand, is a reinforcement learning algorithm based on the Q-learning approach with the use of neural networks to approximate the action-value function. A neural network is a set of artificial neurons which compute nonlinear calculations. The fundamental elements, the neurons, are units that receive specific signals and, through fundamental operations, produce an output [227]. Therefore, neural networks, being formed by a large set of these units, can perform calculations very efficiently and quickly to obtain the desired output from a given input. Furthermore, the use of neural networks allows generalizing different states and making efficient policy approximations so that the amount of memory needed to perform the processes is considerably reduced and it is heavily used in most complex problems.

4.3.1   Learning example I: the faster, the better

To begin to understand the learning process of a swimmer, we will consider simple situations that we have already been able to deal with analytically to compare the theoretical solution of the optimization problem with the solution given by the learning algorithms and understand

the processes that occur and then be able to complexify them. First of all, we are thinking of an organism whose objective is to cover a given distance d in the shortest possible time. In other words, to maximize the swimming speed. Then, we take as a reference the control in forces of the discrete case that we exposed at the beginning of the chapter:

$$\alpha''(t) = \Gamma \sum_{i=0} \epsilon_i \delta(t - i\Delta t),$$

with $\epsilon_i = +1, -1, 0$.

The possible actions of the agent in this case are $a = \{+\Gamma, -\Gamma, 0\}$ and its state is determined by the four variables $s = \{x, \alpha, x', \alpha'\}$. The projection of the state space onto the variables (x, α), as well as the reward/punishment dynamics is shown in figure 4.22. The swimmer, starting near the origin $(0,0)$ performs at each time step Δt an action a and at each of these steps receives a negative reward of -1. The process terminates when one of these three situations occurs:

1. The variable α takes a value greater than α_0, mimicking a biological limit. In that case, the process terminates, and the agent receives a largely negative reward P.

2. The number of time steps exceeds the maximum simulation or learning time, represented by the maximum number of steps N_t. The process ends without any feedback.

3. The fish reaches the desired point d with any given α value as long as it is within the desirable limits. In that case, the reward is positive because the swimmer has met the goal we intended.
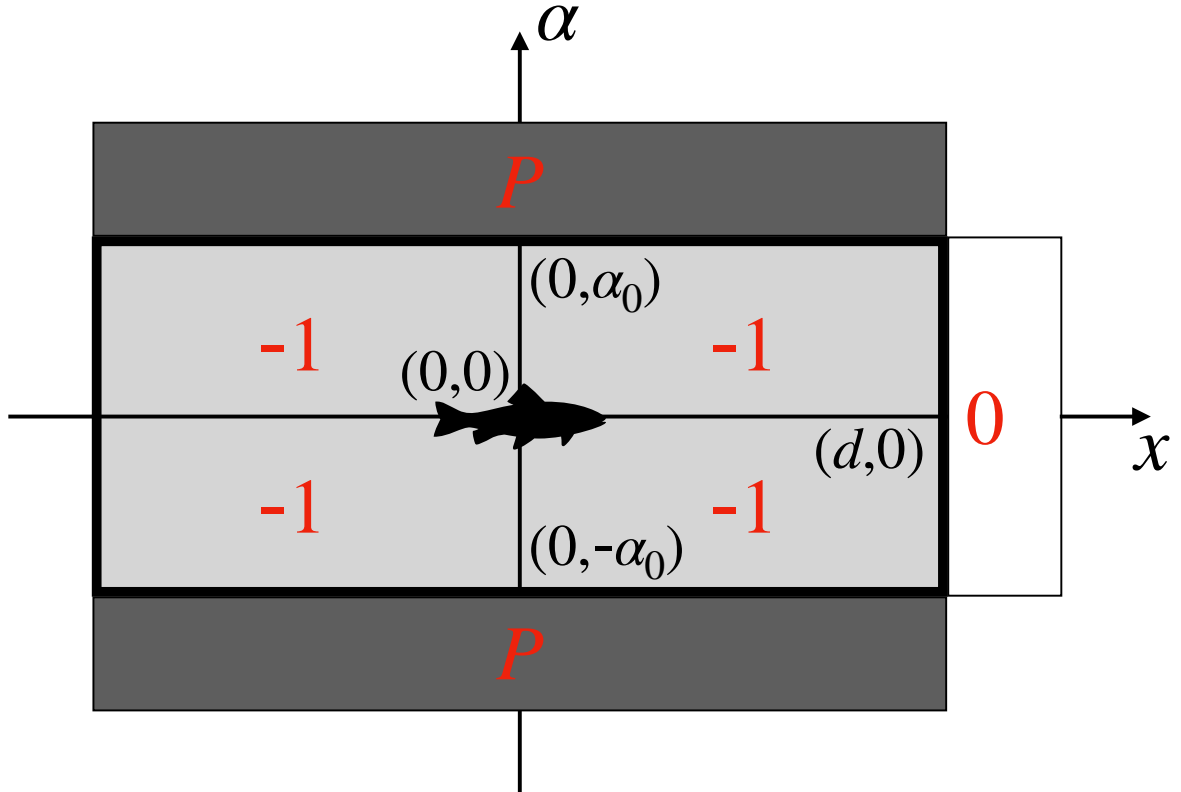
Figure 4.22: Illustration of the state space and the rewards.
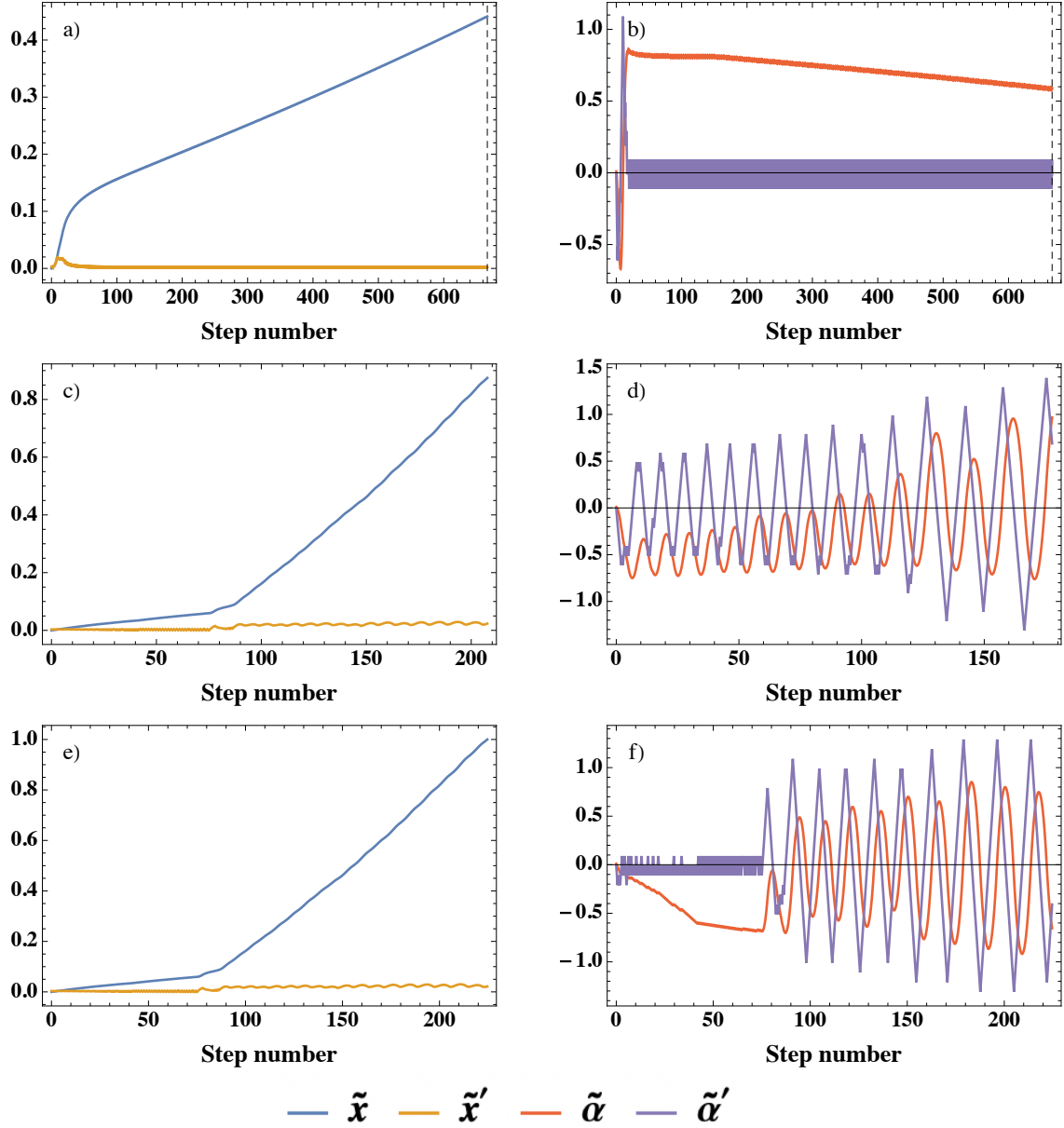
Figure 4.23: Learning results for reaching a maximum swimming velocity. We show the dimensionless position, $\tilde{x}$ (blue), velocity $\tilde{x}'$ (orange), angle $\tilde{\alpha}$ (red), and angular velocity $\tilde{\alpha}'$ (purple). a) and b) images correspond to the end of episode 1000, c) and d) for the episode 5000, and e) and f) the episode 10000.

Of course, the agent will look forward to accomplishing the situation in which the biggest reward is obtained. All the others are detrimental to him, and the learning process must be developed so that the bad scenarios are eliminated and only the one in which the fish travels the distance in the shortest possible time prevails. In addition, other requirements can be added, such as never exceeding a maximum angular velocity.

The optimization problem is expressed as:

$$mu'(t) = -C_{Th}\alpha(t)\alpha''(t) - C_D u(t)|u(t)|,$$

$$\alpha''(t) = \Gamma \sum_{i=0} \epsilon_i \delta(t - i\Delta t),$$

$$|\alpha| \leq \alpha_0.$$

To make the problem dimensionless, it is convenient to choose a characteristic length equal to the distance to travel $l_c = d$, in addition to renormalizing the angle α to α_0. In that case, the dimensionless problem reads:

$$M\tilde{u}'(\tilde{t}) = -\tilde{\alpha}(\tilde{t})\tilde{\alpha}''(\tilde{t}) - \widetilde{C_D}\tilde{u}(\tilde{t})|\tilde{u}(\tilde{t})|,$$
$$\tilde{\alpha}''(\tilde{t}) = \epsilon\delta(\tilde{t} - \widetilde{\Delta t}),$$
$$|\tilde{\alpha}| \leq 1.$$

Where $M = m/C_{Th}d$ and $\widetilde{C_D} = C_{Th}\alpha_0^2/C_D d^2$. This changes slightly the final expression of the average velocity that we obtained in the previous section in the equation 4.2.9, being necessary to add only a factor $\sqrt{\widetilde{C_D}}$ to homogenize with the definition that we have just given.

With the DQN algorithm defined above we solve this system to get the maximum speed. The values chosen for the simulation are:

$$M = 0.1, \qquad \widetilde{C_D} = 0.01, \qquad \widetilde{\Delta t} = 0.1, \qquad N_{\tilde{t}} = 2000/3.$$

As for the number of episodes, i.e., how many times we will simulate the situation in which a fish from the origin reaches or does not reach the target distance in the shortest possible time, we set a number of 10000 to ensure the convergence process to the target. We show three simulations corresponding to three different episodes in the figure 4.23, where we present the position $\tilde{x}$, the velocity, $\tilde{x}'$, the angle $\tilde{\alpha}$ and the angular velocity $\tilde{\alpha}'$, all dimensionless, for the episode 1000 (figure 4.23a and b), 5000 (figure 4.23c and d) and 10000 (figure 4.23e and f). In the episode 1000, we observe how the agent has not learned at all; in fact, the learning process ends because the maximum number of steps $N_{\tilde{t}}$ has been exceeded. Episode 5000 reflects, however, a noticeable improvement, a movement is observed that resembles the one predicted analytically. However, the angle α exceeds the value 1, causing the simulation to stop completely. In episode 10000, we can affirm that the system has learned because the simulation's last three periods are uniform and reflect an oscillatory and almost periodical trend. The period measured averaging the last three oscillations is, in steps number, 17.3, so we calculate the period in dimensionless units using $\tilde{\tau} = 17.3\widetilde{\Delta t} = 1.73$. Thus, the average theoretical swimming speed is:

$$\tilde{U}_{\text{th}} = \frac{\sqrt{\widetilde{C_D}}}{4\sqrt{3}}\tilde{\tau} = 0.0250.$$

We calculate the same magnitude from the simulations averaging the last 3 periods of the figure 4.24a. The value obtained by this procedure is $\tilde{U}_{\text{num}} = 0.0247$, being about 1% the difference between both values, showing the potential of the theoretical calculation as well as of the learning process. The action is also shown in the figure 4.24b. At the end of the episode, we observe the alternating values of the action, between positive and negative values, of the same duration, as predicted by the optimization calculation.
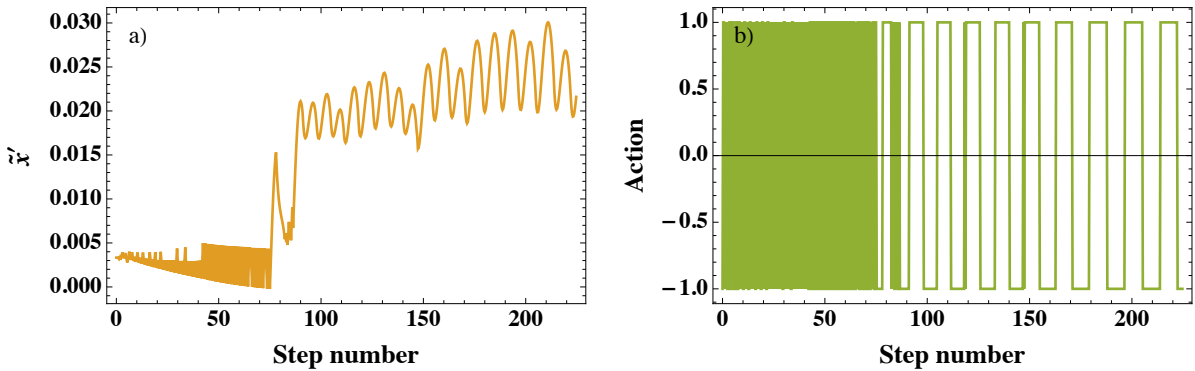
Figure 4.24:   a) Dimensionless velocity and b) action by the end of episode 10000.

4.3.2   Learning example II: maximum propulsion

Another test we have performed is the case where we control the angular amplitude of α. This device is our robot defined in Appendix A, fixed, and that can only move its tail, defined with the angle α. In this case, the control reads:

$$\alpha_c(t) = \alpha_{\max} \sum_{i=0} \epsilon_i \delta(t - i\Delta t).$$
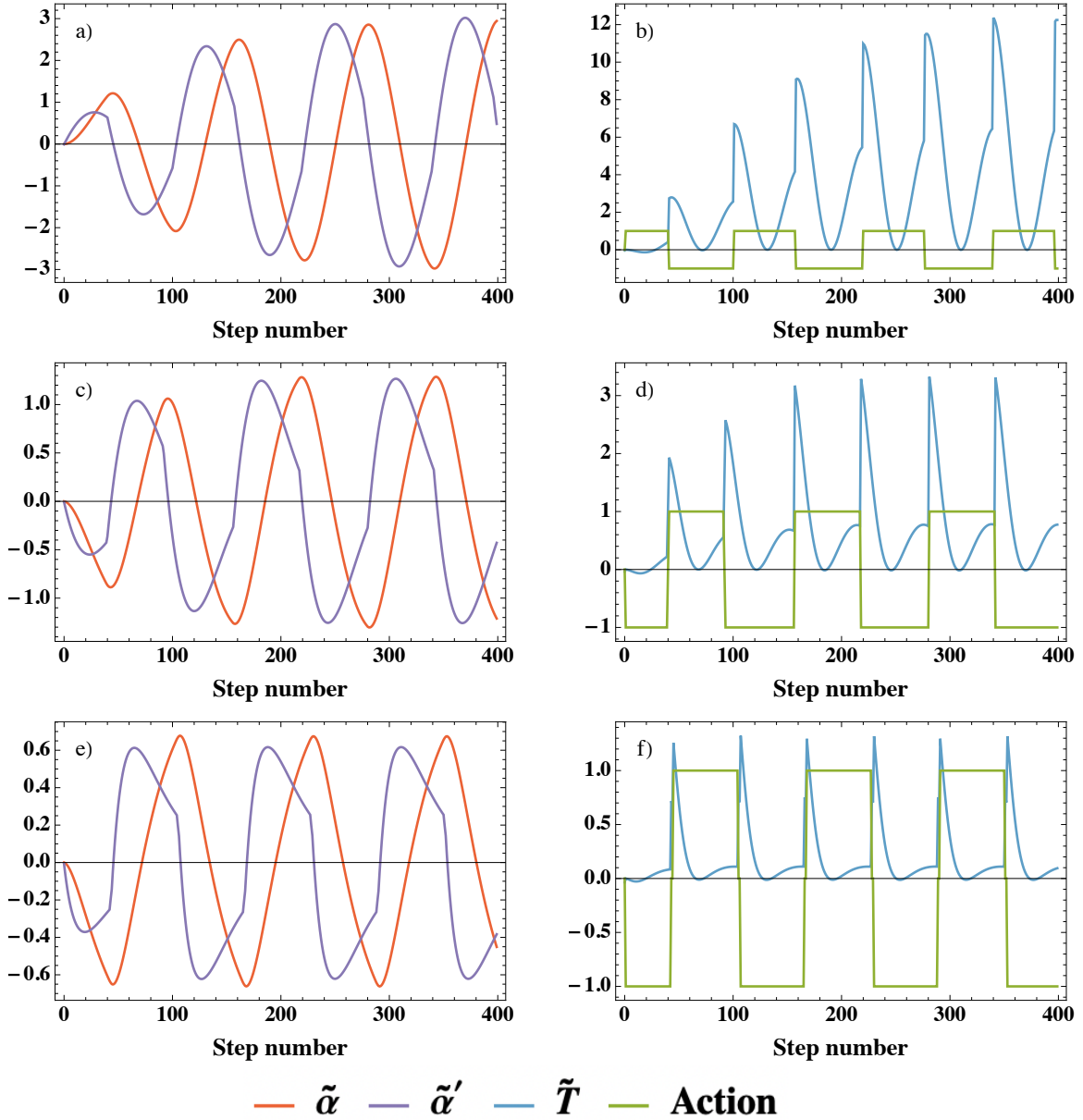
Figure 4.25: Learning results for achieving maximum thrust force. We show the dimensionless angle $\tilde{\alpha}$ (red), angular velocity $\tilde{\alpha}'$ (purple), mean thrust $\tilde{T}$ (turquoise) and action (green). a) and b) images correspond to $\xi = 0.2$, c) and d) to $\xi = 0.5$, and e) and f) to $\xi = 1.0$.

The actions are $a = \{+\alpha_{\max}, -\alpha_{\max}, 0\}$ and the state is defined by $s = \{\alpha, \alpha'\}$. Our objective now is to achieve the most suitable tail dynamics to obtain the highest possible propulsive force

on average. The problem in dimensionless form reads:

$$\tilde{\alpha}''(\tilde{t}) + 2\xi\tilde{\alpha}'(\tilde{t}) + \left(\tilde{\alpha}(\tilde{t}) - \tilde{\alpha}_c\right) = 0,$$
$$\tilde{\alpha}_c(\tilde{t}) = \sum_{i=0} \epsilon_i \delta(\tilde{t} - i\widetilde{\Delta t}),$$

with the dimensionless actions $\{+1, -1, 0\}$.

The best learning results are shown in figure 4.25, where the time step has been $\widetilde{\Delta t} = 0.05$. Each row of images corresponds to a different value of the parameter ξ: a and b to $\xi = 0.2$, c and d to $\xi = 0.5$; finally e and f to $\xi = 1.0$. The process has taken care not only to choose the time proportions of each action but also to choose the period that maximizes the thrust force $\langle \tilde{T} \rangle = -\langle \tilde{\alpha}\tilde{\alpha}'' \rangle$.

ξ	$\tilde{\tau}_{\text{learning}}$	$\tilde{\tau}_{\text{theory}}$	$\langle \tilde{T}_{\text{learning}} \rangle$	$\langle \tilde{T}_{\text{theory}} \rangle$
0.2	6.10	6.28	4.76	5.08
0.5	6.25	6.31	0.811	0.824
1.0	6.40	6.56	0.202	0.213

Table 4.1:   Comparison between theoretical results and the learning process outcomes.

The period and the average thrust force have been calculated by choosing the best parameters in the data from figures 4.11 and 4.12 and show an excellent agreement with the data found from the learning process, as observed in the table 4.1.

4.4   Conclusions

We have proposed a set of control measures of the undulatory gait with which, employing simple models, we have optimized the maximum swimming speed or the energy spent by the swimmer. The results of the simple models have been contrasted with learning simulations using the DQN algorithm within the Reinforcement Learning framework, showing how the numerical results agree very well with those obtained theoretically. This verification represents a starting point to formulate more complex and accurate physical models of swimming that learning techniques can solve.

Chapter 5

Perspectives and conclusions

In this manuscript, we have investigated the locomotion of underwater swimmers from different points of view: one purely mechanical where we have strived to compute the dynamics of a swimmer for already prescribed motions and another in which we have attempted to formulate a modest transition to a biological point of view, where we have characterized the swimmer's deformation (and its velocity) as a function of its interaction with the surrounding environment. In addition, we have theoretically considered a varied set of gaits in order to optimize the most significant variables of the locomotion problem and compare them with learning algorithms performed with Machine Learning techniques.

From the potential fluid theory, we have characterized the fluid-structure interaction for an airfoil-shaped rigid and two-dimensional body performing a kinematic motion of amplitude A and frequency f. Furthermore, we have shown that, by imposing a pressure drag-type resistance force and solving Newton's equations, we obtain a theoretical verification with a simple model of the scaling laws derived by Gazzola et al. [24]. The Strouhal number calculated by this model is strongly correlated to the drag coefficient, while the effect of the other parameters can be neglected at the first-order approximation. For values of the drag coefficient c_d between $0.01 - 0.1$, typically measured in biological swimmers, we find an almost constant Strouhal number, around $0.1 - 0.3$, which agrees perfectly with values of St found in nature. We also show that the Strouhal number of a free-swimming, airfoil-shaped, rigid body does not depend on the frequency, which differs from results found in other types of experiments where airfoils perform pitching and heaving motions [125, 139]. A detailed computation assuming a weak tail beat amplitude α_0 has allowed us to obtain analytical expressions for the swimming velocity and to relate it to the swimmer characteristics and the physical parameters of the fluid.

One way to avoid imposing any kinematic forcing is the proprioceptive hypothesis developed in this manuscript. By conjecturing that the deformation dynamics of the swimmer depends on the normal hydrodynamic force felt by it at each instant we have proposed a mechanism for bioinspired swimming locomotion. We have proved that proprioception is able to generate spontaneous tail oscillations in our experimental device: a biomimetic robot able to sense the forces of its environment. Moreover, these oscillations are univocally characterized by an amplitude and frequency that we do not impose but which depend only on the feedback between the swimmer and the environment. We have also introduced a generic model for describing swimming driven by proprioception, and we found that the feedback loop based on this mechanism results in an instability, provoking the locomotion. Our simple model allows the identification of the most important parameters, and, besides its simplicity, it is shown to have excellent predictive capabilities.

The adaptation of a swimmer to its environment has also led us to consider different situations where it must be able to change its gait to favor the achievement of an objective. We further showed the conditions necessary to maximize the swimming speed for different undulatory gaits; moreover, using the formalism of functional analysis, we have demonstrated how the

minimization of a swimmer's energy goes directly through the performance of sinusoidal swimming dynamics, dynamics that we have used extensively in our studies but that we have never attempted to justify. Finally, using learning algorithms, we have reproduced the dynamics we solved theoretically to show how the optimization results obtained agree perfectly with those we have already achieved analytically using standard techniques.

Throughout this work, new questions have arisen that we had not considered initially and that have been the germ of future projects:

1. So far, our study has focused on a single swimmer and its interactions with the environment. However, in nature, the vast majority of aquatic animals are gregarious and live in groups. There are complex social interactions hidden behind the swimmers' motions that lead to different organization levels that depend on each species needs and ways of living. Fish schools are archetypes of these kinds of cohesive social systems, and they have been discussed over now several decades [228, 229]. Benefits from swimming in groups are, apart from the inherent facts of socialization between individuals, a way to reduce risk from potential predators or to maximize food search [229, 230] and also a way to optimize hydrodynamic interactions for a global power saving of the school [228, 230, 231]. At first, we are content to understand the interaction within the smallest possible group, that is, between two robotic fish. Then, taking advantage of the qualities of our experimental platform and the ease with which we can produce and calibrate our robots (figure 5.1), our goal is to understand the hydrodynamic forces at play that occur when both fish move simultaneously with different sets of amplitude and frequency and how the distance between them can establish an appropriate regime for a locomotory advantage, as proposed in the literature [232, 233].
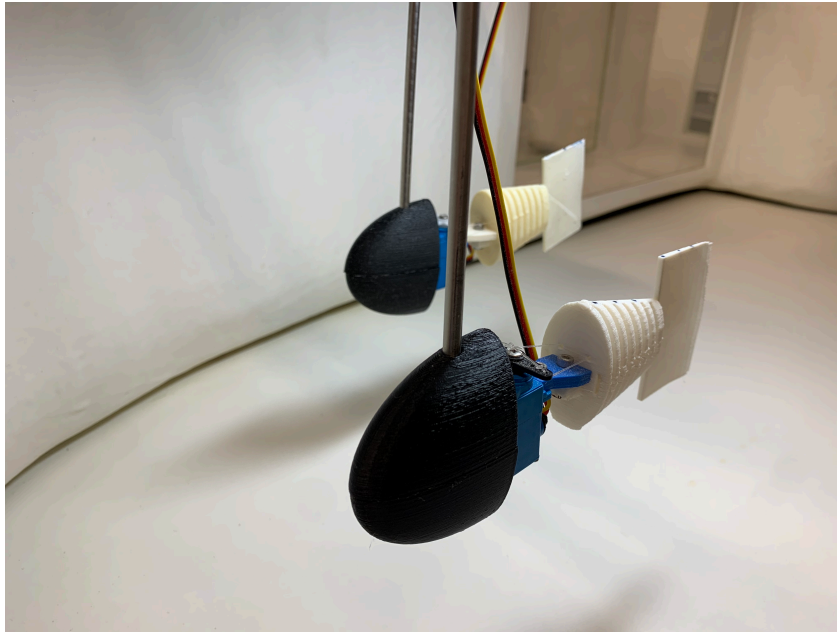
Figure 5.1:   Random configuration of two robotic fish. Both are equipped with normal and longitudinal force sensors.

2. Proprioception is becoming a hot topic due to the widespread use of bioinspired robotics equipped with multiple sensors to better understand the mechanics and control of animal movement [234–236]. Undoubtedly our work on this subject constitutes a starting point to improve this model and make it more realistic, for example, by not considering the tail angle that we have already exposed and considering an accurate measure of the robot

deformation, which we can obtain employing deformation sensors such as the one shown in figure 5.2. In analogy with the previous section, proprioception in two robotic swimmers must be tested. In a first attempt, one of the fish can perform a sinusoidal motion with given amplitude and frequency and act on the other fish in proprioception to observe how its fundamental characteristics change compared to when there was no partner around.
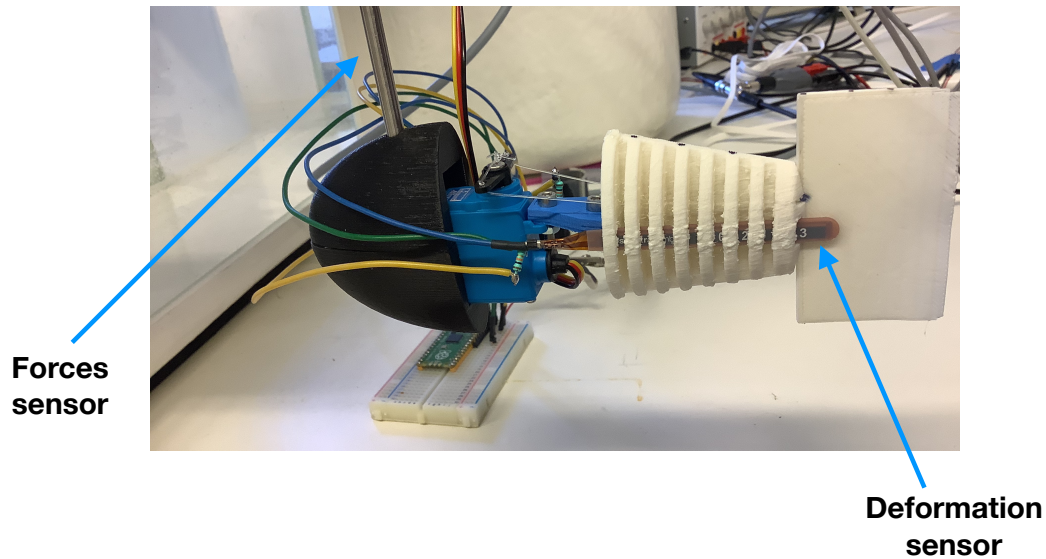
Figure 5.2: First tests with our robotic swimmer once the deformation sensor is in place. The way the sensor is placed on the fish is essential to prevent the sensor from being damaged or preventing the tail from working correctly. In this case, we have chosen to insert it inside the structure to adapt the movement of the sensor to that of the robot.

3. It is indisputable that the robotic fish learning algorithms constitute one of the biggest challenges so far. At this moment, the robot is not yet autonomous because it is still attached to a fixed force sensor and is not equipped with any devices sensing its environment further than normal and longitudinal forces. We plan to equip this robot with a set of sensors to measure distance, pressure, acceleration, inclination, compass, or deformation, as shown in figure 5.2. The current technology offers miniaturized yet simple and efficient solutions to outfit our robots fully. The final objective is to provide an autonomous proprioceptive biomimetic robotic unit, whose swimming gait will be only determined from the measurements of its sensors: the robot will swim following what it feels. We will use Machine Learning algorithms to provide the sought autonomy to our robots. Furthermore, embedded communication ports (infrared, Bluetooth) will provide an efficient way for describing the robot's state or possibly communicating with other robotic fishes in a school configuration. Finally, it will be conceived to ensure compliance in all swimming circumstances (quick start, steady swim at different speeds, turns).

Appendix A

Experimental setup

Water tunnel
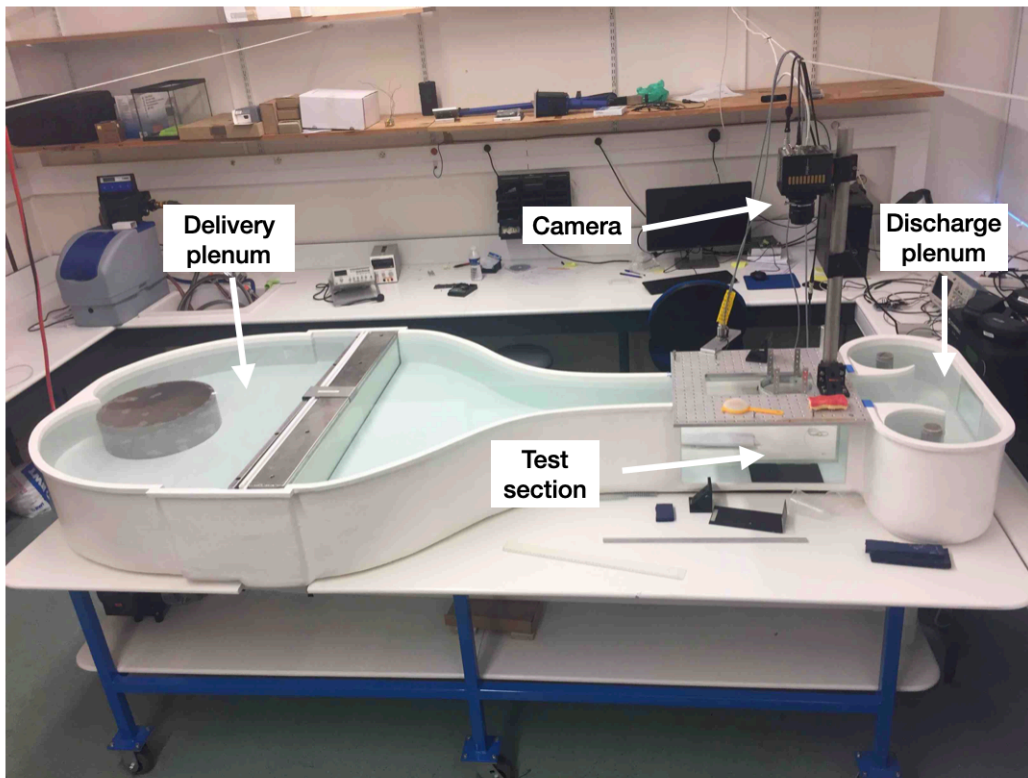
Figure A.1: Water tunnel used in the experiences with the most relevant parts highlighted.

All the experiments have been performed in the water tunnel, model 0710 developed by Rolling Hills Research Corporation. The tunnel, shown in figure A.1, is 270 cm long, 110 cm wide, and 30 cm high, with a capacity of approximately 500 L. The fluid employed is always water, whose properties we consider constant over time with values of density, $\rho = 1000$ kg.m^{-3} and kinematic viscosity, $\nu = 10^{-6}$ m^2.s^{-1}. In working conditions, the tunnel is filled until the water reaches a height of about 25 cm.

The water tunnel is divided into three fundamental parts: the first upstream part from which the liquid begins its movement, the delivery plenum. The working area or test section, in which we place the robotic fish and perform all the experiments. This area is exceptionally well suited for the experiments because of its easy access and good visibility, besides being the section where we can get maximum speeds to test our device. Finally, the discharge plenum

is a discharge area where the water is sucked and through closed-circuit returns accelerated to the first part of the tunnel to continue the cycle. Water from the discharge plenum at the end of the tunnel is drawn and pumped into the delivery plenum to create the flow, creating a pressure differential that forces the liquid to move downstream. The water enters the top of the tunnel through a perforated cylinder that expels the liquid at a constant flow rate by varying the frequency of the pump, f_p. Once water is expelled from the large cylinder in the delivery plenum, the liquid flows through four horizontal perforated plates. The purpose of these plates is to homogenize the outflowing fluid to be as laminar as possible and reduce the transverse component's velocity fluctuations. The rear contraction zone serves a similar purpose. The tunnel length is smoothly reduced to a size six times smaller, which is also beneficial for further reducing turbulence and increasing the velocity within the test zone. The smoothness with which the transition occurs also prevents separation of the boundary layer. The experiments take place in the test section. This zone is a parallelepiped of dimensions 30 high, 46 long, and 16 cm wide with two glass windows on the sides that illuminate the volume with external light to reach high contrast levels in the images. Just at the interface of water-air separation, we placed a tempered glass plate; this plate prevents the vertical oscillations of the fluid at the interface that could affect the quality of the images and distort them. A GO-5100M-USB camera from JAI is placed on top of this glass plate at a variable height and whose objective is to film all the changes of the robot fish undulation. The last part of the water tunnel is the discharge zone. Two perforated cylinders, smaller than the one found in the delivery section, absorb the incoming water and transmit it upstream through a system of pipes. These cylinders are surrounded by tunnel walls and are outside the dimensions of the test area, again to minimize as much as possible a possible turbulence effect that could propagate upstream.
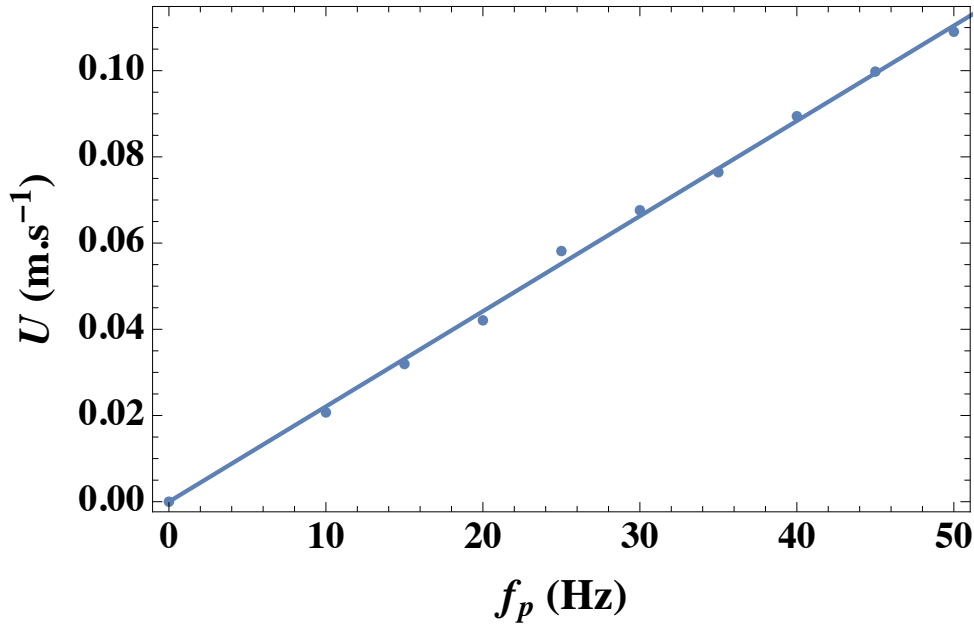
Figure A.2:   Flow velocity U as a function of the pump frequency f_p. The experimental points are shown as disks, and the linear fit is the thick line.

The velocity in the test section depends on the pump frequency which we can vary. A relationship between pump frequency and fluid velocity in the test section is sought to characterize the response of the robotic fish in function of the properties of the flow. We introduce some drops of dye whose trajectory we film for different frequencies of the pump. Assuming a constant velocity, we calculate this magnitude as a function of the duration taken by the stain to cross the entire test section. The trend, shown in figure A.2, reflects a perfect linear behavior

which is well fitted by a linear relation $U \propto f_p$ with a director coefficient $(2.21 \pm 0.02) \cdot 10^{-3}$ m. This characterization fixes the maximum velocity we can obtain in the tunnel at about 11 cm.s^{-1}.

Robotic fish

All the experiments we perform have been realized with a robotic biomimetic fish built in the laboratory, described in a former study [15]. The robot has been designed to resemble as closely as possible a natural biological swimmer and is composed of a flexible body and tail and a rigid head. We denote L the total length of the fish and l the length of the flexible tail with dimensions $L = 0.17$ m and $l = 0.035$ m. The skeleton and tail are the soft parts of the robot. These have been created from a computer-aided design (CAD) program and then printed on a 3D printer by Volumic from NinjaFlex fibers from Ninjatek. This material has been chosen for its mechanical and elastic properties, allowing a flexible movement of the tail and skeleton and good resistance to external forces. In the experimental protocol, we do not directly control the tail dynamics. This task is performed from a Hitec HS-5086WP waterproof servomotor attached directly to the fish skeleton, as shown in figure A.3. The servomotor transmits the rotational motion of its wheels from two wires attached to the tail and guided to the head through holes in the flexible skeleton. The rotation tightens one cable while relaxing the other, mimicking the action of antagonistic muscles. This back and forth rotation causes both an undulation of the flexible tail and a pitching motion. The servomotor has two main limitations that will affect the performance of the robot's motion: first, and imitating biological swimmers, the rotation of the servomotor wheel cannot exceed an angular limit, which for our actual device is $2\pi/3$ rad, although it is true that we can even reduce this angular distance further in some experiments. Furthermore, the maximum speed of the servomotor depends on the applied voltage and is given by the manufacturer, 5.8 rad.s^{-1} at 4.8V and 7 rad.s^{-1} at 6V. As for the rigid parts, we have printed two shells to simulate the front of the animal. In this case, the material is Polylactic acid (PLA), chosen for its rigidity and resistance since flexibility is not a property required by this anatomy. The head fits on the servomotor, partially covering it and decreasing the friction coefficient of the system. Finally, the servomotor is joined to a vertical rod connected to the force sensor, which we introduce in the next section.
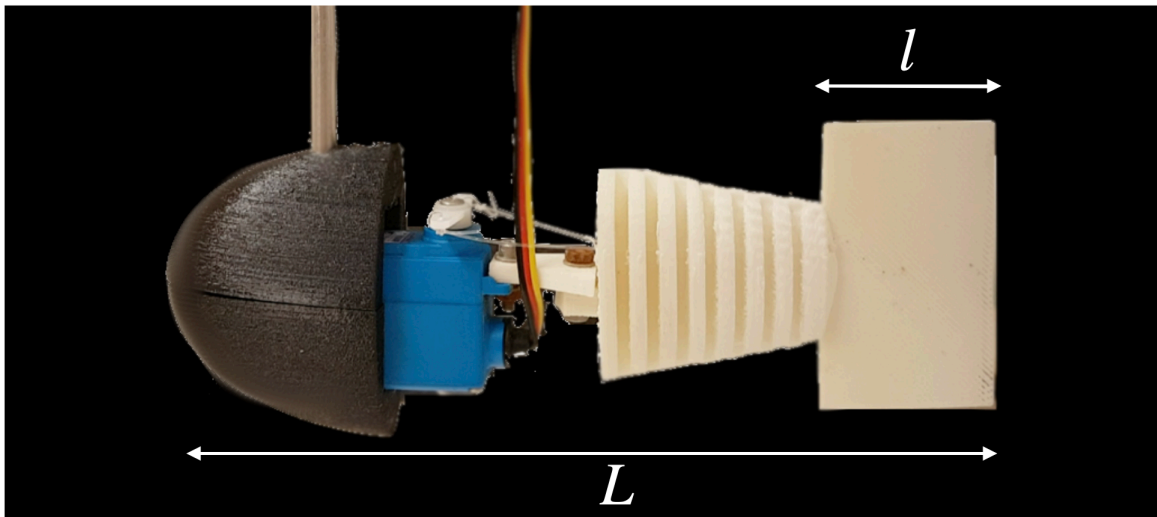

Figure A.3: Side view of the robotic biomimetic swimmer.

An outer covering is desirable in aesthetic terms; however, the effect of covering the robot by simulating an outer skin has been quantified, and we have found that this fact does not affect

the measurements within the accuracy of our devices. Furthermore, it considerably simplifies the measurement and observation of the servomotor dynamics, which would otherwise be very difficult. That is why we will keep the skeleton uncovered in all our experiments.

The control of the servomotor is done via an Arduino Mega micro-controller. The Arduino software allows us to control the rotation of the servomotor in any way we want. The code we have created is a general code in which we can include any time-dependent function to move the servomotor wheel. Parameters such as the amplitude of movement, frequency, waiting times, velocity changes are varied at our convenience and depending on our needs. In general, we call the angular trajectory that we want the servo motor to perform the angular instruction, and we note it by ϕ_c. However, as we have already commented previously, the servomotor is not perfect, nor can it follow instantaneously any instruction. That is why in moments where we demand to go to a higher speed than allowed or to sweep amplitudes superior to the maximum, it will not obey our orders. Therefore the actual trajectory of the servomotor will be different from the imposed one. The actual angle of the servomotor that we measure experimentally is noted by the letter ϕ, as depicted in figure A.4. We ask for a ϕ_c angle, the servomotor responds with an angle ϕ similar, and the servomotor moves the tail an angle α in a way that we will determine in chapter 3. In addition to the servomotor control itself, Arduino is a versatile software that also allows the simultaneous acquisition of data from the force sensor.

Forces sensor
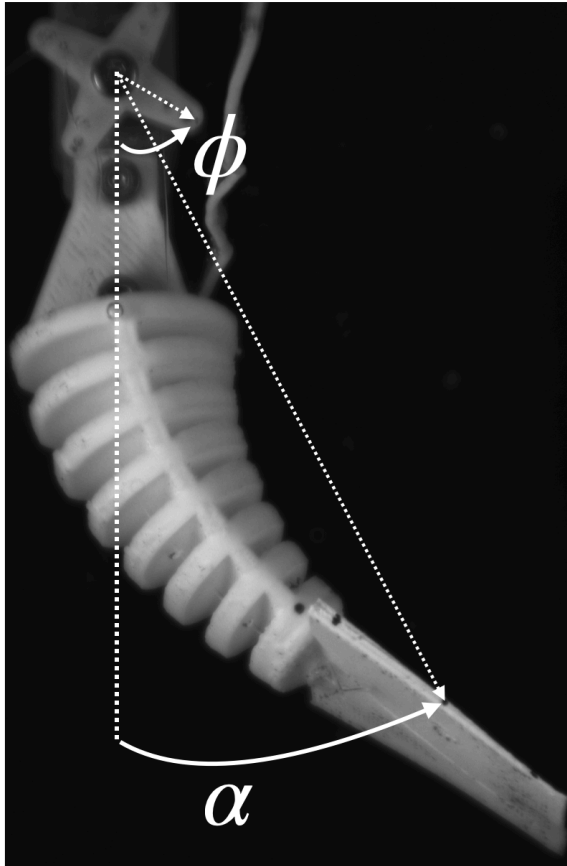
Figure A.4: Definition of the servomotor wheel angle, ϕ, and of the tail deformation angle, α.

The locomotion dynamics is fundamental to understand how the different kinematic parameters are related to thrust and friction forces. In the system, there coexist mainly two groups of forces that we analyze systematically: normal forces, F_y, which act perpendicularly to the fish's motion, and longitudinal forces, F_x, acting parallel. Normal forces are expected to scale as $\rho L^3 A\omega^2$ [24]. Considering the length of our robot fish and the standard operating regime when we impose amplitude and frequency, we would obtain normal forces of the order of $F_y \sim$ 0.8 N.

We expect two types of longitudinal forces; motor forces produced by the tail undulations, responsible for locomotion, and resistive forces, represented by the drag forces that a mobile experiences when moving within a fluid, arising when we impose a non-zero tunnel water velocity. Likewise, these forces scale as $\rho L^2 A^2\omega^2$ and $\rho L^2 U^2$, for propulsive and resistive force, respectively [24], giving estimates of 0.2 and 0.1 N.

The robotic fish is attached to a rod connected to a force sensor, a Honigmann RFS® 150EI, permitting measurements of both longitudinal and normal forces up to 5 N, which is more than enough given the orders of magnitude of the hydrodynamic forces, with a precision of 10^{-4} N. This sensor is a small

cylinder containing some gauges inside it. When a force in either direction is applied, these gauges undergo a deformation involving a change in their length. The gauges are connected to a circuit with a resistance capable of varying according to the deformation suffered by these devices. When deformation occurs, the resistance varies. So does the circuit voltage, which yields a value that we measure and related to the resulting force in the system through the linear law of deformations $F \propto \delta\ell$. The tensions we measure are usually very small, which is why we need an amplifier to be able to measure them correctly. The problem with the amplifier is that in addition to amplifying the signal, it introduces noise at different frequencies that blur the actual measurement. The sensor is connected to a filter to get rid of that noise and keep the pure signal to measure this voltage with the Arduino Mega micro-controller. The sensor calibration is made so that 1 N = 1 V to make our measures easier.

Tracking

Apart from the calculations of the different forces acting on the system, the experimental protocol aims to measure two fundamental characteristics of our robot fish: the amplitude of the tail oscillations and the frequency of these oscillations. Furthermore, and especially in the chapter 3, we also need to know the temporal evolution of the servomotor angle to model the response of the tail in function of the forcing.
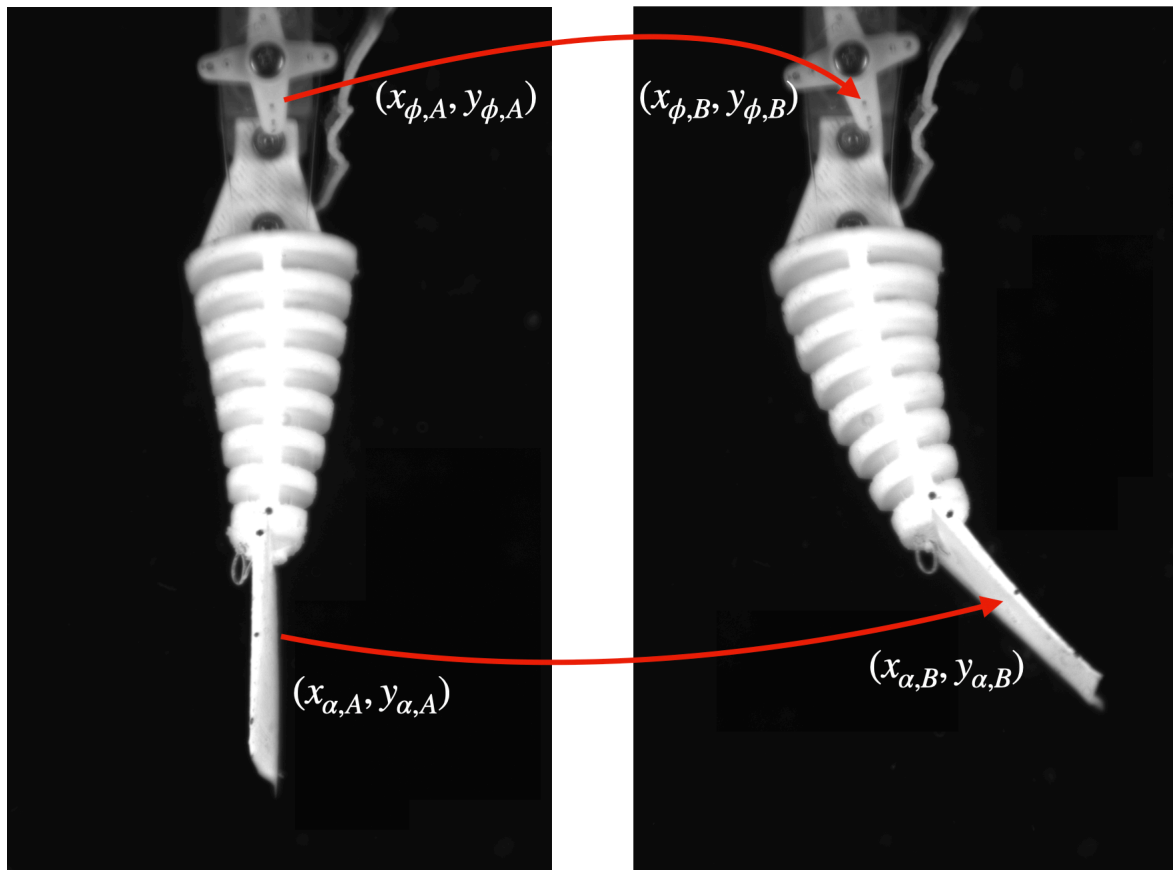
Figure A.5: Tracking of servomotor wheel angle and tail angle from an initial position of coordinates A to a final position B.

Mathematica software allows us to obtain the evolution of any point given a set of images in which that point follows a given trajectory over time. We record a set of images while the fish is moving according to a given instruction. This set of images, together with the frequency of acquisition of these images, is processed using the Mathematica function

```
ImageFeatureTrack[{initial_image, ... ,final_image }, {{xpoint, ypoint}}].
```

We need a sequence of images ordered from the initial to the final image and the coordinates of the point we want to track in time in the initial image. The tracking process then selects the (x, y) coordinates in the initial image that it will follow throughout the image sequence. The duration of the process depends on the number of images, but it usually takes no more than a few minutes. For example, for tracking one point in a sequence of 100 images, the process takes about one and a half minutes.

However, to run smoothly from the first image to the last, two essential factors about the image sequence must be considered. First, the acquisition rate of the camera must be sufficiently high compared to the natural frequency of motion so that there are no abrupt or pronounced "jumps" from one image to the next. The sequence of images must be continuous and uniform in the sense that in two contiguous images, the point to be tracked has not changed its position considerably. Mathematica can have issues, especially when there is a significant change between one image and the previous one. While this is easy to achieve with a high acquisition rate, there have been times in our experiments when the camera's maximum rate (74 frames per second) was not sufficient to track a set of coordinates accurately. Then the only remaining recourse is to increase the number of images in our sequence, with the consequent detriment in terms of the time the software will take to complete the analysis.

Another critical parameter is the contrast of the point we want to follow. The coordinates from which we want to know its temporal evolution must represent a point well differentiated from its surroundings, either by highlighting the point in question or by changing the background surrounding the point. In any case, and particularly for our experiment, highlighting in black the points we want to follow has proved to be a good strategy giving good results in tracking. That is why three black points in the tail have been drawn to contrast nicely with the surrounding skeleton, as shown in figure A.5.

Appendix B

Perturbation Methods: Multiple Scale Method

Equations solutions do not always arise in terms of closed, known functions. Moreover, this is precisely the most common, being impossible to obtain analytical solutions to any equation we are facing. However, on many occasions, and we will justify these situations when appearing in this manuscript, we can find methods to solve the equations under certain conditions or hypotheses. The solutions obtained will not be exact in a general sense; that is to say, they will not represent the authentic solution of the system for any instant of time. Nevertheless, they will constitute an excellent approximation in the description of the system behavior if the hypotheses giving rise to this treatment are not relaxed.

Generally, these conditions consist in assuming that one or more of the parameters included in the equation are "small". As we will always work in dimensionless variables, small here will mean that the unit is much larger than the small dimensionless quantity. Following this spirit, we may imagine the very first, straightforward expansion of an asymptotic solution to solve our equation will be to develop in power series the variable in question:

$$x(t) = \sum_{i=0}^{\infty} \varepsilon^i x_i(t), \tag{B.0.1}$$

where ε is the parameter sought to be small.

This first expansion assumes that the zeroth-order solution consists simply of the solution of the problem without perturbation. To this solution, we add terms that turn out to be small and that take into account the perturbation introduced in the differential equation, but roughly speaking and on time scales smaller than ε^{-1} we expect the error made in the approximation of the whole solution to be small. As a matter of fact, this choice of ansatz may be suitable for some situations, but it fails utterly for others very simple (or not as simple) systems in which there exist two different time scales involved. The prototypical example where this expansion fails is the harmonic oscillator with small damping [237] :

$$x'' + 2\varepsilon x' + x = 0, \tag{B.0.2}$$

whose exact solution is $e^{-\varepsilon t} \left(c_1 \sin\left(\sqrt{1-\varepsilon^2}t\right) + c_2 \cos\left(\sqrt{1-\varepsilon^2}t\right) \right)$, with c_1 and c_2 constants. In effect, a development up to second-order such as the one proposed by equation B.0.1 leads to:

$$x_0'' + x_0 = 0,$$
$$x_1'' + x_1 = -2x_0'.$$

We recognize at zero-order the equation of the harmonic oscillator, whose solution is expressed in terms of periodic functions: $x_0(t) = A\cos t + B\sin t$. Suppose we advance to the following order and solve taking into account the previous answer. In that case, we obtain the solution of the homogeneous equation that mimics the prior result. And also a particular solution, $-2At\cos t - 2Bt\sin t$, due to the time-dependent term, $x_0(t)$ that oscillates at the same frequency as the homogeneous solution with the following known consequence: resonance. The first-order solution x_1 is not bounded; for times of order ε^{-1}, it becomes comparable to the zeroth-order solution, breaking the assumptions of perturbation theory and completely invalidating the obtained result, as shown in figure B.1, where we compare the exact solution of the equation B.0.2 with the straightforward method and the multiple-scale solution. In fact, this expansion is associated with the $\varepsilon \to 0$ limit keeping the time t fixed, something that turns out to be valid only for the time domains already mentioned, but that cannot hold uniformly for any subsequent instance. The appearance of secular terms in the perturbative development becomes a significant obstacle in approximating the solution of a differential equation. If we cannot even solve the damped harmonic oscillator, how will we advance trying to find solutions to problems that are impossible to treat analytically.
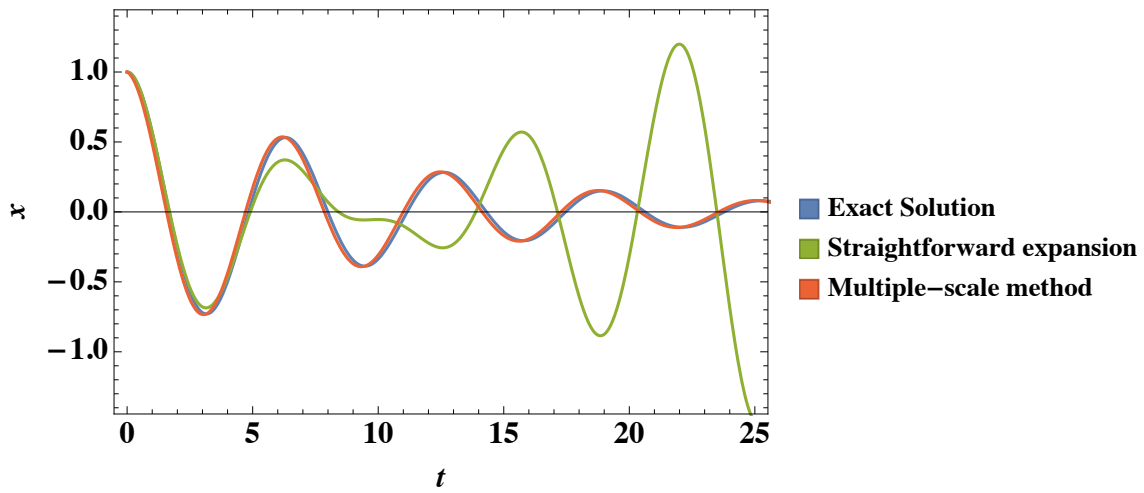
Figure B.1: Comparison between the analytical solution of equation B.0.2, the approximation made by the straightforward expansion and the solution given by the method of multiple scales for $\varepsilon = 0.1$ and initial conditions $x(0) = 1$, $x'(0) = 0$.

But then, why such a straightforward method fails to solve the differential equation? Among the possible reasons that prevent the correct approximation of the system, there is a decisive one. It is precisely the existence of several very different time scales in the problem. First, we find a time scale that governs the period of oscillation, and that is $\mathcal{O}(1)$. In addition, the small damping introduces an amplitude dependence with time which, given the smallness of the perturbation, is $\mathcal{O}(\varepsilon^{-1})$, and finally, there is a phase shift due to friction of $\mathcal{O}(\varepsilon^{-2})$. The uniformity of the perturbative expansion is broken due to the non-uniformity of the time scales. Several physical problems are distinguished by the presence of small disturbances, which, because they are active over a long time, have a non-negligible cumulative effect. The straightforward method is well adapted for solving the problems whose solutions are periodic but cannot correctly determine the behavior of the solutions during the transient regime. This is the obstacle that the introduction of the perturbation adds to the problem; it breaks this periodicity by imposing an amplitude of motion that is no longer constant and decays slowly over time.

That is why for the case at hand, where there are usually many time scales involved, we must take them into account when solving the problem. The method we use and present is the so-called multiple scale method [238, 239], and it is specially adapted to the type of physical

situations we want to deal with, being able to describe both transient and stationary behaviors, besides being a versatile and relatively simple method to implement. This formalism no longer considers time as the only variable that governs the system's evolution but introduces new variables totally independent of each other, each of them representing a characteristic time of the system that describes the evolution of slower or faster phenomena. Thus, these new variables are referred to $t_0, t_1, t_2, \cdots, t_m$ and are defined with respect to absolute time t as:

$$t_i = \varepsilon^i t.$$

The expansion of the time variable leads to a change in the representation of the system's dynamics. The evolution equations that govern the physical processes are ordinary differential equations with only derivatives with respect to the independent variable, the time t. Considering now that different time scales are mathematically independent, the equations completely change their character and become equations in partial derivatives. For example, if we study the first derivative with respect to time and apply the chain rule, we have:

$$\frac{d}{dt} = \sum_{i=0}^{\infty} \frac{\partial}{\partial t_i} \frac{\partial t_i}{\partial t} = \sum_{i=0}^{\infty} \varepsilon^i \frac{\partial}{\partial t_i}. \tag{B.0.3}$$

We see that the application of the chain rule converts the equations into equations in partial derivatives. A priori, we could think that the change from an ODE to a PDE brings more problems than it solves. Solving an equation in partial derivatives is a complicated task, even in the most accessible cases, with nothing to do with ordinary differential equations. There are even techniques to solve strongly nonlinear equations. However, the procedure is clever, and although speaking in explicitly mathematical terms, we are dealing with a system of PDEs, in the application of the method, only ODEs are solved. The reason for this will be found later in the development of the technique. Then, once all the independent variables have been introduced, one can propose a power series expansion analogous to equation B.0.1 but considering that the time dependence has been extended:

$$x(t) = \sum_{i=0}^{\infty} \varepsilon^i x_i(t_0, t_1, \cdots, t_m). \tag{B.0.4}$$

Therefore, the spirit of the process is the same: solve the unperturbed problem and add other terms less critical than the leading one that modifies the solution and takes into account the introduction of the perturbation. The particularity is that phenomena where slow modulations of the pattern occur are already considered and incorporated directly into the solution thanks to the different time scales.

Let us then expose the method, suppose in a general way an equation of evolution of a physical process represented as follows:

$$\frac{d\boldsymbol{x}}{dt} = \boldsymbol{f}(\boldsymbol{x}, \varepsilon),$$

where $\boldsymbol{x}$ is a n components vector and $\boldsymbol{f}(\boldsymbol{x}, \varepsilon)$ is a vector function depending on a small parameter ε and which may be decomposend in a linear and nonlinear part:

$$\frac{d\boldsymbol{x}}{dt} = L\boldsymbol{x} + \varepsilon \boldsymbol{N}(\boldsymbol{x}),$$

where L is a linear matrix operator, and $\boldsymbol{N}$ collects the nonlinear terms. Obviously, ε accompanies the nonlinear part of the equation since it is precisely this term that prevents the analytical resolution of the differential equation. Developing up to ε^2 and introducing the expansions in equations B.0.3 and B.0.4 in the expression we have:

$$\left(\frac{\partial}{\partial t_0} + \varepsilon \frac{\partial}{\partial t_1} + \varepsilon^2 \frac{\partial}{\partial t_2} + \cdots \right) \left(\boldsymbol{x}_0 + \varepsilon \boldsymbol{x}_1 + \varepsilon^2 \boldsymbol{x}_2 + \cdots \right)$$
$$= L \left(\boldsymbol{x}_0 + \varepsilon \boldsymbol{x}_1 + \varepsilon^2 \boldsymbol{x}_2 + \cdots \right) + \varepsilon \boldsymbol{N} \left(\boldsymbol{x}_0 + \varepsilon \boldsymbol{x}_1 + \varepsilon^2 \boldsymbol{x}_2 + \cdots \right).$$

Nonlinear terms may be expanded in Taylor series:

$$\boldsymbol{N}\left(\boldsymbol{x}_0 + \varepsilon\boldsymbol{x}_1 + \varepsilon^2\boldsymbol{x}_2 + \cdots\right) = \boldsymbol{N}(\boldsymbol{x}_0) + \varepsilon\boldsymbol{x}_1 \frac{\partial \boldsymbol{N}\left(\boldsymbol{x}_0\right)}{\partial \boldsymbol{x}_0} + \cdots$$

Equating coefficients of like power of ε, we obtain at zero-order the solution to the unperturbed problem:

$$\frac{\partial}{\partial t_0}\boldsymbol{x}_0 - L\boldsymbol{x}_0 = 0.$$

As expected, this equation, which turns out to be an eigenvalue equation, is easily solvable. Applying the methods of linear algebra and proposing $\boldsymbol{x}_0 = c_0\boldsymbol{\zeta}e^{\lambda t_0}$ we can obtain the solution for both eigenvalues and eigenvectors univocally.

$$|\lambda I - L| = 0, \qquad \lambda\boldsymbol{\zeta} = L\boldsymbol{\zeta}.$$

Before moving on to the following order, it is interesting to know how the solution of the linear problem clearly reflects the dependence on t_0, the fastest time scale. However, in equation B.0.4 we see how each term of the expansion depends on all the time variables involved in the system. Since the eigenvectors cannot reflect a dynamic condition, the only possibility that these additional times are included is that all of them except t_0 are regrouped in the expression of the amplitude c_0. Thus, just as the linear homogeneous problem ultimately determines $\boldsymbol{\zeta}$, this is not the case, for now, for the amplitude c_0, which, in principle, must be written as dependent on the hierarchy of time scales.

At first order of perturbation theory, the equation reads:

$$\left(\frac{\partial}{\partial t_0} - L\right)\boldsymbol{x}_1 = -\frac{\partial}{\partial t_1}\boldsymbol{x}_0 + \boldsymbol{N}(\boldsymbol{x}_0).$$

It is interesting to note how the LHS of the equation resembles the equation of order 0, except that in this case, the operator affects the variable $\boldsymbol{x}_1$. This is a constant for all subsequent orders, the operator $\partial/\partial t_0 - L$, which from now on we rename as $\mathcal{L}$, will appear in all equations in the LHS while the RHS will change. Previously, we mentioned how introducing an equation in partial derivatives would facilitate obtaining an approximate solution to the problem. In this first case, we see how, although theoretically, we are facing a PDE, in practice, the equation to solve is an ODE, since the member of the right just involves functions of $\boldsymbol{x}_0$, whose behavior we know because we have calculated it in the linear problem. We will find precisely the same for higher orders, and the RHS always contains variables that have already been computed in the previous orders. Therefore the whole problem reduces to solving the inhomogeneous differential equation in each case. Thus, rewriting the above equation by introducing the new operator $\mathcal{L}$ leaves:

$$\mathcal{L}\boldsymbol{x}_1 = -\frac{\partial}{\partial t_1}\boldsymbol{x}_0 + \boldsymbol{N}(\boldsymbol{x}_0) = \boldsymbol{q}_1. \tag{B.0.5}$$

To solve the equation, we would have to solve the homogeneous equation and then look for a particular solution as usual. In this case, we would find two obstacles; in the right-hand member, we could observe secular terms that would again break the validity of the perturbative expansion, and on the other hand, it would be impossible to determine the relation between the amplitude c_0 and t_1, because x_0 appears derived with respect to t_1 in the equation.

Without going into the practical details of how to solve the equation, in formal terms, we expect the solution of this equation to be given by $\boldsymbol{x}_1 \sim \mathcal{L}^{-1}\boldsymbol{q}_1$. However, nothing has been said about whether the operator $\mathcal{L}$ is invertible or not, and if so, how to compute it. Reasoning in analogy with linear algebra and substituting the integro-differential operators by matrices, we know the condition that the vector $\boldsymbol{q}_1$ must fulfill concerning the operator for the system to have a solution. This necessary and sufficient condition is known as Fredholm's Alternative

Theorem [240], and it also applies outside linear algebra, being the tool we will use to solve equation B.0.5. To apply the theorem, it is necessary to introduce a certain formalism of functional analysis. Summarizing, we state that it is necessary to define the Hilbert space in which the solutions of the equation live and the inner prbiaoduct that characterizes this space and that we note employing $\langle \cdot, \cdot \rangle$. Applying the alternative, we will say that the equation B.0.5 has solution if and only if $\boldsymbol{q}_1$ is orthogonal to the subspace engendered by the kernel of the adjoint operator, $\boldsymbol{q}_1 \perp \mathrm{Ker}(\mathcal{L}^*)$.

The concept of orthogonality is intimately linked to the existence of an inner product; we will say that two elements of a Hilbert space are orthogonal when their product is 0. The kernel or nullspace of the operator $\mathcal{L}^*$ in this case is the subspace generated by all the Hilbert elements, $\boldsymbol{v}$, which satisfy $\mathcal{L}^* \boldsymbol{v} = 0$. The definition of adjoint operator is standard and for two elements $\boldsymbol{v}_1$ and $\boldsymbol{v}_2$ satisfies:

$$\langle \mathcal{L} \boldsymbol{v}_1, \boldsymbol{v}_2 \rangle = \langle \boldsymbol{v}_1, \mathcal{L}^* \boldsymbol{v}_2 \rangle .$$

The fact of applying the alternative theorem and requiring $\boldsymbol{q}_1 \perp \mathrm{Ker}(\mathcal{L}^*)$ is known as the solvability condition and is of vital importance in the development of the perturbative technique since it is this condition that guarantees the elimination of the secular terms.

Applying the alternative to equation B.0.5, the equation that arises is

$$-\frac{\partial c_0}{\partial t_1} \left\langle \boldsymbol{\zeta} e^{\lambda t_0}, \boldsymbol{x}^* \right\rangle + \left\langle \boldsymbol{N} \left(c_0 \boldsymbol{\zeta} e^{\lambda t_0} \right), \boldsymbol{x}^* \right\rangle = 0,$$

where $\boldsymbol{x}^*$ spans the kernel of the adjoint operator, i.e., $\mathcal{L}^* \boldsymbol{x}^* = 0$. We finally deduce the amplitude equation that gives us the dependence of c_0 (and consequently of $\boldsymbol{x}_0$) as a function of t_1:

$$\frac{\partial c_0}{\partial t_1} = \frac{\left\langle \boldsymbol{N} \left(c_0 \boldsymbol{\zeta} e^{\lambda t_0} \right), \boldsymbol{x}^* \right\rangle}{\left\langle \boldsymbol{\zeta} e^{\lambda t_0}, \boldsymbol{x}^* \right\rangle} .$$

Once this amplitude equation is solved, the usual methods of solving equation B.0.5 will lead to a correct $\boldsymbol{x}_1$ solution with no secular terms. The technique is consistent and extends to subsequent orders both to compute the dependence of c_0 on the other time scales and to obtain the behavior of the future amplitudes of following orders, applying in all steps the alternative theorem to get rid of the terms that break the perturbative expansion. The solution arising from this method is shown in figure B.1, giving a good account of how, unlike the straightforward approach, the multiscale method achieves a reasonably accurate approximation of the analytical solution.

Appendix C

Stability loss of a dynamical system: the Hopf bifurcation

The theory of dynamical systems provides us with tools to describe the complex behavior of a system without the need to know its exact solution. Stability is always a characteristic that, as physicists, we are interested in knowing and interpreting, determining under what conditions the problems we work with present, and how they can change depending on the control parameters of the physical phenomenon. Among all the possibilities by which a system can lose or gain stability as a function of a parameter, we are interested in a specific case, which we will develop within its physical context in chapter 3: the Hopf bifurcation.

The physical laws describing the time evolution of a process can be represented mathematically through:

$$\frac{d\boldsymbol{x}}{dt} = \boldsymbol{f}(\boldsymbol{x}). \tag{C.0.1}$$

Such a system will be called an autonomous or time-independent dynamical system. Undoubtedly the resolution of the set of equations is the best way to obtain the behavior of the system as a function of time. However, as we have seen above, the systems do not offer solutions in the form of generally known functions but rather the opposite. Even so, and without resorting to perturbative methods, we can extract some characteristics of the process. One of the essential features that can be found only through the behavior of $\boldsymbol{f}(\boldsymbol{x})$ is the existence of equilibrium points of the system. These points, generally known as fixed points, are characterized by being solutions that do not vary in time and therefore are identified by fulfilling:

$$\boldsymbol{f}(\boldsymbol{x}_{st}) = 0.$$

These stationary states of the system have an interesting property: their stability. These points can be classified into stable or unstable points depending on whether they behave as attractors or repulsors in the phase space. Strictly speaking, a critical point should be considered a stable state, insofar as once installed in it, the system does not evolve, by definition. However, in the real world, a system never remains in one state as time passes. It is in contact with a complex environment, with which it exchanges energy, momentum and, eventually, matter randomly. To this, we must add the intrinsic variability of every macroscopic system, variability that manifests itself in the form of thermodynamic fluctuations. This means that a stationary state is continuously subjected to perturbations of greater or lesser size. We need to know what happens to a steady state when it is perturbed. Does the subsequent time evolution bring the system back or drive it away for good? We will then have to frame the concept of stability within the context of reaction to perturbations. We will be interested, in short, in the response to an initial perturbation to the stationary state. We will say that systems are classified, roughly speaking, as stable, if for each neighborhood of the point in question, all trajectories tend to it in infinite time or unstable if this neighborhood does not exist and the

127

trajectories move away from the point in phase space. The concept of critical point stability offers an important corollary; generally, the instability of such a point signals the occurrence of more complex behavior. Consequently, the measurement of such a critical point's stability (or instability) is an unavoidable step when investigating the eventuality of complex solutions in a system.

In this measure of stability, we will always speak of "small" perturbations since our formalism does not allow us to consider any type. Consequently, the linear stability principle is postulated: if we analyze the time evolution of small perturbations with respect to the fixed point $\boldsymbol{y}(t) = \boldsymbol{x}(t) - \boldsymbol{x}_{st}$ we will have developing in Taylor series:

$$\frac{d\boldsymbol{x}}{dt} = \frac{d\boldsymbol{x}_{st}}{dt} + \frac{d\boldsymbol{y}}{dt} = \boldsymbol{f}(\boldsymbol{x}_{st}) + \left.\frac{\partial \boldsymbol{f}(\boldsymbol{x})}{\partial \boldsymbol{x}}\right|_{\boldsymbol{x}_{st}} \boldsymbol{y}. \tag{C.0.2}$$

Due to the non-dependence of the fixed point as a function of time and that the function evaluated at the fixed point is identically null, we find:

$$\frac{d\boldsymbol{y}}{dt} = \left.\frac{\partial \boldsymbol{f}(\boldsymbol{x})}{\partial \boldsymbol{x}}\right|_{\boldsymbol{x}_{st}} \boldsymbol{y}, \tag{C.0.3}$$

where the derivative of $\boldsymbol{f}(\boldsymbol{x})$ with respect to $\boldsymbol{x}$ denotes the Jacobian matrix of the system.

Therefore the stability of the fixed points of the equation C.0.2 will depend on the stability or not of equation C.0.3 [241]. In general, the stability of the system is given by the eigenvalues, λ, of the Jacobian matrix. If all eigenvalues have negative real part, then the system is asymptotically stable. On the contrary, if any of them is positive the system becomes unstable.

However, the linear character of these equations immediately raises a question as to how far this justification resolves the appearance of the system adequately. Is there a point at which the nonlinear effects completely change the system's future, and the stability regime is disturbed by them? The topology of a fixed point in the complete system C.0.1 is qualitatively the same as if we consider the associated linear system, equation C.0.3, as long as the real part of the eigenvalues of the matrix are different from 0. All fixed points that satisfy this last condition are known as hyperbolic fixed points. We say in this case that both phase portraits are topologically equivalents. There is an application between both spaces that distorts the trajectories; bending or warping is allowed, but not ripping, yet it does not alter their fundamental characteristics. This statement is known as the Hartman-Grossman theorem and is one of the most important results of dynamical systems theory [242]. In the case of finding that the real parts of the eigenvalues are zero, this theorem cannot solve anything, and it is necessary to resort to more advanced techniques to determine the stability under perturbations, such as the technique of center manifolds and normal forms.

This result is helpful because it allows us to know the behavior of strongly nonlinear systems through the linearization around the fixed point. The treatment of dynamical systems is precisely the same if we now consider more general systems:

$$\frac{d\boldsymbol{x}}{dt} = \boldsymbol{f}(\boldsymbol{x}, \gamma), \tag{C.0.4}$$

where γ is a control parameter that exerts a significant influence on our system. Although it is possible to consider a family of parameters, we focus on the case in which there is only one order parameter. The concepts of fixed point and stability remain unchanged; the computation of them together with the calculation of eigenvalues of their linearization continue to be the indicated methods to treat these systems, with the only problem that now both fixed points and stability will potentially depend on the value of γ. The fixed points of the system now occur on $(\boldsymbol{x}_{st}, \gamma_c)$ and their stability is determined by the eigenvalues of the Jacobian matrix:

$$\frac{d\boldsymbol{y}}{dt} = \left.\frac{\partial \boldsymbol{f}(\boldsymbol{x}, \gamma)}{\partial \boldsymbol{x}}\right|_{(\boldsymbol{x}_{st}, \gamma_c)} \boldsymbol{y}.$$
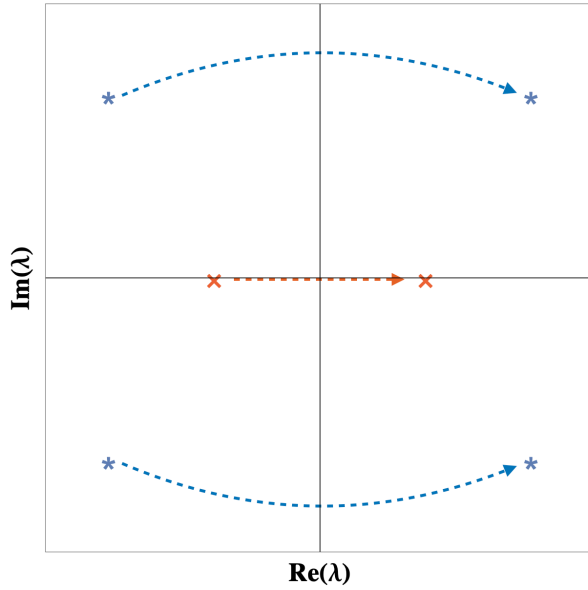
Figure C.1: Eigenvalues crossing the imaginary axis in blue (complex eigenvalues) and red (real eigenvalue). A Hopf bifurcation corresponds to the blue case.

Again, if the eigenvalues of this matrix have a real part different from 0, there is no problem. The Hartman-Grossman theorem solves the stability of the complete nonlinear system. The problem appears when at least one of the eigenvalues has real part equal to 0. In this case, and depending on the value of γ concerning its critical value, the nature of the solutions of the system have qualitatively different behaviors, being able to exhibit creation and destruction of fixed points, the appearance of periodic or even chaotic behaviors. We say that in this case, the system undergoes a bifurcation. More formally, the appearance of a phase portrait of the system that is not topologically equivalent to the initial one due to the variation of parameters is known as a bifurcation.

The classification of bifurcations and their general treatment is extensive and is totally out of our scope. We are somewhat interested in a particular one that receives the name of Hopf bifurcation.

A Hopf bifurcation is a bifurcation of codimension 1: only one parameter is necessary to characterize the bifurcation, and it is characterized by the loss of stability of a fixed point because two imaginary eigenvalues have crossed the axis of the imaginary and have changed the sign of its real part, as outlined in figure C.1. This moment marks the birth of a periodic trajectory independent of initial conditions known as a limit cycle.

Suppose then that the Jacobian matrix of equation C.0.4 has two purely imaginary eigenvalues, $\lambda = \pm i\omega_c$, and the rest with real part other than 0 in $(\boldsymbol{x}_{st}, \gamma_c)$. In this case, we know that the Jacobian matrix criterion is not valid to know the system's behavior and that other techniques are necessary for this. The theory of normal forms proves to be useful when the linearization criterion fails. A normal form is the simplest mathematical expression that can be obtained from the original dynamical system and therefore retains all its characteristics and properties. Formally the calculation of a normal form is tedious and time-consuming, however, the techniques shown in Appendix B may be extremely useful in this calculation.

Suppose then that the system C.0.4 can be written as:

$$\frac{d\boldsymbol{x}}{dt} = L(\gamma)\boldsymbol{x} + \boldsymbol{N}(\boldsymbol{x}, \gamma), \tag{C.0.5}$$

where, as we already know, L and $\boldsymbol{N}$ denote the linear and nonlinear part, respectively. The fixed point condition imposes $\boldsymbol{N}(\boldsymbol{x}_{st}, \gamma_c) = \boldsymbol{0}$ and the existence of non-hyperbolic fixed point $\partial \boldsymbol{N}(x_{st}, \gamma_c)/\partial \boldsymbol{x} = \boldsymbol{0}$. According to the starting assumptions, at $\gamma = \gamma_c$, we have a bifurcation point and the eigenvalues of the matrix L are hyperbolic except for a pair of imaginary eigenvalues. Using the multiscale method, we can construct approximations to the solutions bifurcating at γ_c. While this allows us to approach the solution of the nonlinear problem, on the other hand, it limits the range of validity of the solution, since the very idea of perturbation restricts the solution produced to amplitudes close to the reference solution $\boldsymbol{x} = \boldsymbol{x}_{st}$ or, equivalently, to values of the control parameter close to the critical value itself, $\gamma = \gamma_c$. Let us make an expansion of $\boldsymbol{x}$ in the neighborhood of γ_c in the usual way, i.e., in terms of a parameter ε. It

seems logical to assume that this ε is simply the distance to the bifurcation point $\gamma - \gamma_c$. For this purpose, we will assume that both quantities are expanded in power series as follows:

$$\boldsymbol{x} = \boldsymbol{x}_{st} + \varepsilon\boldsymbol{x}_1 + \varepsilon^3\boldsymbol{x}_3,$$

$$\gamma = \gamma_c + \varepsilon^2\gamma_2.$$

Before the instability, the system is stable, and all modes relax towards $\boldsymbol{x} = \boldsymbol{x}_{st}$. At the same γ_c, the modes whose real part is negative relax, while the two modes that are going to become unstable, which are those that in γ_c change the sign of their real part, vary very slowly until they reach the stationary regime. The same happens when $\gamma > \gamma_c$ since, by continuity, we expect the unstable modes to vary as slowly as they did at the critical point. By extension, we infer that the $\boldsymbol{x}$ solution of the nonlinear system near the critical point must be a function that varies very slowly with time in the transient regime. This manifestation of the system near the critical point allows the introduction of a hierarchy of time scales (t_0, t_2) such that:

$$\frac{d}{dt} = \frac{\partial}{\partial t_0} + \varepsilon^2\frac{\partial}{\partial t_2},$$

as in equation B.0.3. Developing also $L(\gamma)$ and $\boldsymbol{N}(\boldsymbol{x},\gamma)$ around $\boldsymbol{x} = \boldsymbol{x}_{st}$ and $\gamma = \gamma_c$, and introducing all the above in equation C.0.5 we have up to order 3 the following set of equations:

$$\left(\frac{\partial}{\partial t_0} - L(\gamma_c)\right)\boldsymbol{x}_1 = 0, \tag{C.0.6}$$

$$\left(\frac{\partial}{\partial t_0} - L(\gamma_c)\right)\boldsymbol{x}_3 = \gamma_2\frac{\partial L(\gamma)}{\partial \gamma}\bigg|_{\gamma=\gamma_c}\boldsymbol{x}_1 + \frac{1}{6}\boldsymbol{x}_1\boldsymbol{x}_1\boldsymbol{x}_1\frac{\partial^3\boldsymbol{N}(\boldsymbol{x},\gamma_c)}{\partial \boldsymbol{x}^3}\bigg|_{\boldsymbol{x}=\boldsymbol{x}_{st}} - \frac{\partial \boldsymbol{x}_1}{\partial t_2}. \tag{C.0.7}$$

The first of the equations, C.0.6, is an eigenvalue equation that will give us the value of the frequency at the birth of the bifurcation, ω_c. The second, C.0.7, will give us the amplitude equation of $\boldsymbol{x}_1$ with which we will be able to determine the behavior of the solution as a function of t_2. Writing:

$$\boldsymbol{x}_1 = c_1\boldsymbol{v_1}e^{i\omega_c t_0} + \text{c.c.},$$

where c.c. denotes complex-conjugate, $\boldsymbol{v}_1$ is the solution of the homogeneous problem and c_1 is a function of t_2 exclusively. The RHS of equation C.0.7 becomes:

$$\left(c_1\boldsymbol{v}_1\gamma_2\frac{\partial L(\gamma)}{\partial \gamma}\bigg|_{\gamma=\gamma_c} + \frac{1}{2}|c_1|^2 c_1 |\boldsymbol{v}_1|^2\boldsymbol{v}_1\frac{\partial^3\boldsymbol{N}(\boldsymbol{x},\gamma_c)}{\partial \boldsymbol{x}^3}\bigg|_{\boldsymbol{x}=\boldsymbol{x}_{st}} - \boldsymbol{v}_1\frac{\partial c_1}{\partial t_2}\right)e^{i\omega_c t_0}$$

$$+ \frac{1}{6}c_1^3\boldsymbol{v}_1^3\frac{\partial^3\boldsymbol{N}(\boldsymbol{x},\gamma_c)}{\partial \boldsymbol{x}^3}\bigg|_{\boldsymbol{x}=\boldsymbol{x}_{st}}e^{3i\omega_c t_0} + \text{c.c.}.$$

As we saw above, this term must be perpendicular to the subspace generated by the kernel of the adjoint of the operator $\frac{\partial}{\partial t_0} - L(\gamma_c)$ satisfying the Fredholm Alternative [240]. It is clear in this case that the equation contains secular terms, namely the terms accompanied by $e^{i\omega_c t_0}$ and its complex conjugate. Introducing the vectors that generate the nullspace of the adjoint operator, $\boldsymbol{v}^*e^{-i\omega_c t_0} + \text{c.c.}$, the Alternative then imposes:

$$\frac{\partial c_1}{\partial t_2} = \gamma_2\mu c_1 + \beta|c_1|^2 c_1,$$

with μ and β complex quantities defined by:

$$\mu = \boldsymbol{v}_1\frac{\partial L(\gamma)}{\partial \gamma}\bigg|_{\gamma=\gamma_c} \cdot \boldsymbol{v}^*,$$

$$\beta = \frac{1}{2}\boldsymbol{v}_1\boldsymbol{v}_1\boldsymbol{v}_1\frac{\partial^3\boldsymbol{N}(\boldsymbol{x},\gamma_c)}{\partial \boldsymbol{x}^3}\bigg|_{\boldsymbol{x}=\boldsymbol{x}_{st}} \cdot \boldsymbol{v}^*.$$

However, for physical purposes the important quantity is not c_1 but rather the measurable physical amplitude $\varepsilon \boldsymbol{x}_1$. In correspondence $z = \varepsilon c_1$, moreover, considering that $t_2 = \varepsilon^2 t$ and $\gamma_2 = \frac{\gamma - \gamma_c}{\varepsilon^2}$ we finally write the normal form of the Hopf bifurcation [243]:

$$\frac{dz}{dt} = (\gamma - \gamma_c)\mu z + \beta|z|^2 z. \tag{C.0.8}$$

Rewriting in polar coordinates $z = re^{i\theta}$ and making $\mu = \mu_r + i\mu_i$ and $\beta = \beta_r + i\beta_i$ where the subindices r and i correspond to the real and imaginary parts, respectively, we can write the equation C.0.8 as:

$$\frac{dr}{dt} = (\gamma - \gamma_c)\mu_r r + \beta_r r^3,$$
$$\frac{d\theta}{dt} = (\gamma - \gamma_c)\mu_i + \beta_i r^2.$$
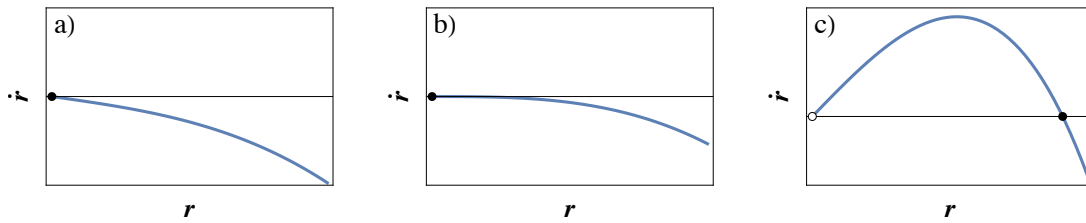

Figure C.2: Phase portrait of the radial coordinate r for $\mu_r > 0$ and $\beta_r < 0$. We show the cases a) $\gamma < \gamma_c$, b) $\gamma = \gamma_c$ and c) $\gamma > \gamma_c$. Just the scenario with $\gamma > \gamma_c$ presents a stable limit cycle.

The phase portrait in figure C.2 shows how the system (for $\gamma - \gamma_c > 0$) give rise to a limit cycle whose amplitude does not depend on the initial conditions:

$$r_{st} = \sqrt{-(\gamma - \gamma_c)\frac{\mu_r}{\beta_r}}.$$

The equation for θ shows how the first correction to frequency depends on the amplitude squared, prototypical behavior in this type of bifurcations. Substituting the limit cycle equation in the corresponding one for θ, we find:

$$\theta = \theta_0 + (\gamma - \gamma_c)\left(\mu_i - \mu_r \frac{\beta_i}{\beta_r}\right)t,$$

where the dependent term of t is the correction to the oscillation frequency to order $\gamma - \gamma_c$, which we call ω_2; at first order for the limit cycle, the solution we have is:

$$\boldsymbol{x} = r_{st}e^{i\theta_0}e^{i(\omega_c + \omega_2)t}\boldsymbol{v}_1.$$

However, the normal form calculation should be used only when we already know which bifurcation we are facing. In any case, identifying a bifurcation involves studying the behavior of the eigenvalues as a function of the control parameter. In recognizing a Hopf bifurcation, there are also methods based on the observation of the phase space that do not involve the calculation of eigenvalues, such as the Poincaré-Bendixson theorem, valid only in systems with two degrees of freedom [213]. However, the following theorem assures the existence of a Hopf bifurcation if there is a system such as the one given by equation C.0.4 having a fixed point at $(\boldsymbol{x}_{st}, \gamma_c)$ and that furthermore obeys [244]:

1. The Jacobian matrix $\frac{\partial \boldsymbol{f}}{\partial \boldsymbol{x}}$ at the fixed point has only one pair of purely imaginary values, and all others have real part other than 0.

2. The so-called transversality condition is satisfied, which implies:

$$\frac{d}{d\gamma}\left[\text{Re}\lambda(\gamma)\right]\bigg|_{\gamma=\gamma_c} \neq 0.$$

In that case, the imaginary eigenvalues, $\lambda(\gamma)$ and $\overline{\lambda}(\gamma)$, vary smoothly with γ in a neighborhood of the bifurcation point and the normal form of the system can be written as in equation C.0.8. Moreover, if $\beta_r \neq 0$, there exist periodically stable trajectories for $\beta_r < 0$ and repulsive ones if $\beta_r > 0$. Thus, if the two conditions of the theorem are satisfied, we know that we are dealing with a Hopf bifurcation, and we can even know whether the limit cycle that arises will be stable or not. Actually, the stability in function of β_r is elementary to prove by analyzing the r-coordinate evolution equation. The sign of β_r further classifies these bifurcations into two types, supercritical if $\beta_r < 0$ and subcritical if $\beta_r > 0$. To summarize, supercritical bifurcations appear when the equilibrium point loses stability and becomes a stable limit cycle for γ greater than γ_c, as shown in figure C.3. In contrast, subcritical bifurcations appear when the stable equilibrium point becomes an unstable limit cycle and can become potentially dangerous for stability as they can lead the system behavior to jump far away to non-desired scenarios [245].
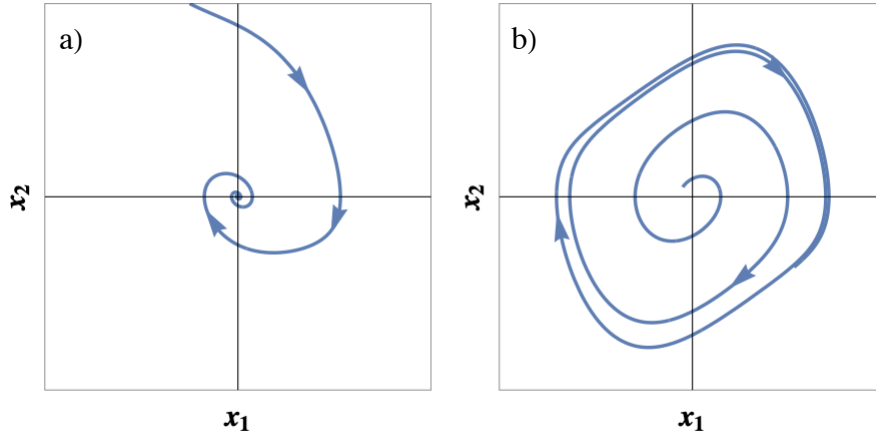

Figure C.3: A supercritical Hopf bifurcation behavior showing a) stability, for $\gamma < \gamma_c$, and b) a stable limit cycle, $\gamma > \gamma_c$.

Bibliography

[1] J. Gayon, *Darwinism's struggle for survival: heredity and the hypothesis of natural selection.* Cambridge University Press, 1998.

[2] C. Sanchez, H. Arribart, and M. M. G. Guille, "Biomimetism and bioinspiration as tools for the design of innovative materials and systems," *Nature materials*, vol. 4, no. 4, pp. 277–288, 2005.

[3] M. O. Aburto, M. de los Angeles Carvajal, B. Barr, E. B. Barbier, D. F. Boesch, J. Boyd, L. B. Crowder, R. Cudney-Bueno, T. Essington, E. Ezcurra, *et al.*, *Ecosystem-based management for the oceans.* Island Press, 2012.

[4] G. Bruzzone, R. Ferretti, and A. Odetti, "Unmanned marine vehicles," 2021.

[5] Cruise Lines International Association, "Contribution of Cruise Tourism to the Economies of Europe 2017." 2018.

[6] Congress of the United States, Congressional Budget Office, "An Analysis of the Navy's Fiscal Year 2017 Shipbuilding Plan." 2017.

[7] National Oceanic and Atmospheric Administration, U.S. Department of Commerce , "Economic impact of U.S. commercial, recreational fishing remains strong." 2018.

[8] J. Gray, "Studies in animal locomotion: VI. the propulsive powers of the dolphin," *Journal of experimental biology*, vol. 13, no. 2, pp. 192–199, 1936.

[9] F. E. Fish, "The myth and reality of gray's paradox: implication of dolphin drag reduction for technology," *Bioinspiration & biomimetics*, vol. 1, no. 2, p. R17, 2006.

[10] F. E. Fish, P. Legac, T. M. Williams, and T. Wei, "Measurement of hydrodynamic force generation by swimming dolphins using bubble dpiv," *Journal of Experimental Biology*, vol. 217, no. 2, pp. 252–260, 2014.

[11] W. Kohnen, "Human exploration of the deep seas: Fifty years and the inspiration continues," *Marine Technology Society Journal*, vol. 43, no. 5, pp. 42–62, 2009.

[12] G. S. Triantafyllou, M. S. Triantafyllou, and M. A. Grosenbaugh, "Optimal thrust development in oscillating foils with application to fish propulsion," *Journal of Fluids and Structures*, vol. 7, no. 2, pp. 205–224, 1993.

[13] J. M. Anderson, K. Streitlien, D. Barrett, and M. S. Triantafyllou, "Oscillating foils of high propulsive efficiency," *Journal of Fluid mechanics*, vol. 360, pp. 41–72, 1998.

[14] C. Rossi, J. Colorado, W. Coral, and A. Barrientos, "Bending continuous structures with smas: a novel robotic fish design," *Bioinspiration & biomimetics*, vol. 6, no. 4, p. 045005, 2011.

[15] F. Gibouin, C. Raufaste, Y. Bouret, and M. Argentina, "Study of the thrust–drag balance with a swimming robotic fish," *Physics of Fluids*, vol. 30, no. 9, p. 091901, 2018.

[16] J. Zhu, C. White, D. K. Wainwright, V. Di Santo, G. V. Lauder, and H. Bart-Smith, "Tuna robotics: A high-frequency experimental platform exploring the performance space of swimming fishes," *Science Robotics*, vol. 4, no. 34, 2019.

[17] J. Yu, S. Chen, Z. Wu, and W. Wang, "On a miniature free-swimming robotic fish with multiple sensors," *International Journal of Advanced Robotic Systems*, vol. 13, no. 2, p. 62, 2016.

[18] A. Ravalli, C. Rossi, and G. Marrazza, "Bio-inspired fish robot based on chemical sensors," *Sensors and Actuators B: Chemical*, vol. 239, pp. 325–329, 2017.

[19] D. Ji, F. U. Rehman, S. A. Ajwad, K. Shahani, S. Sharma, R. Sutton, S. Li, Z. Ye, H. Zhu, and S. Zhu, "Design and development of autonomous robotic fish for object detection and tracking," *International Journal of Advanced Robotic Systems*, vol. 17, no. 3, p. 1729881420925284, 2020.

[20] W. Coral, C. Rossi, O. M. Curet, and D. Castro, "Design and assessment of a flexible fish robot actuated by shape memory alloys," *Bioinspiration & biomimetics*, vol. 13, no. 5, p. 056009, 2018.

[21] R. Bainbridge, "The speed of swimming of fish as related to size and to the frequency and amplitude of the tail beat," *Journal of experimental biology*, vol. 35, no. 1, pp. 109–133, 1958.

[22] M. Triantafyllou, G. Triantafyllou, and R. Gopalkrishnan, "Wake mechanics for thrust generation in oscillating foils," *Physics of Fluids A: Fluid Dynamics*, vol. 3, no. 12, pp. 2835–2837, 1991.

[23] G. K. Taylor, R. L. Nudds, and A. L. Thomas, "Flying and swimming animals cruise at a strouhal number tuned for high power efficiency," *Nature*, vol. 425, no. 6959, pp. 707–711, 2003.

[24] M. Gazzola, M. Argentina, and L. Mahadevan, "Scaling macroscopic aquatic locomotion," *Nature Physics*, vol. 10, no. 10, pp. 758–761, 2014.

[25] M. Saadat, F. E. Fish, A. Domel, V. Di Santo, G. Lauder, and H. Haj-Hariri, "On the rules for aquatic locomotion," *Physical Review Fluids*, vol. 2, no. 8, p. 083102, 2017.

[26] M. Sakai, K. Aoki, K. Sato, M. Amano, R. W. Baird, D. L. Webster, G. S. Schorr, and N. Miyazaki, "Swim speed and acceleration measurements of short-finned pilot whales (Globicephala macrorhynchus) in Hawaii," *Mammal study*, vol. 36, no. 1, pp. 55–59, 2011.

[27] D. E. Cade, K. R. Barr, J. Calambokidis, A. S. Friedlaender, and J. A. Goldbogen, "Determining forward speed from accelerometer jiggle in aquatic environments," *Journal of Experimental Biology*, vol. 221, no. 2, p. jeb170449, 2018.

[28] M. M. Koochesfahani, "Vortical patterns in the wake of an oscillating airfoil," *AIAA journal*, vol. 27, no. 9, pp. 1200–1205, 1989.

[29] L. Schouveiler, F. Hover, and M. Triantafyllou, "Performance of flapping foil propulsion," *Journal of fluids and structures*, vol. 20, no. 7, pp. 949–959, 2005.

[30] D. B. Quinn, G. V. Lauder, and A. J. Smits, "Scaling the propulsive performance of heaving flexible panels," *Journal of fluid mechanics*, vol. 738, pp. 250–267, 2014.

[31] D. Floryan, T. Van Buren, and A. J. Smits, "Efficient cruising for swimming and flying animals is dictated by fluid drag," *Proceedings of the National Academy of Sciences*, vol. 115, no. 32, pp. 8116–8118, 2018.

[32] R. H. Peters and R. H. Peters, *The ecological implications of body size*, vol. 2. Cambridge university press, 1986.

[33] T. Y. Wu, "Introduction to the scaling of aquatic animal locomotion," tech. rep., California Inst. of Tech. Pasadena, 1977.

[34] R. Bale, M. Hao, A. P. S. Bhalla, and N. A. Patankar, "Energy efficiency and allometry of movement of swimming and flying animals," *Proceedings of the National Academy of Sciences*, vol. 111, no. 21, pp. 7517–7521, 2014.

[35] K. Sato, Y. Watanuki, A. Takahashi, P. J. Miller, H. Tanaka, R. Kawabe, P. J. Ponganis, Y. Handrich, T. Akamatsu, Y. Watanabe, *et al.*, "Stroke frequency, but not swimming speed, is related to body size in free-ranging seabirds, pinnipeds and cetaceans," *Proceedings of the Royal Society B: Biological Sciences*, vol. 274, no. 1609, pp. 471–477, 2007.

[36] A. Bejan and J. H. Marden, "Unifying constructal theory for scale effects in running, swimming and flying," *Journal of Experimental Biology*, vol. 209, no. 2, pp. 238–248, 2006.

[37] W. T. Gough, P. S. Segre, K. Bierlich, D. E. Cade, J. Potvin, F. E. Fish, J. Dale, J. di Clemente, A. S. Friedlaender, D. W. Johnston, *et al.*, "Scaling of swimming performance in baleen whales," *Journal of Experimental Biology*, vol. 222, no. 20, p. jeb204172, 2019.

[38] J. Hunter and J. Zweifel, "Swimming speed, tail beat frequency, tail beat amplitude and size in jack mackerel, Trachurus symmetricus, and other fishes," *Fish. Bull.*, vol. 69, pp. 253–266, 1971.

[39] P. W. Webb, "Kinematics of lake sturgeon, Acipenser fulvescens, at cruising speeds," *Canadian Journal of Zoology*, vol. 64, no. 10, pp. 2137–2141, 1986.

[40] P. W. Webb, "Steady swimming kinematics of tiger musky, an esociform accelerator, and rainbow trout, a generalist cruiser," *Journal of Experimental Biology*, vol. 138, no. 1, pp. 51–69, 1988.

[41] J. Videler and F. Hess, "Fast continuous swimming of two pelagic predators, saithe (Pollachius virens) and mackerel (Scomber scombrus): a kinematic analysis," *Journal of experimental biology*, vol. 109, no. 1, pp. 209–228, 1984.

[42] P. Webb and R. S. Keyes, "Swimming kinematics of sharks," *Fishery Bulletin*, vol. 80, no. 4, pp. 803–812, 1982.

[43] L. J. Rosenberger and M. W. Westneat, "Functional morphology of undulatory pectoral fin locomotion in the stingray Taeniura lymma (Chondrichthyes: Dasyatidae)," *Journal of Experimental Biology*, vol. 202, no. 24, pp. 3523–3539, 1999.

[44] F. E. Fish, "Comparative kinematics and hydrodynamics of odontocete cetaceans: morphological and ecological correlates with swimming performance.," *The Journal of experimental biology*, vol. 201, no. 20, pp. 2867–2877, 1998.

[45] F. E. Fish, "Kinematics of undulatory swimming in the american alligator," *Copeia*, pp. 839–843, 1984.

[46] T. Kojeszewski and F. E. Fish, "Swimming kinematics of the florida manatee (trichechus manatus latirostris): hydrodynamic analysis of an undulatory mammalian swimmer," *Journal of Experimental Biology*, vol. 210, no. 14, pp. 2411–2418, 2007.

[47] J. A. Goldbogen, J. Calambokidis, R. E. Shadwick, E. M. Oleson, M. A. McDonald, and J. A. Hildebrand, "Kinematics of foraging dives and lunge-feeding in fin whales," *Journal of Experimental Biology*, vol. 209, no. 7, pp. 1231–1244, 2006.

[48] K. Sato, K. Shiomi, Y. Watanabe, Y. Watanuki, A. Takahashi, and P. J. Ponganis, "Scaling of swim speed and stroke frequency in geometrically similar penguins: they swim optimally to minimize cost of transport," *Proceedings of the Royal Society B: Biological Sciences*, vol. 277, no. 1682, pp. 707–714, 2010.

[49] B. D. Clark and W. Bemis, "Kinematics of swimming of penguins at the Detroit Zoo," *Journal of Zoology*, vol. 188, no. 3, pp. 411–428, 1979.

[50] R. J. Wassersug and K. V. S. Hoff, "The kinematics of swimming in anuran larvae," *Journal of experimental Biology*, vol. 119, no. 1, pp. 1–30, 1985.

[51] F. E. Fish, S. Innes, and K. Ronald, "Kinematics and estimated thrust production of swimming harp and ringed seals," *Journal of Experimental Biology*, vol. 137, no. 1, pp. 157–173, 1988.

[52] M. R. Hirt, W. Jetz, B. C. Rall, and U. Brose, "A general scaling law reveals why the largest animals are not the fastest," *Nature Ecology & Evolution*, vol. 1, no. 8, pp. 1116–1122, 2017.

[53] D. A. Pabst, "Springs in swimming animals," *American Zoologist*, vol. 36, no. 6, pp. 723–735, 1996.

[54] B. K. Ahlborn, R. W. Blake, and W. M. Megill, "Frequency tuning in animal locomotion," *Zoology*, vol. 109, no. 1, pp. 43–53, 2006.

[55] F. E. Fish and C. A. Hui, "Dolphin swimming–a review," *Mammal Review*, vol. 21, no. 4, pp. 181–195, 1991.

[56] C. M. Pollock and R. E. Shadwick, "Relationship between body mass and biomechanical properties of limb tendons in adult mammals," *American Journal of Physiology-Regulatory, Integrative and Comparative Physiology*, vol. 266, no. 3, pp. R1016–R1021, 1994.

[57] J. E. Bertram, *Understanding mammalian locomotion: concepts and applications*. John Wiley & Sons, 2016.

[58] A. C. Economos, "Elastic and/or geometric similarity in mammalian design," 1983.

[59] A. C. Economos, "On structural theories of basal metabolic rate," *Journal of theoretical Biology*, vol. 80, no. 4, pp. 445–450, 1979.

[60] C. M. Pollock and R. E. Shadwick, "Allometry of muscle, tendon, and elastic energy storage capacity in mammals," *American Journal of Physiology-Regulatory, Integrative and Comparative Physiology*, vol. 266, no. 3, pp. 1022–1031, 1994.

[61] J. H. Marden and L. R. Allen, "Molecules, muscles, and machines: universal performance characteristics of motors," *Proceedings of the National Academy of Sciences*, vol. 99, no. 7, pp. 4161–4166, 2002.

[62] J. L. Krans, "The sliding filament theory of muscle contraction," *Nature Education*, vol. 3, no. 9, p. 66, 2010.

[63] C. Cohen, B. D. Texier, G. Laffaye, L. Auvray, and C. Clanet, "Weightlifting and the actomyosin cycle," *Proceedings of the Royal Society A: Mathematical, Physical and Engineering Sciences*, vol. 471, no. 2184, p. 20150473, 2015.

[64] J. T. Finer, R. M. Simmons, and J. A. Spudich, "Single myosin molecule mechanics: piconewton forces and nanometre steps," *Nature*, vol. 368, no. 6467, pp. 113–119, 1994.

[65] E. H. Dill, *Continuum mechanics: elasticity, plasticity, viscoelasticity.* CRC press, 2006.

[66] J.-Y. Cheng, T. Pedley, and J. Altringham, "A continuous dynamic beam model for swimming fish," *Philosophical Transactions of the Royal Society of London. Series B: Biological Sciences*, vol. 353, no. 1371, pp. 981–997, 1998.

[67] T. Pedley and S. Hill, "Large-amplitude undulatory fish swimming: fluid mechanics coupled to internal mechanics," *Journal of Experimental Biology*, vol. 202, no. 23, pp. 3431–3438, 1999.

[68] S. Ramananarivo, R. Godoy-Diana, and B. Thiria, "Passive elastic mechanism to mimic fish-muscle action in anguilliform swimming," *Journal of The Royal Society Interface*, vol. 10, no. 88, p. 20130667, 2013.

[69] L. Landau and E. Lifshitz, "Fluid mechanics," *Course of Theoretical Physics*, vol. 6, 1987.

[70] K. V. Mackenzie, "Nine-term equation for sound speed in the oceans," *The Journal of the Acoustical Society of America*, vol. 70, no. 3, pp. 807–812, 1981.

[71] C. Wang, "Exact solutions of the steady-state navier-stokes equations," *Annual Review of Fluid Mechanics*, vol. 23, no. 1, pp. 159–177, 1991.

[72] S. Childress, *Mechanics of swimming and flying.* No. 2, Cambridge University Press, 1981.

[73] E. M. Purcell, "Life at low reynolds number," *American journal of physics*, vol. 45, no. 1, pp. 3–11, 1977.

[74] E. Lauga and T. R. Powers, "The hydrodynamics of swimming microorganisms," *Reports on Progress in Physics*, vol. 72, no. 9, p. 096601, 2009.

[75] O. S. Pak, E. Lauga, C. Duprat, and H. Stone, *Theoretical models of low-Reynolds-number locomotion.* Royal Society of Chemistry, 2015.

[76] R. M. Alexander, *Principles of animal locomotion.* Princeton University Press, 2013.

[77] G. V. Lauder and E. D. Tytell, "Hydrodynamics of undulatory propulsion," *Fish physiology*, vol. 23, pp. 425–468, 2005.

[78] C. Wardle, J. Videler, and J. Altringham, "Tuning in to fish swimming waves: body form, swimming mode and muscle function," *The Journal of experimental biology*, vol. 198, no. 8, pp. 1629–1636, 1995.

[79] Wikimedia Commons, "Pacific sea nettle (Chrysaora fuscescens) at the Monterey Bay Aquarium in California," 2005.

[80] Wikimedia Commons, "Octopus Vulgaris," 2007.

[81] Wikimedia Commons, "Dugong Picture," 2015.

[82] Wikimedia Commons, "Great white shark at Isla Guadalupe, Mexico, August 2006. Shot with Nikon D70s in Ikelite housing, in natural light," 2006.

[83] J. Gray, "Studies in animal locomotion: I. the movement of fish with special reference to the eel," *Journal of experimental biology*, vol. 10, no. 1, pp. 88–104, 1933.

[84] G. B. Gillis, "Undulatory locomotion in elongate aquatic vertebrates: anguilliform swimming since Sir James Gray," *American Zoologist*, vol. 36, no. 6, pp. 656–665, 1996.

[85] G. I. Taylor, "Analysis of the swimming of long and narrow animals," *Proceedings of the Royal Society of London. Series A. Mathematical and Physical Sciences*, vol. 214, no. 1117, pp. 158–183, 1952.

[86] P. K. Kundu and I. M. Cohen, "Fluid mechanics," 2002.

[87] M. Lighthill, "Note on the swimming of slender fish," *Journal of fluid Mechanics*, vol. 9, no. 2, pp. 305–317, 1960.

[88] S. J. Lighthill, *Mathematical biofluiddynamics*. SIAM, 1975.

[89] M. Lighthill, "Hydromechanics of aquatic animal propulsion," *Annual review of fluid mechanics*, vol. 1, no. 1, pp. 413–446, 1969.

[90] M. J. Lighthill, "Aquatic animal propulsion of high hydromechanical efficiency," *Journal of Fluid Mechanics*, vol. 44, no. 2, pp. 265–301, 1970.

[91] M. J. Lighthill, "Large-amplitude elongated-body theory of fish locomotion," *Proceedings of the Royal Society of London. Series B. Biological Sciences*, vol. 179, no. 1055, pp. 125–138, 1971.

[92] F. Candelier, F. Boyer, and A. Leroyer, "Three-dimensional extension of Lighthill's large-amplitude elongated-body theory of fish locomotion," *Journal of Fluid Mechanics*, vol. 674, pp. 196–226, 2011.

[93] Z. Yu and C. Eloy, "Extension of lighthill's slender-body theory to moderate aspect ratios," *Journal of Fluids and Structures*, vol. 76, pp. 84–94, 2018.

[94] T. Y. Wu, "Swimming of a waving plate," *Journal of Fluid Mechanics*, vol. 10, no. 3, pp. 321–344, 1960.

[95] T. Y. Wu, "Hydromechanics of swimming propulsion. Part 1. Swimming of a two-dimensional flexible plate at variable forward speeds in an inviscid fluid," *Journal of Fluid Mechanics*, vol. 46, no. 2, pp. 337–355, 1971.

[96] T. Y. Wu, "On theoretical modeling of aquatic and aerial animal locomotion," *Advances in applied mechanics*, vol. 38, pp. 291–353, 2002.

[97] T. Y. Wu, "A nonlinear theory for a flexible unsteady wing," *Journal of Engineering Mathematics*, vol. 58, no. 1, pp. 279–287, 2007.

[98] T. Y. Wu, "Fish swimming and bird/insect flight," *Annual Review of Fluid Mechanics*, vol. 43, pp. 25–58, 2011.

[99] H. Wagner, "Über die entstehung des dynamischen Auftriebes von Tragflügeln," *ZAMM - Journal of Applied Mathematics and Mechanics / Zeitschrift für Angewandte Mathematik und Mechanik*, vol. 5, no. 1, pp. 17–35, 1925.

[100] T. Theodorsen and W. Mutchler, "General theory of aerodynamic instability and the mechanism of flutter," 1935.

[101] I. Garrick *et al.*, "Propulsion of a flapping and oscillating airfoil," *NACA report*, vol. 567, pp. 419–427, 1937.

[102] H. G. Kussner, "Zusammenfassender bericht über den instationären auftrieb von flügeln," *Luftfahrtforschung*, vol. 13, pp. 420–423, 1936.

[103] T. H. von Karman and W. R. Sears, "Airfoil theory for non-uniform motion," *Journal of the Aeronautical Sciences*, vol. 5, no. 10, pp. 379–390, 1938.

[104] W. R. Sears, *A systematic presentation of the theory of thin airfoils in non-uniform motion*. Phd thesis, California Institute of Technology, 1938.

[105] H. Kussner and I. Schwarz, "The oscillating wing with aerodynamically balanced elevator," *NACA report*, vol. 991, 1941.

[106] J. M. Greenberg, "Airfoil in sinusoidal motion in a pulsating stream," 1947.

[107] J. E. McCune, C. M. G. Lam, and M. T. Scott, "Nonlinear aerodynamics of two-dimensional airfoils in severe maneuver," *AIAA journal*, vol. 28, no. 3, pp. 385–393, 1990.

[108] J. E. McCune and T. S. Tavares, "Perspective: Unsteady wing theory—the Kármán/Sears Legacy," 1993.

[109] T. Weis-Fogh, "Unusual mechanisms for the generation of lift in flying animals," *Scientific American*, vol. 233, no. 5, pp. 80–87, 1975.

[110] J. Rayner, "Estimating power curves of flying vertebrates," *Journal of Experimental Biology*, vol. 202, no. 23, pp. 3449–3461, 1999.

[111] A. B. Kesel, "Aerodynamic characteristics of dragonfly wing sections compared with technical aerofoils," *Journal of experimental biology*, vol. 203, no. 20, pp. 3125–3135, 2000.

[112] A. L. Thomas and G. K. Taylor, "Animal flight dynamics I. Stability in gliding flight," *Journal of theoretical biology*, vol. 212, no. 3, pp. 399–424, 2001.

[113] J. Katz and A. Plotkin, *Low-speed aerodynamics*, vol. 13. Cambridge university press, 2001.

[114] J. W. Brown and R. V. Churchill, *Complex variables and applications*. McGraw-Hill Book Company, 2009.

[115] W. P. Walker, *Unsteady Aerodynamics of Deformable Thin Airfoils, Master Thesis*. PhD thesis, Virginia Tech, 2009.

[116] E. Guyon, J.-P. Hulin, L. Petit, and P. G. de Gennes, *Hydrodynamique physique*. EDP sciences Les Ulis, France, 2001.

[117] M. Abramowitz and I. A. Stegun, eds., *Handbook of mathematical functions: with formulas, graphs, and mathematical tables*. Dover books on mathematics, New York, NY: Dover Publ, 9. dover print. ed., 1972.

[118] W. F. Durand, *Basic Ideas of Wing Theory: Flow around an Airfoil*, pp. 1–24. Berlin, Heidelberg: Springer Berlin Heidelberg, 1935.

[119] R. Fernandez-Feria, "Linearized propulsion theory of flapping airfoils revisited," *Physical Review Fluids*, vol. 1, no. 8, p. 084502, 2016.

[120] R. Fernandez-Feria, "Note on optimum propulsion of heaving and pitching airfoils from linear potential theory," *Journal of Fluid Mechanics*, vol. 826, pp. 781–796, 2017.

[121] J. W. Edwards, *Unsteady aerodynamic modeling and active aeroelastic control*. PhD thesis, Dept. of Aeronautics and Astronautics, Stanford University., 1977.

[122] W. Walker and M. Patil, "Unsteady aerodynamics of deformable thin airfoils," in *48th AIAA Aerospace Sciences Meeting Including the New Horizons Forum and Aerospace Exposition*, p. 322, 2010.

[123] W. P. Walker, *Optimization of harmonically deforming thin airfoils and membrane wings for optimum thrust and efficiency, PhD Thesis*. PhD thesis, Virginia Tech, 2012.

[124] C. O. Johnston, "Review, extension, and application of unsteady thin airfoil theory," *CIMSS Report*, pp. 04–101, 2004.

[125] D. B. Quinn, G. V. Lauder, and A. J. Smits, "Maximizing the efficiency of a flexible propulsor using experimental optimization," *Journal of Fluid Mechanics*, vol. 767, pp. 430–448, 2015.

[126] K. N. Lucas, G. V. Lauder, and E. D. Tytell, "Airfoil-like mechanics generate thrust on the anterior body of swimming fishes," *Proceedings of the National Academy of Sciences*, vol. 117, no. 19, pp. 10585–10592, 2020.

[127] J. Videler, "Swimming movements, body structure and propulsion in cod Gadus morhua," in *Symp. Zool. Soc. Lond*, vol. 48, pp. 1–27, 1981.

[128] J. Videler and P. Kamermans, "Differences between upstroke and downstroke in swimming dolphins," *Journal of Experimental Biology*, vol. 119, no. 1, pp. 265–274, 1985.

[129] T. Tandler, E. Gellman, D. De La Cruz, and D. J. Ellerby, "Drag coefficient estimates from coasting bluegill sunfish Lepomis macrochirus," *Journal of fish biology*, vol. 94, no. 3, pp. 532–534, 2019.

[130] T. G. Lang, *Speed, Power, And Drag Measurements of Dolphins and Porpoises*, pp. 553–572. Boston, MA: Springer US, 1975.

[131] E. Buckingham, "On physically similar systems; illustrations of the use of dimensional equations," *Physical review*, vol. 4, no. 4, p. 345, 1914.

[132] M. Goldstein and R. Thaler, "Bessel functions for large arguments," *Mathematics of Computation*, vol. 12, no. 61, pp. 18–26, 1958.

[133] J. J. Rohr and F. E. Fish, "Strouhal numbers and optimization of swimming by odontocete cetaceans," *Journal of Experimental Biology*, vol. 207, no. 10, pp. 1633–1642, 2004.

[134] A. Lowndes, "XXXII —density of fishes: Some notes on the swimming of fish to be correlated with density, sinking factor and load carried," *Annals and Magazine of Natural History*, vol. 8, no. 88, pp. 241–256, 1955.

[135] A. Mackowski and C. Williamson, "Direct measurement of thrust and efficiency of an airfoil undergoing pure pitching," *Journal of Fluid Mechanics*, vol. 765, pp. 524–543, 2015.

[136] R. Fernandez-Feria and E. Sanmiguel-Rojas, "Comparison of aerodynamic models for two-dimensional pitching foils with experimental data," *Physics of Fluids*, vol. 31, no. 5, p. 057104, 2019.

[137] W. H. Press, S. A. Teukolsky, W. T. Vetterling, and B. P. Flannery, *Numerical Recipes 3rd Edition: The Art of Scientific Computing*. USA: Cambridge University Press, 3 ed., 2007.

[138] D. A. Read, F. Hover, and M. Triantafyllou, "Forces on oscillating foils for propulsion and maneuvering," *Journal of Fluids and Structures*, vol. 17, no. 1, pp. 163–183, 2003.

[139] D. Floryan, T. Van Buren, C. W. Rowley, and A. J. Smits, "Scaling the propulsive performance of heaving and pitching foils," *Journal of Fluid Mechanics*, vol. 822, pp. 386–397, 2017.

[140] D. Gross, Y. Roux, C. Raufaste, and M. Argentina, "Drag analysis with a self-propelled flexible swimmer," *Phys. Rev. Fluids*, vol. 6, p. 053101, May 2021.

[141] M. Gazzola, M. Argentina, and L. Mahadevan, "Gait and speed selection in slender inertial swimmers," *Proceedings of the National Academy of Sciences*, vol. 112, no. 13, pp. 3874–3879, 2015.

[142] J. Sánchez-Rodríguez, C. Raufaste, and M. Argentina, "A minimal model of self propelled locomotion," *Journal of Fluids and Structures*, vol. 97, p. 103071, 2020.

[143] H. Bleckmann, J. Mogdans, and S. L. Coombs, eds., *Flow Sensing in Air and Water*. Springer Berlin Heidelberg, 2014.

[144] T. Hara, "Olfaction and gustation in fish: an overview," *Acta Physiologica Scandinavica*, vol. 152, no. 2, pp. 207–217, 1994.

[145] T. W. Gillespie, "Remote sensing of animals," *Progress in Physical Geography: Earth and Environment*, vol. 25, no. 3, pp. 355–362, 2001.

[146] H. Bleckmann and R. Zelick, "Lateral line system of fish," *Integrative Zoology*, vol. 4, no. 1, pp. 13–25, 2009.

[147] J. C. Liao, D. N. Beal, G. V. Lauder, and M. S. Triantafyllou, "The Kármán gait: novel body kinematics of rainbow trout swimming in a vortex street," *Journal of experimental biology*, vol. 206, no. 6, pp. 1059–1073, 2003.

[148] J. C. Liao, "Neuromuscular control of trout swimming in a vortex street: implications for energy economy during the Karman gait," *Journal of Experimental Biology*, vol. 207, no. 20, pp. 3495–3506, 2004.

[149] D. Beal, F. Hover, M. Triantafyllou, J. Liao, and G. V. Lauder, "Passive propulsion in vortex wakes," *Journal of Fluid Mechanics*, vol. 549, pp. 385–402, 2006.

[150] R. D. Blevins, *Flow-induced vibration*. Van Nostrand Reinhold Company, 1990.

[151] J. C. Liao, D. N. Beal, G. V. Lauder, and M. S. Triantafyllou, "Fish exploiting vortices decrease muscle activity," *Science*, vol. 302, no. 5650, pp. 1566–1569, 2003.

[152] D. M. Guthrie, *Role of Vision in Fish Behaviour*, pp. 75–113. Boston, MA: Springer US, 1986.

[153] H. Bleckmann, *Reception of Hydrodynamic Stimuli in Aquatic and Semiaquatic Animals*. Fortschritte der Zoologie, G. Fischer Verlag, 1994.

[154] J. C. Liao, *Functional Architecture of Lateral Line Afferent Neurons in Larval Zebrafish*, pp. 319–332. Berlin, Heidelberg: Springer Berlin Heidelberg, 2014.

[155] L. Ristroph, J. C. Liao, and J. Zhang, "Lateral line layout correlates with the differential hydrodynamic pressure on swimming fish," *Phys. Rev. Lett.*, vol. 114, p. 018102, Jan 2015.

[156] A. J. Ijspeert, "Central pattern generators for locomotion control in animals and robots: A review," *Neural Networks*, vol. 21, no. 4, pp. 642–653, 2008. Robotics and Neuroscience.

[157] G. Orlovski, T. Deliagina, and S. Grillner, *Neuronal Control of Locomotion: From Mollusc to Man*. Oxford Neuroscience Series, Oxford University Press, 1999.

[158] P. A. Guertin, "The mammalian central pattern generator for locomotion," *Brain Research Reviews*, vol. 62, no. 1, pp. 45–56, 2009.

[159] B. L. Roberts, "The Response of a Proprioceptor to the Undulatory Movements of Dogfish," *Journal of Experimental Biology*, vol. 51, pp. 775–785, 12 1969.

[160] E. Örjan, G. Sten, and L. Anders, "The neural control of fish swimming studied through numerical simulations," *Adaptive Behavior*, vol. 3, no. 4, pp. 363–384, 1995.

[161] S. Rossignol, R. Dubuc, and J.-P. Gossard, "Dynamic sensorimotor interactions in locomotion," *Physiological Reviews*, vol. 86, no. 1, pp. 89–154, 2006. PMID: 16371596.

[162] S. Grillner, "Biological pattern generation: The cellular and computational logic of networks in motion," *Neuron*, vol. 52, no. 5, pp. 751–766, 2006.

[163] V. Dietz, "Proprioception and locomotor disorders," *Nature Reviews Neuroscience*, vol. 3, pp. 781–790, Oct. 2002.

[164] J. C. Tuthill and E. Azim, "Proprioception," *Current Biology*, vol. 28, no. 5, pp. R194–R203, 2018.

[165] K. G. Pearson, "Proprioceptive regulation of locomotion," *Current Opinion in Neurobiology*, vol. 5, no. 6, pp. 786–791, 1995.

[166] D. Ryczko, A. Simon, and A. J. Ijspeert, "Walking with salamanders: From molecules to biorobotics," *Trends in neurosciences*, vol. 43, p. 916—930, November 2020.

[167] B. E. Flammang and G. V. Lauder, "Pectoral fins aid in navigation of a complex environment by bluegill sunfish under sensory deprivation conditions," *Journal of Experimental Biology*, vol. 216, no. 16, pp. 3084–3089, 2013.

[168] R. Williams IV, N. Neubarth, and M. E. Hale, "The function of fin rays as proprioceptive sensors in fish," *Nature communications*, vol. 4, no. 1, pp. 1–6, 2013.

[169] R. Williams IV and M. E. Hale, "Fin ray sensation participates in the generation of normal fin movement in the hovering behavior of the bluegill sunfish (Lepomis macrochirus)," *Journal of Experimental Biology*, vol. 218, no. 21, pp. 3435–3447, 2015.

[170] S. A. Binning, "Touchy-feely fish fins," *Journal of Experimental Biology*, vol. 219, no. 11, pp. 1586–1586, 2016.

[171] Ö. Ekeberg and S. Grillner, "Simulations of neuromuscular control in lamprey swimming," *Philosophical Transactions of the Royal Society of London. Series B: Biological Sciences*, vol. 354, no. 1385, pp. 895–902, 1999.

[172] L. Guan, T. Kiemel, and A. H. Cohen, "Impact of movement and movement-related feedback on the lamprey central pattern generator for locomotion," *Journal of Experimental Biology*, vol. 204, no. 13, pp. 2361–2370, 2001.

[173] A. Visioli, *Practical PID Control.* Advances in Industrial Control, Springer London, 2006.

[174] K. Healy, T. H. Ezard, O. R. Jones, R. Salguero-Gómez, and Y. M. Buckley, "Animal life history is shaped by the pace of life and the distribution of age-specific mortality and reproduction," *Nature ecology & evolution*, vol. 3, no. 8, pp. 1217–1224, 2019.

[175] R. M. Alexander, *Locomotion of animals*, vol. 163. Springer, 1982.

[176] S. Grillner, "Neurobiological bases of rhythmic motor acts in vertebrates," *Science*, vol. 228, no. 4696, pp. 143–149, 1985.

[177] S. Grillner, "Neural networks for vertebrate locomotion," *Scientific American*, vol. 274, no. 1, pp. 64–69, 1996.

[178] H. L. Smith, *An introduction to delay differential equations with applications to the life sciences*, vol. 57. Springer New York, 2011.

[179] P. A. Dewey, B. M. Boschitsch, K. W. Moored, H. A. Stone, and A. J. Smits, "Scaling laws for the thrust production of flexible pitching panels," *Journal of Fluid Mechanics*, vol. 732, pp. 29–46, 2013.

[180] F. Paraz, C. Eloy, and L. Schouveiler, "Experimental study of the response of a flexible plate to a harmonic forcing in a flow," *Comptes Rendus Mécanique*, vol. 342, no. 9, pp. 532–538, 2014.

[181] F. Paraz, L. Schouveiler, and C. Eloy, "Thrust generation by a heaving flexible foil: Resonance, nonlinearities, and optimality," *Physics of Fluids*, vol. 28, no. 1, p. 011903, 2016.

[182] M. Brennan, I. Kovacic, A. Carrella, and T. Waters, "On the jump-up and jump-down frequencies of the duffing oscillator," *Journal of Sound and Vibration*, vol. 318, no. 4-5, pp. 1250–1261, 2008.

[183] J. Sánchez-Rodríguez, F. Celestini, C. Raufaste, and M. Argentina, "Proprioceptive mechanism for bioinspired fish swimming," *Physical Review Letters*, vol. 126, no. 23, p. 234501, 2021.

[184] L. Bernatchez and J. J. Dodson, "Relationship between bioenergetics and behavior in anadromous fish migrations," *Canadian Journal of Fisheries and Aquatic Sciences*, vol. 44, no. 2, pp. 399–407, 1987.

[185] V. van Ginneken, E. Antonissen, U. K. Müller, R. Booms, E. Eding, J. Verreth, and G. van den Thillart, "Eel migration to the sargasso: remarkably high swimming efficiency and low energy costs," *Journal of Experimental Biology*, vol. 208, no. 7, pp. 1329–1335, 2005.

[186] B. McElroy, A. DeLonay, and R. Jacobson, "Optimum swimming pathways of fish spawning migrations in rivers," *Ecology*, vol. 93, no. 1, pp. 29–34, 2012.

[187] G. E. Davis, J. Foster, C. E. Warren, and P. Doudoroff, "The influence of oxygen concentration on the swimming performance of juvenile pacific salmon at various temperatures," *Transactions of the American Fisheries Society*, vol. 92, no. 2, pp. 111–124, 1963.

[188] J. Brett, "The respiratory metabolism and swimming performance of young sockeye salmon," *Journal of the Fisheries Board of Canada*, vol. 21, no. 5, pp. 1183–1226, 1964.

[189] J. Brett, "Swimming performance of sockeye salmon (Oncorhynchus nerka) in relation to fatigue time and temperature," *Journal of the Fisheries Board of Canada*, vol. 24, no. 8, pp. 1731–1741, 1967.

[190] F. E. J. Fry and J. Hart, "Cruising speed of goldfish in relation to water temperature," *Journal of the Fisheries Board of Canada*, vol. 7, no. 4, pp. 169–175, 1948.

[191] J. C. Macleod and L. L. Smith Jr, "Effect of pulpwood fiber on oxygen consumption and swimming endurance of the fathead minnow, pimephales promelas," *Transactions of the American Fisheries Society*, vol. 95, no. 1, pp. 71–84, 1966.

[192] R. Bainbridge, "Speed and stamina in three fish," *Journal of Experimental Biology*, vol. 37, no. 1, pp. 129–153, 1960.

[193] R. Bainbridge, "Training, speed and stamina in trout," *Journal of Experimental Biology*, vol. 39, no. 4, pp. 537–555, 1962.

[194] A. E. Thomas, R. E. Burrows, and H. H. Chenoweth, *A device for stamina measurement of fingerling salmonids*, vol. 67. Bureau of Sport Fisheries and Wildlife, 1964.

[195] J. Brett, "The relation of size to rate of oxygen consumption and sustained swimming speed of sockeye salmon (Oncorhynchus nerka)," *Journal of the Fisheries Board of Canada*, vol. 22, no. 6, pp. 1491–1501, 1965.

[196] J. Brett, "The swimming energetics of salmon," *Scientific American*, vol. 213, no. 2, pp. 80–87, 1965.

[197] E. M. Goolish, "Aerobic and anaerobic scaling in fish," 1991.

[198] D. S. Glazier, "Beyond the '3/4-power law': variation in the intra-and interspecific scaling of metabolic rate in animals," *Biological reviews*, vol. 80, no. 4, pp. 611–662, 2005.

[199] M. Kleiber *et al.*, "Body size and metabolism," *Hilgardia*, vol. 6, no. 11, pp. 315–353, 1932.

[200] G. B. West, J. H. Brown, and B. J. Enquist, "A general model for the origin of allometric scaling laws in biology," *Science*, vol. 276, no. 5309, pp. 122–126, 1997.

[201] G. Li, I. Ashraf, B. François, D. Kolomenskiy, F. Lechenault, R. Godoy-Diana, and B. Thiria, "Burst-and-coast swimmers optimize gait by adapting unique intrinsic cycle," *Communications biology*, vol. 4, no. 1, pp. 1–7, 2021.

[202] W. W. Schultz and P. W. Webb, "Power requirements of swimming: do new methods resolve old questions?," *Integrative and Comparative Biology*, vol. 42, no. 5, pp. 1018–1025, 2002.

[203] J. J. Videler, *Fish swimming*, vol. 10. Springer Science & Business Media, 1993.

[204] D. Weihs, "Energetic advantages of burst swimming of fish," *Journal of Theoretical Biology*, vol. 48, no. 1, pp. 215–229, 1974.

[205] J. Videler, "Swimming movements, body structure and propulsion in cod gadus morhua," in *Symp. Zool. Soc. Lond*, vol. 48, pp. 1–27, 1981.

[206] J. J. Videler and D. Weihs, "Energetic advantages of burst-and-coast swimming of fish at high speeds," *Journal of Experimental Biology*, vol. 97, no. 1, pp. 169–178, 1982.

[207] L. Schwartz, *Théorie des distributions: Tome 1.* Hermann (Chartres), 1950.

[208] V. Plagianakos and E. W. Weisstein, "Differential evolution." https://mathworld.wolfram.com/DifferentialEvolution.html.

[209] I. M. Gelfand, R. A. Silverman, *et al.*, *Calculus of variations.* Courier Corporation, 2000.

[210] C. Lowe, "Kinematics and critical swimming speed of juvenile scalloped hammerhead sharks," *The Journal of experimental biology*, vol. 199, no. 12, pp. 2605–2610, 1996.

[211] K. P. Balanda and H. MacGillivray, "Kurtosis: a critical review," *The American Statistician*, vol. 42, no. 2, pp. 111–119, 1988.

[212] A. H. Salas and J. E. Castillo, "Exact solution to duffing equation and the pendulum equation," *Applied Mathematical Sciences*, vol. 8, no. 176, pp. 8781–8789, 2014.

[213] S. H. Strogatz, *Nonlinear dynamics and chaos with student solutions manual: With applications to physics, biology, chemistry, and engineering.* Addison-Wesley Pub, 1994.

[214] S. L. Brunton, B. R. Noack, and P. Koumoutsakos, "Machine learning for fluid mechanics," *Annual Review of Fluid Mechanics*, vol. 52, pp. 477–508, 2020.

[215] R. S. Sutton and A. G. Barto, *Reinforcement learning: An introduction.* MIT press, 2018.

[216] G. Reddy, A. Celani, T. J. Sejnowski, and M. Vergassola, "Learning to soar in turbulent environments," *Proceedings of the National Academy of Sciences*, vol. 113, no. 33, pp. 4877–4884, 2016.

[217] M. Gazzola, B. Hejazialhosseini, and P. Koumoutsakos, "Reinforcement learning and wavelet adapted vortex methods for simulations of self-propelled swimmers," *SIAM Journal on Scientific Computing*, vol. 36, no. 3, pp. B622–B639, 2014.

[218] M. Gazzola, A. A. Tchieu, D. Alexeev, A. de Brauer, and P. Koumoutsakos, "Learning to school in the presence of hydrodynamic interactions," *Journal of Fluid Mechanics*, vol. 789, pp. 726–749, 2016.

[219] S. Verma, G. Novati, and P. Koumoutsakos, "Efficient collective swimming by harnessing vortices through deep reinforcement learning," *Proceedings of the National Academy of Sciences*, vol. 115, no. 23, pp. 5849–5854, 2018.

[220] Y. Jiao, F. Ling, S. Heydari, E. Kanso, N. Heess, and J. Merel, "Learning to swim in potential flow," *Physical Review Fluids*, vol. 6, no. 5, p. 050505, 2021.

[221] S. Colabrese, K. Gustavsson, A. Celani, and L. Biferale, "Flow navigation by smart microswimmers via reinforcement learning," *Physical review letters*, vol. 118, no. 15, p. 158004, 2017.

[222] J. Schulman, S. Levine, P. Abbeel, M. Jordan, and P. Moritz, "Trust region policy optimization," in *International conference on machine learning*, pp. 1889–1897, PMLR, 2015.

[223] J. Schulman, F. Wolski, P. Dhariwal, A. Radford, and O. Klimov, "Proximal policy optimization algorithms," *arXiv preprint arXiv:1707.06347*, 2017.

[224] V. Mnih, K. Kavukcuoglu, D. Silver, A. Graves, I. Antonoglou, D. Wierstra, and M. Riedmiller, "Playing atari with deep reinforcement learning," *arXiv preprint arXiv:1312.5602*, 2013.

[225] C. J. Watkins, "Learning from delayed rewards," 1989.

[226] J. Christopher, "Watkins and Peter Dayan," *Q-Learning. Machine Learning*, vol. 8, no. 3, pp. 279–292, 1992.

[227] C. C. Aggarwal *et al.*, "Neural networks and deep learning," *Springer*, vol. 10, pp. 978–3, 2018.

[228] E. Shaw, "Schooling fishes: the school, a truly egalitarian form of organization in which all members of the group are alike in influence, offers substantial benefits to its participants," *American Scientist*, vol. 66, no. 2, pp. 166–175, 1978.

[229] B. L. Partridge, "The structure and function of fish schools," *Scientific american*, vol. 246, no. 6, pp. 114–123, 1982.

[230] D. Weihs, "Hydromechanics of fish schooling," *Nature*, vol. 241, no. 5387, pp. 290–291, 1973.

[231] M. Gazzola, P. Chatelain, W. M. Van Rees, and P. Koumoutsakos, "Simulations of single and multiple swimmers with non-divergence free deforming geometries," *Journal of Computational Physics*, vol. 230, no. 19, pp. 7093–7114, 2011.

[232] I. Ashraf, R. Godoy-Diana, J. Halloy, B. Collignon, and B. Thiria, "Synchronization and collective swimming patterns in fish (Hemigrammus bleheri)," *Journal of the Royal Society Interface*, vol. 13, no. 123, p. 20160734, 2016.

[233] R. Godoy-Diana, J. Vacher, V. Raspa, and B. Thiria, "On the fluid dynamical effects of synchronization in side-by-side swimmers," *Biomimetics*, vol. 4, no. 4, p. 77, 2019.

[234] L. Li, M. Nagy, J. M. Graving, J. Bak-Coleman, G. Xie, and I. D. Couzin, "Vortex phase matching as a strategy for schooling in robots and in fish," *Nature communications*, vol. 11, no. 1, pp. 1–9, 2020.

[235] L. Li, D. Liu, J. Deng, M. J. Lutz, and G. Xie, "Fish can save energy via proprioceptive sensing," *Bioinspiration & biomimetics*, vol. 16, no. 5, p. 056013, 2021.

[236] F. Schwab, E. T. Lunsford, T. Hong, F. Wiesemüller, M. Kovac, Y.-L. Park, O. Akanyeti, J. C. Liao, and A. Jusufi, "Body caudal undulation measured by soft sensors and emulated by soft artificial muscles," *Integrative and Comparative Biology*.

[237] A. H. Nayfeh, *Perturbation methods*. John Wiley & Sons, 2008.

[238] J. Kevorkian and J. D. Cole, *Perturbation methods in applied mathematics*, vol. 34. Springer, New York, 1981.

[239] J. K. Kevorkian and J. D. Cole, *Multiple scale and singular perturbation methods*, vol. 114. Springer Science & Business Media, 2012.

[240] L. Kantorovich and G. Akilov, *Functional analysis 2nd rev.* Pergamon Press English translation, 1982.

[241] S. Wiggins, S. Wiggins, and M. Golubitsky, *Introduction to applied nonlinear dynamical systems and chaos*, vol. 2. Springer, 1990.

[242] V. Arnold, *Ordinary Differential Equations*. Springer Textbook, Springer Berlin Heidelberg, 1992.

[243] J. E. Marsden and M. McCracken, *The Hopf bifurcation and its applications*, vol. 19. Springer Science & Business Media, 2012.

[244] J. Guckenheimer and P. Holmes, *Nonlinear oscillations, dynamical systems, and bifurcations of vector fields*, vol. 42. Springer Science & Business Media, 2013.

[245] A. H. Nayfeh and B. Balachandran, *Applied nonlinear dynamics: analytical, computational, and experimental methods.* John Wiley & Sons, 2008.